Multi-functionalization of micro- and nanoparticles for cancer theranostics

Ezhil Amirthalingam

ADVERTIMENT. La consulta d'aquesta tesi queda condicionada a l'acceptació de les següents condicions d'ús: La difusió d'aquesta tesi per mitjà del servei TDX (**www.tdx.cat**) i a través del Dipòsit Digital de la UB (**diposit.ub.edu**) ha estat autoritzada pels titulars dels drets de propietat intel·lectual únicament per a usos privats emmarcats en activitats d'investigació i docència. No s'autoritza la seva reproducció amb finalitats de lucre ni la seva difusió i posada a disposició des d'un lloc aliè al servei TDX ni al Dipòsit Digital de la UB. No s'autoritza la presentació del seu contingut en una finestra o marc aliè a TDX o al Dipòsit Digital de la UB (framing). Aquesta reserva de drets afecta tant al resum de presentació de la tesi com als seus continguts. En la utilització o cita de parts de la tesi és obligat indicar el nom de la persona autora.

ADVERTENCIA. La consulta de esta tesis queda condicionada a la aceptación de las siguientes condiciones de uso: La difusión de esta tesis por medio del servicio TDR (**www.tdx.cat**) y a través del Repositorio Digital de la UB (**diposit.ub.edu**) ha sido autorizada por los titulares de los derechos de propiedad intelectual únicamente para usos privados enmarcados en actividades de investigación y docencia. No se autoriza su reproducción con finalidades de lucro ni su difusión y puesta a disposición desde un sitio ajeno al servicio TDR o al Repositorio Digital de la UB. No se autoriza la presentación de su contenido en una ventana o marco ajeno a TDR o al Repositorio Digital de la UB (framing). Esta reserva de derechos afecta tanto al resumen de presentación de la tesis como a sus contenidos. En la utilización o cita de partes de la tesis es obligado indicar el nombre de la persona autora.

WARNING. On having consulted this thesis you're accepting the following use conditions: Spreading this thesis by the TDX (**www.tdx.cat**) service and by the UB Digital Repository (**diposit.ub.edu**) has been authorized by the titular of the intellectual property rights only for private uses placed in investigation and teaching activities. Reproduction with lucrative aims is not authorized nor its spreading and availability from a site foreign to the TDX service or to the UB Digital Repository. Introducing its content in a window or frame foreign to the TDX service or to the UB Digital Repository is not authorized (framing). Those rights affect to the presentation summary of the thesis as well as to its contents. In the using or citation of parts of the thesis it's obliged to indicate the name of the author.

UNIVERSITAT DE BARCELONA

MULTI-FUNCTIONALIZATION
OF MICRO- AND NANOPARTICLES
FOR CANCER THERANOSTICS

Ezhil Amirthalingam

UNIVERSITAT DE BARCELONA

FACULTAT DE FARMÀCIA I CIÈNCIES DE L'ALIMENTACIÓ

DEPARTAMENT DE FARMACOLOGIA, TOXICOLOGIA I QUÍMICA TERAPÈUTICA

MULTI-FUNCTIONALIZATION OF MICRO- AND NANOPARTICLES FOR CANCER THERANOSTICS

Ezhil Amirthalingam

Barcelona, 2018

Universitat de Barcelona

Facultat de Farmàcia i Ciències de l'Alimentació

Departament de Farmacologia, Toxicologia i Química Terapèutica

Doctoral Programme: Research, Development and Control of Medicines

MULTI-FUNCTIONALIZATION OF MICRO- AND NANOPARTICLES FOR CANCER THERANOSTICS

PhD Candidate	**Thesis Directors**	
Ezhil Amirthalingam	Prof. M. Lluïsa Pérez-García	Dr. Arántzazu González-Campo

Barcelona, 2018

The work described in this thesis was carried out in the following places:

Nov 2013 – Aug 2014	At the Departament de Farmacologia, Toxicologia i Química Terapèutica, Facultat de Farmàcia i Ciències de l'Alimentació, Universitat de Barcelona.
Sep 2014 – Apr 2017	At the Institut de Ciència de Materials de Barcelona (ICMAB-CSIC).
Jul 2017 – Dec 2017	At the GlaxoSmithKline Carbon Neutral Laboratory for Sustainable Chemistry (GSK-CNL), University of Nottingham.

I would like to thank the *Generalitat de Catalunya*: Agència de Gestió d'Ajuts Universitaris i de Recerca (AGAUR), (FI-DGR 2015) for the 3 year scholarship to do my PhD and a research stay abroad for 3 months.

I would also like to thank the *Beca Montcelimar*, Universitat de Barcelona to help with the research stay abroad for 8 weeks.

The research work has been funded by *Ministerio de Ciencia e Innovación* (MICINN), Research projects: TEC2011-29140-C03-01/02, TEC2014-51940-C2-1/2-R and TEC2017-85059-C3-2-R.

- *To my parents*

ACKNOWLEDGEMENTS

First and foremost, I wish to thank my Director Prof. M. Lluïsa Pérez-García for all the guidance she has given me throughout my PhD. I am very grateful to have her as my Director, she has very patiently made me understand different concepts of science in chemistry as well as of my life (from nano- to macroscale).

I would also like to thank my Co-Director Dr. Arántzazu González-Campo for her support during my three years at Institut de Ciència de Materials de Barcelona (ICMAB-CSIC). She has not only been my Director but has been a very good friend with whom I could freely talk and discuss about everything.

My sincere thanks to Prof. Núria Aliaga Alcalde, Universitat Autònoma de Barcelona and Prof. David B Amabilino, University of Nottingham for welcoming me in their group and giving me the opportunity to work and learn in their laboratories.

I express my gratitude to all our collaborators, group of Prof. J. A. Plaza, Centro Nacional de Microelectrónica (CNM-CSIC), especially Marta Duch and group of Prof. Teresa Suárez, Centro de Investigaciones Biológicas (CIB).

I thank all the services provided from the Centres Cientifics i Tecnologics de la Universitat de Barcelona (CCiTUB), Scientific and Technical services at ICMAB-CSIC, Nanoscale and Microscale Research centre (nmRC) and Centre for bimolecular sciences (CBS) at University of Nottingham.

I am very lucky to have found beautiful friends during my PhD. Very special thanks to David, Sandra and Alicia for being there with me and for me. Thanks for supporting me through all the ups and down of my life in Europe (Barcelona + Nottingham). I would also like to thank all my lab mates and officemates at ICMAB.

Last but not the least, my parents. I have been very grateful for having a loving mother and a caring father. They are the reason behind who encouraged me to take PhD program and have been a constant support all the way through my life. There is no way in which I could put my love towards them in writing.

PROLOGUE

The interdisciplinary work presented in this Thesis concerns the chemical (bio)-functionalization of micro- and nanoparticles for the preparation of micro- and nanotools, whose functionality targets towards cancer theranostics (sensing and therapy) in living cells.

The Thesis is structured in 9 Chapters and one Appendix:

- Chapter 1 shows a general Introduction to Nanoscience and the application of nanomaterials for sensing and therapy
- Chapter 2 describes the Objectives of the Thesis.
- Chapter 3 describes the Experimental section.
- In Chapters 4-8, each chapter is related to each specific objective, and includes a brief introduction, followed by its Results and Discussion.
- Chapter 9 shows the Conclusions.
- The final Appendix contains the abbreviations and acronyms, fabrication process and the dissemination of the results.

INDEX

CHAPTER 1 .... **19**

Introduction 21

CHAPTER 2 .... **27**

Objectives 29

CHAPTER 3 .... **33**

Methodology 35

3.1. Materials 35

3.2. Characterization techniques and instruments 36

RESULTS AND DISCUSSION **47**

CHAPTER 4 .... **49**

Functionalization of star-shaped and discoidal polysilicon microparticles with lectins for their adhesion to cell membranes 51

4.1. Introduction 51

4.2. Functionalization and characterization of star shaped polysilicon particles on surfaces 56

4.3. Functionalization and characterization of star shaped polysilicon microparticles in suspension with lectins 72

4.4. Functionalization and characterization of disc shaped polysilicon microparticles in suspension with lectins 81

4.5. Characterization analysis 88

4.6. Difference in surface reactivity between polysilicon and silicon oxide 105

4.7. Biological Results 108

CHAPTER 5 .... **111**

Functionalization of star-shaped and discoidal polysilicon microparticles with Boronic Acids (BAs) for their adhesion to cell membranes 113

5.1. Introduction 113

5.2. Functionalization and characterization of polysilicon microparticles on surfaces using BA 115

5.3. Functionalization and characterization on polysilicon microparticles in suspension using BA 120

5.4. Biological Results 125

CHAPTER 6 .... **127**

Functionalization of hexahedral bi-functional microparticles using fluorescent probes for pH sensing in cells 129

6.1. Introduction 129

6.2. Functionalization of polysilicon surfaces using pH dependent fluorophores 134

6.3. Functionalization of gold surfaces using phrodo 139

6.4. Functionalization of bi-functional surfaces and microparticles using Oregon green and pHrodo 142
6.5. Quantification of Oregon green and pHrodo on bi-functional microparticles 154
CHAPTER 7 157
Functionalization of hexahedral bi-functional microparticles using Reactive Oxygen Species (ROS) generator and ROS sensor for Photodynamic therapy (PDT) 159
7.1. Introduction 159
7.2. Testing the pair of ROS producer and BODIPY sensor: Controls in solution 162
7.3. Functionalization and characterization of Cyt c and BODIPY: Controls on surfaces 164
7.4. Bi-functionalization and characterization of hexahedral bi-functional microparticles (polysilicon-gold) with Cyt c and BODIPY 170
CHAPTER 8 173
Delivery of anionic drugs using macrocyclic-imidazolium based gold nanoparticles 175
8.1. Introduction 175
8.2. Anion binding properties of bis-imidazolium salts 178
8.3. Synthesis and characterization of AuNPs using imidazolium macrocycles 181
8.4. Interaction of carboxylate incorporating drugs and AuNPs: loading and release of sodium ibuprofenate 187
CHAPTER 9 191
Conclusions 193
BIBLIOGRAPHY 197
APPENDIX 215
I Abbreviations and acronyms 217
II Fabrication of the microparticles 218
III. Dissemination of Results 221

CHAPTER 1

CHAPTER 1

Introduction

With over 10 million new cases per year worldwide, cancer remains a difficult disease to treat and a significant cause of morbidity and mortality. It is a complex cluster of diseases that arise from DNA mutations impacting cell growth and cell cycle processes. The fact that cancer encompasses a heterogeneous spectrum of conditions and is highly unpredictable causes numerous challenges for early diagnosis and effective treatment. Current treatments include chemotherapy, radiation and surgery, but the effects of these procedures may damage not only the cancer tissue but also normal tissue. Researchers have been working on delivering chemotherapeutic agents selectively at the molecular level in the cancer tissue, developing a new approach for treating cancer [1-3].

Nanomedicine, the use of nanotechnology for medical applications, offers great opportunities and challenges in both fundamental research and practical applications, such as therapy, diagnosis, imaging or tissue regeneration [4-5]. Nanomedicine relies on the preparation and study of nanomaterials, structures with at least one of the three dimensions in the length scale between ~1 and ~100 nm [6]. Some of the examples of nanomaterials are represented in **Figure 1-1** [7-12].

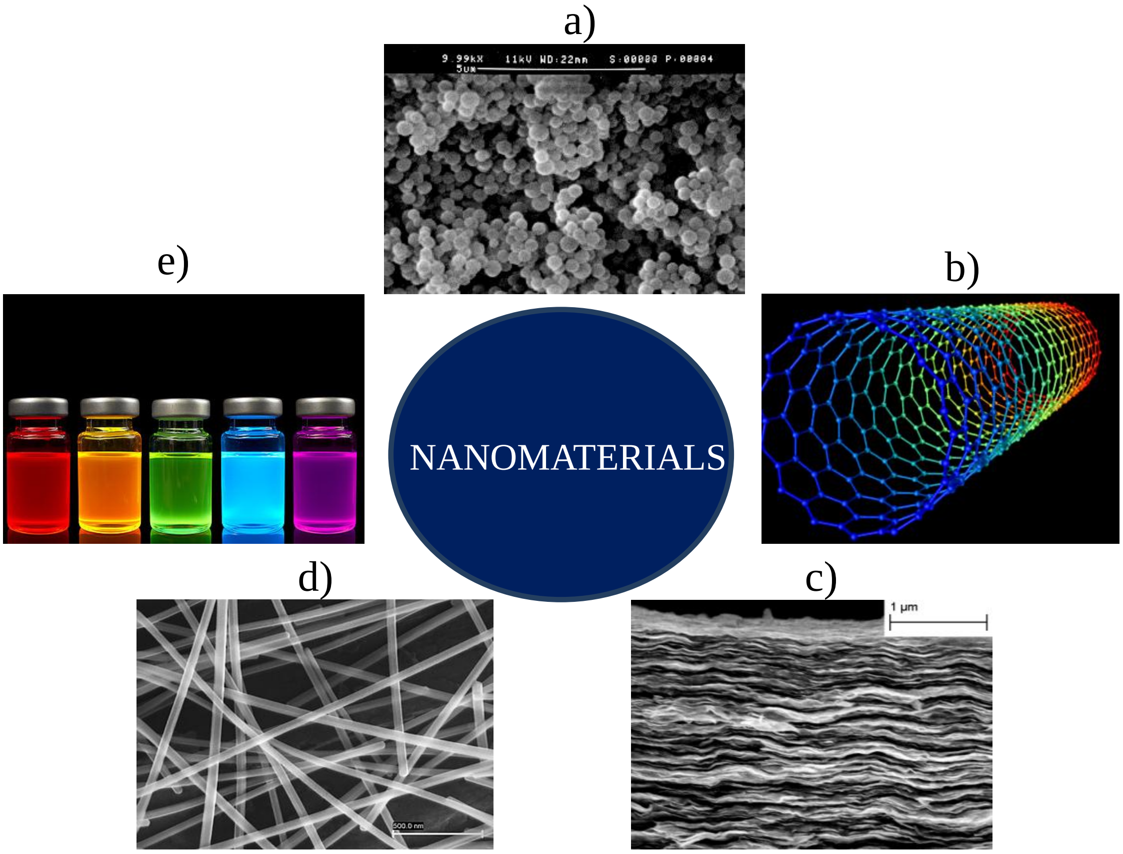

Figure 1-1. Examples of nanomaterials, **a)** nanoparticles, **b)** nanotubes, **c)** nanosheets, **d)** nanowires and **e)** quantum dots.

Due to their small dimension, nanomaterials have high surface area to volume ratio, where the surface/interface states become important and even dominant compared to normal bulk materials [13-15]. Nanomaterials exhibit many valuable properties such as high absorbance, bright fluorescence and catalytic activities, which can be modulated by their physical and chemical environment [16]. In addition, these materials show plenty of intriguing phenomena and extraordinary electronic, optical, thermal, mechanical, and chemical properties [17-20], which provides a lot of fascinating research topics for both fundamental and applied research (**Figure 1-2**) [21-29].

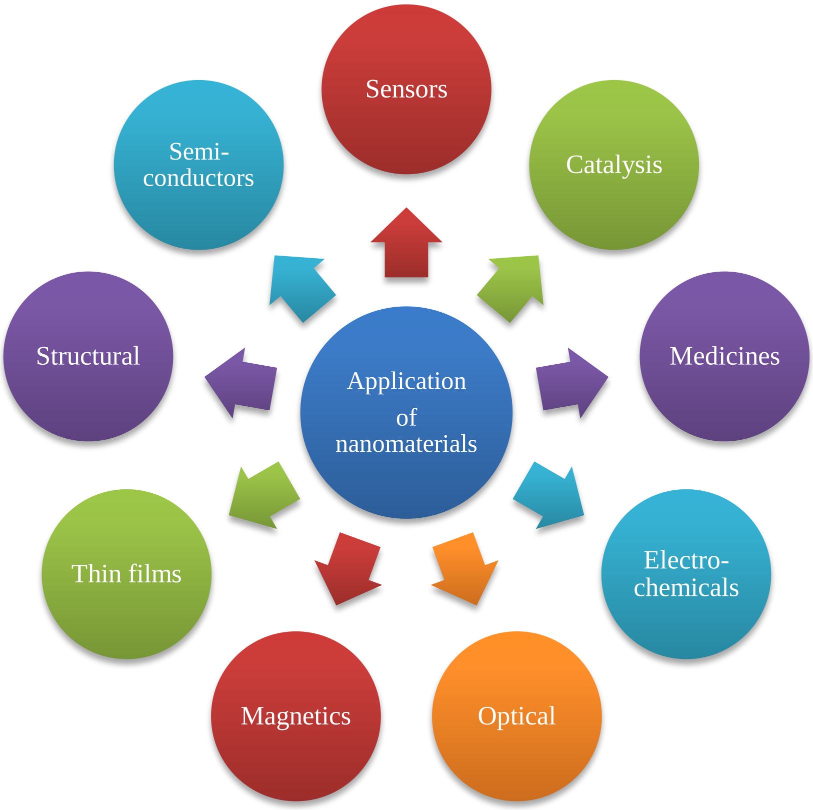
Sensors
Semi-conductors
Catalysis
Structural
Application of nanomaterials
Medicines
Thin films
Electro-chemicals
Magnetics
Optical

Figure 1-2. Schematic representation showing fields of application of nanomaterials.

Nanomaterials can be obtained by two different approaches, named either the top-down or the bottom-up approach, (**Figure 1-3**). In the top-down, a block of material is taken and carved away until the object that is wanted is reached using techniques such as engraving, photolithography or milling. Thus, the top-down approach is based in using nano-engineering and erosion to form the nanomaterials [30]. In the case of bottom-up approach, individual atoms and molecules are driven to or are placed precisely where they are needed by tools such as chemical synthesis, self-assembly or self-organisation [31]. Therefore, the driving force in the bottom-up approach to the formation of nanomaterials is based on the supramolecular chemistry and the use of non-covalent interactions [32].

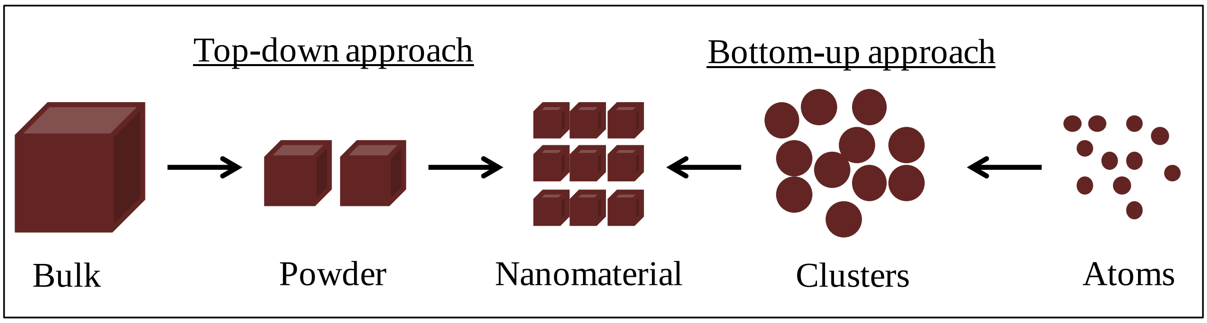
Top-down approach
Bottom-up approach
Bulk
Powder
Nanomaterial
Clusters
Atoms

Figure 1-3. Top-down and bottom-up approaches for the preparation of nanomaterials.

Recent years have witnessed a significant interest in biological applications of novel nanomaterials [33-35]. The unique physic-chemical properties of nanomaterials when utilized in conjunction with the remarkable biomolecular recognition capabilities could lead to nano-biological devices such as probes and sensors [36-38]. Not only could these devices exhibit advantages over existing technology in size but also in performance [39-40]. Several issues are important regarding nanomaterial/biosystems. One of them is biocompatibility, especially for *in-vivo* applications [41-43]. Another is specificity that requires bio-functionalization of nanomaterials for recognition of only one type of target biomolecule and rejection of others [44-46]. Central to tackling these issues is surface functionalization of nanomaterials and elucidating the interfaces and interactions between nanomaterials and biosystems [474849]. Recent progress in nanomedicine has also stimulated the development of multi-functional nanomaterials, achieving a compound effect using one system in which each component has a specially designed function [48,50-51]. Multi-functional nanomaterials provide a platform to integrate therapy and diagnostics “theranostics”, which is an emerging direction in nanomedicine [52]. Beyond simply therapeutic functionality, theranostic nanomaterials have been designed to deliver multiple components and imaging agents, facilitating simultaneous and synergistic diagnosis and therapies [53-55].

The design and preparation of such multi-functional materials for theranostics is a challenging task, guided by a careful precise complementary selection of relevant probes and carriers chosen for sensing specific parameters of a pathogenic cell or tissue, and delivering drugs that could rectify an anomalous condition. When these nanomaterials are designed to target cancer cells many different guiding principles may apply, such as sensing and modifying differences in cell adhesion, or acidity.

Cell adhesion is an essential aspect for fundamental cellular processes such as cell proliferation, migration, differentiation, and survival [56-57]. Finding innovative methods to probe the adhesion of cells in their native state can greatly advance the understanding of control and regulation of cellular behaviour, such as cell morphology, cell mechanics, cell motility and cell signalling [58-62], all of which can potentially be applied to medical diagnosis and/or pharmaceutical development. Abnormality in cell adhesion can result in various cellular disorder associated with a wide range of human diseases [63-67]. Cell adhesion molecules play a significant role in cancer progression and metastasis. The alterations in the adhesion properties of neoplastic cells play a pivotal role in the development of recurrent, invasive and distant metastasis [63,68-70]. Use of different nanomaterials with biological functionality to control the cell behaviour has been explored widely [71-73]. Surface bio-functionalization with cell-adhesion molecules has attracted significant interest of the surfaces with tailored properties, such as wettability, adhesion and biocompatibility [74]. In our group, we have successfully developed a device for individual embryo tagging [58]. These devices are based on polysilicon substrates, microfabricated enclosing a characteristic pattern code, enabling individual external cell identification. Furthermore, bio-functionalization of these devices has driven their excellent adhesion ability to the zona pelucida of the mouse embryos (**Figure 1-4**), with extremely successful retention rates and high embryo survival.

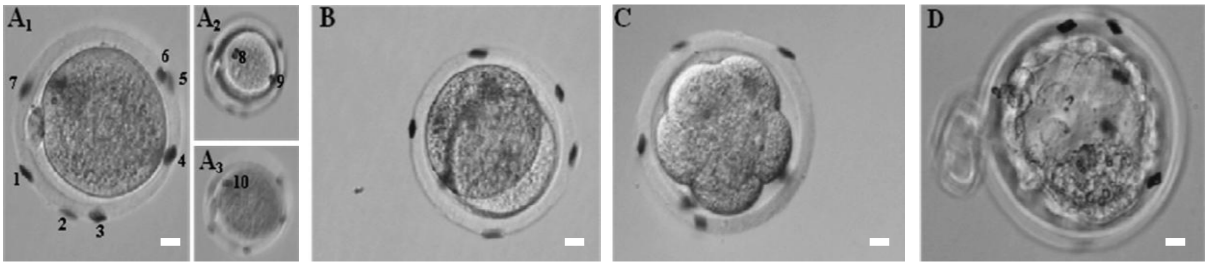

Figure 1-4. Optical microscopy images of mouse embryos at different development stages tagged with polysilicon bio-functionalized devices, (**A1−3**) one-cell, (**B**) two-cell, (**C**) morula, and (**D**) blastocyst stage. Scale bar – 4 µm.

On the other hand, intracellular pH is also one of the most important cellular parameters to be measured because cells change their intracellular pH depending on their environment, specific location or their development stage [75]. For instance, different organelles such as endosomes or lysosomes, have a typically acidic pH between 4 and 5, in comparison on the pH of the cytosol and the nucleus that in normal conditions have a pH near 7.2-7.4 [76]. Furthermore, different kinds of cells such as apoptotic, inflammatory, or cancer cells also show changes in their intracellular pH, which normally become slightly more acidic [77-78]. This dysregulated pH is emerging as a hallmark of cancer, which enables cancer progression by promoting proliferation, the evasion of apoptosis, metabolic adaptation, migration and invasion [79-82]. In this context, tools with the capability to measure intracellular pH should be an important aim to study the cell stage, cell behaviour or processes involved with the cell's death. Novel systems have been described recently, based in these fluorescent structures supported on polymeric or metallic nanoparticles in order to deliver the sensors inside the cells [83-85]. However, despite the existence of even several commercially pH chemosensors to be used in solution, their toxicity for the cells hamper their use in long term studies in cell cultures. Immobilization of any of these systems in either micro- or nanoparticles would offer the advantage or increasing their specificity and reduce their toxicity. To the best of our knowledge, there are only a few examples of pH probes successfully incorporated on nanoparticles [86], and only one example on gold nanoparticles [87]. Recently, our group has also successfully immobilized 3 different pH-dependent fluorophores using micro-contact printing on silicon oxide substrates, which sets the principle to identify and determine the physiological pH changes in HeLa cells [88].

Moreover, the therapeutic properties of light have been known for thousands of years, but it was only in the last century that photodynamic therapy (PDT) was developed [89-91]. At present, PDT is being used in the clinic for use in oncology - the head and neck, brain, lung, pancreas, breast, prostate and skin [92-96]. PDT involves two individually non-toxic components that are combined to induce cellular and tissue effects in an oxygen-dependent manner. The first component of PDT is a photosensitizer -a photosensitive molecule that localizes to a target cell and/or tissue [97]. The second component involves the administration of light of a specific wavelength that activates the sensitizer. The photosensitizer transfers energy from light to molecular oxygen, to generate reactive oxygen species (ROS) [98-101]. Since 1993, Photofrin®, a commercially available hematoporphyrin derivatized photosensitizer, is used in patients with early and advanced stage of lung cancer [102]. Additionally, most of the photosensitizers are also good for imaging [103-105]. One of the problems encountered in administrating photosensitizers is their bad distribution inside the body, therefore, resulting in side effects and damaging nearby tissues. For this reason, there is a need of developing a target specific drug delivering systems [106] which can be achieved using micro- and nanoparticles. In our group, we have prepared novel porphyrin derivatives and have immobilized them onto gold or iron oxide nanoparticles to build a suitable device for potential use in PDT, **Figure 1-5** [107-112].

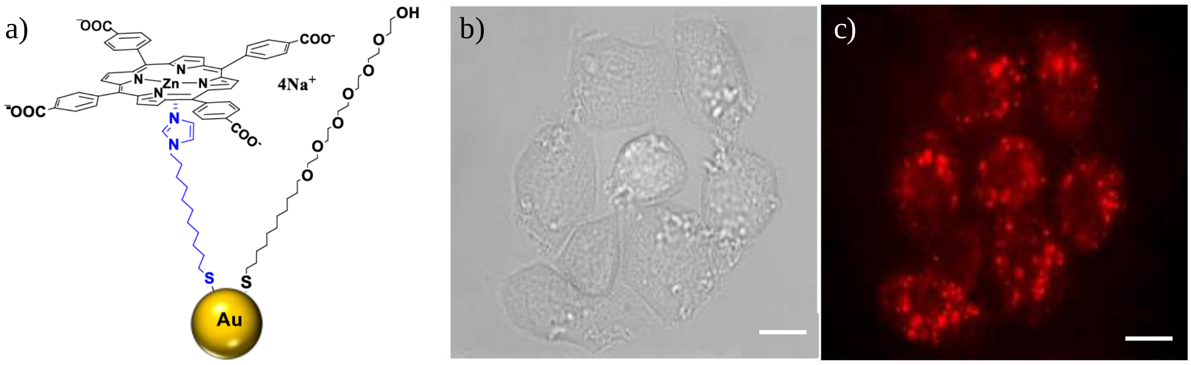

Figure 1-5. a) Schematic representation of gold nanoparticles functionalized with porphyrins for photodynamic therapy and **(b-c)** bright field and fluorescence image of SK-BR-3 cells loaded with functionalized gold nanoparticles. Scale bar – 20 µm.

Over recent years, advancement in nanoparticles drug delivery is widely expected to change the landscape of pharmaceutical industries for the foreseeable future [111-116]. Controlled drug delivery systems have several advantages compared to the traditional forms of drugs. A drug is transported to the place of action, hence, its influence on vital tissues and undesirable side effects can be minimized. Accumulation of therapeutic agents in the target site increases and, consequently, the required doses of drugs are lower [117-119]. Nanoparticles, specially metallic or inorganic nanoparticles such as gold nanoparticles, have been extensively investigated thanks to their easy fabrication, biocompatibility and multi-functionalization capability [120]. The two most widely used methods for the synthesis of gold nanoparticles are the citrate method, developed by Turkevich, and the Brust-Schiffrin method [121-122]. Gold nanoparticles have been widely studied to be used in different types of applications, including catalysis, medical diagnosis, biological sensors and imaging [123-128]. In particular drug delivery is one of the main biological applications of the gold nanoparticles because they are able to incorporate a particular bioactive molecule or drug and deliver it to a certain tissue or cell [116]. Based on the Brust-Schiffrin method, our group has developed a novel method for obtaining gold nanoparticles, using bis-imidazolium or bis-pyridinium amphiphiles of gemini type synthesized in our laboratory. This method proved to be suitable for obtaining gold nanoparticles that are monodisperse, able to enter cells, with low toxicity, that furthermore could be loaded with model drugs such as, ibuprofen, piroxicam and also porphyrin-based photosensitizers, pursuing its delivery, **Figure 1-6** [109,129-131].

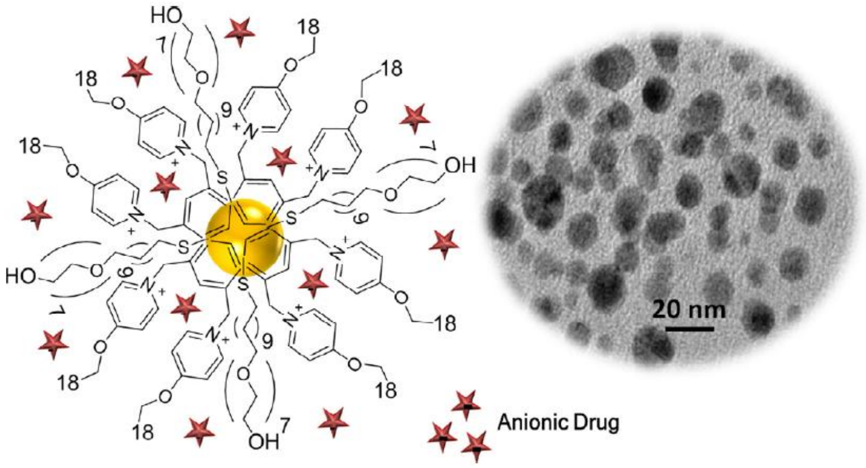

Figure 1-6. Schematic representation of gemini pyridinium based gold nanoparticles for drug delivery and its image obtained using Transmission Electron Microscopy (TEM).

This thesis has its main focus on developing multi-functional nanomaterials, that we called nano- and microtools through two different approaches, top-down to provide support and bottom up to give functionality to prepare nanomaterials for diagnosis and therapy in cancer cells (theranostics). It includes functionalization of inorganic and or metallic nano- and microparticles with natural and synthetic receptors capable of acting as sensors to monitor different cellular parameters in living cells and deliverers.

Self-assembled monolayers (SAMs) are the functional component of the nano- and microtools described in this thesis. It is a process based on the spontaneous assembly of molecules forming a well ordered structure on a surface. The activity and the utility of the SAMs depend on the molecule that will be immobilized into the SAMs using the reactivity between the functional group of the SAMs and the desired molecule [132]. Functional nanomaterials are formed by three main elements (**Figure 1-7**):

- a metallic or inorganic substrate, in particular polysilicon and gold surfaces or gold nanoparticles.
- a self assembled monolayer as linker and
- a bioactive molecule

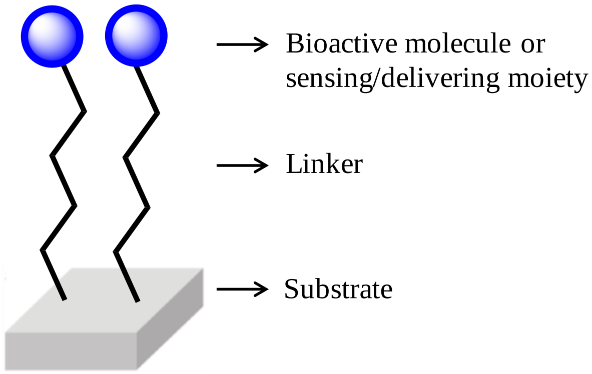

Figure 1-7. Schematic representation of elements of a microtool.

CHAPTER 2

CHAPTER 2

Objectives

The main objectives of this thesis are to develop novel multifunctional micro- and nanoparticles for intra- and extracellular sensing for cancer theranostics, through different, but complementary approaches:

- Functionalization of polysilicon microparticles of different shapes and sizes, targeting membrane receptors to induce cell adhesion of the microparticles (described in **Chapter 4** and **Chapter 5**):

    1. To optimize the immobilization of lectins and boronic acids on polysilicon surfaces and microparticles using self-assembled monolayers.
    2. Characterization of (bio)-functionalized surfaces and microparticles.
    3. To assess the ability of bio-functionalized microparticles to adhere to cell membranes of Dictyostelium discoideum (Dicty) and HeLa cells. (**Figure 2-1**)

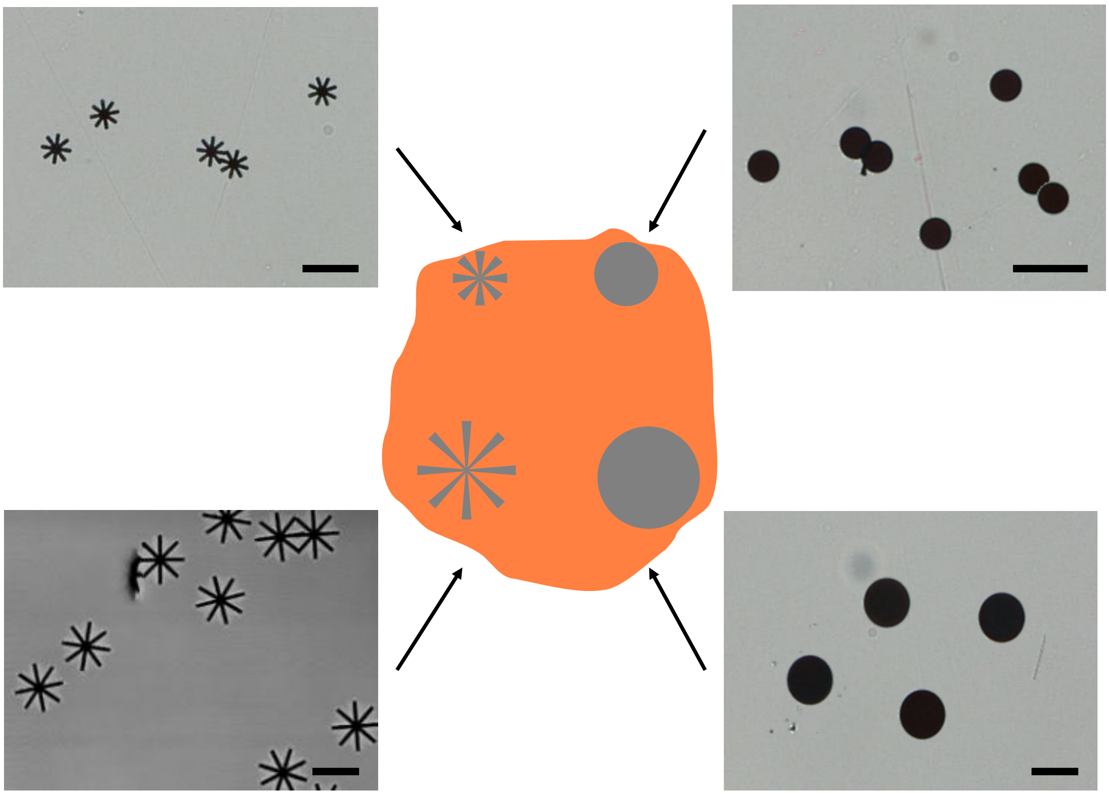

Figure 2-1. Representation of cell adhesion using (bio)-functionalized microparticles of different shapes and sizes. Scale bar – 20 µm.

- Preparation of microparticles for pH sensing in cells based on hexahedral bi-functionalized fluorescent probes (described in **Chapter 6)**:

    1. Selection of suitable pH dependent fluorescent dyes.
    2. To immobilize pH dependent fluorescent dyes on polysilicon surfaces and microparticles.
    3. To immobilize pH dependent fluorescent dyes on gold surfaces.
    4. Bi-functionalization of hexahedral bi-functional (polysilicon-gold) microparticles using pH dependent fluorescent dyes. (**Figure 2-2**)

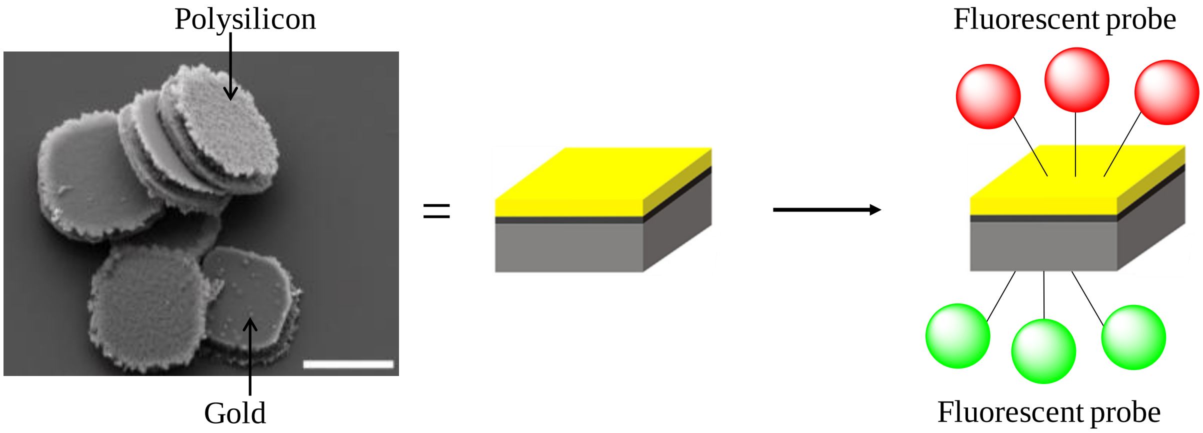

Figure 2-2. Representation of hexahedral bi-functionalized microparticles either for pH sensing or Photodynamic Therapy (PDT) in cells. Scale bar – 3 µm.

- Preparation of microparticles for intracellular sensing of Reactive Oxygen Species (ROS) using hexahedral bi-functionalized fluorescent probes for Photodynamic Therapy (PDT) (described in **Chapter 7**):

    1. Selection of suitable ROS producer and a sensor.
    2. To assess the production of ROS using a bio-photosensitizer.
    3. To immobilize the bio-photosensitizer on polysilicon surfaces and microparticles.
    4. To immobilize a suitable ROS sensor on gold surfaces.
    5. Bi-functionalization of hexahedral bi-functional (polysilicon-gold) microparticles using bio-photosensitizer (ROS producer) and a ROS sensor. (**Figure 2-2**)

- Synthesis and characterization of gold nanoparticles based on imidazolium macrocycles to incorporate anionic drugs for drug delivery (described in **Chapter 8**):

    1. To study the anionic binding properties of imidazolium macrocycles.
    2. Synthesis and characterization of gold nanoparticles using imidazolium macrocycles.
    3. To study the incorporated release of anionic drugs from the macrocyclic-imidazolium based gold nanoparticles. (**Figure 2-3**)

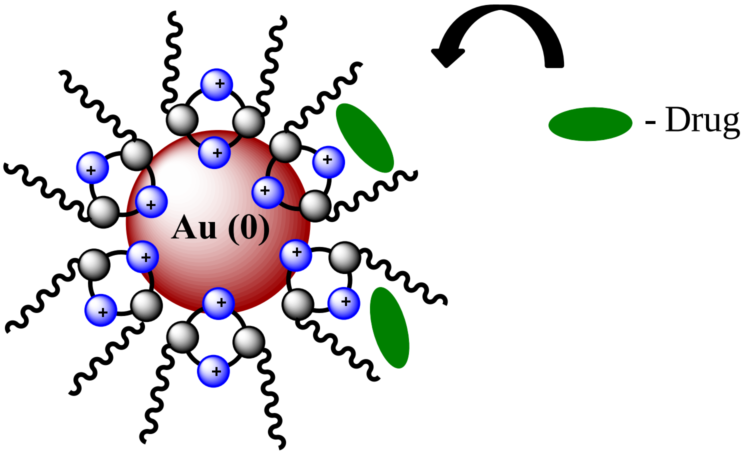

Figure 2-3. Representation of gold nanoparticles as drug delivery agents.

CHAPTER 3

CHAPTER 3

Methodology

3.1. Materials

Solvents and reagents

Absolute ethanol (99.8%), sulphuric acid (H_2SO_4, 98%), hydrogen peroxide (H_2O_2, 30%), ammonium hydroxide (NH_4OH, 20%) and acetic acid (99.8%) were purchased from Sigma–Aldrich. Water used in the experiments was HPLC grade produced by a MilliQ plus system from Millipore (Milli-Q water). Phosphate buffered saline (PBS), sterile (pH 7.4) and Sorensen buffer (pH 5.5) was purchased from Scharlab.

The dialysis membrane, Cellu·Sep T3, MWCO12000-14000Da was brought from Membrane filtration products international (MFPI).

Commercial compounds

3-minopropyltriethoxysilane (99%) (**APTES**), 2-(2-aminoethoxy)ethanol, *N*-acetylglucosamine (**GlcNAc**), triglycolamine, Tween® 20, Tween® 80, sodium cyanoborohydride, 4-formylphenylboronic acid, cysteamine, 11-amino-1-undecanethiol hydrochloride, cytochrome c from equine heart (**Cyt c**), hydrogen tetrachloroaurate(III), sodium borohydride and ibuprofen sodium salt were purchased from Sigma–Aldrich. 11-(Triethoxysilyl)undecanal (**TESUD**) was purchased from ABCR. Texas red-X conjugate Wheat germ agglutinin (**WGA**), Concanavalin A, Texas red conjugate (**Con A**) and **Oregon green**™ 488 carboxylic acid, succinimidyl ester, 6-isomer (**Oregon green**), **pHrodo**™ red, succinimidyl ester (**pHrodo**), SNARF™-1 carboxylic acid, acetate, succinimidyl ester (**SNARF**), **Alexa fluor**™ 647, succinimidyl ester (**Alexa fluor**) and BODIPY™ 581/591, succinimidyl ester (**BODIPY**) were purchased from Thermofisher Scientific. 2-(1-Hydroxy)ethoxyeth-1-yl methanesulfonate (**EG2OMs**) was purchased from ProChimia Surfaces.

Compounds

1·2Br, **2·2Br** and **3·2Br** were synthesized according to literature [129,133].

Substrates

The silicon and silicon/gold substrates for this work were provided by our collaborators. They were manufactured in the group of Prof. J. A. Plaza using semiconductor microtechnologies based on photolithographic processes at the *Centro Nacional de Microelectrónica* (CSIC-CNM) in Barcelona, Spain. The fabrication processes of the substrates are explained in the Appendix, Section II.

Two different types of substrates were used for the functionalization process.

1. **Surfaces**. They were selected initially due to the feasibility of carrying out the preliminary experiments and for the optimization of the functionalization protocol. The surfaces (0.5 cm^2) used incorporated patterns of polysilicon microparticles with different morphologies.
2. **Microparticles**. After the optimization of the protocol on surfaces, polysilicon microparticles with different morphologies were used as the substrates. The polysilicon microparticles were etched from the above mentioned surfaces and were collected in an eppendorf with 1 mL of absolute ethanol. The dimension of these microparticles permits their

easy detection, even while using an optical microscope. Two different shapes of microparticles, Star shaped (**Batch 1-Batch 4**) and Disc shaped (**Batch 5-Batch 6**) microparticles were used, **Figure 3-1 (a-f**) respectively.

Additionally, a microparticle of 3 x 3 µm^2 and 500 nm thickness, made up of two different materials (polysilicon and gold) for bi-functionalization of the microparticles were also fabricated, **Figure 3-1 (g)**.

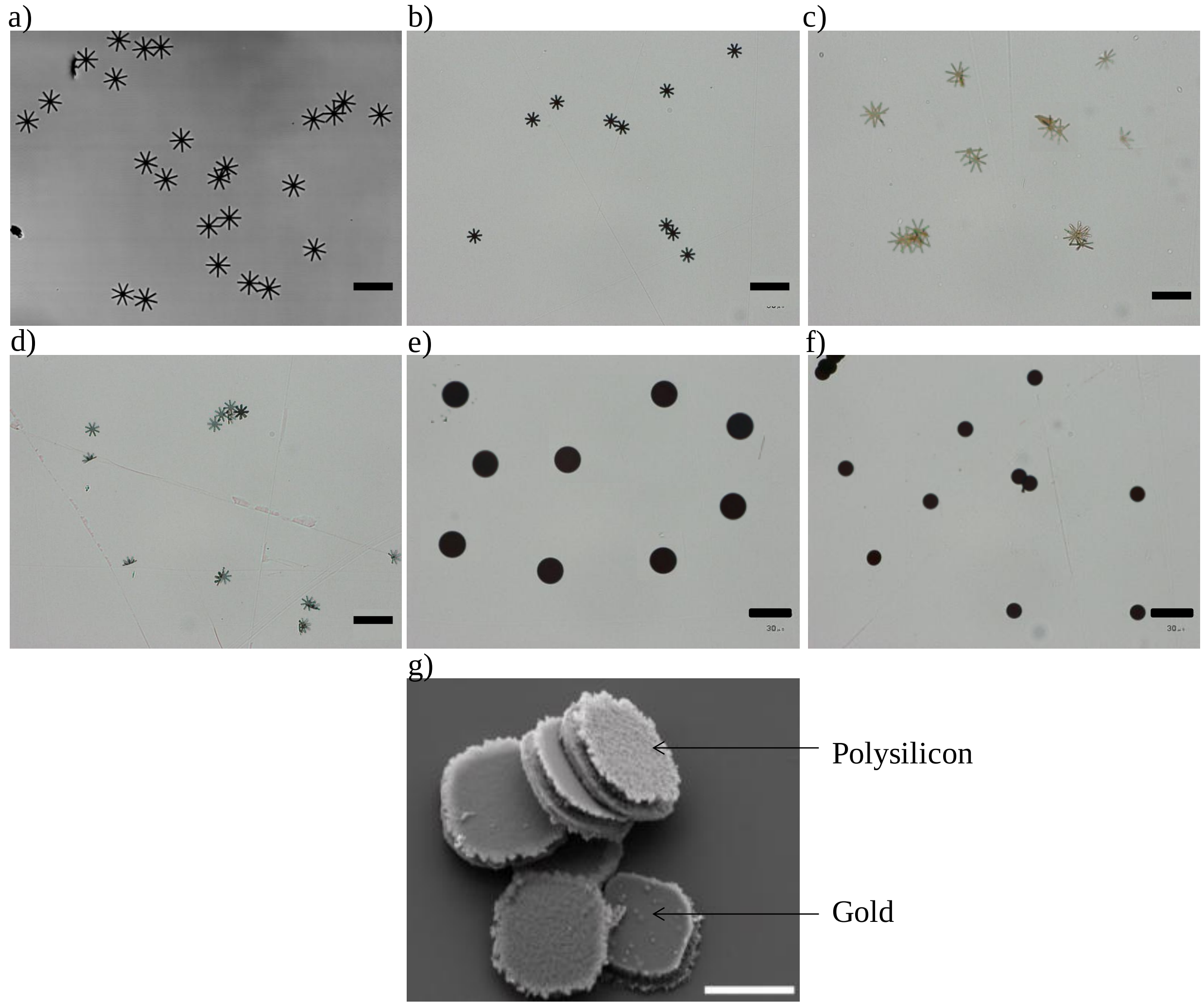

Figure 3-1. Star shaped polysilicon microparticles, **a) Batch 1** (20 µm, 500 nm thick), **b) Batch 2** (10 µm, 500 nm thick), **c) Batch 3** (20 µm, 50 nm thick), **d) Batch 4** (10 µm, 50 nm thick), Disc shaped microparticle **e) Batch 5** (20 µm, 500 nm thick), **f) Batch 6** (10 µm, 500 nm thick), **g)** Bi-functional microparticle. Scale bar – 30 µm **(a-f)** and 3 µm **(g)**.

3.2. Characterization techniques and instruments

Fluorescence microscopy

Fluorescence images were obtained with OLYMPUS-DP 20 (BX51) microscope at the *Institut de Ciència de Materials de Barcelona* (ICMAB) equipped with a fluorescence setup using mercury lamp. The samples were observed in fluorescence and transmitted light simultaneously. Samples emitting green fluorescence were excited using a blue excitation filter (460 - 490 nm) and emission wavelength ≥ 515 nm. In the case of red fluorescence emission, the samples were excited using a green excitation filter (530 - 550 nm) and emission wavelength ≥ 590 nm.

Additionally, the fluorescence images were also obtained using OLYMPUS-IX73 at *GlaxoSmithKline-Carbon Neutral Laboratory* (GSK-CNL), University of Nottingham. Samples emitting green fluorescence were excited using a blue excitation filter (470 - 495 nm) and emission filter (510 - 550 nm). In the case of red fluorescence emission, the samples were excited using a green excitation filter (540 - 550 nm) and emission filter (575 - 625 nm).

The samples surfaces were analyzed together with control surfaces (without any fluorophore). The control surfaces were analysed first and the resulting auto fluorescence from the surface was made to zero by adjusting the exposition time and the aperture of the excitation filter. The sample surfaces were then analyzed and captured using the similar settings adjusted for control surfaces.

Super Resolution Microscopy:

The fluorescence images using super resolution microscopy were obtained from a Zeiss 780 high resolution confocal microscope combined with a Zeiss Super resolution system with full environmental control at the *Centre for Biomolecular Sciences* (CBS), University of Nottingham.

Total Internal Reflection Fluorescence (TIRF) microscopy

TIRF microscopy exploits the unique properties of an induced evanescent wave or field in a limited specimen region immediately adjacent to the interface between two media having different refractive indices. In practice, the most commonly utilized interface in the application of TIRF microscopy is the contact area between a sample and a glass coverslip.

HiLo microscopy

HiLo microscopy involves ‘structured illumination’ which means projecting a pattern of illumination (usually a grid-like pattern) onto the sample. The pattern is projected with the same lens used for imaging, resulting in an illumination pattern which is in focus at the imaging focal plane, and blurred everywhere else. This provides a way of distinguishing between the in-focus and out-of-focus components of the image. The in-focus parts of the image are illuminated with a high fidelity pattern, while the out-of-focus parts are illuminated by a blurred pattern. For layers of the sample which are sufficiently far from the focal plane, this blurring will be so severe that the illumination is essentially uniform. Thus, HiLo microscopy is used to eliminate the out-of-focus contributions.

Stochastic Optical Reconstruction Microscopy (STORM) Imaging

STORM imaging improves the resolution by ~10 times over conventional imaging systems in that it does not observe all the fluorescently labelled molecules on the sample at the same time, but activates only a low percentage at any given time. At each time point/frame, Gaussian fitting enables precise localization of the centroid of each activated molecule image. By repeating this process and acquiring multiple frames, thousands of molecules in the field of view can be localized with nanometer accuracy. Combining these localizations results in the final super-resolution image.

Fluorescence spectroscopy

Fluorescence spectroscopy was performed using a FLS980 spectrometer from Edinburgh Instruments at the *Carbon Neutral Laboratory for Sustainable Chemistry* (CNL), University of Nottingham. The samples were excited using a 450 W ozone free xenon arc lamp that covers a range of 230 nm to 1000 nm using right-angle geometry.

Ultraviolet-Visible absorption spectroscopy (UV-Vis)
UV absorption spectra were obtained on UV-1800 Shimadzu UV spectrophotometer present at the ICMAB.

Contact angle measurements
The contact angles were measured in air inside a clean room with high-purity deionized water by a 3 µL drop using a contact angle measuring system (DSA 100, KRUSS) from Nanoquim platform of the ICMAB to determine the hydrophobicity of the modified surfaces. Values of the contact angle on at least three samples were measured to give statistical significance.

Raman spectroscopy
All spectra were acquired using the Horiba LabRAM HR Raman Microscope available at the *Nanoscale and Microscale Research Centre* (nmRC), University of Nottingham. The spectra were collected with 532 nm excitation at either (i) 1% laser power for 10 seconds per spectral window (10s) or (ii) 100% laser power for 0.1s per spectral window (1s). In either case, 2 accumulations per window were required to remove spectral artefacts.

Atomic Force Microscopy (AFM)
Topographic AFM images were acquired using Keysight 5100 AFM in the dynamic tapping mode using a Si tip at the ICMAB using a PicoSPM (Molecular Imaging) microscope.

Scanning Electron Microscopy (SEM)
SEM samples in Chapter 4 were measured on QUANTA FEI 200 FEG-ESEM microscope at the nmRC, University of Nottingham. The samples were measured at high and low vacuum conditions where the electron beam acceleration voltage was set between 10 kV and 20 kV. The microscope was equipped with a field emission gun (FEG) for optimal spatial resolution.

In the case of AuNP (Chapter 8), the SEM images were obtained using a JEOL JSM-7100F field emission scanning electron microscope at 5 kV, at CCiTUB. Samples were mounted on microscope holders using carbon tabs and then they were coated with a thin film of amorphous carbon. The images were captured using the software PC-SEM version 5.1.

X-ray Photoelectron Spectroscopy (XPS)
XPS measurements in Chapter 4 were performed with Kratos Liquid Phase Photoelectron Spectroscopy Machine (LiPPS) at the nmRC, University of Nottingham, in ultra-high vacuum conditions (base pressure $5E^{-10}$ mbar). XPS measurements were performed with a monochromatic X-ray source Al Ka emission at 1486.6 eV.

XPS measurements in Chapter 5 were performed with a Phoibos 150 analyzer (SPECS GmbH, Berlin, Germany) at the *Institut Català de Nanociència i Nanotecnologia* (ICN2), in ultra-high vacuum conditions (base pressure $5E^{-10}$ mbar). XPS measurements were performed with a monochromatic Kalpha X-ray source (1486.74 eV). The pass energy values used was 20 eV for the high resolution spectrum and the energy resolution as measured by the FWHM of the Ag $3d_{5/2}$ peak for a sputtered silver foil was 0.6 eV.

Matrix-Assisted Laser Desorption and Ionization - Time-of-flight - Mass Spectrometry (MALDI-TOF-MS)

MALDI-TOF-MS analysis were performed using a Voyager-DE-RP mass spectrometer (Applied Biosystems, Framingham, USA) from *Centres Científics i Tecnològics de la Universitat de Barcelona* (CCiTUB). A 3 ns pulse nitrogen laser (337 nm) was used for desorption and ionization with an accelerating voltage of 20 kV. Positive ions were detected in a time-of-flight mass detector in the reflector mode. The matrix used was 2, 5-dihydroxybenzoic acid (DHB).

Transmission Electron Microscopy (TEM)

TEM images were obtained with a JEOL JEM-1010 transmission electron microscope at 80 kV, from CCiTUB. The images were captured by a Megaview III Soft Imaging System camera and the size of the nanoparticles was measured with Analysis software (Olympus).

Dynamic Light Scattering (DLS)

The hydrodynamic size of the gold nanoparticles (AuNPs) was determined by Dynamic Light Scattering using a Malvern Zetasizer Nano ZS series from Malvern Instruments at *Universitat de Barcelona*.

Thermogravimetric Analysis (TGA)

TGA was performed on a Mettler Toledo TGA/SDTA 851e, at CCiTUB, with a temperature ramp from 30°C to 600°C and a heating rate of 10°C min^{-1}.

Neubauer Chamber

Particle counting was performed by adding 5 μl of microparticle suspension into a Neubauer Chamber and counting the particles using an optical microscope.

3.3. Experimental section

3.3.1. Optimization of functionalization protocols:

3.3.1.1. Activation of the surfaces

The surfaces (0.5 cm^2) were submerged in a freshly prepared mixture of H_2SO_4 (98%) and H_2O_2 (30%) (piranha solution), at a volume ratio of 7:3 (1 mL) for 1hr, and then rinsed with Milli-Q water (5×3 mL). The surfaces were then submerged in a solution of NH_4OH (20%), H_2O_2 (30%) and Milli-Q water, at a volume ratio of 1:1:5 (1 mL) for 30 mins. The freshly hydroxylated surfaces were then rinsed abundantly with Milli-Q water (5×3 mL) and dried in a stream of nitrogen gas.

Silanization step

1. Using different concentrations of linker (TESUD)

The hydroxylated surfaces were then submerged with different solutions of 11-(triethoxysilyl)undecanal (TESUD) of concentration 67.5, 135, 200 mM in 1 mL of absolute ethanol. To this solution, 50 µL of acetic acid (0.05 mmol) was also added maintaining the final volume up to 1 mL.

2. Using different incubation times in linker (TESUD)

The hydroxylated surfaces were then submerged in a solution of TESUD in absolute ethanol (135 mM, 1 mL). To this, 0.05 mM of acetic acid was also added. The solution was then made to stir using an orbital shaker at 600 rpm for different time periods such as 3 hrs and for overnight.

WGA immobilization

1. Using different concentrations of lectin (WGA)

After the incubation, the surfaces were rinsed abundantly with absolute ethanol (5×3 mL) and dried with nitrogen. TESUD functionalized surfaces were later immersed in PBS with different concentration of WGA lectin (15, 35, 70 and 120 µg/mL) and were left for overnight stirring in dark on an orbital shaker at 300 rpm. A solution of sodium cyanoborohydride (5 mM, 0.25 mL) in PBS was also added. Next, to cover the unreacted active groups on the surface, a PBS solution of 2-(2-aminoethoxy)ethanol (15 mM, 1 mL) was added. After 30 mins, the surface was rinsed with PBS (5×3 mL), to eliminate unspecific protein adsorption.

2. Lectin immobilization on surfaces using mixed monolayers

The activation step was performed as indicated in the previous section.

The TESUD functionalized surfaces were obtained using the optimized conditions, 135 mM of TESUD incubated for 3 hours.

To the TESUD functionalized surfaces, 2-[2-(2-aminoethoxy)ethoxy]ethanol (TGA) was added with the WGA lectin (35 µg/mL) in PBS in order to form mixed monolayers on the surfaces. Different ratios of WGA lectin to TGA were studied, such as (1:1, 1:3 and 3:1). A solution of sodium cyanoborohydride (5 mM) in PBS was also added. The surfaces were then left for overnight stirring in dark on an orbital shaker at 300 rpm. The surfaces were then rinsed with PBS (5×3 mL), and dried under nitrogen flow.

3.3.1.2. Lectin immobilization on microparticles

Initially, the microparticles from the surfaces were collected in an eppendorf and were suspended in 1 mL of ethanol solution. The microparticles were then centrifuged for 3 mins at 13,000 rpm forming a pellet of the microparticles. The supernatant (ethanol) was removed and the microparticles were again suspended in a freshly prepared 100 µL of piranha solution, H_2SO_4 (98%): H_2O_2 (30%) in the ratio 7:3 for surface activation and hydroxylation. The microparticles were mixed well using a micropipette (×3) and were ultrasonicated for 5 sec to remove any aggregates of microparticles. The eppendorf was then left for stirring in a thermoshaker for 1 hour. The microparticles after the hydroxylation step were then centrifuged for 10 mins at 13,000 rpm. The supernatant (piranha solution) was removed, and the pellet was washed with Milli-Q water (3×100 µL), by centrifuging for 10 mins at 13,000 rpm.

The freshly activated microparticles were incubated in a basic solution: 100 µL of basic solution containing, NH_4OH (20%), H_2O_2 (30%) and Milli-Q water in the volume ratio of 1:1:5 was added to the eppendorf. The microparticles were mixed using the micropipette (×3) and ultrasonicated for 5 sec. The eppendorf was then left for stirring in a thermoshaker for 30 mins. The microparticles after the basic treatment were centrifuged for 10 mins at 13,000 rpm. The supernatant (basic solution) was removed, and the remaining pellet of the microparticles was washed with Milli-Q water (3×100 µL), centrifuged for 10 mins at 13,000. An additional washing step with 100 µL of absolute ethanol was performed.

After the basic treatment, the hydroxylated microparticles were incubated in a solution of TESUD in absolute ethanol. The solution of 135 mM TESUD was prepared separately by mixing, 50 µL of TESUD, 50 µL of acetic acid (0.05 mM) and 900 µL of absolute ethanol. 100 µL of this solution was added to the microparticles containing eppendorf and was mixed well using a micropipette (×3) and ultrasonicated for 5 sec. The eppendorf was then stirred for 3 hrs on a thermoshaker at room temperature. After this step, the eppendorf was centrifuged for 5 mins at 13,000 rpm, and the supernatant (TESUD in ethanol) was removed. The microparticles in the pellet were washed with absolute ethanol (6×100 µL), centrifuged for 5 mins at 13,000 rpm.

TESUD functionalized microparticles were then incubated with 100 µL of lectin, WGA/Con A (35 µg/mL) in PBS in an eppendorf. To this, 5 mM of sodium cyanoborohydride was also added, ultrasonicated (5 sec) and stirred in a thermoshaker for overnight in dark at room temperature. The following day, the lectin functionalized microparticles were washed with PBS (3×100 µL), by centrifuging for 10 mins at 13,000 rpm. Next, to cover the unreacted active groups on the microparticles, a PBS solution of 2-(2-aminoethoxy)ethanol (15 mM, 100 µL) was added. After 30 mins, the microparticles were washed with PBS (3×100 µL), by centrifuging for 10 mins at 13,000 rpm to eliminate unspecific protein adsorption. The microparticles were finally resuspended in 100 µL of PBS solution.

1. Lectin immobilization on microparticles using different washing treatments

The protocol remains the same as above. But, an additional washing step at the end of the protocol is performed. In order to remove WGA/Con A aggregates, the microparticles were treated with Tween solution. Two different Tween solutions were tested (Tween 20 or Tween 80). The microparticles were incubated in a PBS solution of Tween (0.5 %, 100 µL) for 15 mins. After, the microparticles were washed with PBS (3×100 µL), by centrifuging for 10 mins at 13,000 rpm.

2. Lectin immobilization on microparticles using mixed monolayers

The TESUD functionalized microparticles were obtained as described before.

TESUD functionalized microparticles were then incubated in 100 µL PBS solution of WGA/Con A lectin (35 µg/mL) and 5 mM of sodium cyanoborohydride. To this, a PBS solution of TGA was added in different ratios such as lectin: TGA (1:1, 1:3 and 3:1). The microparticles were mixed well using ultrasonication (5 sec) and were left for stirring in a thermoshaker for overnight in dark at room temperature. The following day, the lectin functionalized microparticles were washed with PBS (3×100 µL), by centrifuging for 10 mins at 13,000 rpm.

Next, to remove the WGA/Con A aggregates, the microparticles were incubated in a PBS solution of Tween 20 (0.5 %, 100 µL) for 15 mins. After, the microparticles were washed with PBS (3×100 µL), by centrifuging for 10 mins at 13,000 rpm. The microparticles were finally resuspended in 100 µL of PBS solution.

Boronic acid (BA) immobilization on surfaces

The surfaces were activated as described before.

The activated surfaces were then treated with 2% (v/v) of (3-aminopropyl)triethoxysilane (APTES) in 1 mL of absolute ethanol. The surfaces were incubated for 3 hours stirring on an orbital shaker at 600 rpm. The amino functionalized surfaces were then washed using ethanol (5×3 mL) to remove the excess APTES solution and then dried under nitrogen. Finally, the surface was incubated in a solution of absolute ethanol of 4-formylphenylboronic acid (BA) (5 mg/mL) and sodium cyanoborohydride (5 mg/mL) for overnight. The next day, the surfaces were washed with ethanol (5×3 mL) and dried with nitrogen.

Boronic acid (BA) immobilization on microparticles

The microparticles were activated as described before.

After the basic treatment, the hydroxylated microparticles were incubated in a 100 µL solution of APTES (2% v/v) in absolute ethanol. The solution was mixed well using a micropipette (×3) and ultrasonicated for 5 sec. The eppendorf was then stirred for 3 hrs on a thermoshaker at room temperature. After this step, the eppendorf was centrifuged for 5 mins at 13,000 rpm, and the supernatant was removed. The microparticles in the pellet were washed with absolute ethanol (3×100 µL), centrifuged for 5 mins at 13,000 rpm.

APTES functionalized microparticles were then incubated with 100 µL of absolute ethanol solution of 5 mg/mL of both 4-formylphenylboronic acid (BA) and sodium cyanoborohydride. The microparticles were ultrasonicated (5 sec) and were left for overnight stirring in dark on a thermoshaker at room temperature. Next, the BA functionalized microparticles were washed with absolute ethanol (3×100 µL), by centrifuging for 5 mins at 13,000 rpm.

Immobilization of pH dependent fluorophores (**Oregon green**/ **pHrodo**/ **SNARF**/ **Alexa fluor**)

Polysilicon surfaces: The surfaces were initially activated using the protocol described before. The APTES functionalization was carried out following the protocol described in BA immobilization. The APTES functionalized polysilicon surfaces were finally treated with the fluorophore solution (17 µM, 1 mL) in anhydrous DMSO and left for overnight stirring in dark on an orbital shaker at 300 rpm. Next, the surfaces were rinsed using DMSO (5×3 mL), and dried with nitrogen.

Polysilicon microparticles: The functionalization protocol remains the same, but final volume of the solution was made to 100 µL. Also, at every step of functionalization, the microparticles were washed using centrifugation for 5 mins at 13,000 rpm.

Gold surfaces: The gold surfaces were firstly cleaned using 1 mL of piranha solution, H_2SO_4 (98%): H_2O_2 (30%) in the ratio 7:3 and stirred for 30 mins on an orbital shaker at 300 rpm. The surfaces were then rinsed using milli-Q water (5×3 mL). The freshly cleaned surfaces were then incubated with cysteamine (25 mM, 1 mL) in absolute ethanol solution, stirred for 3 hrs on an orbital shaker at 300 rpm. After, the surfaces were rinsed using ethanol (5×3 mL) and dried with nitrogen. The cysteamine functionalized gold surfaces were finally incubated with the fluorophore (17 µM, 1mL) in anhydrous DMSO for overnight in dark on an orbital shaker at 300 rpm. Next, the surfaces were rinsed using DMSO (5×3 mL), and dried with nitrogen.

Bi-functionalization of bi-functional (polysilicon-gold) surfaces with **Oregon green-pHrodo**

The bi-functional surfaces were treated with piranha solution, H_2SO_4 (98%): H_2O_2 (30%) in the volume ratio of 7:3 respectively and were stirred for 1 hr to clean and activate the surface. The gold surface was functionalized prior to the polysilicon surface. Therefore, the freshly cleaned surfaces were treated with cysteamine (25 mM, 1 mL) in absolute ethanol and stirred for 3 hours in an orbital shaker at 300 rpm. After, the surfaces were rinsed using ethanol (5×3 mL) and dried with nitrogen. The amino functionalized surfaces were then incubated in **pHrodo** (17 µM, 1 mL) in anhydrous DMSO and stirred in dark for overnight using an orbital shaker at 300 rpm. The following day the surface was washed with DMSO (5×3 mL) in order to remove the unbounded fluorophore. A blocking agent, 2% solution of 2-(1-

hydroxy)ethoxyeth-1-yl methanesulfonate (EG2OMs) for 30 mins in absolute ethanol to block the unreacted amino groups on the gold surface. The surface was again rinsed using ethanol (5×3 mL) and dried with nitrogen. The next step was to functionalize the polysilicon surface and thus incubated in 1 mL of 2% APTES solution in absolute ethanol for 3 hours under stirring. Later, the surface was rinsed with ethanol (5×3 mL) to remove the excess unbounded silane from the surface. The final step was to functionalize the polysilicon surface with **Oregon green** (17 µM, 1 mL) in anhydrous DMSO and incubated overnight in dark under stirring. Next day, the surface was rinsed using DMSO (5×3 mL) and dried under nitrogen.

In the case of hexahedral bi-functional microparticles, the bi-functionalization follows a similar protocol, but the final volume used was 100 µL. Also, the microparticles were washed at every step using centrifugation for 5 min at 13,000 rpm. The microparticles were finally stored in PBS solution.

Functionalization of polysilicon surfaces with Cytochrome c (Cyt c)

The surfaces were initially activated using the similar protocol as described before.

TESUD functionalized surfaces were later immersed in PBS with different concentration of Cyt c (35 µg/mL). To this, a solution of sodium cyanoborohydride (5 mM, 0.25 mL) in PBS was also added) and were left for overnight stirring in dark on an orbital shaker at 300 rpm. Next, to cover the unreacted active groups on the surface, a PBS solution of 2-(2-aminoethoxy)ethanol (15 mM, 1 mL) was added. After 30 mins, the surface was rinsed with PBS (5×3 mL), to eliminate unspecific protein adsorption.

In the case of bi-functional microparticles, the functionalization protocol remains the same, but final volume of the solution was made to 100 µL. Also, at every step of functionalization, the microparticles were washed using centrifugation for 5 mins at 13,000 rpm.

Immobilization of BODIPY on gold surfaces

The surfaces were cleaned and functionalized using cysteamine as described before.

The amino functionalized gold surfaces were finally incubated with BODIPY (20 µM, 1mL) in anhydrous DMSO for overnight in dark on an orbital shaker at 300 rpm. Next, the surfaces were rinsed using DMSO (5×3 mL), and dried with nitrogen.

In the case of bi-functional microparticles, the functionalization protocol remains the same, but final volume of the solution was made to 100 µL. Also, at every step of functionalization, the microparticles were washed using centrifugation for 5 mins at 13,000 rpm.

Anion exchange protocol of bis-imidazolium salts

A solution of silver hexafluorophosphate (0.11 g, 0.42 mmol) in dry acetonitrile (2 mL) was added to a solution of **2•2Br** (0.13 g, 0.14 mmol) in dry acetonitrile (54 mL) at 40°C. The stirring was continued in darkness for 1 hour. A yellow solid precipitated, which was filtered off and the solvent was evaporated. The white residue was washed with water (10 mL) and filtered off to give **2•2PF$_6$** as a pale brown solid (0.13 g, 93 %). The same protocol was followed for compound **4•2Br**.

Anion binding properties of bis-imidazolium salts

Titration experiments were carried out as follows. First, the ^{1}H NMR spectra were acquired for the bis-imidazolium salts **2·2PF$_6$**, **3·2Br** (0.5 mM in 0.7 mL of $(CD_3)_2SO$) and **4·2PF$_6$** (0.5 mM in 0.7 mL of $CDCl_3$). Consecutive additions of 10 µL of tetrabutylammonium salts (TBA·X, X= Cl^-, $H_2PO_4^-$, AcO^-) corresponding to 1 equivalent were done to the initial solutions, with bis-imidazolium:TBA·X ratios of 1:0, 1:1, 1:2, 1:3, 1:7, 1:10, 1:13, 1:15, 1:20. The spectra were interpreted and the increment in chemical shifts was plotted as a function of salt concentration. The degree of anion binding was determined by nonlinear curve-regression fitting using Origin 7.0 software. The fitting procedure allowed the calculation of the stability constant (K_a) from the best approximation curve for experimental points, which corresponded to a one-site binding model. Additionally, the complexation free energy ($\Delta G°$) was deduced using the equation: $\Delta G° = - RT\ln K_a$.

Synthesis of AuNPs

For the preparation of the AuNPs, a solution of $HAuCl_4.H_2O$ (0.12 g, 0.32 mmol) in 10 mL of water was added to an extraction funnel containing 10 mL of a chloroform solution with 0.24 mmol of the imidazolium derivatives **3·2Br - 5·2Br**. The organic phase was separated and collected in a round bottom flask to which a freshly prepared solution of $NaBH_4$ (1.28 g, 6.40 mmol) in water (5 mL) was added drop wise under constant stirring. The stirring continued for 4 hours in the dark at room temperature. Later, the organic phase was separated using an extraction funnel and the solvent were evaporated in a rotary evaporator. The residue was washed with ethanol (2 x 1 mL), and with acetone (2 x 1 mL) and centrifuged at 13400 rpm for 10 minutes after each washing.

Drug incorporation with **5·AuNP** and in vitro release study

The drug incorporation and release was done following a previously published protocol [129]. Briefly, to 5 mL of **5·AuNP** solution in chloroform, 5 mL of an aqueous solution of 10 mM sodium ibuprofenate were added and mixed in an extraction funnel. The organic phase was collected and was extracted with water (2 x 5 mL) to remove the excess ibuprofenate. The presence of ibuprofenate was determined in aqueous and organic phases through UV/Visible absorption spectroscopy. The release of the drug incorporated in the AuNPs was performed in a Microette transdermal diffusion system with vertically assembled Franz-type diffusion cells. The dialysis membrane (Cellu·Sep T3 dialysis membrane, MWCO12000-14000Da, MFPI, USA) was treated overnight in a solution of water:methanol 2:1 to hydrate the membrane and remove grease prior to the start of the experiment. The membranes were then placed in the Franz-type diffusion cells and 260 µL of the nanoparticle solution loaded with the drug was placed on top of the membranes. The solutions were air dried and resuspended with 250 µL of Sorensen buffer 1/15 M pH 5.5 that was used as the donor solution. NaOH 71 mM solution was taken as a receptor solution. The Franz-type cells were connected to a controlled heating water bath set to 32°C. The cells were sealed and samples were taken along 2 weeks at 24 hours intervals. The same protocol was followed to study the release at the physiological pH 7.4 at 37°C.

Drug determination in samples

Drug determination in samples was done by HPLC in a Waters LC Module I. The column used was ODS-2 5 µm (4.6 mm x 150 mm) from Waters Spherisorb®. The mobile phase was acetonitrile-water pH 3, adjusted with orthophosphoric acid (65:35 v/v). The flow rate was

1.5 mL min^{-1} and the detection wavelength was 220 nm. The data was collected using the software Millennium 32 version 4.0.0 from Waters Corporation.

3.3.2. Chemical characterization

Quantification of immobilized lectin on polysilicon microparticles

Using fluorescence spectroscopy, a calibration curve was achieved by recording the spectra of the lectin solution having different concentrations ranging from 5 µg/mL to 40 µg/mL. Then, the fluorescence of the supernatants from the functionalized microparticles before and after the functionalization was recorded. The amount of immobilized lectin was obtained calculating the difference between the initial and final fluorescence emission intensity and by using the obtained calibration curve, to relate the intensity with the lectin concentration. The spectra of fluorescence emission at 620 nm were recorded by exciting the samples at 595 nm.

Similar protocol was adopted for quantifying immobilized pH-sensitive fluorophores on bi-functional microparticles. Using fluorescence spectroscopy, a calibration curve was obtained between 0.2 µM to 17 µM. In the case of **Oregon green**, the excitation/emission wavelength at 496/520 nm was obtained. Whereas, for **pHrodo**, the excitation/emission wavelength at 560/595 nm was obtained.

Quantification of immobilized Cyt c on polysilicon microparticles

Using absorbance spectroscopy, a calibration curve was obtained for different concentration of Cyt c ranging between 10 µg/mL to 75 µg/mL. Then, the absorbance of the supernatants from the functionalized microparticles before and after the functionalization was recorded in the range of 300 to 750 nm. The amount of immobilized Cyt c was obtained calculating the difference between the initial and final absorbance and by using the obtained calibration curve, to relate the absorbance intensity with the Cyt c concentration.

Characterization of BA using ARS

The BA functionalized substrates were treated with 10 µM solution of Alizarin Red S (ARS) in PBS at pH 7.4 for 5 mins. The substrates after incubation in ARS, were washed using PBS solution, dried under nitrogen and then characterized using fluorescence microscopy.

Study of BA with GlcNAc

The BA functionalized surfaces were incubated with 5 mg/mL of GlcNAc in PBS solution for 5 mins. The surfaces were then rinsed, dried under nitrogen and characterized using fluorescence microscopy.

Production and sensing of Reactive Oxygen Species (ROS)

In order to measure ROS production by Cyt C, BODIPY was used for monitoring fluorescence spectroscopy changes after irradiation of a PBS solution containing Cyt c (10 µM) and BODIPY (20 µM) in 2 mL of PBS. Samples were irradiated with Horiba-Jobin-Yvon SPEX Nanolog-TM spectrofluorometer at 408 nm (Soret band) with slit 5 for 5 min for exciting Cyt c. Then, immediately fluorescence emission from the BODIPY was measured after exciting the solution at 550 nm and monitoring the fluorescence emission decay of BODIPY at 590 nm every 5 mins for duration of 30 mins.

3.3.3. *In vitro* experiments

Bio-functionalized microparticles were further tested on Dictyostelium discoideum and HeLa cells in order to assess their behaviour in cell adhesion. The experiments were performed by the group of Prof. Teresa Suárez at the *Centro de Investigaciones Biológicas* (CIB-CSIC), Madrid.

RESULTS AND DISCUSSION

CHAPTER 4

CHAPTER 4

Functionalization of star-shaped and discoidal polysilicon microparticles with lectins for their adhesion to cell membranes

4.1. Introduction

Immobilization of biomolecules or synthetic bioactive molecules onto solid supports is a key step in the assembly of biosensors [134-137]. Since molecular recognition between protein receptors and their ligands is a central event in a wide variety of important biological processes, protein immobilization has become a fundamental tool to aid understanding of these interactions and in the search for applications of the phenomenon in many fields from bio-analytical chemistry to drug discovery [138-141]. One of the most currently used methods to immobilize biomolecules to substrates is the formation of an organic monolayer that will act as a linker, the so called self-assembled monolayers (SAMs). This organized layer of molecules induced by the chemisorption between the substrate and a functional headgroup provides one of the most elegant approaches to making stable ultrathin organic films spontaneously [142-148]. SAMs are also used as model substrates in biological studies because of their well-defined structure, controlled surface properties, and biocompatibility. SAM formation allows the possibility to change surface properties or add new characteristics to the materials. Different materials have been employed as substrates for the formation of monolayers, but gold and silicon are the most widely used and studied because of the ease of using thiol and silane chains, respectively, to be attached onto the corresponding surfaces; they form well-organized SAMs and they are biocompatible materials [141-142]. Chemical immobilization methodologies are of determinant importance in preserving the activity of biomolecules, and covalent binding renders the most robust and reliable devices [142,147]. Unfortunately, characterization of the monolayers is often not sufficiently thorough, which does not allow a direct relationship between chemical functionality and bioactivity [149-151].

On the other hand, cell adhesion is a topic of interest in nanomedicine as a tool to evaluate cell behaviour. Cell adhesion plays a critical role in cells because it triggers signal transduction inside the cells, while affecting cellular growth, proliferation, and differentiation [56-57]. The interactions between cells and surfaces have been the focus of studies in biological and medical research fields and many biocompatible materials having cell attachable or detachable properties have been developed [60,72-73]. Because cells can be attached to a hydrophobic surface via extracellular matrix proteins, hydrophobic modification is a popular method for cell patterning, where cells can be positioned on a substrate [152]. Different nanomaterials, such as quantum dots or metallic particles, introduced inside cells have been envisaged for numerous applications, but in general these materials are complex and could be harmful for living cells [45,153].

Microfabrication opens up huge opportunities to obtain new materials for studying living cells [154]. For instance, silicon substrates could offer cell adhesion, provided that the substrates are sufficiently small to be attached to the cell surface. To this end, it has been possible to adhere to Vero cells, through attachment of bio-functionalized materials to their plasma membranes [155]. Additionally, in our group we have achieved specific adhesion of bio-functionalized polysilicon encoded microparticles to the zona pellucida of mouse embryos. These bio-functionalized microparticles were found adhered to the embryos for more than 96 hrs, as well as resulted in high embryo viability, indicating the robustness of the bio-functionalization and therefore, the potential of these microparticles to be used for cell tagging [156].

As a step forward, in this work cell adhesion of a particle to the cell membrane, using polysilicon microparticles of different shapes and sizes is targeted. In order to design a microtool which is biocompatible and has specificity to the cell membrane, bio-functionalization of the polysilicon microparticles will become a decisive process to induce cell adhesion of the microparticles. Preparation of microtools for cell applications requires an extremely cautious and demanding selection of the components. Therefore, an accurate methodology to produce them, at the level of both microfabrication and chemical bio-functionalization, must be established.

To achieve our goal, lectins are initially regarded as optimal recognition to link a bio-functionalized SAM with the cell surface, because of their ability to recognize saccharide structures (**Figure 1-1**) [157-164]. Specific interactions between lectins and their complementary carbohydrates on cell surfaces have been thoroughly studied because of their importance in processes like cell−cell recognition or cellular adhesion.

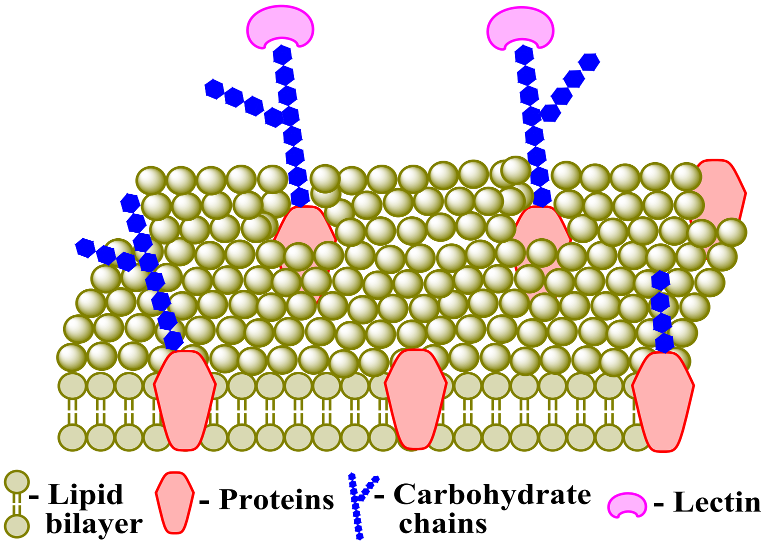

Figure 1-1. A model of a cell membrane, showing lectin-carbohydrate interaction.

Wheat germ agglutinin (WGA) is one of the most widely characterized and least immunogenic lectins [165-166]. WGA is a highly stable homodimer composed of subunits of 35,000 Da [167]. This lectin has been sequenced with 171 amino acids per polypeptide chain [168]. WGA has four domains each with two unique carbohydrate binding site [169-170]. **Figure 4-2 a)** shows the schematic representation of the WGA [171]. The carbohydrate-binding specificity of WGA is higher towards *N*-acetylglucosamine (GlcNAc) and *N*-Acetylneuraminic acid (Neu5Ac) [172-175]. Both carbohydrate residues are the key components on the surface of the cell membranes [176-183]. The reactivity of agglutinin of WGA in normal cells and cancer cells has been also studied, which showed that the WGA has more affinity towards cancer cells than normal cells [184-186]. Thus, WGA lectin was selected for functionalizing the microparticles to study their adhesion to cells.

Additionally, Concanavalin A (Con A), has also been proven to be one of the most useful lectins for biological applications [187]. Con A is a homotetramer composed of subunits of 26,500 Da. **Figure 4-2 b)** shows the crystallographic structure of Con A [188-190]. The carbohydrate-binding specificity of Con A has been widely studied in great detail [191]. It binds to D-glucose, D-fructose, D-mannose, GlcNAc and related monosaccharides [192]. Therefore, the microparticles were also functionalized with Con A lectin to study the cell adhesion of the microparticles to the cell membrane.

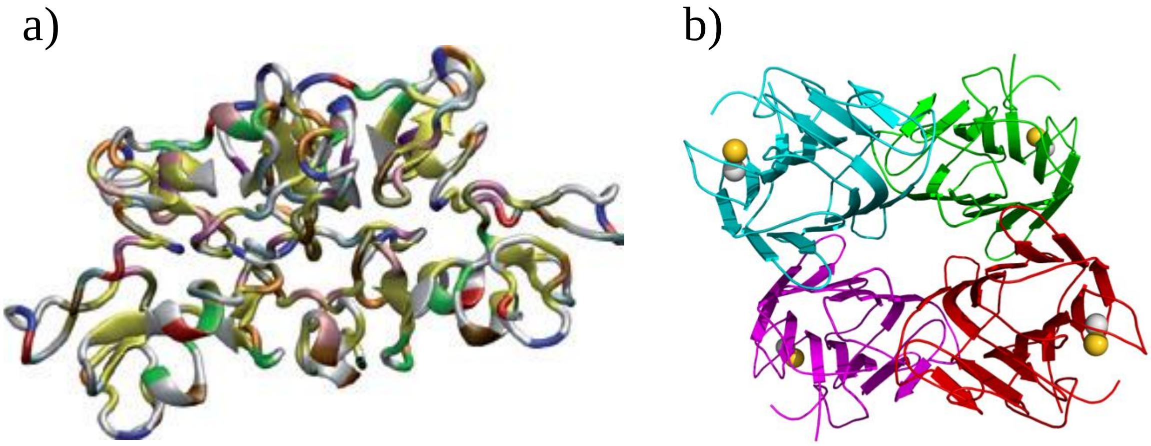

Figure 4-2. a) A schematic representation of the WGA lectin and **b)** Crystallographic structure of a tetramer of Con A lectin.

In this context, the present interdisciplinary research involves the covalent bio-functionalization of polysilicon microparticles of different shapes and sizes through synthetic organic moieties to obtain microtools designed for cell adhesion. In particular, in this work we aimed to use lectins such as WGA and Concanavalin A (Con A) as the key elements for adhesion to the cell membrane, once they have been covalently immobilized through SAMs to polysilicon substrates, to build up a device destined for cell adhesion.

As a proof of concept, the cell adhesion of the microparticles was studied on two different biological models: the social amoeba Dictyostelium discoideum (Dicty) and human-tumor HeLa cells. Dicty is an important model organism for studies of fundamental features that are essential in multicellular organisms [193-196]. On the other hand, HeLa is one of the most studied cell lines used for research. HeLa cells have the distinction of being the first immortal cell line, because of their remarkable ability to divide indefinitely [197-198].

The commercially available lectins that we used were fluorescently tagged with Texas Red. This traditional red fluorescent dye that has been used extensively to label protein conjugates for cellular imaging applications [199-200].

The following component was the fabrication of the microparticles, performed by our collaborators in the group of Prof. J. A. Plaza at *CNM*, explained in Appendix, Section 2. In this work, microparticles made up of polysilicon material, because polysilicon is robust, biocompatible, and a common material in the semiconductor industry were selected [58-59,88]. Different shapes and sizes of polysilicon microparticles were designed, star and disc shaped microparticles. The star shape was chosen due to the flexible arms of the stars which could favour the cell attachment, by having more points of contact with the cell membrane. In order to study cell adhesion on various cell lines, four different types of star shaped microparticles were fabricated. Large (20 μm in diameter) and small (10 μm in diameter) of 500 nm thickness, which we call **Batch 1** and **Batch 2** respectively. Also, with 50 nm thickness, which we call **Batch 3** and **Batch 4** respectively (**Figure 4-3**). In the case of disc shaped microparticles, two different types- Large (20 µm in diameter) and small (10 µm in diameter) of 500 nm thickness, which we call **Batch 5** and **Batch 6** respectively.

	Batch	a	b	c	Surfaces	Microparticles
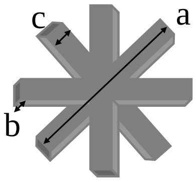	1	20 µm	500 nm	1.5 µm	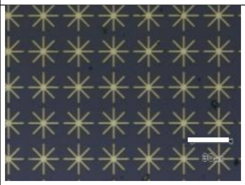	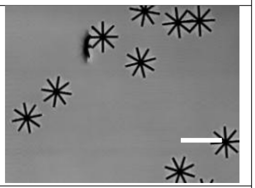
	2	10 µm	500 nm	1.5 µm	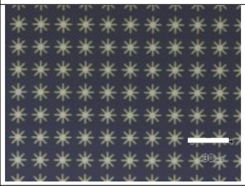	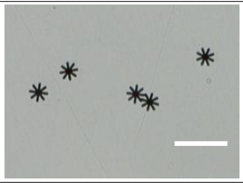
	3	20 µm	100 nm	1.5 µm	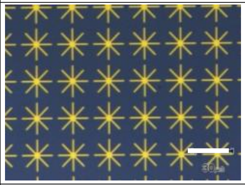	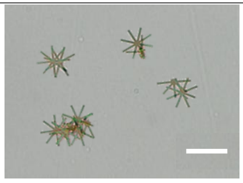
	4	10 µm	100 nm	1.5 µm	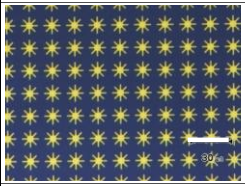	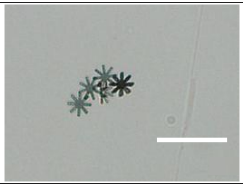
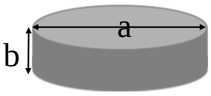	5	20 µm	500 nm	-	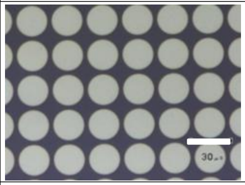	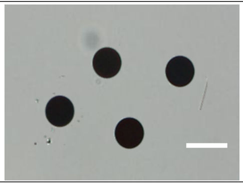
	6	10 µm	500 nm	-	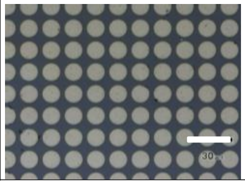	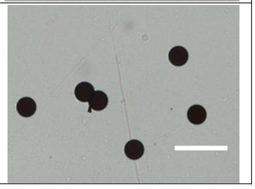

Figure 4-3. Bright field images of different types of polysilicon microparticles on a silicon wafer and microparticles in suspension, with their micrometric dimensions. Scale bar – 30 µm.

For functionalization, two different substrates were used, Surfaces and Microparticles. a) Surfaces (approximately 0.5 cm^2) were cut from wafers; incorporating polysilicon microparticles of size 20/10 µm and thickness 50/500 nm were used. Bio-functionalization was always attempted first using surfaces, mainly because they are easier to manipulate and characterize, and the synthetic methodology was then adapted to microparticle functionalization. b) Microparticles, the released microparticles were obtained by treating the silicon wafer using hydrogen fluoride solution to detach the polysilicon particles from the thermal oxide layer. **Figure 4-4** shows surfaces from **Batch 1**, bearing polysilicon microparticles on silicon wafer, using a 100 nm thick silicon oxide layer and microparticles, released from the surfaces (Appendix, Section 2).

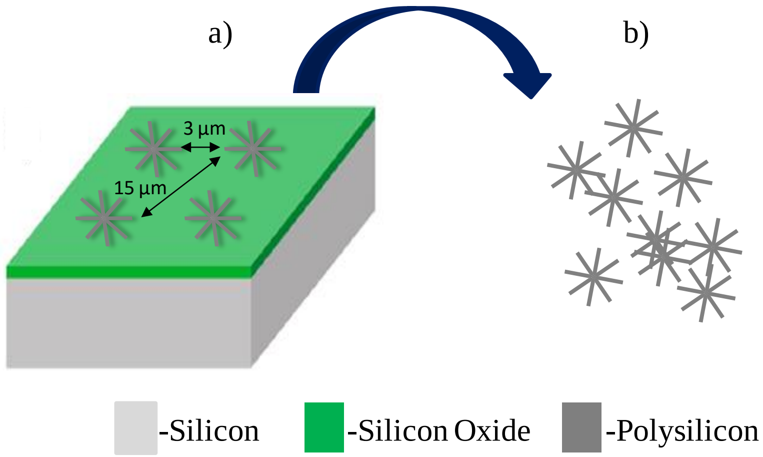

Figure 4-4. Release of polysilicon microparticles of **Batch 1** from the silicon wafer, using silicon oxide as a sacrificial layer.

The external dimensions of the microparticles were 10/20 µm in diameter and 50/500 nm thickness. In the case of star shaped microparticles, the centre of the star and the width of the arms of the stars were 1.5 µm.

4.2. Functionalization and characterization of star shaped polysilicon particles on surfaces

The functionalization protocol was initially optimized on **Batch 1** surfaces, bearing polysilicon microparticles of 20 µm in size with 500 nm thickness, using the lectin WGA conjugated with Texas Red (WGA-TR).

4.2.1. Chemical functionalization

Initially, the previously established protocol for bio-functionalizing polysilicon substrates with WGA lectin by our group was tested on these surfaces [156,201]. The bio-functionalization consists of three steps, as seen in **Scheme 4.1**:

1. **Activation:** The surfaces were first cleaned and activated using piranha solution, increasing the amount of hydroxyl groups on the surfaces. In order to increase the activation, the surfaces were treated with a basic piranha solution to achieve complete hydroxylation.

2. **Silanization:** The hydroxylated surfaces were then made to react with a silane coupling agent as a linker molecule for the surfaces. The silanes have the ability to form covalent bond with the inorganic surface, which is essential to achieve a stable functionalization [202-204].

In our case we used as linker 11-(triethoxysilyl)undecanal (TESUD), the triethoxy silane moiety as the reactive group with the activated polysilicon surface, and an aldehyde as the organic functional group to bind the protein at a later step. The triethoxy group of the TESUD reacts with the hydroxylated polysilicon surface forming a stable covalent bond between the linker and the surface. The surfaces after the treatment results in a uniform layer of an aldehyde, which we call CHO self-assembled monolayer (CHO-SAM).

3. **WGA immobilization:** The final step was the immobilization of the lectin, WGA on the surfaces through a reductive amination process. Thereby, treating the CHO-SAM on the surface with the WGA lectin in the presence of a reducing agent, sodium cyanoborohydride ($NaBH_3CN$). The reaction between the aldehydes and the amino group would result in the formation of an imine bond, which was further reduced to form a stable secondary amine bond on the surface.

Scheme 4-1, shows the schematic representation of the bio-functionalization of star patterned surfaces.

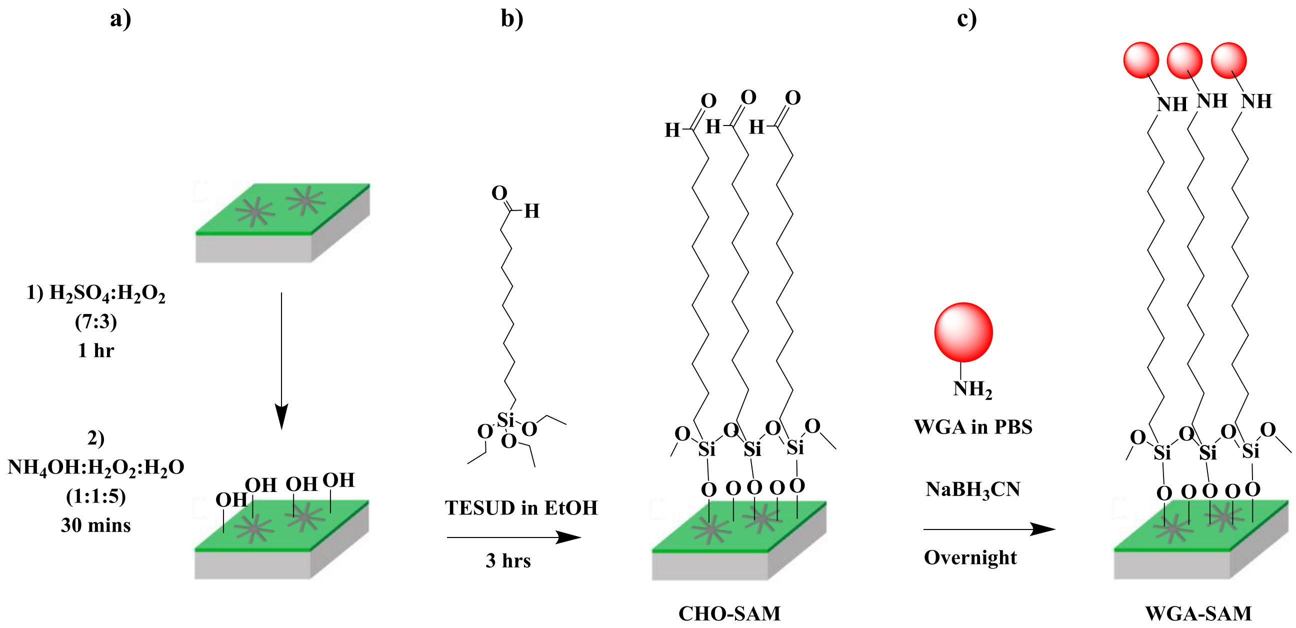

Scheme 4-1. Schematic representation of bio-functionalization of WGA on surfaces. **a)** Activation, **b)** Silanization, using 135 mM of TESUD for 3 hrs to form CHO-SAM and **c)** WGA immobilization, incubated in 35 µg/mL of WGA for overnight forming WGA-SAM [156].

The functionalized surfaces were characterized using fluorescence microscopy along with a control (non-functionalized surface). The control surfaces were characterized after the activation step. **Figure 4-6** shows the control and WGA functionalized surface, an optical image taken in bright field and fluorescent image excited using a green filter (λ= 530-550 nm) in fluorescence microscopy. The control surface did not show any fluorescence; on the other hand, the fluorescence image of WGA functionalized surface shows uniformity in the functionalization.

It is also observed that the fluorescence is higher on the background (SiO_2) layer than on the microparticles (polysilicon). This could be attributed to the difference in the surface reactivity between the silicon oxide and the polysilicon. The fluorescence image clearly shows higher functionalization on silicon oxide than polysilicon, thus making the polysilicon microparticle on the top appear darker. This difference in surface has been further studied (Section 4.6).

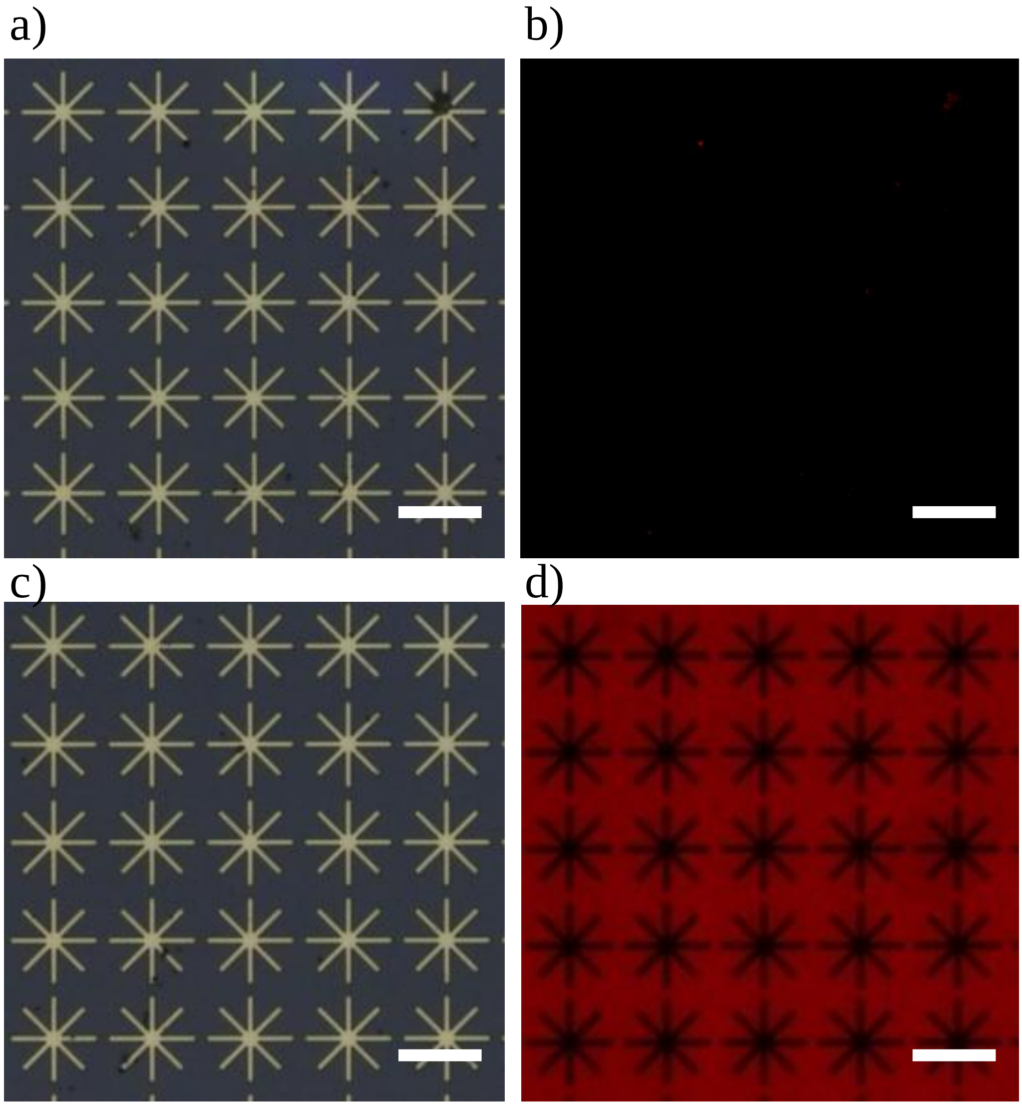

Figure 4-6. Bright field and fluorescence microscopy images of control (non-functionalized) surface **a)** in bright field, **b)** excited using green filter and WGA immobilized surface, **c)** in bright field, **d)** excited using green filter. Scale bar – 20 µm

4.2.1.1. Influence of TESUD concentration

Functionalization was further studied using different concentrations of TESUD, to see the influence on the monolayer formation and to the final bio-functionalization. The concentration of WGA (35 µg/mL) was kept constant for all experiments. The difference in the homogeneity of functionalization was compared using fluorescence microscopy. The fluorescence microscopy images of WGA functionalized surfaces using 67.5, 135 and 200 mM solutions of TESUD, to prepare the CHO-SAM respectively are shown in **Figure 4-7**. The fluorescence microscopy images obtained after the WGA immobilization on the different CHO-SAMs resulted in homogenous functionalization of the silicon oxide. In the silicon oxide, this could be confirmed by the plot profile of the **Figure 4-7**. The surface with 67.5 mM of TESUD showed lower fluorescence intensity. This could be due to the presence of lower aldehyde groups immobilized on the surface. On the other hand, in the case of higher concentration of TESUD (200 mM), the fluorescence intensity increased, due to the presence of more aldehyde groups. But the fluorescence intensity observed was not uniform when compared to that of other TESUD concentrations. This could be due to the non-specific functionalization or polymerization of the CHO-SAM in some regions of the surface. Non-specific functionalization refers to the immobilization of more number of aldehyde groups on the surface which resulted in higher fluorescence intensity. Whereas, polymerization of the CHO-SAM in some region resulted in non-uniform fluorescence, due to the blocking of the terminal aldehyde group to react with the WGA lectin. The CHO-SAM formed using 135 mM of TESUD showed homogenous and uniform functionalization and therefore, this was the concentration selected for further CHO-SAM formation.

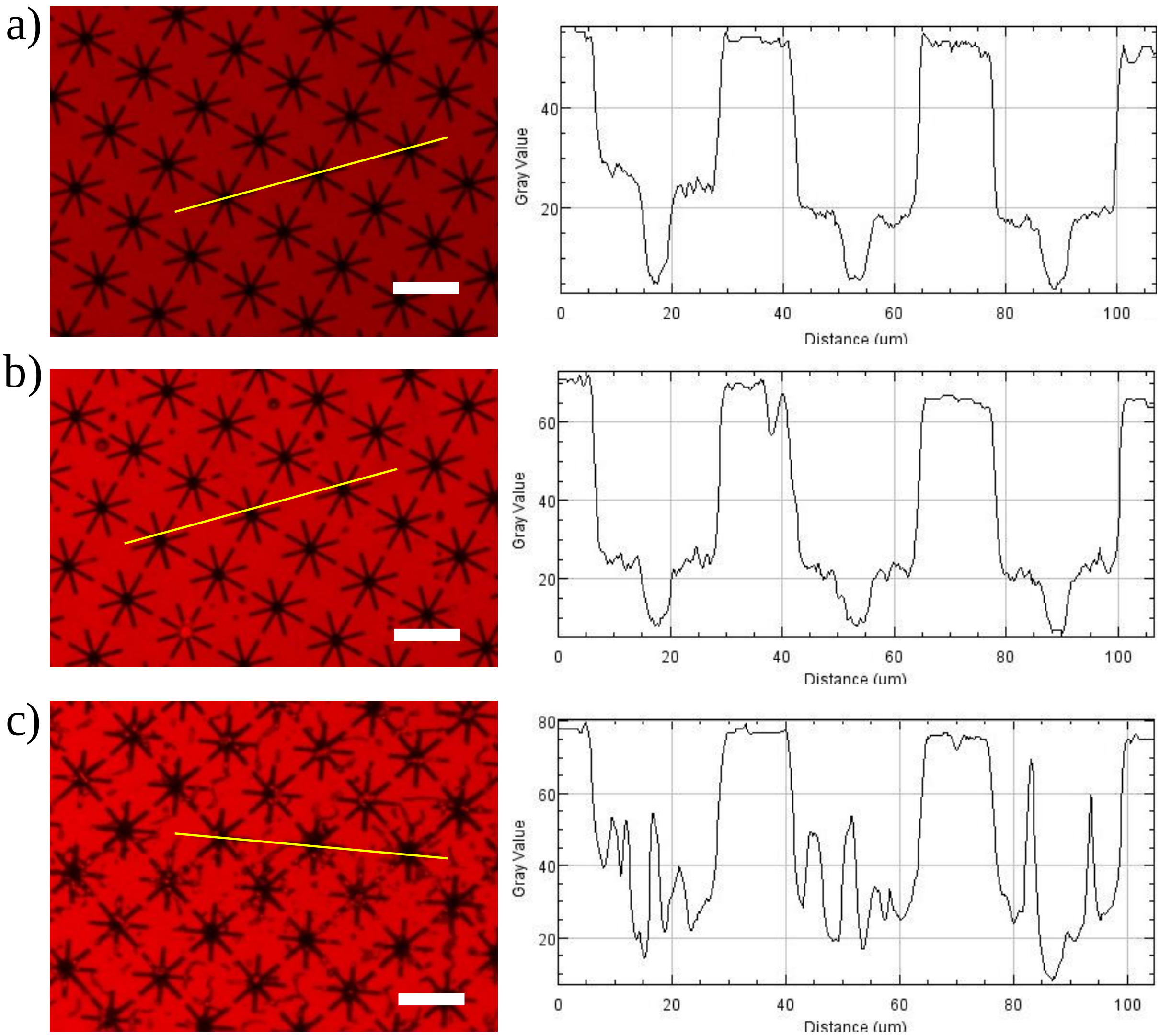

Figure 4-7. Fluorescence microscopy images of WGA functionalized surfaces using **a)** 67.5 mM, **b)** 135 mM and **c)** 200 mM of TESUD followed by treatment with WGA (35 µg/mL) and their plot profiles. Scale bar – 30 µm.

4.2.1.2. Influence of TESUD incubation time

Additionally, the influence of the incubation time for TESUD immobilization was also studied. The surfaces were incubated in the TESUD solution for 3 hours or overnight and the corresponding fluorescence, after WGA treatment, images are shown in **Figure 4-8**. As observed, there is a slight increase in the fluorescence intensity in the case of overnight

TESUD immobilization, but no other significant difference was seen between the two surfaces. This result suggests that the CHO-SAM was formed uniformly within 3 hours. Therefore, the final optimized conditions were 135 mM of TESUD for 3 hours.

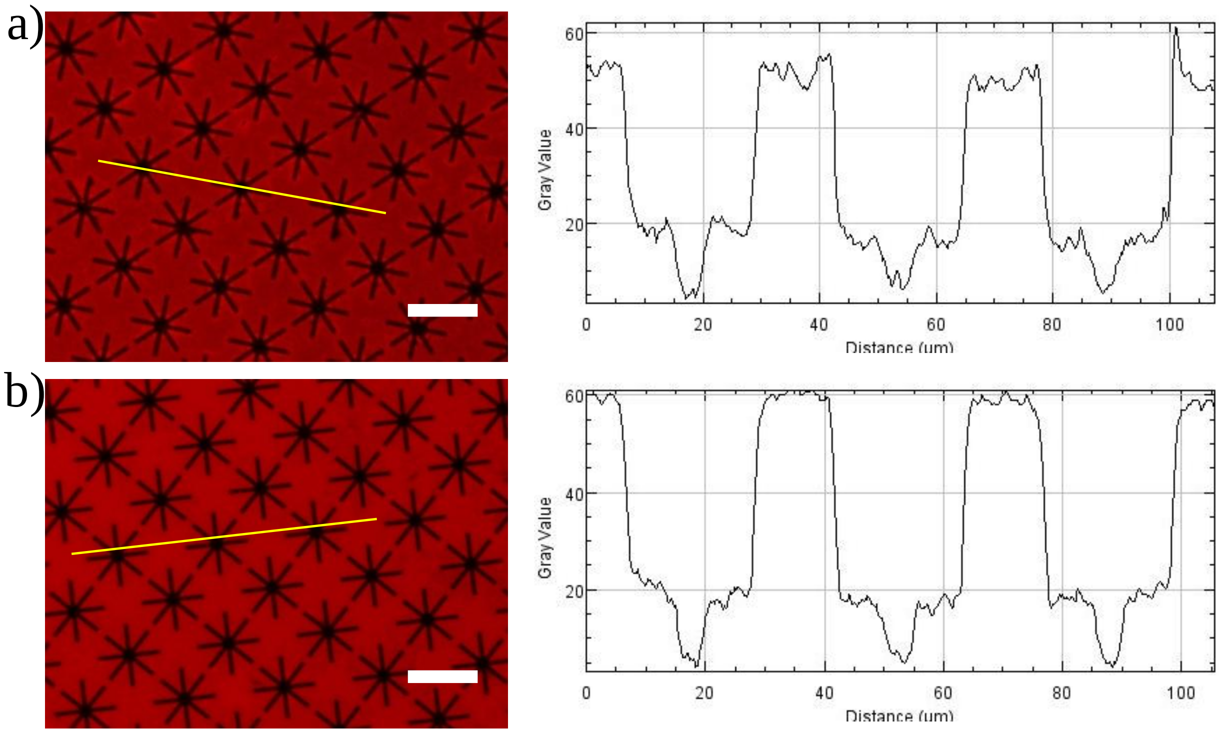

Figure 4-8. Fluorescence microscopy images of WGA functionalized surfaces incubated in TESUD for **a)** 3 hours and **b)** overnight, with their plot profiles. Scale bar – 30 µm.

4.2.1.3. Influence of WGA concentration

On the other hand, different concentrations of WGA were tested on the surfaces in order to monitor any changes in the homogeneity or the fluorescence intensity of the immobilized WGA. Various concentrations such as 15, 35 and 70 µg/ mL of WGA on surfaces were studied. From the fluorescence images observed in **Figure 4-9**, the fluorescence intensity increased with the increase in the concentration of the lectin.

Though, in the first case, 15 µg/mL of WGA, the surfaces were not homogenous and some dark patches could be observed. That could be due to the lack of fluorescent WGA molecules on the surface. Whereas, in the other two cases, it resulted in homogenous functionalization. As shown in the plot profiles, the difference in the fluorescence intensity between 35 and 70 µg/mL was not very significant. To avoid later the formation of multilayers of WGA on to the microparticles, 35 µg/mL of WGA was selected as an optimized concentration for the bio-functionalization of WGA on surfaces. Therefore, the final optimized conditions to achieve homogenous bio-functionalization on star shaped microparticles were, using TESUD (135 mM) for 3 hours followed by immobilizing WGA (35 µg/mL).

All the functionalized surfaces were further characterized using contact angle measurements, and values obtained for the different steps of the functionalized protocol are tabulated in

Table 4-1, which informs about the degree of hydrophobicity and the hydrophilicity of the surface, after each step of functionalization.

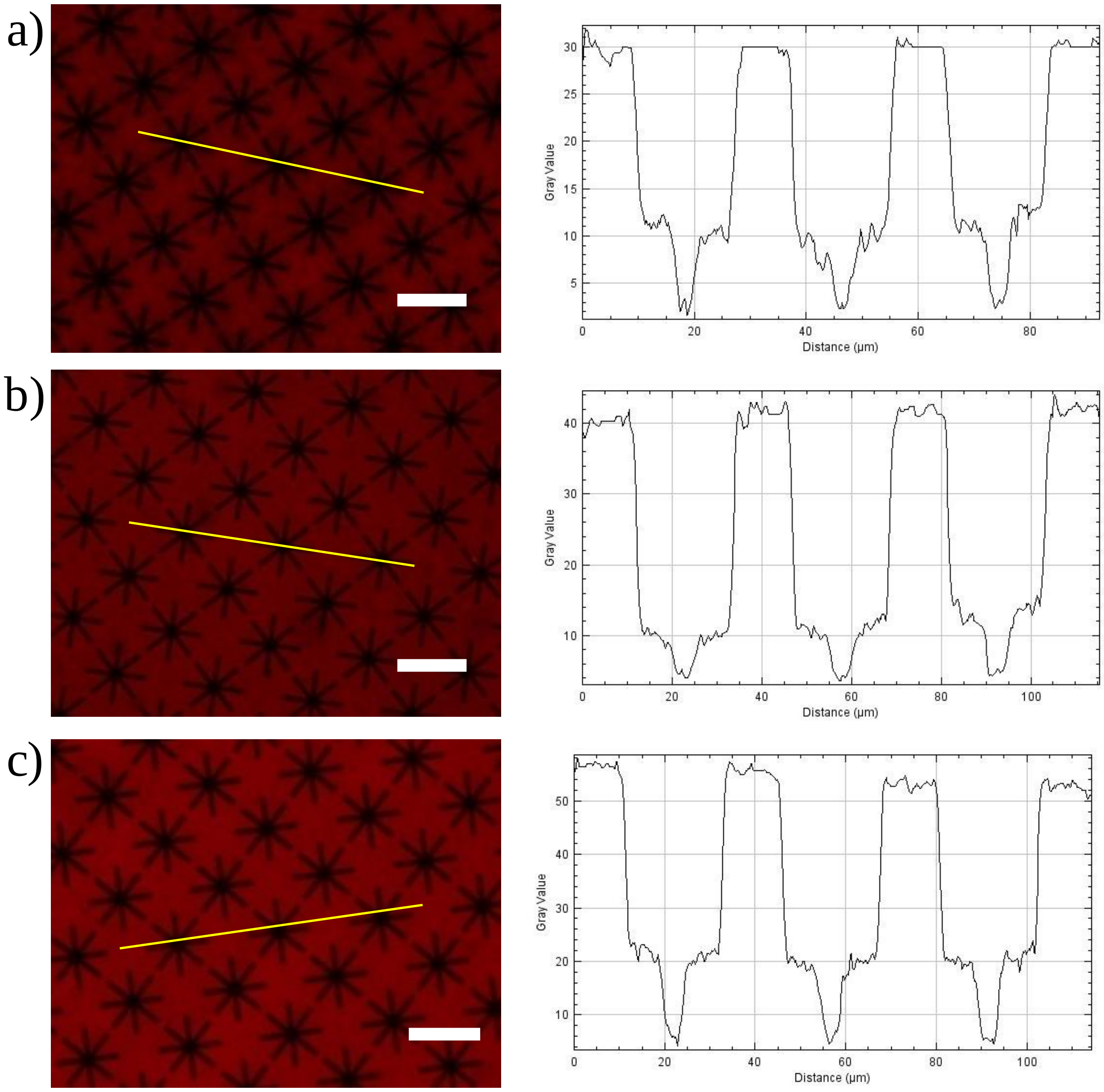

Figure 4-9. Fluorescence images of surfaces functionalized with **a)** 15 µg/mL, **b)** 35 µg/mL and **c)** 70 µg/mL of WGA, with their plot profiles. Scale bar – 30 µm.

The contact angle value of before the activation treatment was found to be 38°. This higher contact angle can be due to the presence of dirt from the atmosphere; this is partially why we need the cleaning step before starting the functionalization. After the piranha treatment, the contact angle of the hydroxylated surface was notably decreased making the surface more hydrophilic, thereby confirming the formation of hydroxyl groups on the surface. A further decrease in the contact angle to 10° was observed after the basic treatment indicating activation of the surfaces.

Table 4-1. Contact angle measurements ϴ (⁰) for the different chemically modified polysilicon/ silicon oxide surafces (**Batch 1**)

Sample Name	Contact angle ϴ (⁰)
Initial surface (before cleaning)	38 ± 4
After Piranha	12 ± 3
After Basic	10 ± 2
TESUD-SAM	87 ± 1
WGA-SAM	45 ± 3

After treatment with TESUD, a significant increase in the hydrophobicity of the surface to 87° was observed, due to the presence of the hydrophobic TESUD-SAM (11 carbon atoms) in its alkyl chain indicating the success of the silanization step. This value also corresponds to the value of immobilized TESUD found in the literature [201,205-207]. The contact angle after the immobilization of lectin decreased to 45°, this is due to the presence of various hydrophilic amino acids. The value observed after WGA immobilization is also similar to the value reported in the literature [156].

4.2.2. Characterization using AFM

In order to study the topography and the thickness of the functionalized surfaces, these were analyzed using Atomic Force Microscopy (AFM) at each step of the functionalization protocol. **Figure 4-10** shows three surfaces analyzed using AFM, after activation, after TESUD immobilization and after WGA immobilization.

From the above micrographs, it is seen that the functionalization at each step is uniform and homogenous. An increase in the intensity profile of the micrographs is seen at each step of the functionalization, indicating the formation of layers after every treatment. It is observed that the height in each plot profiles of the surface is similar i.e., 500 nm. This is because the thickness of a layer is very small. Thus, only seeing the topography and the uniformity of the layers formed on the surface at each step of functionalization.

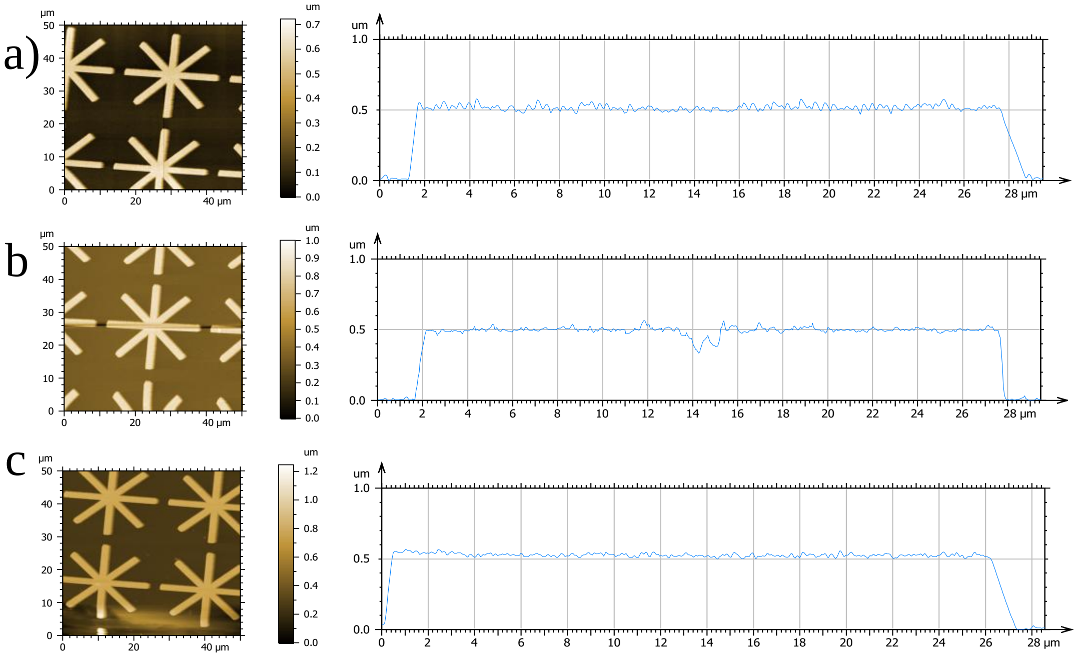

Figure 4-10. Micrographs of surfaces treated with **a)** piranha and basic solution, **b)** TESUD and **c)** WGA, with their plot profiles respectively.

In order to measure the thickness of the functionalized layer, a scratch was made on the surface using the AFM tip. For this experiment, the thickness of the microparticle (500 nm) and the silicon oxide layer (100 nm) below the microparticle was also taken into account. This experiment shows that the surfaces were very rough. **Figure 4-11** shows the 3-D image of the surface before any treatment (Control) and after the WGA immobilization.

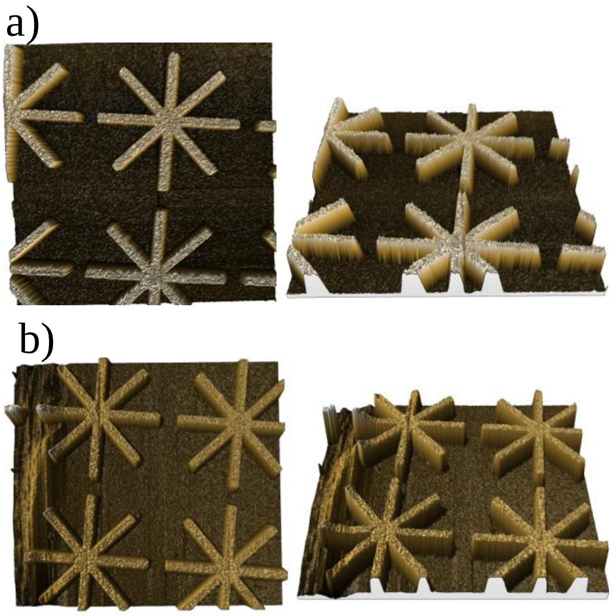

Figure 4-11. 3-D images of the surfaces **a)** control and **b)** after WGA immobilization, obtained using AFM

As shown in **Figure 4-11**, due to the roughness and hardness of the surface, it was very difficult to perform a scratch, as the tips of the AFM were breaking. This could also suggest that the monolayers after the functionalization are of few nanometers, thus not being able to scratch only the monolayers but the silicon layer as well. Since, the AFM tips were breaking, a manual scratch was made on the functionalized surface. **Figure 4-12** shows the micrographs obtained after the manual scratch, topographic image, 3-D image from the top and from the side of the WGA functionalized surface.

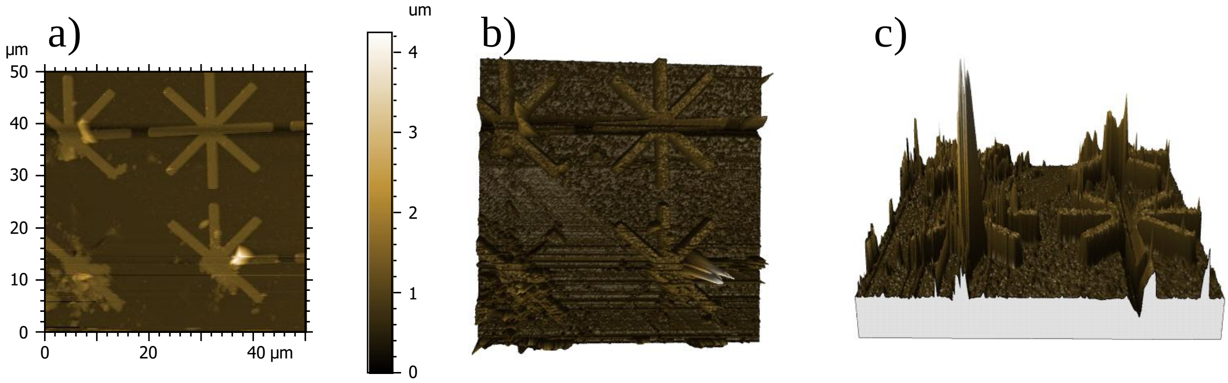

Figure 4-12. Micrographs obtained after the manual scratch showing **a)** topographic image, 3-D image **b)** from the top and **c)** from the side of the WGA functionalized surface.

From the above micrograph, it is clearly seen, that the manual scratch resulted in the removal of silicon layers. Which could be seen on the sides, and thus, some bits/fragments of silicon were seen on the topographic image of the surface. This was confirmed, when a scan was performed on a single star microparticle having a scratch. **Figure 4-13** shows the topographic image, 3-D image and step height profile of a single microparticle. From the 3-D image, it is clear that the manual scratch resulted in the removal of not only the polysilicon layer (500 nm) but also the silicon oxide layer (100 nm). As we know the size of each layer, the step height profile acquired does not correspond to the same value.

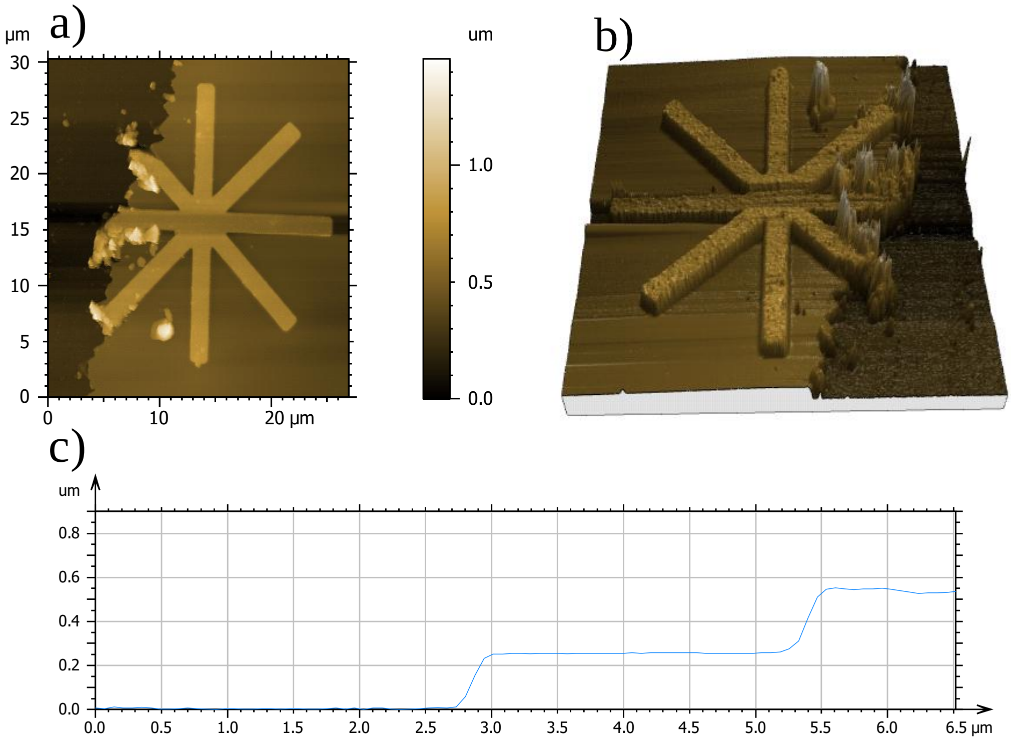

Figure 4-13. Micrographs obtained for a single microparticle with a scratch, **a)** its topographic image, **b)** 3-D image and **c)** step height profile of the microparticle.

Finally implying, the AFM results for these functionalized surfaces do not allow an estimation of the thickness of each monolayer, because is lower than the roughness of the polysilicon. However, the plot profiles of the topographic micrographs demonstrate the uniform and homogeneous functionalization on the surfaces.

4.2.3. Surface functionalization with mixed monolayers

Surface functionalization by forming mixed monolayers of WGA and Triglycolamine (TGA) were also analyzed **(Figure 4-14)**, with the idea to compare the uniformity and the homogeneity of functionalization of the surfaces [208-211]. TGA was selected to enhance the water dispersability of the microparticles.

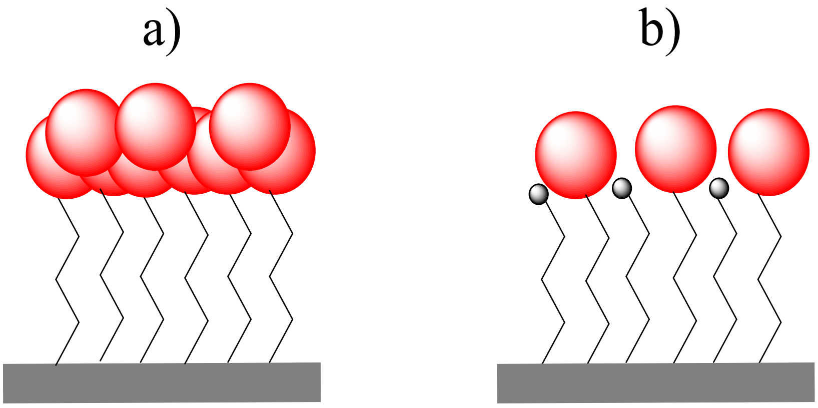

Figure 4-14. Surface functionalization with **a)** monolayers and **b)** mixed monolayers.

In order to form mixed monolayers, the surfaces were incubated in WGA with Triglycolamine (TGA) and were left for overnight. TGA is a molecule bearing functional groups, amino group and an alcohol on its terminal end. The amino group of the TGA reacts with the CHO-SAM competing for the aldehyde groups with the amino groups of the protein, as shown in **Scheme 4-2**. Different ratios of WGA: TGA were tested on the surfaces such as 1:1, 1:3 and 3:1, keeping the concentration of WGA as 35 µg/mL.

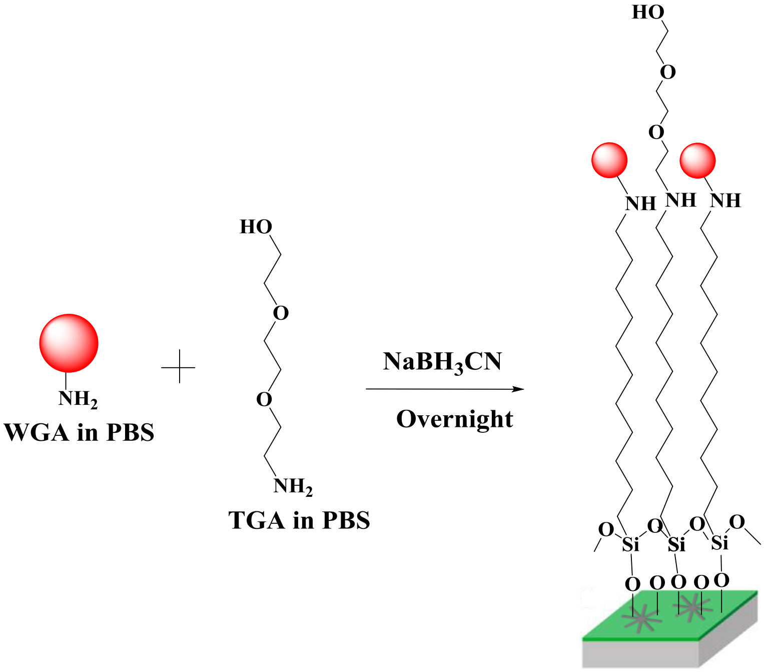

Scheme 4-2. Schematic representation of surface functionalization using mixed monolayers of WGA.

The functionalized surfaces were characterized using fluorescence microscopy, and **Figure 4-15** shows the fluorescence images of the surfaces functionalized with different ratios of WGA: TGA. The images obtained clearly showed significant difference between the different mixed monolayers of WGA and TGA. In the first case, 1:1 of WGA: TGA, the fluorescence intensity was less and non-homogenous. Areas around the star microparticles were lower in fluorescence intensity than the rest of the surface. This could be due to the faster kinetics of the TGA molecule. TGA being much smaller in size than WGA could get immobilized first blocking the aldehyde groups for further WGA immobilization, thus explaining the dark patches around the star microparticles. Also, the functionalization was not homogenous as shown in the plot profile, **Figure 4-15 a)**.

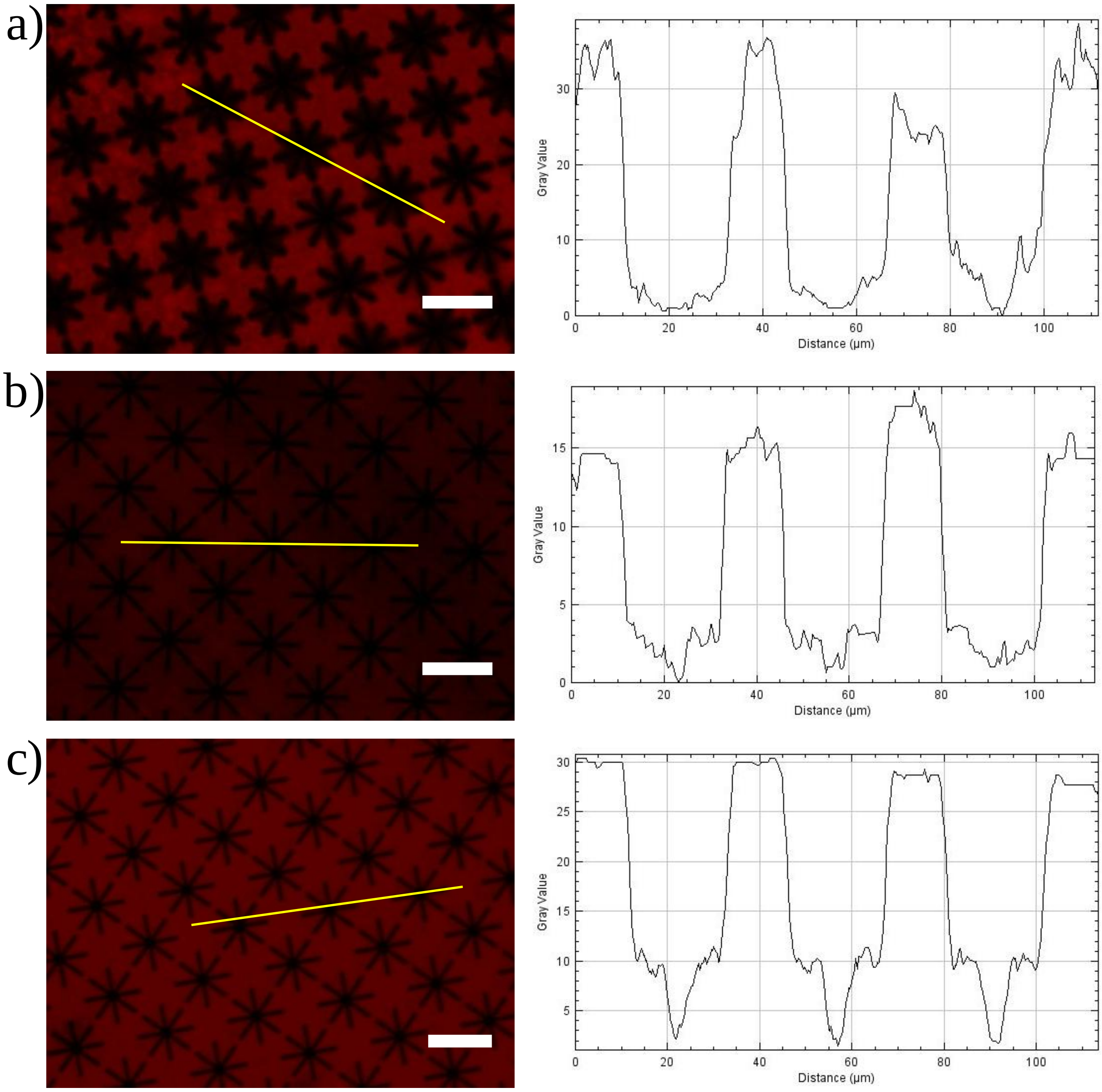

Figure 4-15. Fluorescence images of the surfaces functionalized with different ratios of WGA: TGA **a)** 1:1, **b)** 1:3 and **c)** 3:1, with their plot profiles. Scale bar – 30 µm.

On the other hand, in the case of WGA: TGA (1:3), the fluorescence intensity was lower when compared to the rest of the ratios. This could be due to the equal competition between the two molecules. Dark non-uniform patches were observed, explaining higher reactivity of TGA when compared to WGA. This is in agreement that the TGA molecule immobilizes prior to the WGA molecule.

The results obtained using the ratio 3:1 (WGA: TGA) indicate that the surfaces were very uniformly functionalized, and there was an increase in the fluorescence intensity than the rest of the cases. Thus, the ratio 3:1 was considered the best ratio for the functionalizing the WGA using the mixed monolayers.

Although, when the functionalization using mixed monolayers (3:1) was compared with the monolayers (1:0), no significant difference was observed on the surface. Both the surfaces were uniformly and homogenously functionalized. The fluorescence intensity of both the surfaces was similar. Thus, no enhancement in the functionalization was seen.

4.2.4. Elimination of silicon oxide layer from the surfaces

As mentioned earlier, there is a difference in the surface reactivity between the polysilicon (microparticles) and silicon oxide (layer below the microparticles). The surfaces characterized until now using fluorescence microscopy, showed high fluorescence in the background than on the microparticles which indicates that the functionalization on silicon oxide competes with that the polysilicon. Therefore, the silicon oxide layer was removed below the microparticles in order to characterize the functionalization on polysilicon microparticles. Thus, resulting in polysilicon microparticle on silicon wafer (**Figure 4-16 b**)). This step was done in order to study the functionalization on the microparticles. The silicon oxide from the surface was etched on time dependent basis using HF, explained in the Appendix, Section 2.

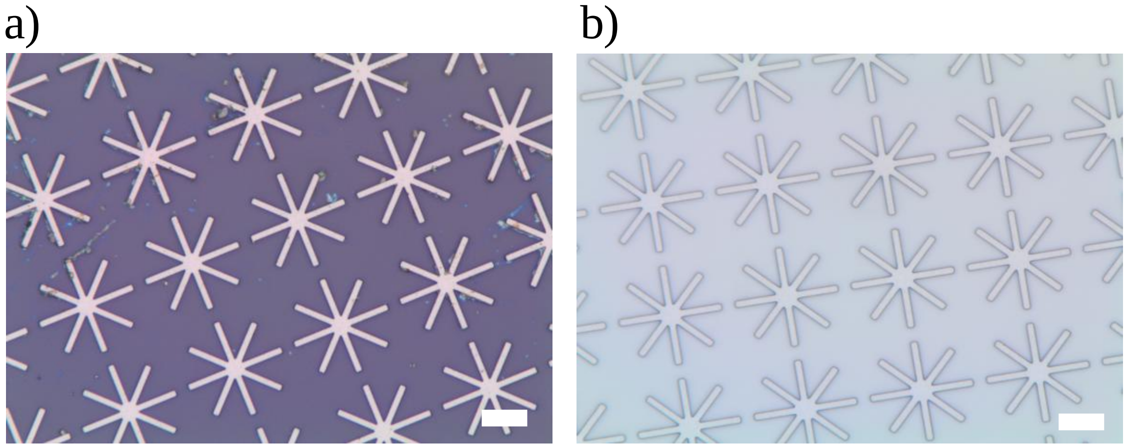

Figure 4-16. Bright field images of **Batch 1** surface **a)** with silicon oxide and **b)** without silicon oxide layer below the microparticles. Scale bar – 10 µm.

The previously optimized protocol for the CHO-SAM was used, using 135 mM of TESUD and 3 hours respectively. Different concentrations of WGA and mixed monolayers were studied.The different concentrations of WGA were tested on the surfaces were 15, 35 and 70 µg/mL. The functionalized surfaces were then characterized using fluorescence microscopy. **Figure 4-17** shows the 3-D fluorescence image of the surfaces functionalized with WGA at different concentrations with their plot profiles.

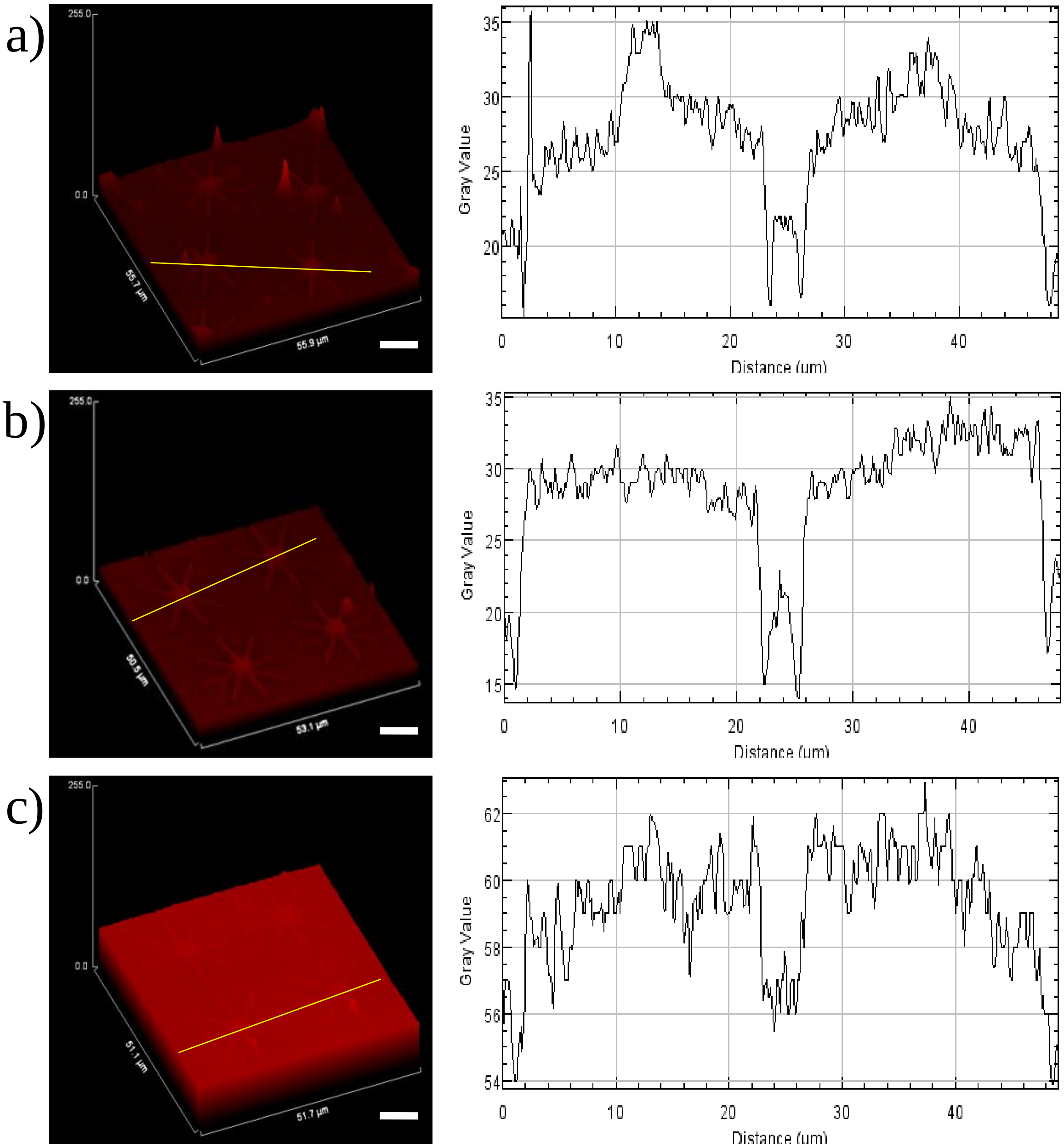

Figure 4-17. 3-D fluorescence image of surfaces functionalized with different concentrations of WGA **a)** 15 µg/mL, **b)** 35 µg/mL and **c)** 70 µg/mL, and their plot profiles. Scale bar – 10 µm.

As observed the fluorescence intensity increases with the increase in the concentration of the WGA. In the first case, surfaces functionalized with 15 µg/mL of WGA, the functionalization was not homogenous as indicated by the plot profile on the microparticles that was non-uniform. Whereas, in the case of 35 µg/mL, the surfaces showed uniform and homogenous functionalization. On the other hand, in the case of 70 µg/mL, the fluorescence intensity was much higher. However, the functionalization was similar on the whole surface (below and on the microparticles), this could be due to the formation of multilayers of WGA and/or functionalization of silicon.

Analysing the plot profiles for all the cases, it is observed that in the first two cases, there is a 10 fold increase in the fluorescence intensity on the microparticle than on the silicon wafer. Whereas, in the case of 70 µg/mL, not much difference was observed. This could be due to the excess of WGA molecules sitting on the silicon wafer, thus making it difficult to analyse the functionalization on the top of the microparticle. Therefore, the concentration 35 µg/mL, was chosen to work with surfaces. These results are also in agreement with the results obtained previously (see previous section).

Furthermore, functionalization using mixed monolayers was also analyzed on these surfaces. Similarly, the surfaces were incubated in WGA: TGA with ratios (1:1, 1:3 and 3:1). **Figure 4-18** shows the fluorescence images of functionalized surfaces by forming mixed monolayers of WGA: TGA at different ratios. On comparing the plot profiles, the fluorescence intensity on top of the microparticles was around 50 units (in gray scale value), in all the cases. The functionalization on the surface was uniform, homogenous and similar in all the cases.

From the images, all the surfaces showed similar fluorescence, implying that no significant difference in functionalization is observed on the polysilicon surfaces. Whereas, in the case of surfaces with silicon oxide layer, there was a significant difference observed in the functionalization using different ratios of WGA:TGA. This also suggests the difference in the surface reactivity between polysilicon and silicon oxide surfaces.

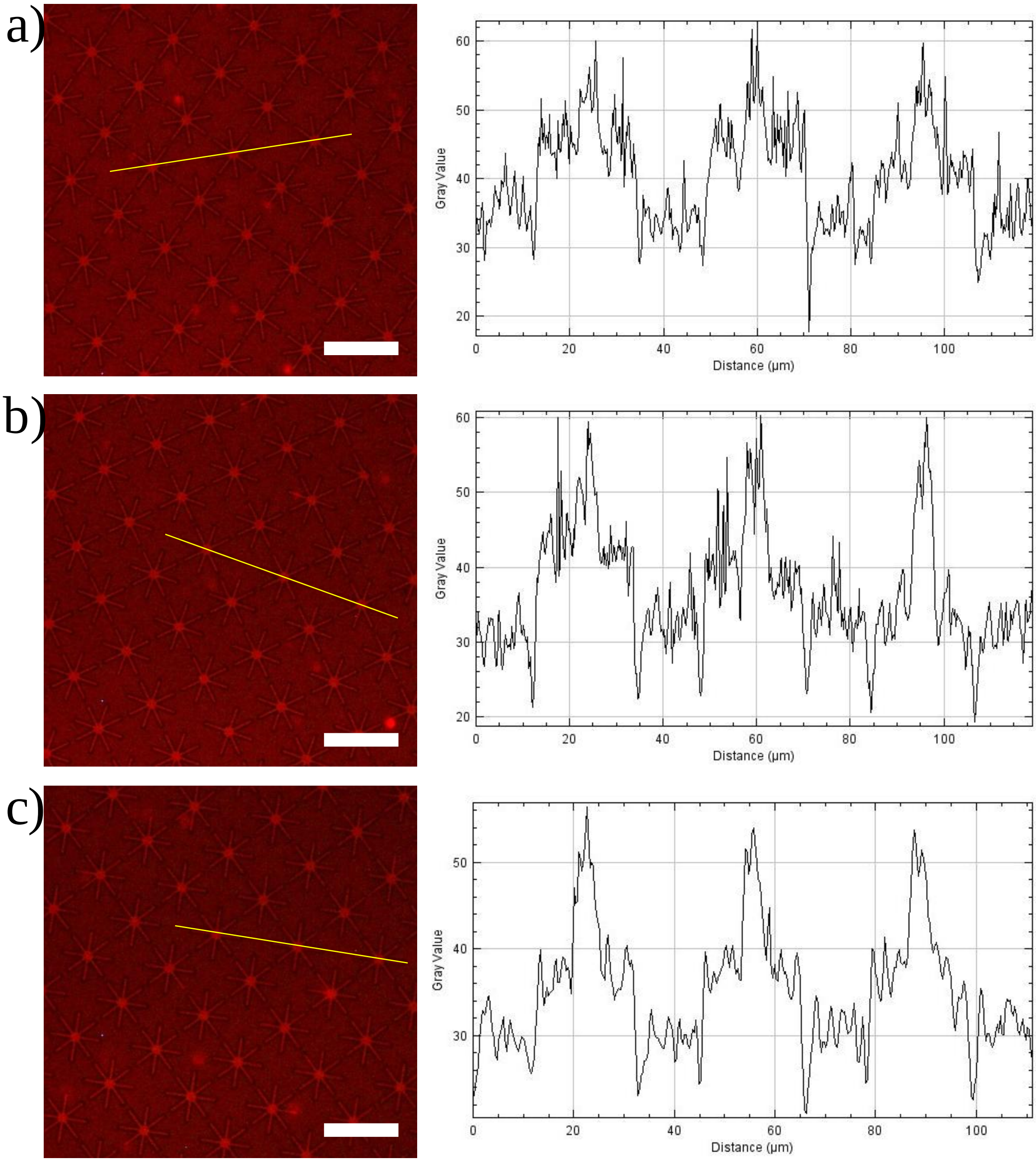

Figure 4-18. Fluorescence images of the surfaces functionalized with different ratios of WGA: TGA **a)** 1:1, **b)** 1:3 and **c)** 3:1, with their plot profiles. Scale bar – 30 µm.

4.3. Functionalization and characterization of star shaped polysilicon microparticles in suspension with lectins

The optimized bio-functionalization protocol on surfaces was applied to bio-functionalize the released microparticles in suspension. The polysilicon microparticles were etched from the silicon wafer by dissolving the underneath silicon oxide layer using HF, as explained in Appendix, Section 2. The etched polysilicon microparticles were then collected in 1 mL of ethanol and were stored in an eppendorf. **Figure 4-19** shows the four different batches of star shaped microparticles, **Batch 1** (20 µm, 500 nm thick), **Batch 2** (10 µm, 500 nm thick), **Batch 3** (20 µm, 50 nm thick) and **Batch 4** (10 µm, 50 nm thick).

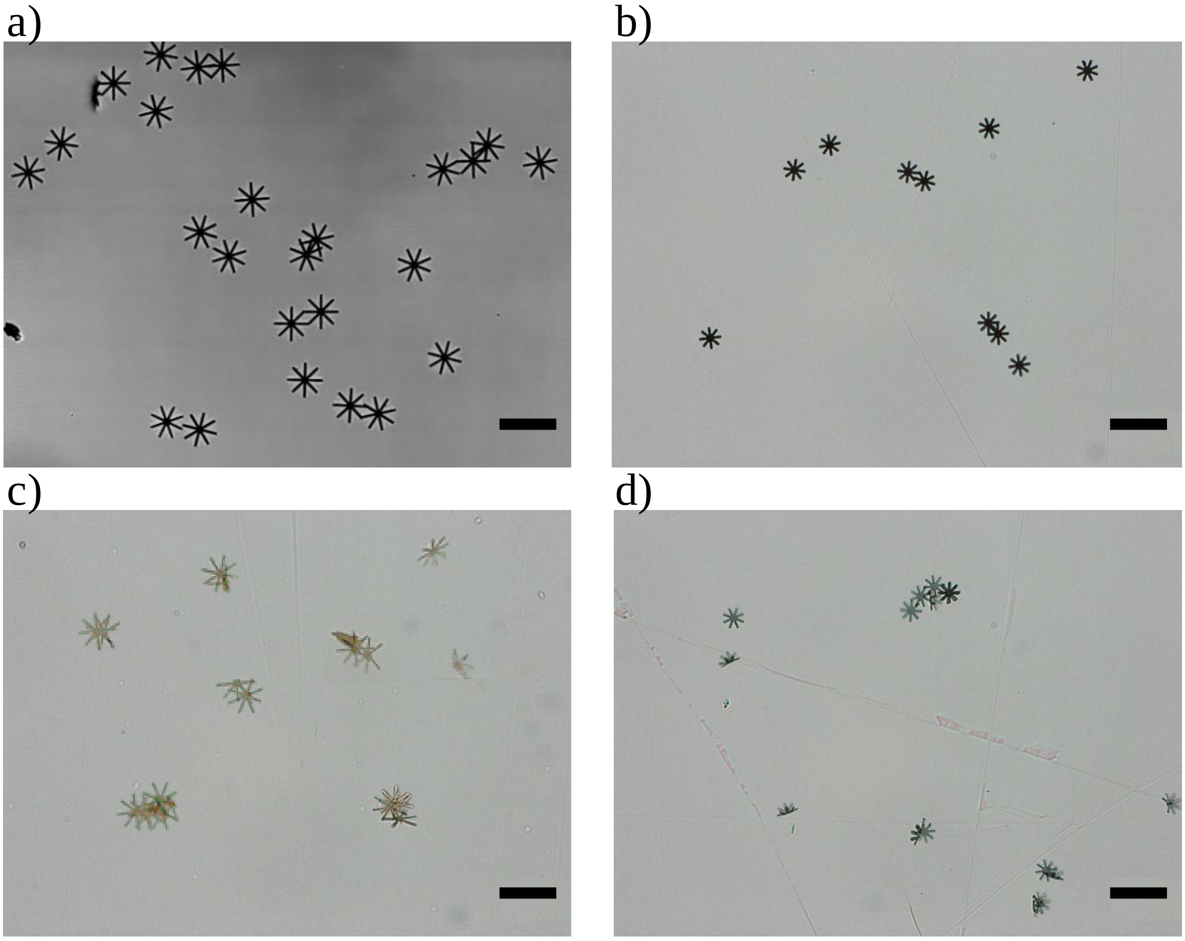

Figure 4-19. Bright field images of microparticles of **a) Batch 1**, **b) Batch 2**, **c) Batch 3** and **d) Batch 4**. Scale bar – 30 µm.

4.3.1. Initial experiments of bio-functionalization in suspension

All the four Batches were bio-functionalized with WGA lectin following the previously optimized protocol, see **Scheme 4.1**. It is important to mention that all the functionalization steps were carried out (in an eppendorf). During the functionalization, at each step the microparticles were centrifuged in order to change the previous solution to a new one. The time and the speed of centrifugation varied between the different batches. In the case of **Batch 1** and **Batch 2**, a 10 mins centrifugation at 13,400 rpm was sufficient enough to form the pellet, microparticles sedimented at the bottom of the eppendorf, whereas in the case of **Batch 3** and **Batch 4**, the microparticles could not withstand the mechanical force during the centrifugation and were breaking easily. This is due to the lower thickness (50 nm) of the **Batch 3** and **Batch 4** microparticles. When the speed of the centrifugation was reduced, the microparticles did not form any pellet, suggesting that the microparticles were still in the supernatant solution. The inability to form the pellet was also resulting in the high loss of microparticles at each step of the functionalization.

The bio-functionalized microparticles were characterized using fluorescence microscopy. In the case of **Batch 1,** Control (non-functionalized) microparticles were also characterized using fluorescence microscopy (**Figure 4-20 b**), which showed no fluorescence. On the other hand, the functionalization on the WGA functionalized microparticles was homogenous; there were also microparticles which had aggregates of WGA on them (**Figure 4-20 d**). Aggregates of WGA were also seen in the suspension. Therefore, the microparticles needed more washing after the functionalization step with WGA. On the other hand, more washes of the microparticles also resulted in the loss of microparticles (see Section 4.5).

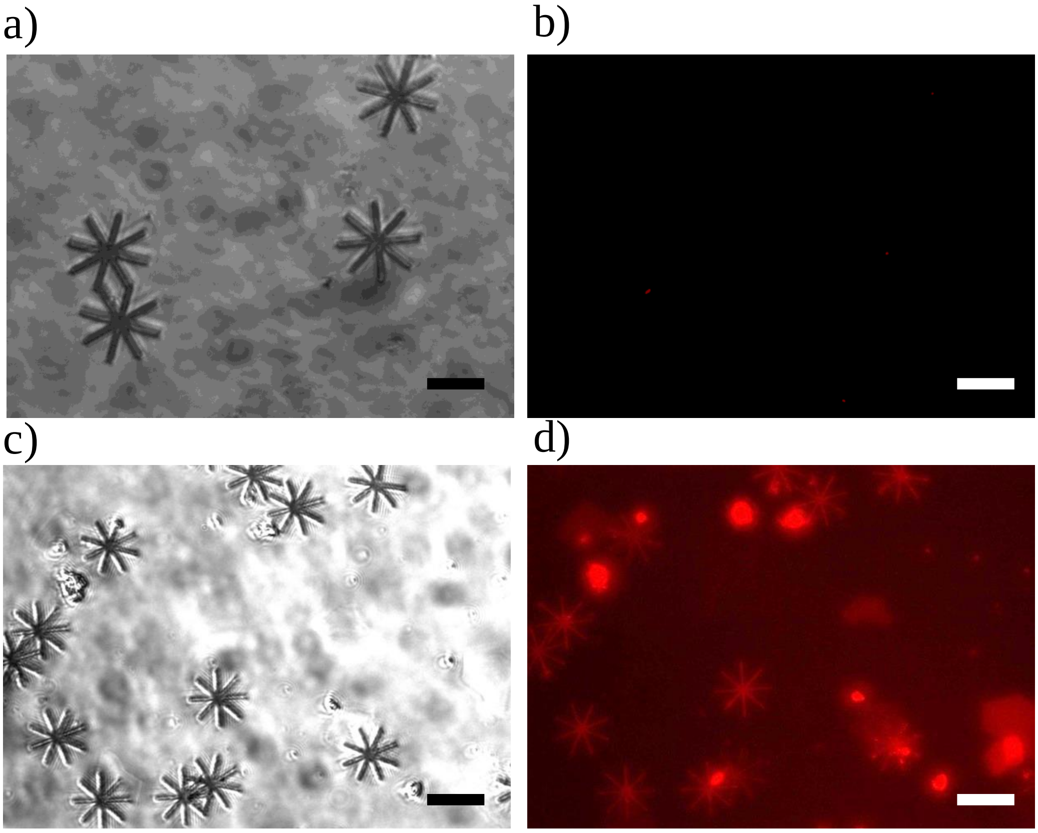

Figure 4-20. Optical microscopy images of **Batch 1** non-functionalized microparticles **a)** bright field, **b)** fluorescence image and WGA functionalized microparticles **c)** bright field and **d)** fluorescence image. Scale bar – 20 µm

Similar results were obtained in the case of **Batch 2** as shown in **Figure 4-21**. Functionalization appeared homogenous in most of the microparticles, but there were many with WGA aggregates. Also in the case of **Batch 2**, an increase in the WGA aggregates in the suspension was seen when compared to **Batch 1**. In this case, the bigger aggregates are due to an error while fabricating the microparticles. These aggregates were the remains of the silicon wafers, which were also functionalized during the process.

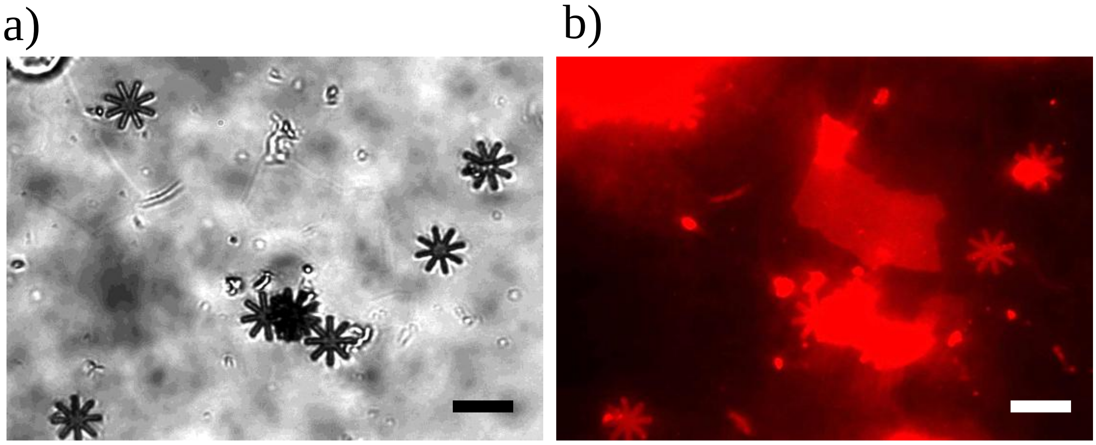

Figure 4-21. WGA functionalized **Batch 2** microparticles **a)** bright field and **b)** fluorescence image. Scale bar – 10 µm

On the other hand, in the case of **Batch 3** as shown in **Figure 4-22**, the functionalization was homogenous. But, very few functionalized microparticles were seen. As explained before, the microparticles of 50 nm thickness were not forming a good pellet during the centrifugation, resulting in the loss of microparticles at each step of the functionalization. Moreover, in some of the microparticles, the arms of the stars were broken, suggesting the microparticles of **Batch 3** were not able to withstand the mechanical force during the centrifugation.

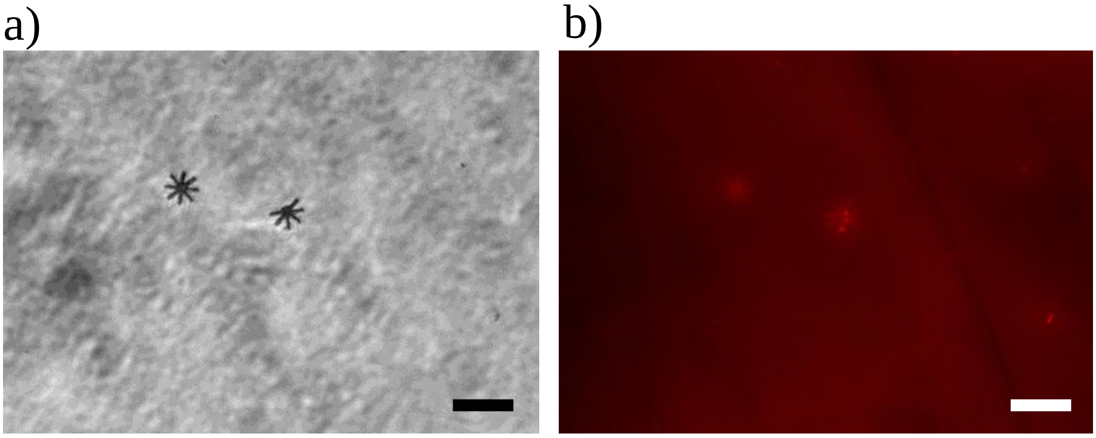

Figure 4-22. WGA functionalized **Batch 3** microparticles **a)** bright field and **b)** fluorescence image. Scale bar – 30 µm

Similar results were obtained in the case of **Batch 4**. As shown in **Figure 4-23**, very few functionalized microparticles and with broken arms were seen.

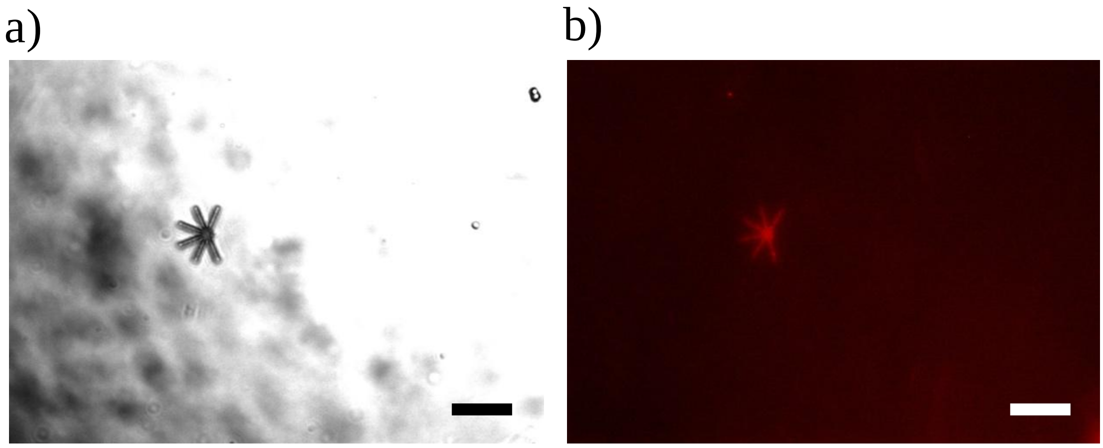

Figure 4-23. WGA functionalized **Batch 4** microparticles **a)** bright field and **b)** fluorescence image. Scale bar – 10 µm

After observing the preliminary results of the functionalized microparticles, **Batch 3** and **Batch 4** were discarded due to the loss in the number of microparticles after the functionalization process, and also due to its morphology, 50 nm thickness, which resulted in the breakage of the microparticles. The final aim was to achieve cell adhesion, which required mechanical force. Therefore, **Batch 1** and **Batch 2** were selected for further experiments. The microparticles of these batches were stable and could withstand the mechanical force needed for the functionalization.

The results obtained on WGA functionalized microparticles of **Batch 1** and **Batch 2** using the fluorescence microscope showed the need of improvement in functionalization. It was evident that the optimization on surfaces was not sufficient to achieve a uniform and homogenous functionalization on microparticles. As the microparticles are in suspension, additional parameters such as volume of each solution, microparticle aggregation, speed and time of centrifugation needed optimization.

4.3.2. Optimization of the functionalization in suspension

Batch 1 was selected for optimizing the WGA functionalization on the microparticles. During the functionalization, the microparticles were washed 5 times at each step with the solutions used. The washing step after the CHO-SAM formation was a crucial step, to achieve uniform monolayers of CHO-SAM thereby resulting in uniform and homogenous monolayers of WGA. This was performed in order to avoid the TESUD polymerization on microparticles as well as in the solution containing microparticles. Therefore, an additional wash was performed after the CHO-SAM formation. **Figure 4-24** shows the WGA functionalized microparticles characterized using fluorescence microscopy.

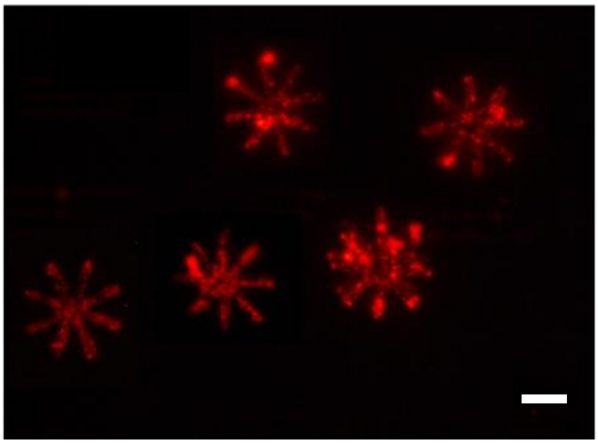

Figure 4-24. Fluorescence image of WGA functionalized **Batch 1** microparticles with an additional wash after the CHO-SAM formation. Scale bar – 10 µm

From the results obtained, there was a significant difference in the functionalization of the microparticles. The WGA aggregates in the suspension had significantly decreased, but Though, the WGA aggregates on the microparticles were still present. As shown in the fluorescence image of the microparticles, the aggregates were found mostly on the arms of the microparticles. After performing several washes of the bio-functionalized microparticles, there were still some visible WGA aggregates. Also, the loss of the microparticles after each wash was taken into consideration, which will be discussed in the Section 4.5. Therefore, decreasing or eliminating the formation of WGA aggregates and achieving a homogenous functionalization was a great challenge with the microparticles.

Use of TWEEN

The WGA aggregates on the microparticles could also be due to the protein-protein electrostatic interaction [212-214]. Immobilized WGA molecule could be electrostatically bound to another WGA molecule in solution. For avoiding this behaviour of the WGA molecule, the functionalized microparticles were washed with a surfactant solution.

In this case, surfactants such as TWEEN solutions were used, in order to remove the physisorbed WGA molecules from the microparticles [215-218]. Two different solutions, TWEEN 20 and TWEEN 80, were used to incubate the bio-functionalized microparticles, TWEEN 20 showing improved and better results. There was a significant decrease in the number of WGA aggregates on the microparticles. **Figure 4-25** shows the microparticles after the treatment with TWEEN 20 solution.

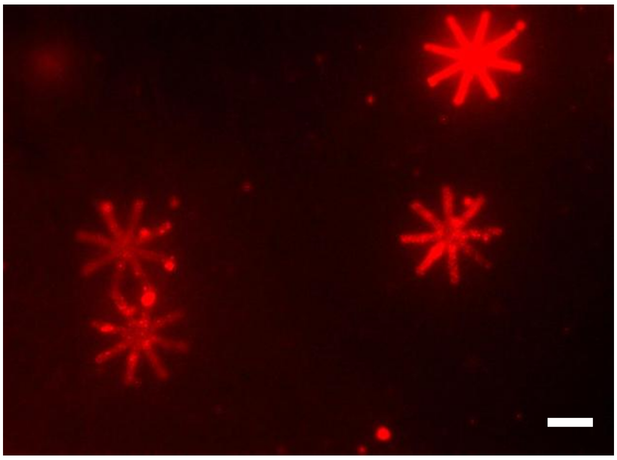

Figure 4-25. Fluorescence image of WGA functionalized microparticles washed with TWEEN 20. Scale bar – 10 µm

TWEEN 80, due to its higher molecular weight, was highly viscous and was difficult to remove from the microparticles suspension. To do so, more washes were required, resulting in the loss of microparticles (explained in Section 4.5). Therefore, once bio-functionalized the microparticles were washed using TWEEN 20 solution.

4.3.3. Bio-functionalization of **Batch 1** microparticles using mixed monolayers

Functionalization using mixed monolayers was also tested on the microparticles of **Batch 1**. The microparticles were incubated with similar concentrations of WGA: TGA solutions, as used for the surfaces (1:1, 1:3 and 3:1). **Figure 4-26** shows representative fluorescence microscopy image of the microparticles bio-functionalized with different ratios of WGA: TGA.

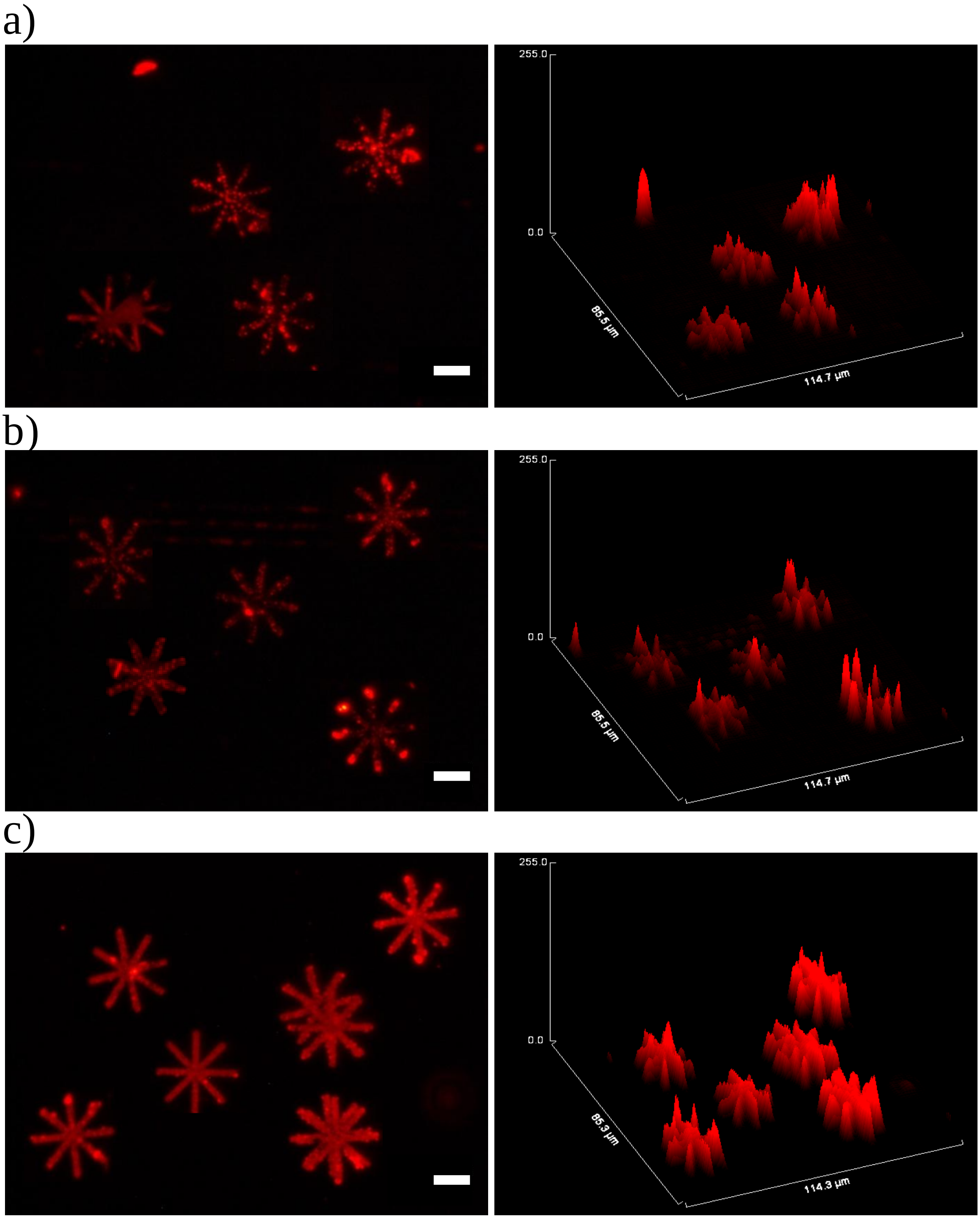
a)
255.0
0.0
85.5 µm
114.7 µm
b)
255.0
0.0
85.5 µm
114.7 µm
c)
255.0
0.0
85.3 µm
114.3 µm

Figure 4-26. Fluorescence image of microparticles functionalized with different ratios of WGA:TGA, **a)** 1:1, **b)** 1:3 and **c)** 3:1. Scale bar – 20 µm

As observed in the case of the ratio WGA:TGA, (1:1) and (1:3), the particles were not homogenously functionalized. There were WGA aggregates on the microparticles, more on the arms of the stars than the centre area of the particle. Also, after the washes of the microparticles with TWEEN 20 solution, the suspension did not show much WGA aggregates. On the other hand, there is a significant improvement in the case of the ratio

WGA: TGA (3:1). The microparticles are homogenously functionalized. Small aggregates of WGA are visible on the arms, but are relatively, smaller in size. Also the fluorescence intensity on the microparticles in this case of WGA: TGA (3:1) is higher when compared with (1:1) and (1:3). Also, the functionalization observed was uniform and homogenous. Thus, the functionalization using the ratio WGA: TGA (3:1) was selected as an optimized protocol for WGA functionalization on microparticles. This result is in agreement with the results obtained in the case of surface immobilization. On the other hand, aggregation of the microparticles was also seen while characterizing these microparticles. This could be due to the interlocking of the arms of the stars of the microparticles, thereby making again the functionalization more challengeable.

4.3.4. Bio-functionalization of **Batch 2** microparticles

Bio- functionalization of **Batch 2** microparticles was performed using the optimized mixed monolayer protocol of WGA: TGA (3:1). **Figure 4-27** shows the fluorescence image of WGA functionalized microparticles using mixed monolayers. The functionalization on the microparticles was homogenous. There was some presence of WGA aggregates on the microparticles. The fluorescence intensity is similar to that in the case of **Batch 1**.

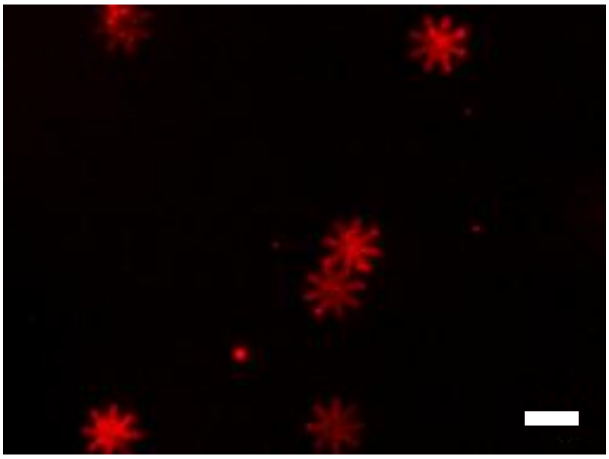

Figure 4-27. Batch 2 microparticles functionalized using mixed monolayers of WGA. Scale bar – 10 µm

4.3.5. Bio-functionalization of microparticles using Concanavalin A (Con A)

The optimized protocol for immobilization of WGA was used for lectin, Concanavalin A (Con A), using **Batch 1** and **Batch 2** microparticles.

The fluorescence images in **Figure 4-28** show the microparticles of **Batch 1** and **Batch 2** functionalized using either WGA or Con A. In both the cases, 80 % of the microparticles resulted in homogenous and uniform functionalization using the optimized protocol which had been a great challenge (discussed in Section 4.4).

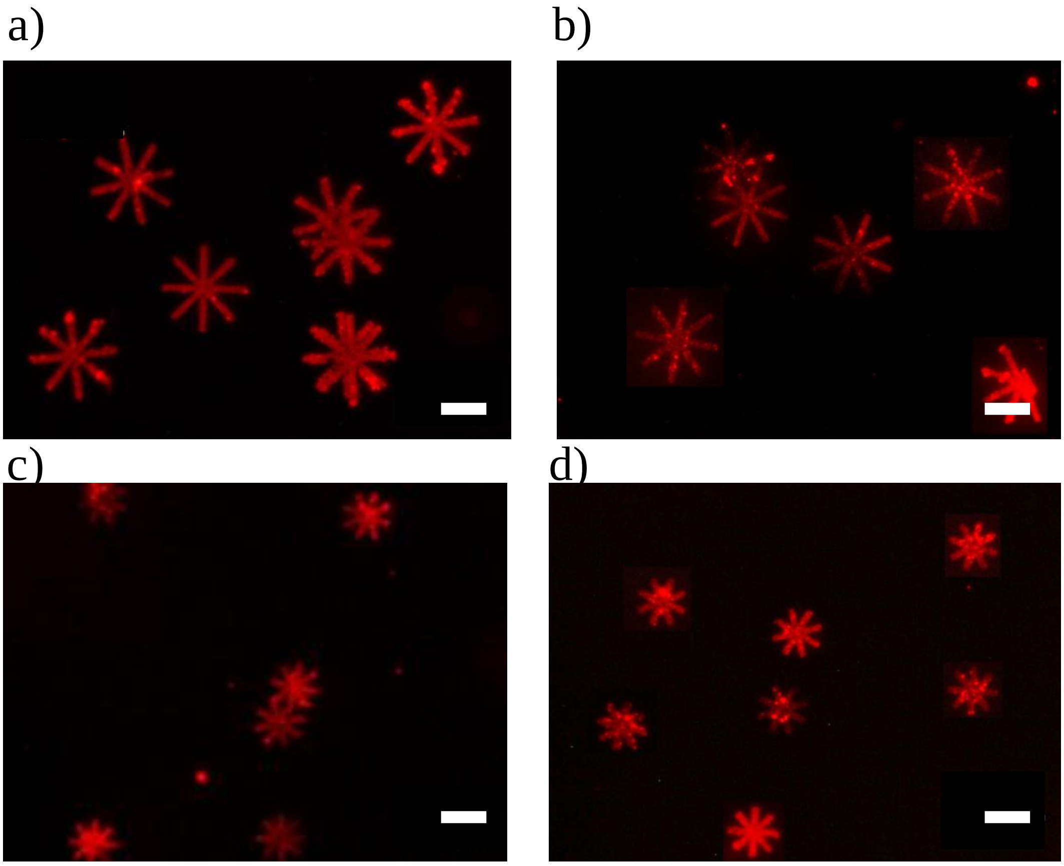

Figure 4-28. Functionalized microparticles of **Batch 1 a)** WGA and **b)** Con A; and **Batch 2 c)** WGA and **d)** Con A. Scale bar – 20 µm

Once the microparticles were bio-functionalized with both the lectins, we assessed their adhesion to cell membrane, and some preliminary results are shown in Section 4.7.

4.4. Functionalization and characterization of disc shaped polysilicon microparticles in suspension with lectins

Different morphology of the microparticles was taken into account, from which the disc shape had similar surface area to the star shape, but was more compact. Therefore, disc-shaped microparticles were considered in order to increase the surface contact with the cell membrane and the functionalized microparticle, and see the influence of morphology in cell adhesion (see before, **Figure 4-3**). Two different sizes of discs were fabricated with 500 nm thickness, Large - 20 µm, which we call **Batch 5**; and Small - 10 µm, which we call **Batch 6**. As mentioned before, also the disc shaped microparticles were microfabricated by Prof. J. A. Plaza explained in Appendix, Section 2.

4.4.1. Bio-functionalization of disc-shaped microparticles

For the functionalization of the disc shaped microparticles, the polysilicon microparticles were etched form the silicon wafer, and collected in suspension in an eppendorf. The functionalization was studied directly on the released microparticles using the experience obtained after the functionalization of the star shaped microparticles. **Figure 4-29**, shows the optical images of the surfaces and the corresponding etched polysilicon microparticles of **Batch 5** and **6** respectively. The surfaces in the **Figure 4-29**, **Batch 5** and **Batch 6** consist of polysilicon microparticles on the silicon surface (without a silicon oxide layer).

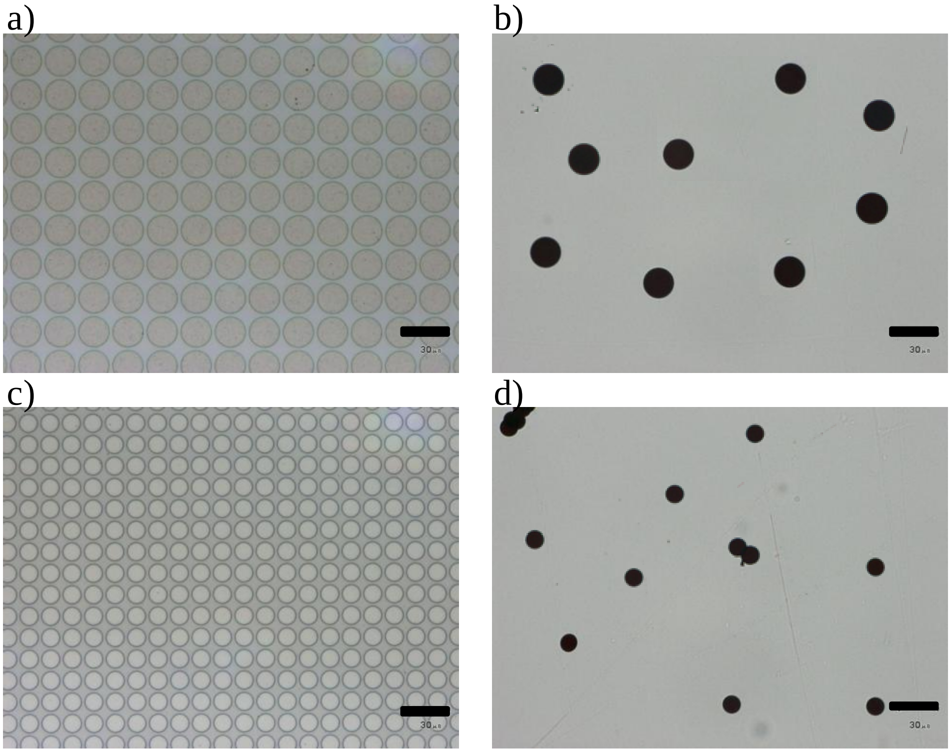

Figure 4-29. Bright field images of **Batch 5 a)** surfaces, **b)** microparticles; and **Batch 6 c)** surfaces and **d)** microparticles. Scale bar – 30 µm.

The bio-functionalization protocol of the microparticles was tested on **Batch 5** microparticles using WGA. The microparticles were functionalized using two different previously optimized protocols: pure WGA and using mixed immobilization of WGA:TGA (3:1).

The disc shaped microparticles were treated with TESUD (135 mM) for 3 hours which was followed by WGA (35 µg/mL) immobilization overnight. The WGA functionalized microparticles were then washed with TWEEN 20 solution. **Figure 4-30 a)** shows fluorescence microscopy images of initial results of bio-functionalized microparticles using pure WGA. Here the microparticles shows homogenous and uniform functionalization. Though some aggregates of WGA were seen in the suspension. Also, we noticed, that in some case of the microparticles, the functionalization is not homogenous, due to the overlapping of the microparticles, and not exposing the microparticles completely for the WGA immobilization. Therefore, for the following functionalization, the initial concentration of the microparticles was reduced to half, in order to improve functionalization (**Figure 4-30 b**)

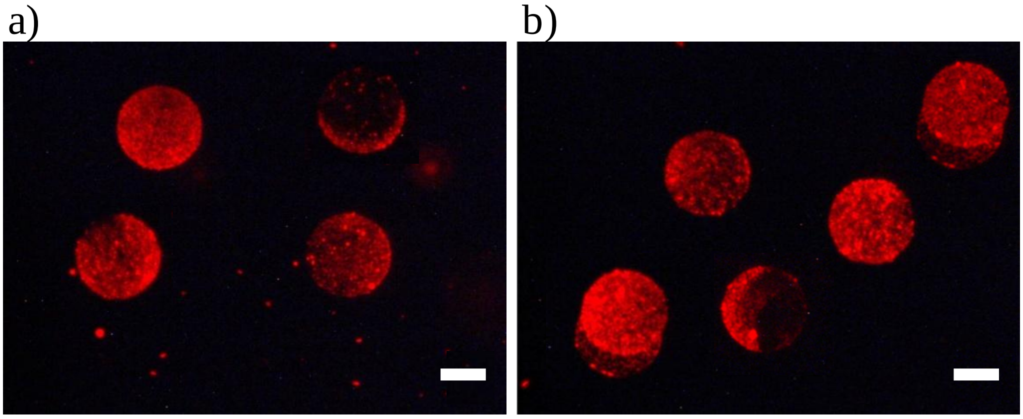

Figure 4-30. Fluorescence microscopy images of the WGA functionalized microparticles using pure WGA **a)** initial concentration and **b)** after reducing the concentration to half. Scale bar – 10 µm.

As shown in **Figure 4-30 b)**, the functionalization is homogenous, and the aggregates of the WGA in the suspension were lower. However, there were still microparticles with partial functionalization. Though, the number of microparticles with partial functionalization has reduced, so had the final number of functionalized microparticles. Therefore, initial concentration of microparticles were selected for functionalization, as sufficient amount of microparticles are required for the biological studies.

The microparticles were also functionalized using previously optimized protocol of mixed immobilization of WGA, where the microparticles were treated with 135 mM of TESUD for 3 hours, followed by incubation in WGA:TGA in ratio of 3:1 for overnight. The functionalized microparticles were then washed with TWEEN 20 solution. **Figure 4-31** shows the fluorescence images obtained using both full monolayers of WGA and mixed monolayers of WGA:TGA (3:1). As observed in **Figure 4-31**, there is no significant difference in functionalization between the two protocols. The functionalization in both cases appears homogenous and uniform. The fluorescence intensity of the microparticles looks alike. Though there was a slight increase in the case of the microparticles functionalized using only WGA monolayers.

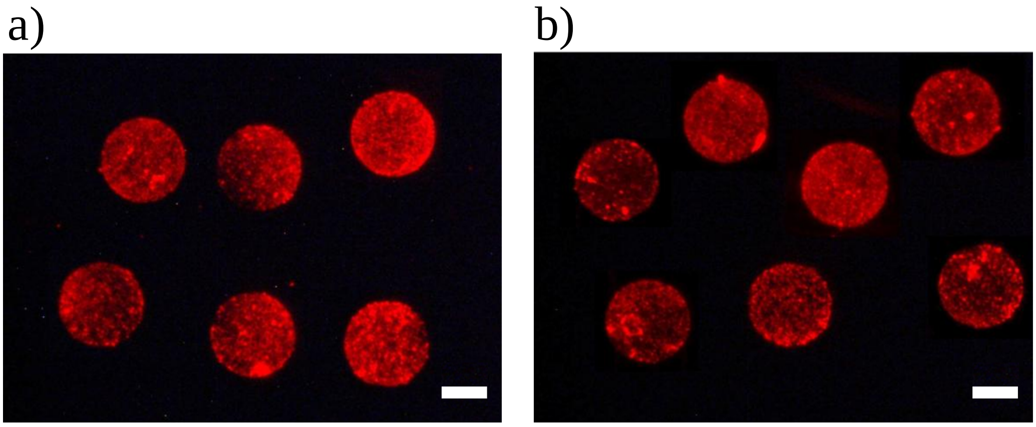

Figure 4-31. Fluorescence microscopy images of **Batch 5** microparticles functionalized using **a)** pure WGA and **b)** mixed immobilization of WGA:TGA (3:1). Scale bar – 10 µm.

Therefore, the optimized protocol selected for functionalizing the disc microparticles was using only WGA. This shows the influence of morphology of the microparticle in functionalization and therefore the necessary optimization for each batch of microparticles.

4.4.2. Characterization of **Batch 5** surfaces using AFM

In order to study the homogeneity in the functionalization, silicon surfaces containing polysilicon microparticles were scanned using AFM. The **Batch 5** surfaces were functionalized using the optimized protocol, and the WGA functionalized surfaces were characterized using fluorescence microscopy. **Figure 4-32** shows the image obtained in bright field, and its fluorescence image respectively. The functionalization as seen in the figure looks homogenous, though some circular patterns in the centre of the microparticles was observed. But that was also visible on the optical image, thus it could be an error in fabrication process, but not in functionalization.

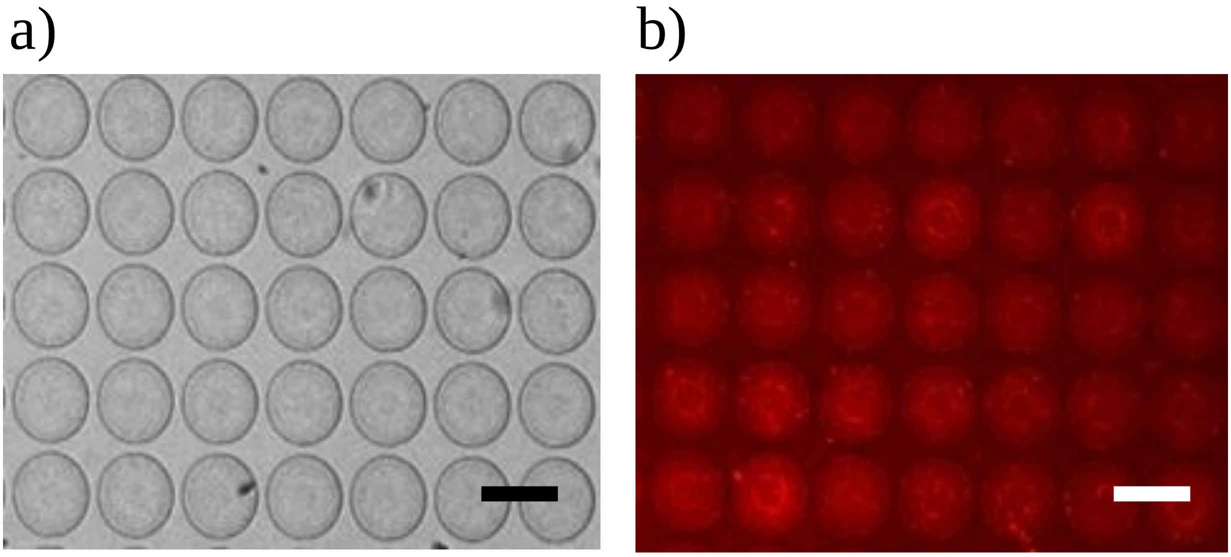

Figure 4-32. Batch 5 WGA functionalized surface **a)** Bright field and **b)** fluorescence image. Scale bar – 20 µm.

The functionalized surface was then characterized using AFM in order to study the topography of the surface. **Figure 4-33** shows the micrographs of WGA functionalized surfaces obtained using AFM. The functionalization was found to be homogenous and uniform, though there were some aggregates present on the microparticles. These little aggregates were of the polysilicon crystals, which results in making the surface rough [156,219]. The plot profile of the surface shown in the figure, confirms that the functionalization achieved is uniform.

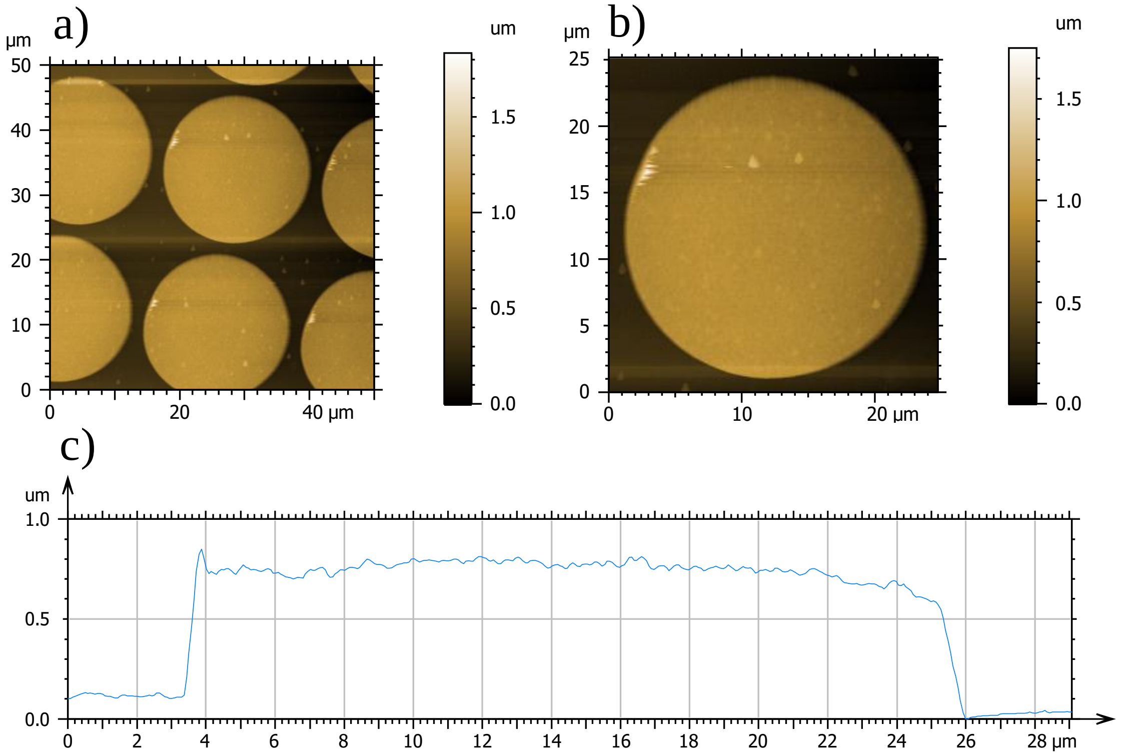

Figure 4-33. Micrographs of **Batch 5** WGA functionalized surface **a)** topographic image, **b)** topographic image of a single particle and **c)** its plot profile.

Due to the roughness of the surface, as explained in the case of star shaped microparticle, the thickness of the functionalized monolayers on the disc microparticle was not measured.

4.4.3. Bio-functionalization of **Batch 6** microparticles

Microparticles of **Batch 6** were functionalized with WGA using the optimized protocol, TESUD (135 mM) for 3 hours followed by incubation in WGA (35 µg/mL) for overnight. **Figure 4-34** shows the fluorescence image of WGA functionalized microparticles obtained using fluorescence microscopy.

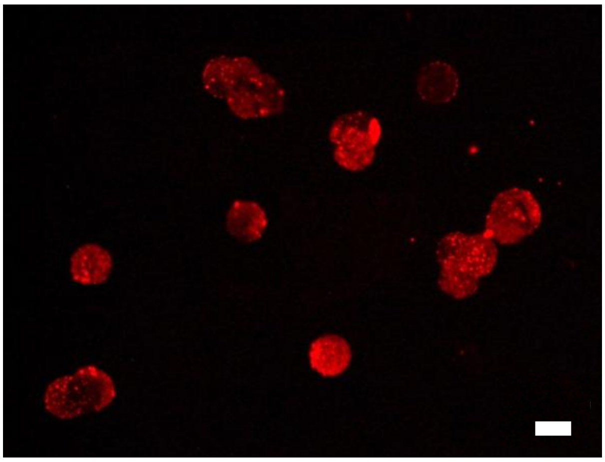

Figure 4-34. Fluorescence image of WGA functionalized microparticle of **Batch 6**. Scale bar – 10 µm.

The functionalization on the **Batch 6** microparticles was not very homogenous. In spite of several washing treatment with TWEEN 20, some aggregates of WGA remain present on/ or in the suspension of the microparticles. This confirms that for each batch an optimization of the functionalization protocol is required.

It has been observed, also in the case of **Batch 2** (star shaped) that as the size of the microparticles decreases, the number of aggregates of WGA in the suspension increase. Due to the small size (10 µm) and therefore lower weight, the microparticles of these batches (**Batch 2** and **6**) during the centrifugation do not form the pellet easily. Thus, the microparticles in these cases have to be centrifuged for longer time, which could make the aggregates of WGA to settle down and form a pellet with the microparticles. This issue was tried to overcome by increasing the number of washes, but it always resulted in some WGA aggregates. Functionalization of disc-shaped microparticles (**Batch 6**) did not improve by using a mixture of WGA:TGA (3:1).

Both functionalized and non-functionalized disc-shaped microparticles of **Batch 5** were analysed. **Figure 4-35** shows the micrographs of non-functionalized microparticle. As the microparticles were suspended in PBS solution, crystals of PBS were seen on the background of the microparticles while scanning the sample.

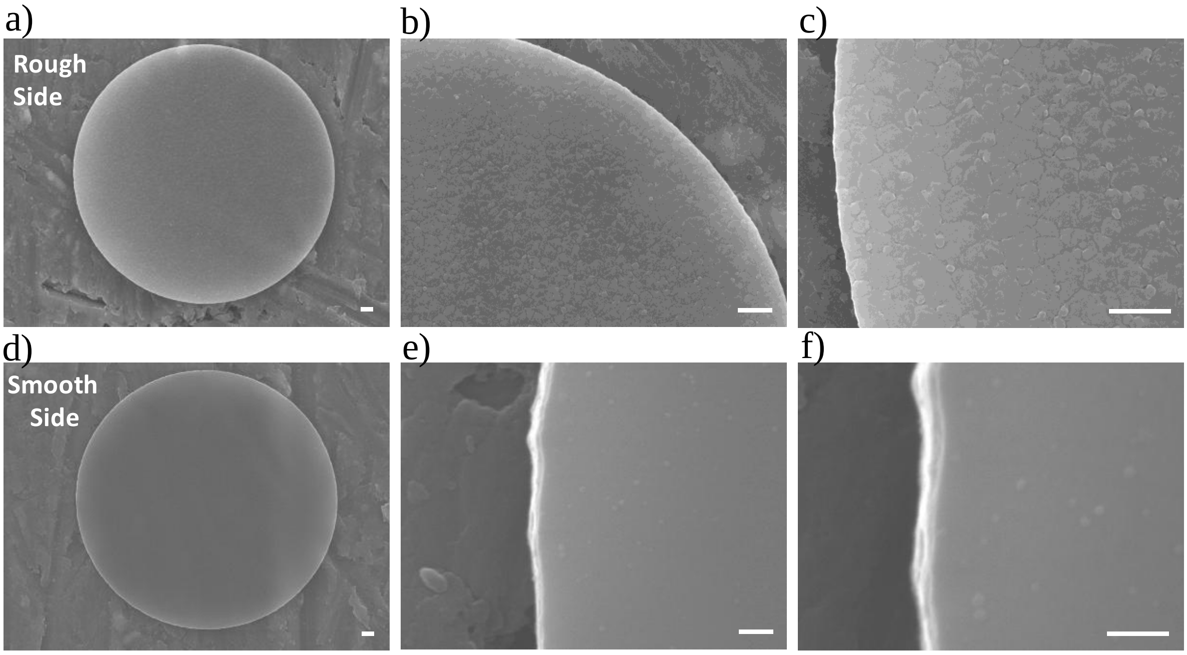

Figure 4-35. Micrographs of non-functionalized microparticles of **Batch 5** obtained using SEM **a-c)** rough side and **d-f)** smooth side. Scale bar – 1 µm (a-d), 100 nm (e-f).

As noticed, from the micrographs, the two sides of the polysilicon microparticles are different. The side of the microparticle in contact with the silicon oxide was smoother, than compared to the side exposed to the air.

As the polysilicon crystals are grown on the silicon oxide (Appendix, Section 2), the final layer of the microparticles have larger grain size of the polysilicon than the initial new layers. Therefore, having two different sides, the smooth and rough side, which could be clearly differentiated in the micrographs obtained from SEM. The grain size of the polysilicon on the rough side was analysed and they varied between 0.1 - 0.6 µm.

On the other hand, **Figure 4-36** shows the micrographs of the WGA functionalized microparticles, rough and smooth side respectively.

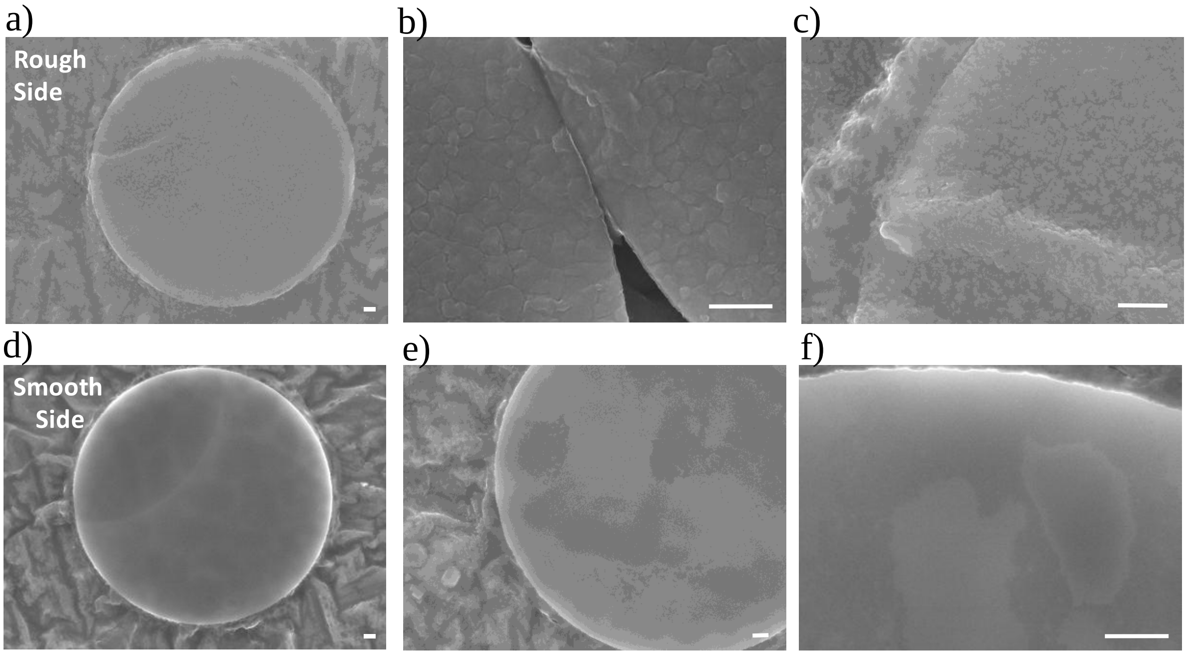

Figure 4-36. Micrographs of WGA functionalized microparticles of **Batch 5** obtained using SEM **a)** rough side and **b)** smooth side. Scale bar – 1 µm.

After comparing the micrographs of the functionalized and non-functionalized microparticles, the size of the aggregates found in the functionalized microparticles is similar to the polysilicon crystals found on the rough side of the non-functionalized microparticle. The calculated size of the WGA molecule is 5 nm [220]. But as shown from the micrograph of the non-functionalized microparticle, the grain size of the polysilicon crystals are much bigger than the WGA molecule. And the resolution of the SEM did not permit to see the WGA aggregates which were much smaller in size (~ 5 nm).

On the other hand, on the smooth side of the microparticles, there were some irregular patterns in the case of functionalized microparticles. Whereas in the case of non-functionalized microparticles, no such behaviour was seen. Therefore, these patterns could be attributed to the immobilization of the WGA.

4.5. Characterization analysis

WGA functionalized microparticles of **Batch 1**, **Batch 2**, **Batch 5** and **Batch 6** were selected to analyze parameter such as: uniformity of various particles for each Batch after functionalization, quantification of the number of particles at each step of functionalization, quantification of lectin immobilized on the microparticles and their stability after the functionalization.

Additionally, it also important to mention that fluorescence microscopy was used as a primary characterization technique for both star and disc shaped microparticles. But, not much characterization was performed on the star shaped microparticles due to its shape and size (**Figure 4-37**).

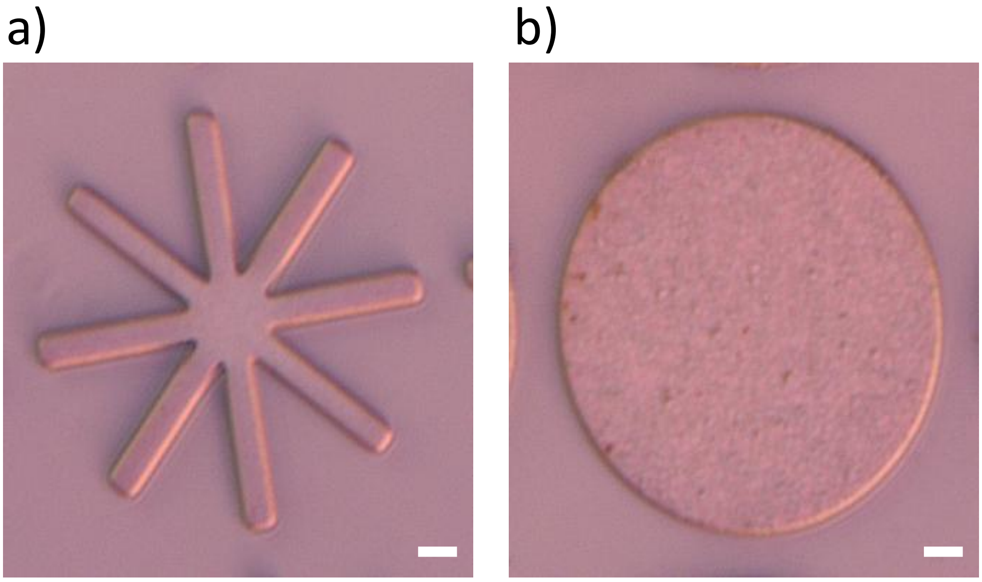

Figure 4-37. Optical microscope images of **a) Batch 1** star and **b) Batch 5** disc shaped microparticles on silicon surface. Scale bar – 1.5 µm.

On the other hand, disc shaped microparticles due to its larger surface area, were feasible to be characterized using Scanning Electron Microscopy (SEM), Stochastic Optical Reconstruction Microscopy (STORM) Imaging, X-ray Photoelectron Spectroscopy (XPS) and Raman scattering.

4.5.1. Intensity profiles of WGA functionalized microparticles

Characteristic microparticles of each Batch were selected and were analyzed by measuring the fluorescence intensity observed on each microparticle.

In the case of **Batch 1**, **Figure 4-37** shows 2D and 3D fluorescence images of five representative microparticles with their plot profiles. The majority of the microparticles are homogenously functionalized, in some cases, there are still some WGA aggregates in spite of washing them with TWEEN 20 solution. The aggregates are more seen on the arms of the microparticles. As seen in the case of **Figure 4-37**, **b)** and **d)** the microparticles were seen attached with one another. This also indicates the difficulty in functionalization the microparticles homogenously.

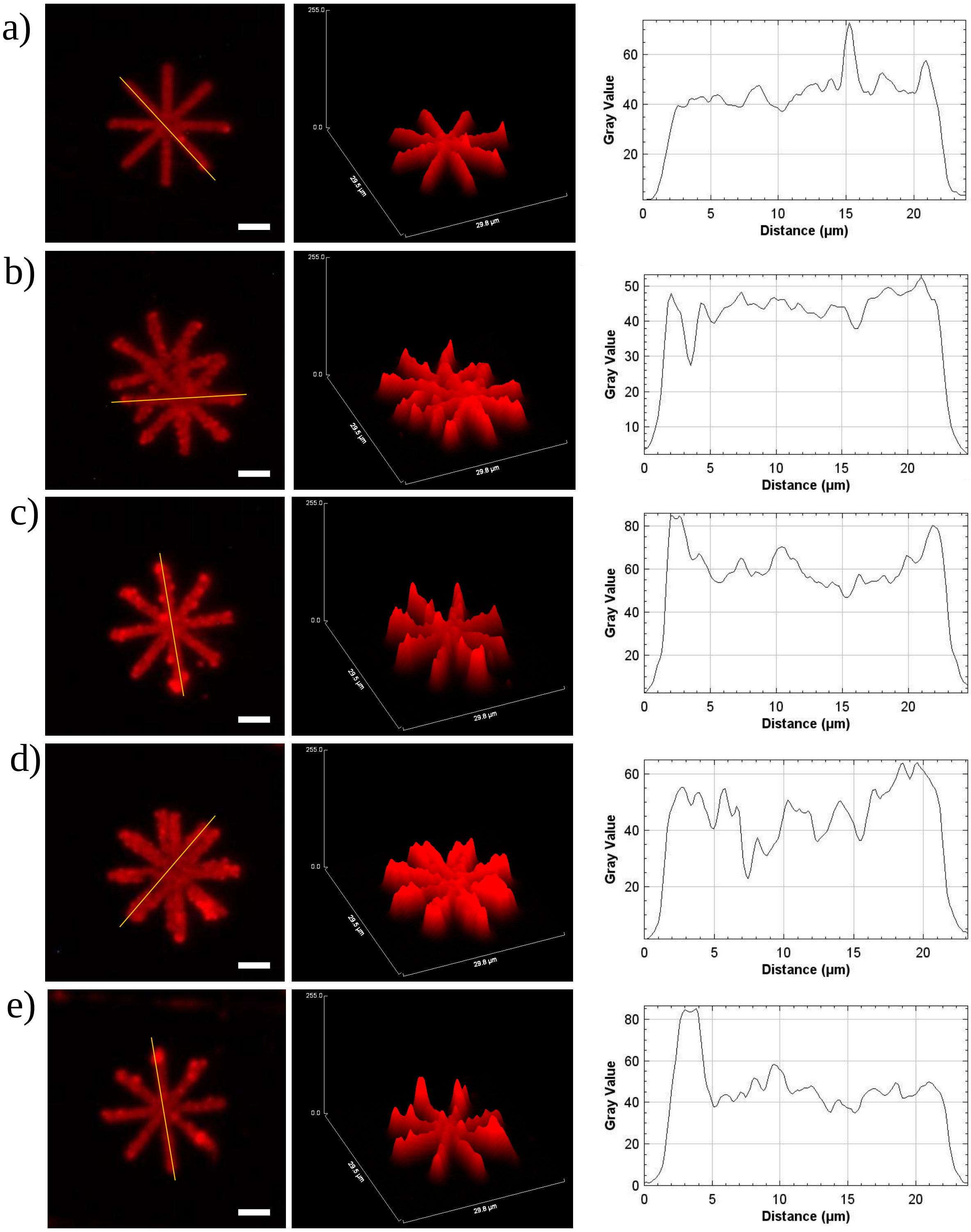

Figure 4-37. Fluorescence image of **Batch 1** WGA functionalized microparticles using mixed monolayers (WGA:TGA, 3:1), with their plot profiles, (a-e) respectively. Scale bar – 5 µm.

The average fluorescence intensity profile of these functionalized microparticles is represented in the histogram, **Figure 4-38**. The microparticles of **Batch 1** are mono-dispersed with fluorescence intensity around 40 ± 10 a.u.

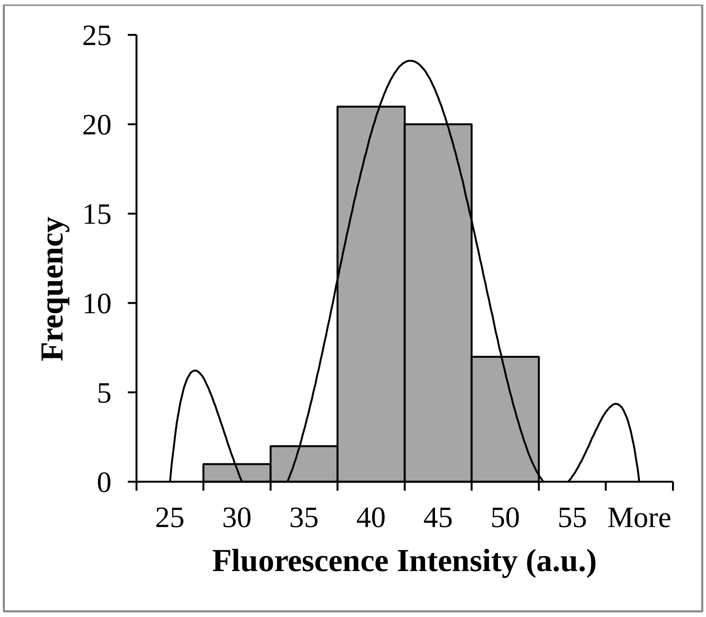

Figure 4-38. Histogram representing the fluorescence intensity of **Batch 1** WGA functionalized microparticles.

Similarly, **Batch 2** was also studied at the microparticle level. **Figure 4-39** shows the fluorescence image of each WGA functionalized microparticles. However, the fluorescence intensity in this case was lower when compared to **Batch 1** microparticles. Here, the average fluorescence intensity was reduced to 35 a.u., from the plot profiles.

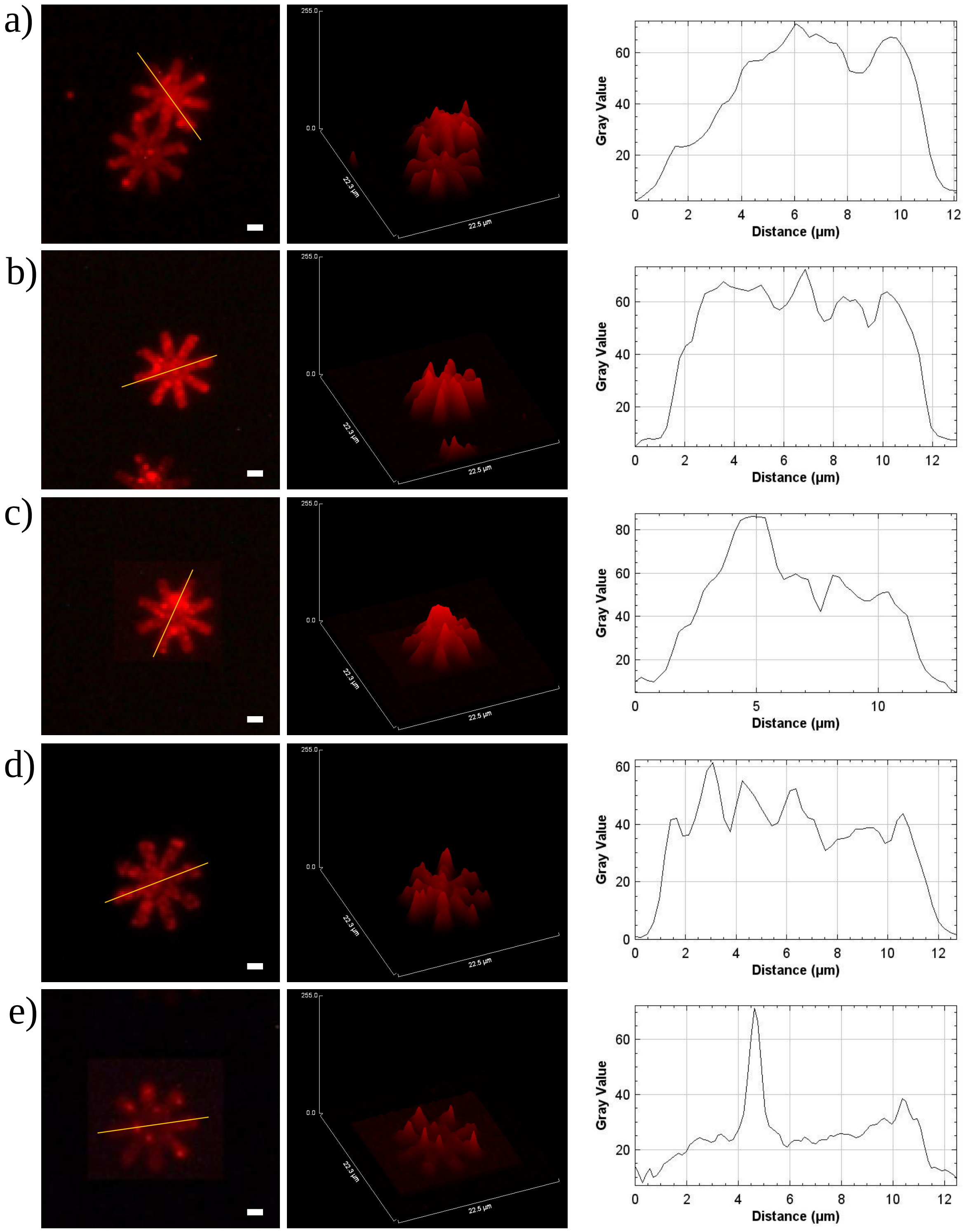

Figure 4-39. Fluorescence image of **Batch 2** WGA functionalized microparticles with their plot profiles, (a-e) respectively. Scale bar – 2 µm.

Figure 4-40 illustrates the different fluorescence intensity of the **Batch 2** WGA functionalized microparticles. The histogram in this case demonstrates a bimodal distribution, suggesting, different fluorescence intensities of the functionalized microparticles. This difference could also relate to the higher number of WGA aggregates on **Batch 2** microparticles. The average fluorescence intensity was calculated to be 40 ± 20 a.u.

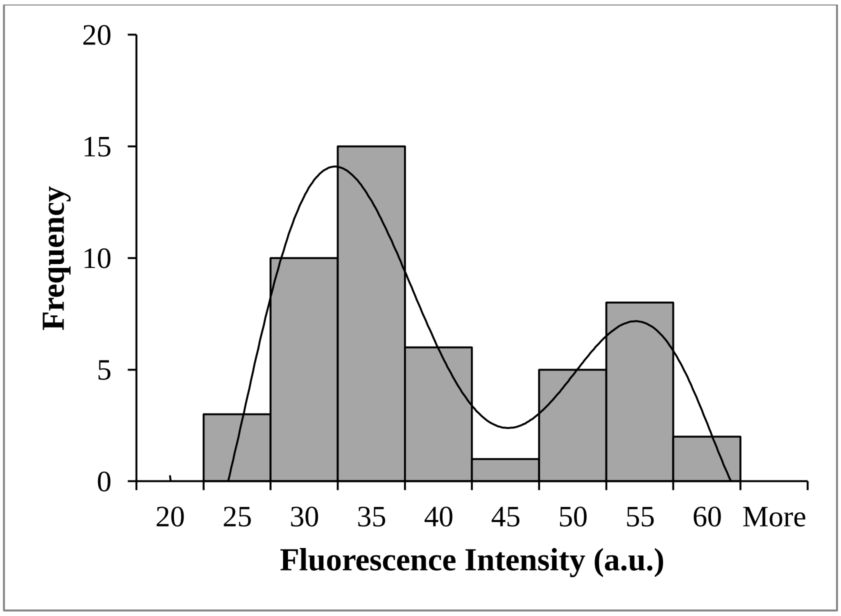

Figure 4-40. Histogram of the fluorescence intensity of **Batch 2** WGA functionalized microparticles.

Figure 4-41 shows the fluorescence image of disc-shaped **Batch 5** WGA functionalized microparticles. As observed in the figure, the fluorescence is homogenous and uniform on the microparticle. From the plot profile, the average fluorescence intensity is around 40 a.u., similar to the case of **Batch 1** microparticle. Some microparticles were spotted with WGA aggregates, as shown in **Figure 4-41 b)**.

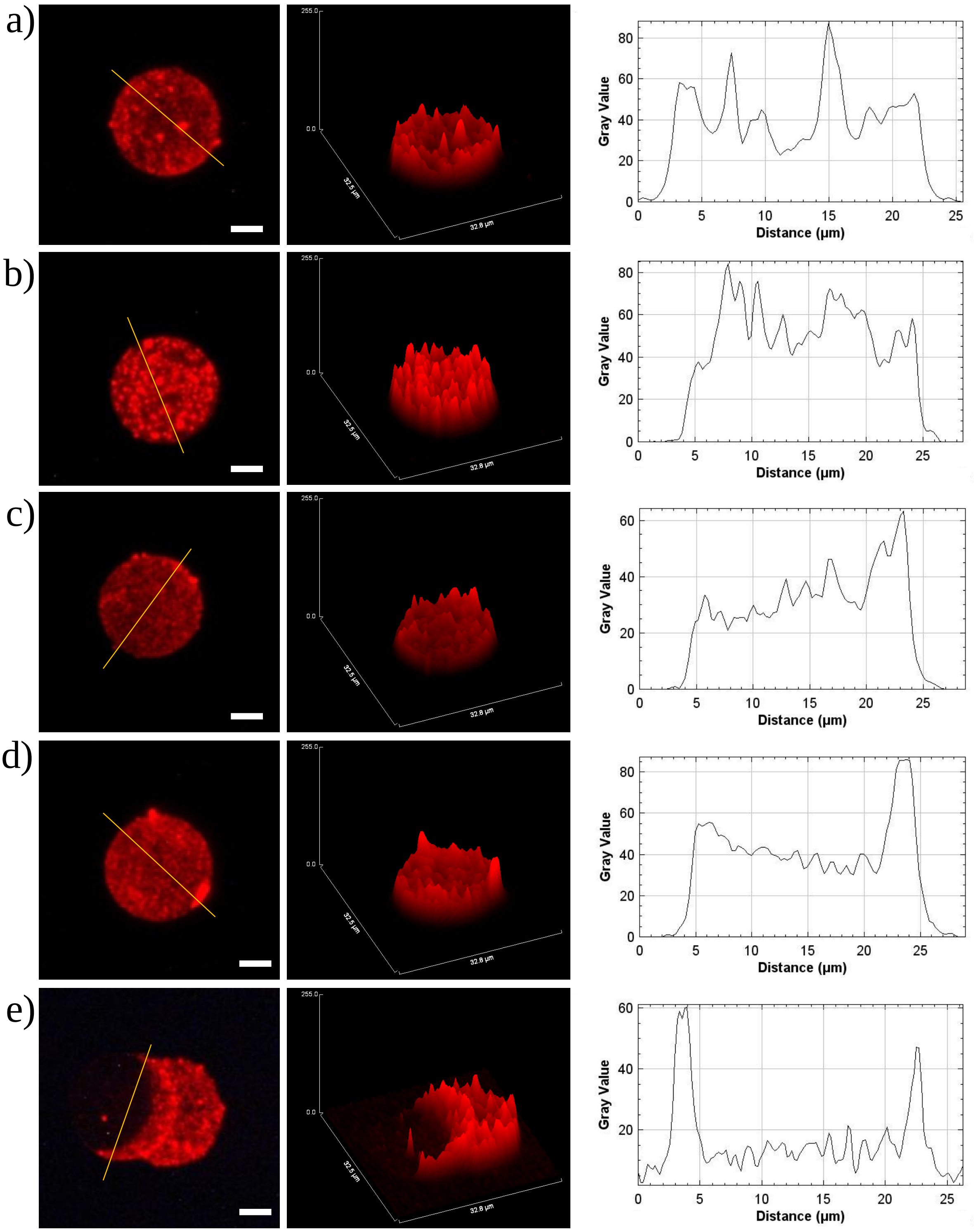
a)
b)
c)
d)
e)
255.0
0.0
32.5 µm
32.8 µm
Gray Value
Distance (µm)
0
5
10
15
20
25
20
40
60
80

Figure 4-41. Fluorescence image of **Batch 5** WGA functionalized microparticles with their plot profiles, (a-e) respectively. Scale bar – 5 µm.

Moreover, overlapping of the some microparticle as shown in **Figure 4-41 e)** resulted in non-functionalization of some areas on the microparticles. But, this behaviour was eliminated while optimization protocol, and thus very few microparticles with such behaviour was observed.

Different fluorescence intensity of the **Batch 5** WGA functionalized microparticles is illustrated in the histogram, **Figure 4-42**. Here, the histogram demonstrates a plateau distribution, suggesting microparticles functionalized with different monolayers of WGA, thus different fluorescence intensity. The fluorescence intensity of the microparticles in this case ranges between 35 ± 10 a.u.

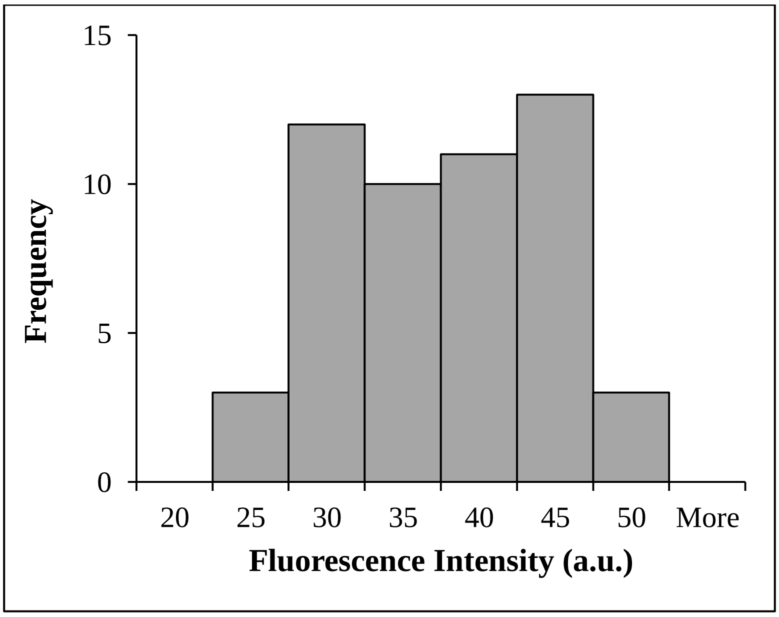

Figure 4-42. Histogram of the fluorescence intensity of **Batch 5** WGA functionalized microparticles.

On the other hand, in the case of **Batch 6**, fluorescence image obtained with their plot profile is shown in **Figure 4-43**. The average fluorescence intensity was approximately 30 a.u., similar but lower to **Batch 2** (35 a.u.). In this case, it is also observed, that the number of aggregates is much lower when compared to **Batch 2**. In **Figure 4-43 d)**, we could see the presence of an aggregate on the side of the microparticle, thus exhibiting the possibility of the formation of aggregates all around the microparticles. This was a great challenge to overcome to achieve homogenous functionalization.

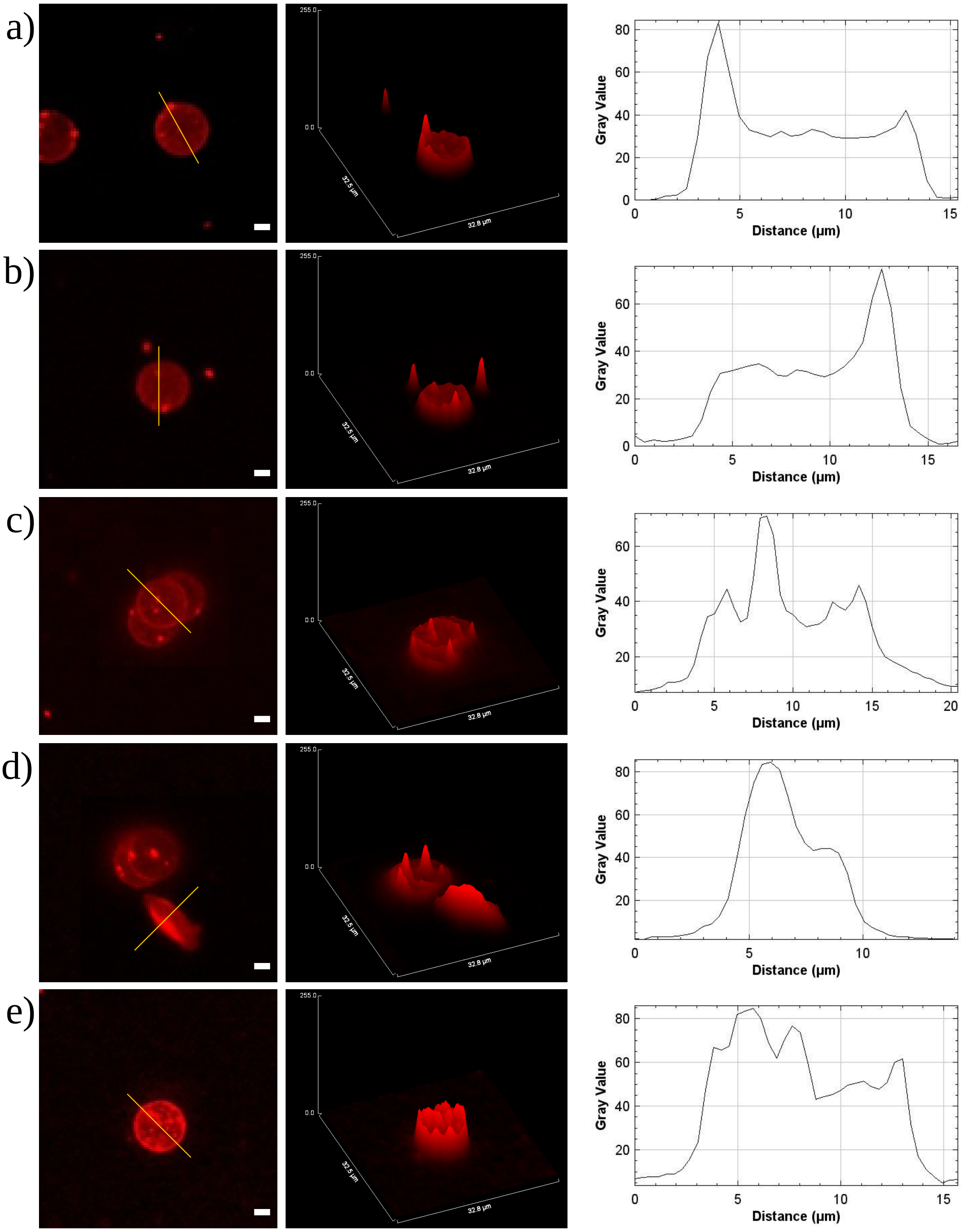

Figure 4-43. Fluorescence image of **Batch 6** WGA functionalized microparticles with their plot profiles, (a-e) respectively. Scale bar – 2 µm.

The average fluorescence intensity of **Batch 6** WGA functionalized microparticles is represented in the histogram **Figure 4-44**, indicating bimodal distribution. The average fluorescence intensity calculated was around 30 ± 20 a.u.

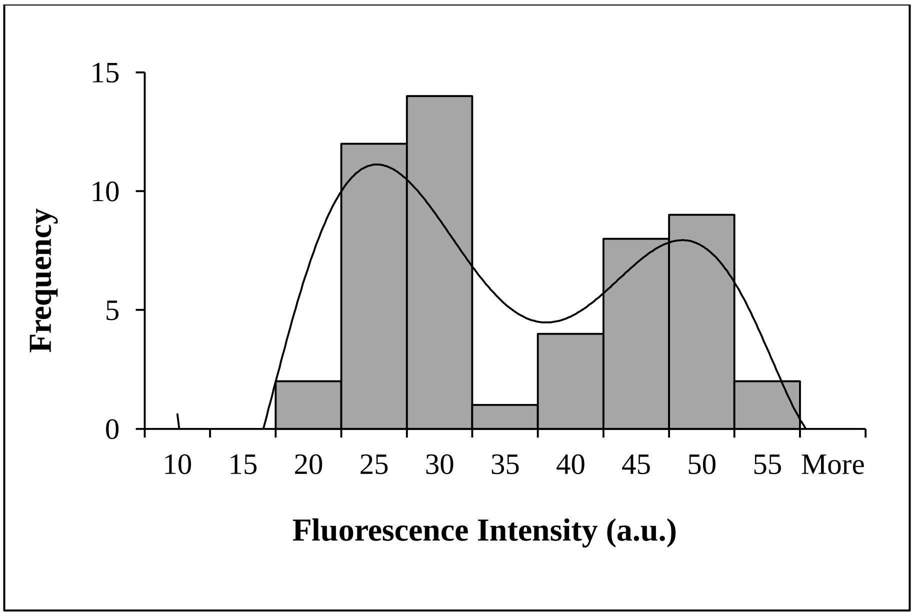

Figure 4-44. Histogram of the fluorescence intensity of **Batch 6** WGA functionalized microparticles.

Hence, after analysing the results it is observed that functionalization on **Batch 1** and **Batch 5** microparticles show similar results. On the other hand, **Batch 2** and **Batch 6** also shows similar results, both having bimodal distribution.

4.5.2. Particle quantification

The collection yield, number of microparticles collected after each step of functionalization, is a very important parameter especially when biological experiments are made. We observed that, microparticle functionalization in suspension induced a big loss of microparticles, at each chemical step. In order to improve the collection rate of microparticles, an accurate study of the amount of loss of the microparticles was done. The microparticles were counted at each step of the functionalization using a Neubauer Chamber. The collection rate after each step of functionalization is tabulated in **Table 4-2** for all the four different batches, **Batch 1**, **Batch 2**, **Batch 5** and **Batch 6**.

From the results obtained, the overall particle yields for all the batches are very low. As observed the major loss of microparticles occur during the activation step. After the piranha treatment, when the microparticles are washed with milli-Q water, the hydroxylated microparticles are well suspended in water, and do not form a good pellet even after 10 mins of centrifugation. This could relate to the loss of microparticle after the piranha treatement. Additionally, when the microparticles are later treated with the basic solution, small air bubbles in the eppendorf are formed, inspite of ultasonication. Thus, the air bubble formation could also lead in the loss of microparticles. It is noted that the washes with milli-Q water results in high loss of microparticles. Whereas, when the microparticles are suspended in ethanol solution, the microparticles, form a very good pellet, and have a high collection rate from the previous functionalization step, as shown in the **Table 4-2**, after TESUD treatment.

Table 4-2. Number of microparticles per eppendorf collected after each step of functionalization

Batch number	**No. of microparticles (x 1000)**						**Global loss %**	**Overall yield %**
	Initial	**After Piranha**	**After Basic**	**After TESUD**	**After Lectin**	**After Tween 20**		
1	137	72	63	54	42	30	**79**	**21**
2	346	200	174	153	70	48	**87**	**13**
5	142	96	68	59	50	30	**79**	**21**
6	356	273	222	182	95	45	**88**	**12**

Similarly, when the microparticles were suspended in PBS, the loss of microparticles increased, which could be noted in **Table 4-2**, After WGA and TWEEN 20 step. This could be due to the hydrophilic nature after the WGA functionalization, by remaining in the PBS suspension and not forming a pellet during centrifugation, resulting in the loss of microparticles.

Also, it is important to mention the necessity of washes in between every step is 3 times and after TESUD treatment, 5 times. These washes with milli-Q water, ethanol and PBS lead to loss of microparticles, but are an essential step to achieve homogenous functionalization.

Also, it is observed that the loss of microparticles is higher in the case of **Batch 2** and **Batch 6**. The WGA functionalized microparticles of these batches were taking longer time to form a pellet. This could be due to their lower density of the microparticles when compared to **Batch 1** and **Batch 5**. In spite of having more number of microparticles at the beginning of the functionalization, the loss in the case of **Batch 2** and **Batch 6** is higher, 87 % and 88 % respectively. On the other hand, in the case of **Batch 1** and **Batch 5**, the loss of microparticles is 79 % and 88 % respectively.

Consequently, total number of WGA functionalized microparticles in the case of **Batch 1** is 30,000; **Batch 2** is 48,000; **Batch 5** is 30,000 and **Batch 6** is 45,000, which should be enough for the biological experiments. When in need of more number of microparticles for certain biological experiments, the number of functionalized microparticles was increased by functionalizing more than one eppendorf simultaneously.

4.5.3. Quantification of WGA immobilization by fluorescence spectroscopy

Concentration of WGA immobilized on the microparticles can be quantified by fluorescence spectroscopy using the supernatant of the functionalization solution. Using WGA in PBS solution, a calibration curve was obtained following the peak at 620 nm (emission wavelength of WGA-Texas red), as shown in **Figure 4-45**. The WGA concentration range used was between 5 and 35 µg/mL because it was the range of WGA used for the bio-functionalization protocol. As noticed from the poor R^2 of 0.97, the calibration curve obtained is not a straight line. This could be due to the aggregation of the WGA molecules with the increase in the concentration, forming dimers or trimers [170].

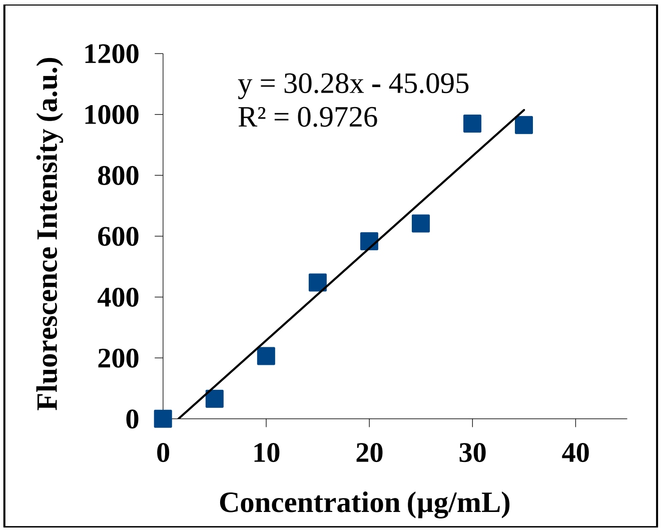

Figure 4-45. Calibration curve of WGA at different concentrations obtained using fluorescence spectroscopy.

To achieve a relative quantification of WGA bonding to the microparticles, CHO-SAM functionalized microparticles were kept overnight in a WGA solution (35 µg/mL). To obtain the number of WGA molecules immobilized on the microparticles, the WGA concentration in the starting solution and in the supernatant after the immobilization was determined by measuring the fluorescence at 620 nm, as shown in **Figure 4-46**. Interpolation of the fluorescence values in the calibration curve allowed the corresponding WGA concentrations to be calculated. **Batch 1** and **Batch 2**, were functionalized using mixed monolayers of WGA, whereas **Batch 5** and **Batch 6** were functionalized using monolayers of WGA and TGA. The experiment was done in triplicate and the average value for the immobilized WGA is tabulated in **Table 4-3**.

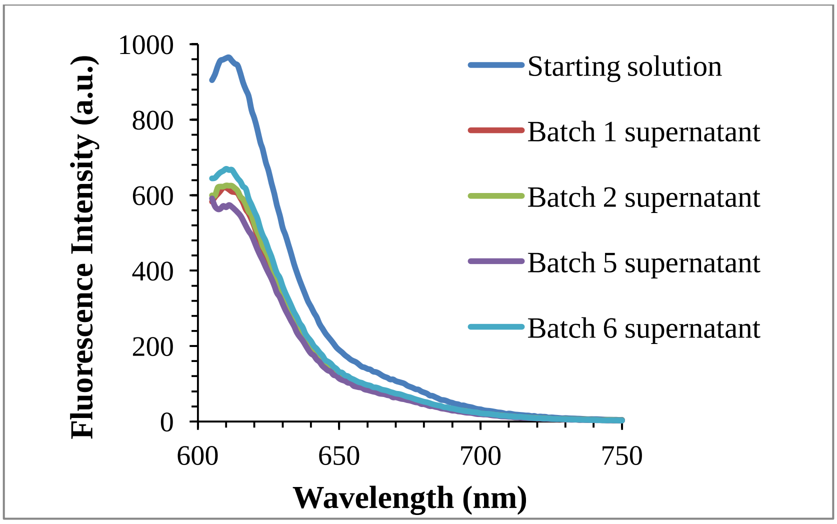

Figure 4-46. Fluorescence spectra of WGA supernatant in PBS solution, before (35 µg/ml) and after immobilization for **Batch 1**, **Batch 2**, **Batch 5** and **Batch 6**.

WGA immobilization was higher for **Batch 1** and **Batch 5**, when compared to **Batch 2** and **Batch 6**. This difference also corresponds with the higher fluorescence intensity observed in the case of **Batch 1** and **Batch 5**. On comparing, not much significance difference is observed for all the batches except for **Batch 5**. The higher immobilization could also be due to the higher surface area when compared to the rest of the batches.

After quantifying the concentration of WGA on the functionalized microparticles (from **Table 4-3**), and knowing the total number of microparticles functionalized (from **Table 4-2**), we can calculate the number of molecules of WGA functionalized per particle and also µm^2 of the microparticle. The results are tabulated in **Table 4-3**.

The average value for the immobilized WGA was similar for **Batch 1** and **Batch 2**. Whereas, in the case of **Batch 5**, lower number of molecules/µm^2 of WGA was immobilized on the microparticle, half the number of molecules obtained for **Batch 1** and **Batch 2**. In spite of lower number of WGA molecules per µm^2, the fluorescence intensity observed in **Batch 5** remains high (when characterized using fluorescence microscopy), due to the higher surface area (911.48 µm^2) as compared to **Batch 1** (358 µm^2) and **Batch 2** (197.99 µm^2). On the other hand for **Batch 6**, the average value for the immobilized WGA was higher when compared to B**atch 5**, this high value could also result due to the aggregates of WGA present in the suspension.

Table 4-3. Quantification of WGA lectin immobilized on the microparticles and number of WGA molecules per µm^2 of a microparticle

Batch	**Functionalization**	**Conc. of supernatant (µg/mL)**	**Final Conc. on microparticles (µg/mL)**	**No. of WGA functionalized microparticles**	**No. of WGA molecules per µm^2**
1	**WGA:TGA**	23.0	12.6	30,000	1,954,693
2		24.3	11.2	48,000	1,969,534
5	**WGA**	21.0	14.6	30,000	893,147
6		22.6	13.0	45,000	1,544,202

4.5.4. Stability in suspension of microparticles (Batch 1 and Batch 2)

The stability in suspension of PBS with time of the functionalized microparticles was examined by studying the fluorescence intensity of the microparticles. **Figure 4-47** shows the fluorescence intensity of the functionalized microparticles of **Batch 1** and **Batch 2** in PBS, with respect to time. The stability of the microparticles was studied for duration of three weeks. It is noticed from the graph below (**Figure 4-47**), that the fluorescence of the functionalized microparticles for both the batches, were stable. After the first week, when characterized, there was presence of WGA aggregates in the suspension, which relates to the loss of 5 a.u. of the fluorescence intensity from the functionalized microparticles. Though, this decrease in the intensity was not observed later on. The WGA functionalized microparticles were found stable enough for the duration of next two more weeks.

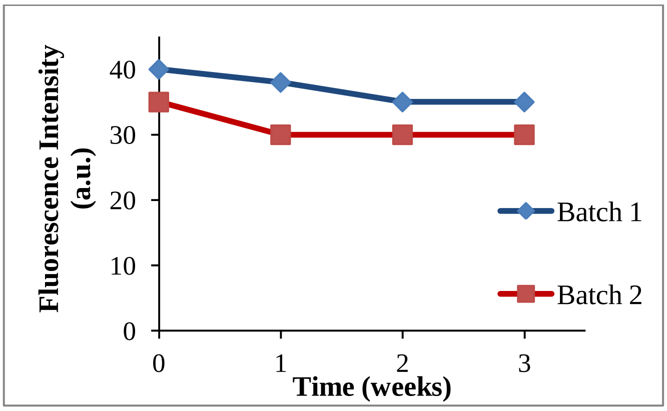

Figure 4-47. Stability study of WGA functionalized microparticles of **Batch 1** and **Batch 2** in PBS.

4.5.5. Characterization of Batch 5 using confocal microscopy

On the other hand, while characterizing the **Batch 5** WGA functionalized microparticles using fluorescence microscopy, some unexpected patterns of fluorescence were noticed on the microparticles, as shown in **Figure 4-48**. The functionalization was repeated again numerous times, in order to see the reproducibility of these patterns. Therefore, this morphology of functionalization on the microparticles encouraged us to explore them further using super resolution microscopy.

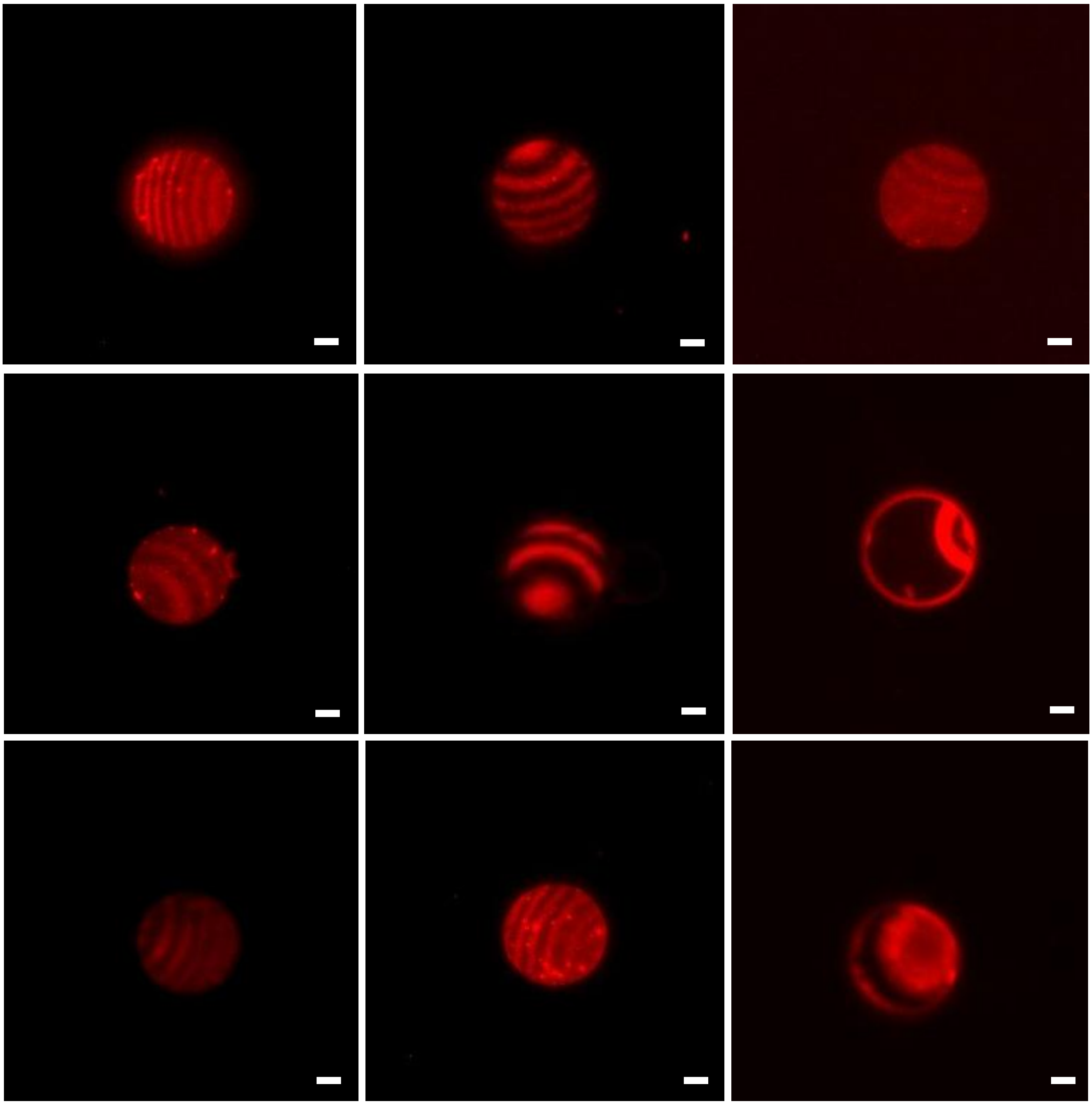

Figure 4-48. Fluorescence microscope images of **Batch 5** WGA functionalized microparticles. Scale bar – 5 µm.

The **Batch 5** WGA functionalized microparticles were characterized using different techniques, such as Stochastic Optical Reconstruction Microscopy (STORM), Total Internal Reflection microscopy (TIRF) and HiLo microscopy, in order to analyse the ring shape patterns (**Figure 4-49**).

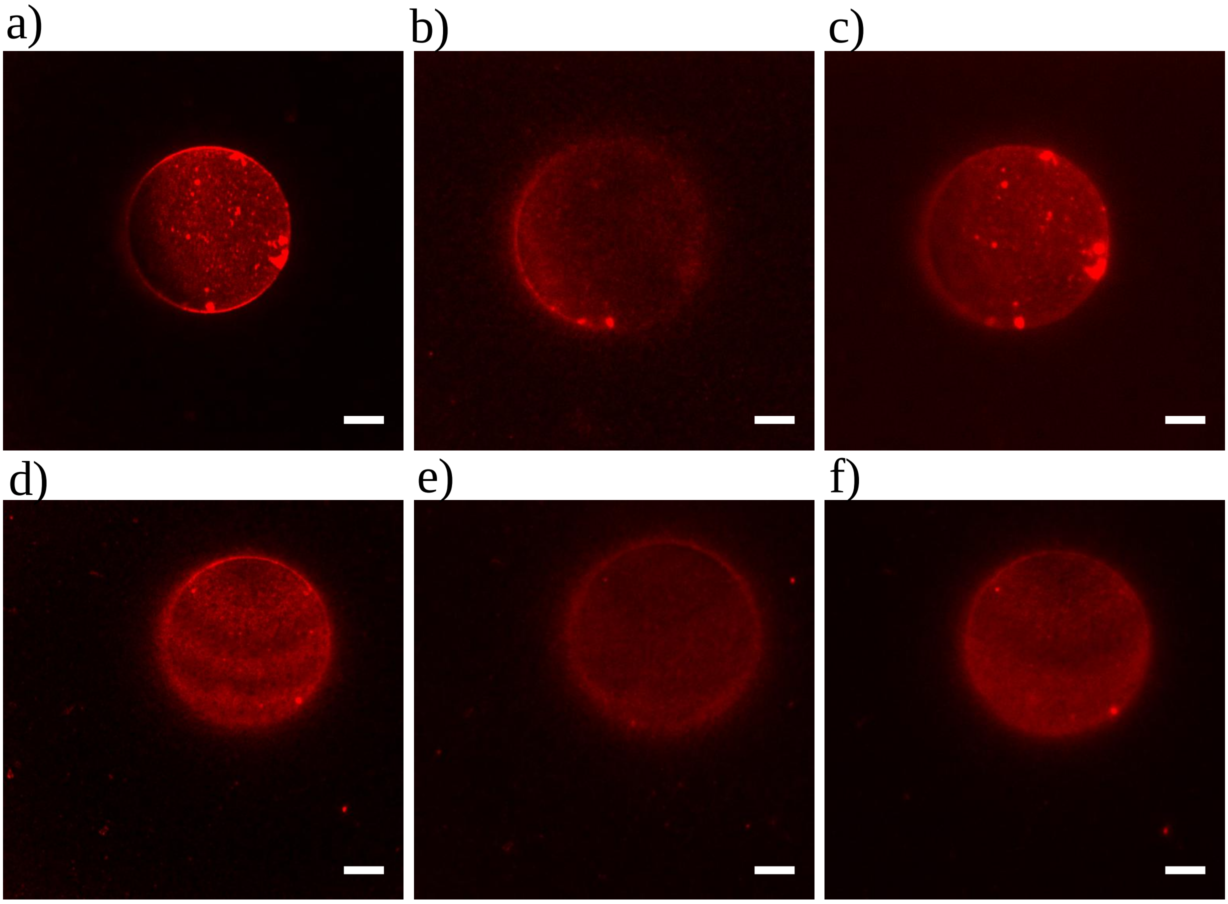

Figure 4-49. Fluorescence image of Microparticle **1** obtained using **a)** confocal, **b)** TIRF and **c)** HiLo microscopy; and Microparticle **2** obtained using **d)** confocal, **e)** TIRF and **f)** HiLo microscopy. Scale bar – 5 μm.

When the microparticles were analyzed using the super resolution microscopy, we did not observe any ring shape patterns. Using confocal microscopy, we have the advantage of studying the fluorescence of different planes (in z axis) of the microparticles, using TIRF, we could study the fluorescence of the microparticle at the interface (first layer of the microparticle in contact with the objective lens), while using HiLo, we could focus the fluorescence only from the microparticles, and reject the out-of –focus regions. With all the above mentioned benefits of the super resolution microscope, we found that the patterns observed using normal fluorescence microscopy were just an interference pattern, called Newton's Rings [221-222].

As observed from the **Figure 4-49**, the confocal microscopy image shows the top of the microparticle, whereas, the TIRF gives the fluorescence of bottom of the microparticle. Characterizing both sides of the functionalized microparticles. From the image it was evident that the microparticles were homogenously functionalized. Though, there were some microparticles with small WGA aggregates.

In order to characterize these aggregates, the functionalized microparticles were analyzed using STORM. This technique improves the resolution by ~ 10 times over conventional imaging systems by providing nanometer accuracy. **Figure 4-50** shows the fluorescence image of a microparticle characterized using wide field and using STORM.

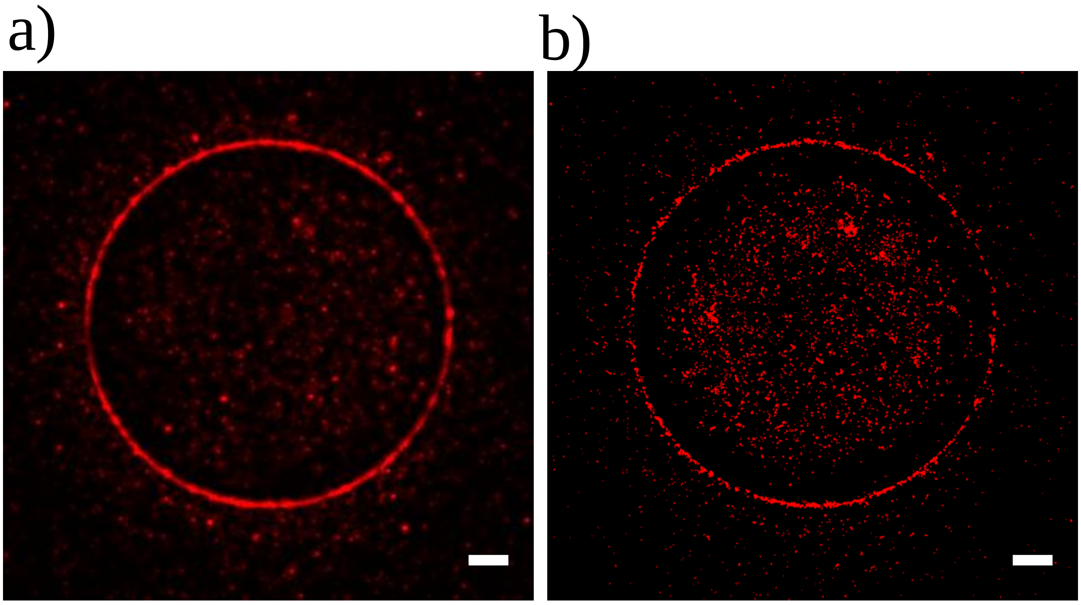

Figure 4-50. Fluorescence microscopy images of **Batch 5** WGA functionalized microparticle obtained using **a)** wide field and **b)** STORM. Scale bar – 2 µm.

There is a clear difference observed in the fluorescence of the microparticle for both the cases. The WGA aggregates on the left image appear more blurred, while on the right image, the aggregates have more resolution and can be differentiated from the adjacent aggregates.

Figure 4-51 shows the fluorescence images of a quadrant of a microparticle reconstructed after the STORM imaging analysis. **Figure 4-51 b)** shows the super resolution image. As observed in **Figure 4-51 c)**, the aggregate of WGA ranges from ~ 50-200 nm. The size of the WGA molecule is ~ 5 nm. By analyzing the size of the WGA aggregates from the super resolution image, it is evident that there is a presence of more than one monolayer of WGA on the microparticle.

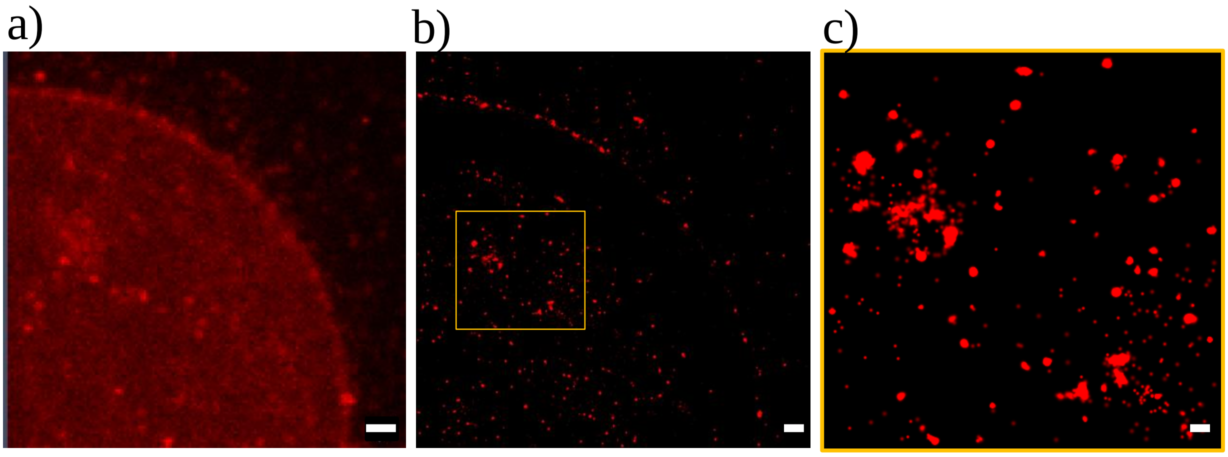

Figure 4-51. Fluorescence image of a quadrant of a microparticle obtained using **a)** confocal microscopy, **b)** super resolution image using STORM and **c)** magnified region of Figure-b. Scale bar – 1 µm (a-b) and 0.2 µm (c).

Consequently, using this technique, an improvement in the resolution of functionalization on the microparticles is seen. It is also noticed that the periphery of the microparticles are redder. Additionally, the functionalization is also higher in the middle of the microparticle. A further study has to be done in optics in order to study the functionalization better per each microparticle.

4.6. Difference in surface reactivity between polysilicon and silicon oxide

As mentioned before, we observed a big difference in the extent of functionalization between silicon oxide and polysilicon surfaces. Therefore, this difference was studied and characterized using different techniques such as X-Ray Photoelectron Microscopy (XPS).

Since most of the surface characterization techniques have the limitation to reach at the microparticle level, surfaces of **Batch 5**, 20 µm polysilicon microparticles on silicon oxide surface, were selected as shown in **Figure 4-52**. This Batch was selected due to the presence of larger surface area and the ease to analyze the functionalization, when compared to the rest of the batches.

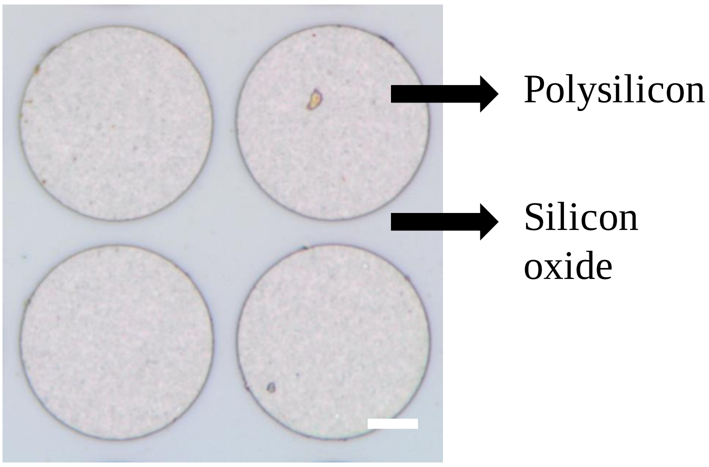

Figure 4-52. Bright field image of **Batch 5** surface. Scale bar – 5 µm.

Initially, we looked at the difference in the activation step in the different materials (polysilicon and silicon oxide) of the surface and both polysilicon and silicon oxide were analyzed using XPS [223-224]. **Table 4-4** shows the quantification of different elements present on the surface.

Table 4-4. Quantification of different elements on the surface of **Batch 5**.

Area	Surface Activation	Quantification (%)		
		O	**C**	**Si**
Polysilicon	Before	55.5	12.2	32.3
	After	57.1	12.3	30.6
Silicon oxide	Before	50.0	20.4	29.5
	After	56.3	13.3	30.5

It was observed that the value for quantified oxygen after the activation step has increased significantly in the case of silicon oxide, but a very small change is observed in the case of polysilicon. Thus, implying more hydroxylation on the silicon oxide surface thereby explaining the higher fluorescence intensity in silicon oxide than polysilicon. The rest of the elements such as carbon and silicon were quantified equally. But, a remarkable difference in the initial value of the quantified oxygen in the case of silicon oxide (before activation) was found to be much lower than that for polysilicon.

This lower value of oxygen on silicon oxide was unreasonable, and therefore, this experiment was again characterized on non-patterned surfaces (either polysilicon or silicon oxide). Two different surfaces of polysilicon and silicon oxide were selected and analyzed using XPS. **Table 4-5** shows the quantification of elements on polysilicon and silicon oxide surfaces.

Table 4-5. Quantification of different elements on polysilicon and silicon oxide surface.

Surface	Surface Activation	Quantification (%)		
		O	**C**	**Si**
Polysilicon	Before	22.3	10.6	67.1
	After	22.1	11.2	66.6
Silicon oxide	Before	62.4	5.6	32.0
	After	62.0	6.0	32.0

An increase in the quantified oxygen was expected for both the cases. But, the values of quantified elements before and after the activation step gave similar values. No difference was observed for both the surfaces. This either implies that the degree of hydroxylation is very low, therefore the difference could not be measured. Or, the activation of the surface, is not stable enough, therefore, the surface again reaches to the state of atmospheric oxidation. Thus, resulting in similar values for, before and after the activation step.

Batch 5 surfaces were further characterized using Raman Spectroscopy in order to see the different vibrational modes from the different monolayers formed on the surface of both polysilicon and silicon oxide [225]. The surfaces were excited with wavelength 550 nm laser on the top of the disc microparticle to analyse the behaviour on polysilicon, and below the disc microparticle in order to focus the silicon oxide. The surfaces were analysed at each step of the functionalization. Three different surfaces, after activation, after TESUD treatment and after WGA treatment were characterized respectively. In the first case, after the activation step, as shown in **Figure 4-53**, the difference in the vibrational band of hydroxylation in polysilicon and silicon oxide was expected, but no significant difference was observed in both the cases. Only a shoulder at 450 cm^{-1} was observed in the case of polysilicon. This could mean that the technique was not sensitive enough to differentiate the hydroxylation between the two surfaces (polysilicon and silicon oxide).

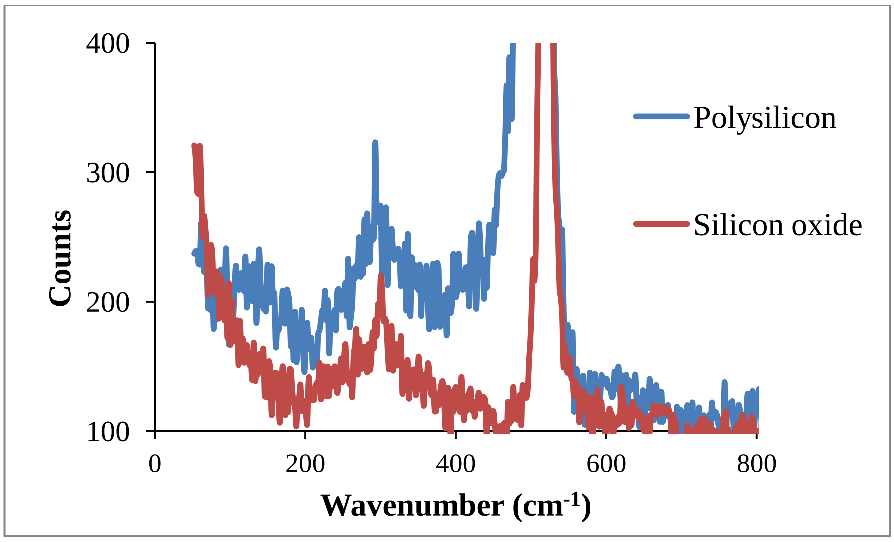

Figure 4-53. Raman spectra of activated polysilicon and silicon oxide surface.

Fuerthermore, the surfaces functionalized with TESUD did not show any stretching for the terminal aldehyde groups in both the cases, polysilicon and silicon oxide. This confirmed that the instrument was not sensitive enough in order to detect the molecules functionalized on the surfaces. The surfaces functionalized with the WGA showed high fluorescence band, due to the Texas Red, in both the cases (polysilicon and silicon oxide), as shown in **Figure 4-54**. Though, we noticed a shift in the fluorescent band in the case of polysilicon from 2842 to 2094 cm^{-1} and, an additional peak at 3490 cm^{-1}. This difference in the fluorescence band, between the polysilicon and silicon oxide was interesting. Thereby, emphasizing the difference in the surface reactivity between polysilicon and silicon oxide.

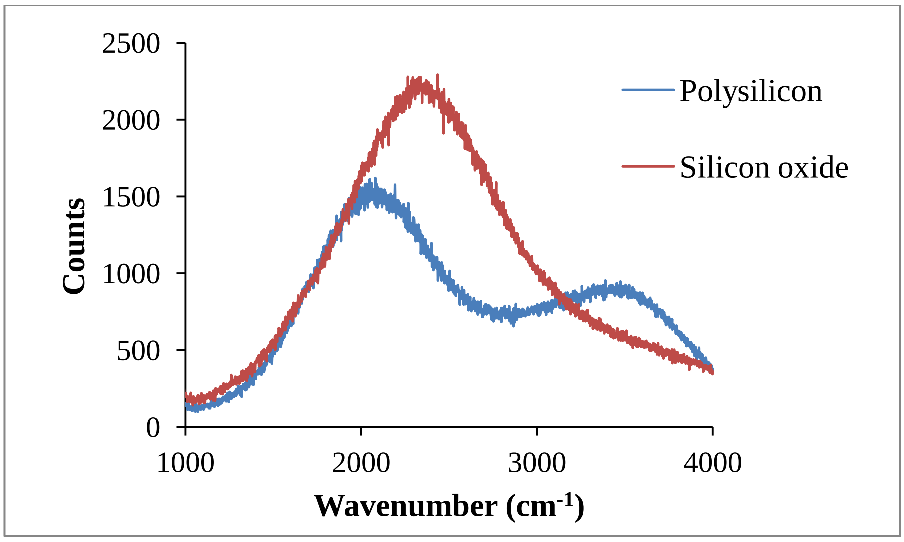

Figure 4-54. Raman spectra of WGA functionalized polysilicon and silicon oxide surface.

4.7. Biological Results

The biological experiments were performed by the group of Prof. Teresa Suárez at the *CIB-CSIC*.

The fully characterized and homogenously functionalized microparticles were then tested on cells in order to assess their adhesion to cell membranes. For this reason, the bio-functionalized microparticles with WGA and Con A were tested on two different cell lines: Dictyostelium discoideum (Dicty) and HeLa.

4.7.1. Cell adhesion of Star shaped bio-functionalized microparticles

Dicty is a unicellular amoeba and is a powerful system for basic biomedical research in cell biology [226-227]. This organism has been used widely for studying fundamental cellular processes. The life cycle of Dicty is rapid and easy to understand [227].

4.7.1.1. Study of cell adhesion on Dicty

The microparticles of both **Batch 1** and **Batch 2** functionalized using WGA and Con A, were tested initially on Dicty. In order to study the behaviour of cell adhesion of the functionalized microparticles, the Dicty were also simultaneously incubated with non-functionalized microparticles as a control experiment. In the case of **Batch 1** (20 µm) functionalized microparticles, it was observed that the microparticles were big for the size of the Dicty, and therefore was not suitable to study the cell attachment of the microparticles. Therefore, **Batch 2** (10 µm) functionalized with WGA and Con A was further chosen to study the cell adhesion behaviour.

In the case of **Batch 2** WGA functionalized microparticles, there was no difference observed in the cell adhesion behaviour when compared with the control. The functionalized and the non-functionalized microparticles, both behaved in the similar fashion. The microparticles in both the cases were seen attached to the cell surface, but then due to the rapid movement of the Dicty, the microparticles were not adhered to cell membranes of Dicty longer period (they attached and dettached).

Whereas, in the case of **Batch 2** functionalized with Con A, the microparticles were seen attached to the cell membrane of the Dicty, for longer time periods when compared with non-functionalized microparticles. Thus, showing a positive result for the cell attachment of the microparticles functionalized with Con A. **Figure 4-55** shows the **Batch 2** Con A functionalized microparticle attached on the cell membrane of the Dicty.

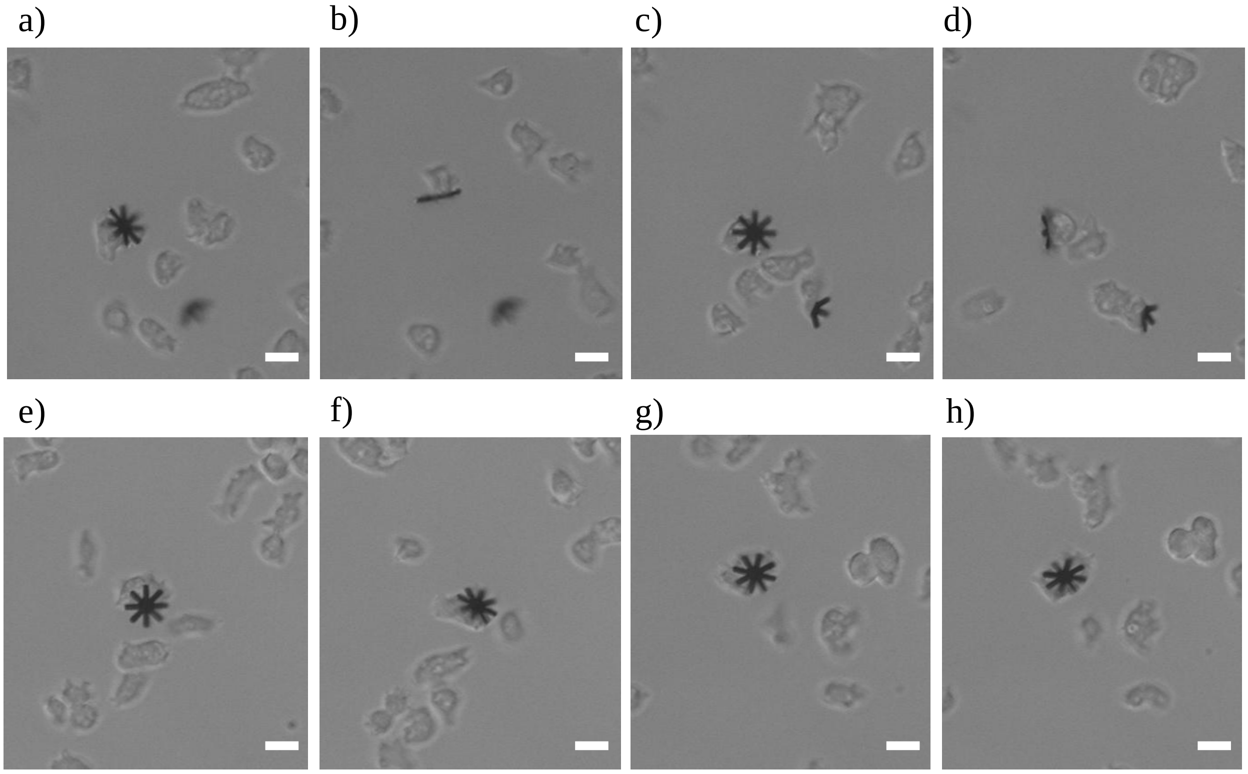

Figure 4-55. Optical images of **Batch 2** Con A functionalized microparticles attached to Dicty cell membranes at various positions, Dicty 1 (**a-d**) and Dicty 2 (**e-h**). Scale bar – 10 µm.

The difference in the binding affinity between different lectins could also be due to the presence of difference membrane receptors for the lectins present on the cell membrane of a cell. It is known that the Dicty has higher binding affinity to Con A than WGA [210,228-231]. Thus, explaining the difference in the cell attachment behaviour of the functionalized microparticles.

4.7.1.2. Study of cell adhesion on HeLa cells

The second cell line used for testing the cell attachment was on HeLa cells. In the case of HeLa cell line, the **Batch 1** and **Batch 2** WGA functionalized microparticles did not show any significant increase in adhesion time in the cell attachment when compared to the non-functionalized microparticles. Some of the microparticles were found attached to the cell membrane, but not for long duration.

As, the WGA functionalized microparticles did not show any significant improvement in both the above cells lines, Dicty and HeLa, the functionalized microparticles were further tested on human derived cell lines, such as neuroblastoma (SH-SSSy) and breast cancer cells (MCF-7). These experiments are still under progress.

4.7.2. Cell adhesion of Disc shaped bio-functionalized microparticles

The cell adhesion behaviour of the functionalized disc shaped microparticles, **Batch 5** and **Batch 6** on Dicty and HeLa cells was investigated. The WGA functionalized microparticles did not show any change with disc shaped microparticles. The binding behaviour of the functionalized microparticles to the cell membrane was same as observed for the non-functionalized microparticles. These results imply that the lectin WGA does not promote cell adhesion for the specific, Dicty and HeLa cell lines.

CHAPTER 5

CHAPTER 5

Functionalization of star-shaped and discoidal polysilicon microparticles with Boronic Acids (BAs) for their adhesion to cell membranes

5.1. Introduction

Many efforts have been dedicated to exploit artificial materials with specific sugar-binding capability to mimic and replace lectins. The lectin-mimics include two major categories based on their binding forces with carbohydrates: (1) noncovalent systems such as supramolecules; (2) covalent systems mainly represented by boronate affinity-based covalent systems. The noncovalent systems often require complicated designs such as hydrogen bond groups, while the boronate affinity-based covalent systems possess known and strong binding forces as the straightforward design basis, represented in **Scheme 5-1** [232-235]. The boron–diol interaction enables elaborate design of Boronic acid (BA) based saccharide sensors. Over the last decade, this research topic has been well developed thanks to the integration of BA chemistry with a range of techniques, including supramolecular chemistry, materials chemistry, surface modification, and nanotechnology [236-237]. New sensing strategies and platforms have been introduced and remarkable progress has been achieved to fully utilize the unique property of boron–diol interaction and to improve the binding affinity towards different targets, especially under physiological conditions.

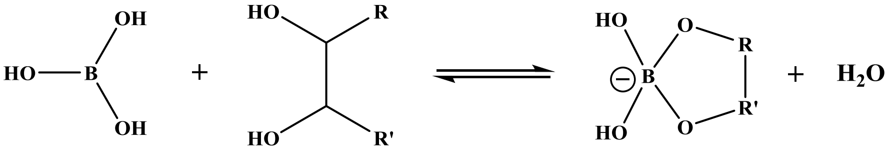

Scheme 5-1. Schematic representation of BA-diol interaction.

BAs are well known for their ability to reversibly interact with the diol groups, a common motif of biomolecules including sugars and ribose [238]. Due to their ability to interact with carbohydrates, they can be regarded as synthetic mimics of lectins. They are very important in synthetic organic, materials, bioorganic, medicinal chemistry and as well as chemical biology [239-241]. They are important in functionalization of nanostructures, separation and purification of glycosylated products and controlled drug delivery [242]. They are also commonly used as recognition moieties for the design and synthesis of sensors for carbohydrates, amino acids and amino alcohols [243-246]. In medicinal chemistry, they are important for the preparation of inhibitors of hydrolytic enzymes [247]. Among all the biologically active BAs, bortezomib is an FDA-approved anticancer agent [248]. Additionally, they have been exploited extensively as chemo/biosensors in the detection of carbohydrates, anions, and reactive oxygen and nitrogen species (ROS/RNS) through electrochemical, fluorescence, and colorimetric measurements [249-251]. Notably, over the physiological pH range, BAs are ideal molecular receptors for monosaccharides since BA derivatives rapidly and reversibly interact with carbohydrates in aqueous media, and thus importantly the method does not consume the analyte [236,252]. Because of the tremendous importance of BAs, there is interest in finding ways to increase their structural diversity and to tether them to other scaffolds. In terms of common cell attachment and detachment protocols, thus BA derivatives can be utilised to bind with native oligosaccharides which are present in the outer cellular wall or membrane. It is worth noting that the boronate anion in general has stronger binding strength towards diol. Therefore, higher pH is favorable in sugar binding as most of the boron-containing species will then exist in their anion form. For practical application, it is required that the sensing system should perform well under physiological conditions (pH 7.4) [236].

Based on the well known interaction between BA and carbohydrates, BA could be a plausible alternative to induce adhesion of microparticles. We selected 4-formylphenylboronic acid, for it contains a formyl group for chemical attachment onto the microparticles [253-256]. **Figure 5-1** shows the chemical structure of 4-formlylphenylboronic acid (PBA). The affinity of this BA towards the carbohydrates is well known [233,237]. For instance, PBA containing polymer brushes on different surfaces have been fabricated for sensor chips of glycoproteins, glucose detection, and controllable cell adhesion, depending on the fast and stable formation of boronate esters between PBA and diols [256].

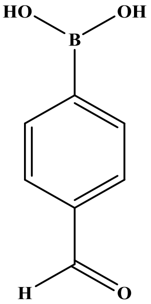

Figure 5-1. Chemical structure of 4-formylphenylboronic acid (PBA).

5.2. Functionalization and characterization of polysilicon microparticles on surfaces using BA

5.2.1. Functionalization of polysilicon microparticles on Surfaces using BA

The functionalization of polysilicon microparticles with BA was initially optimized on surfaces and then carried out on the polysilicon microparticles in suspension. For this purpose, **Batch 5** surfaces (20 µm in diameter, 500 nm thickness) as shown in **Figure 5-2** were selected. These surfaces were chosen due to their large surface area and their feasibility in characterization upon functionalization.

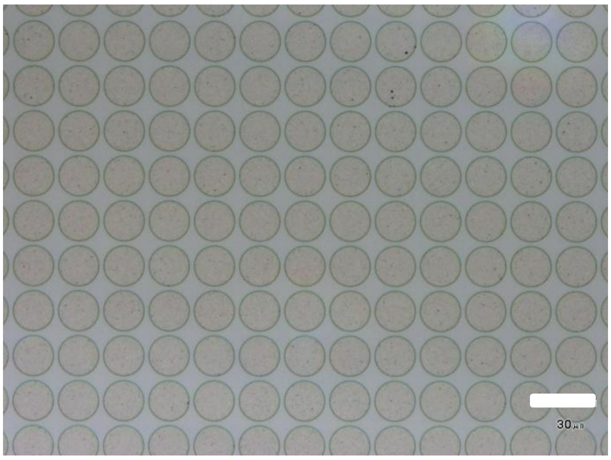

Figure 5-2. Bright field image of 20 µm polysilicon microparticles on silicon surface (**Batch 5**). Scale bar – 30 µm.

First, the surfaces were cleaned and activated using piranha and basic solution, increasing the amount of hydroxyl groups on the surfaces. Then, the hydroxylated surfaces were then made to react with aminopropyltriethoxy silane (APTES). The triethoxy group of the APTES reacts with the hydroxylated polysilicon surface forming a stable covalent bond between the linker and the surface. The surfaces upon immobilization of APTES resulted in a uniform layer of primary amines, which we call (NH_2-SAM). The NH_2-SAM on the surface reacts with the formyl group of PBA in the presence of sodium cyanoborohydride ($NaBH_3CN$) through reductive amination process resulting in the formation of an amine bond.

Scheme 5-2, shows the schematic representation of the functionalization of polysilicon microparticles on surfaces. The activated surfaces were treated with 2 % of APTES and were incubated for 3 hours to form the NH_2-SAM. The APTES functionalized surfaces were then incubated in BA (5 mg/mL) overnight.

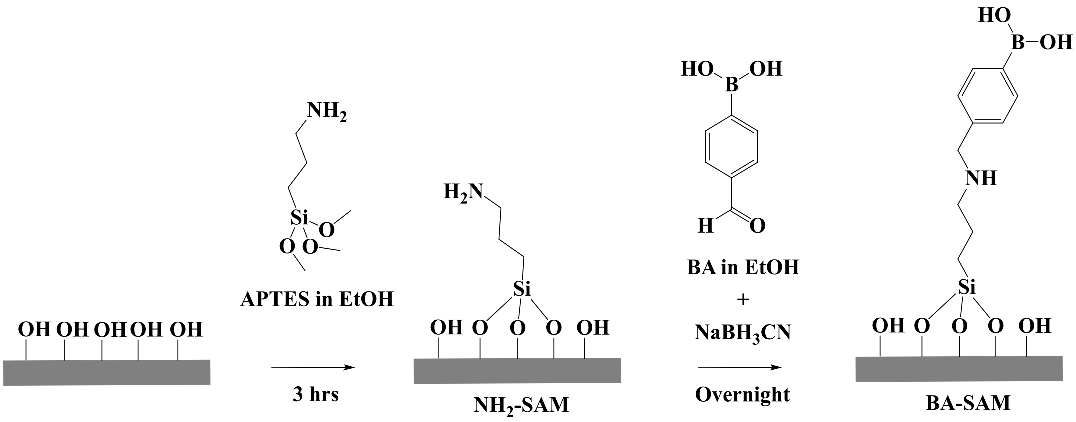

Scheme 5-2. Schematic representation of functionalization of polysilicon surfaces with BA.

5.2.2.Characterization of BA functionalized surfaces

The BA functionalized surfaces were characterized using various techniques such as contact angle measurements, Fluorescence microscopy and X-ray Photoelectron Spectroscopy (XPS).

Contact angle measurements for each step of functionalization are tabulated in **Table 5-1**. The contact angle value before the activation treatment was found to be 38°. This higher contact angle can be due to the presence of dirt from the atmosphere and because polysilicon is not so hydrophilic. After the piranha treatment, the contact angle value decreased to 12° indicating that the surface hydrophilic, implying the formation of hydroxyl groups on the surface. A further decrease in the contact angle value to 10° after the basic treatment confirms the increase in the hydroxylation of the surface. These values were similar to the contact angle values obtained in Chapter 4.

Table 5-1. Contact angle values obtained after each step of functionalization on Batch 5.

Sample Name	Contact angle (ϴ)
Initial surface	38 ± 3
After Piranha	12 ± 2
After Basic	10 ± 2
NH_2-SAM	40 ± 2
BA-SAM	49 ± 3

After immobilizing APTES, the contact value of the surface increased to 40° indicating the surface is more hydrophobic. This increase in the hydrophobicity is due to the formation of NH_2-SAM, which agrees to the values reported in the literature [257]. The further increase in the contact angle value to 49° after the BA treatment confirms the immobilization of BA on the surfaces [249].

Fluorescence microscopy was used to monitor the homogeneity of BA-SAMs. BA functionalized surfaces were incubated with Alizarin Red S (ARS) solution in PBS at pH 7.4. ARS produces a strong fluorescent signal in response to the binding of a boronic acid, as shown in **Scheme 5-3** [236,258-261].

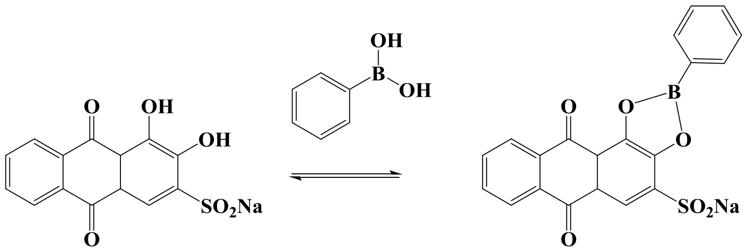

Scheme 5-3. Schematic representation of binding of BA with ARS.

Thus three surfaces, control (without SAM), NH_2-SAM and BA-SAM were incubated in the ARS solution, and were then characterized using fluorescence microscopy. **Figure 5-3** shows the fluorescence microscopy images of surfaces characterized using ARS.

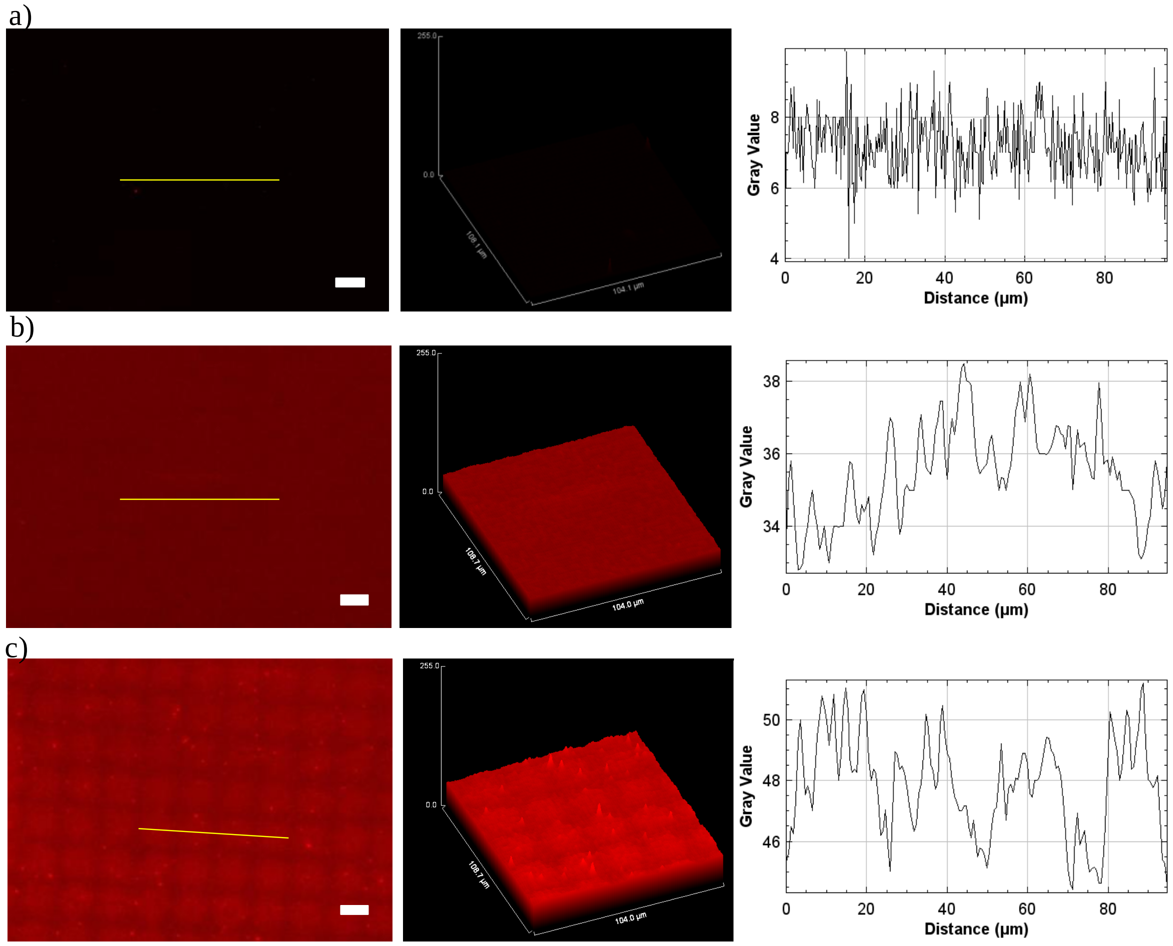

Figure 5-3. Fluorescence microscopy images of surfaces characterized using ARS, excited using a green filter (λ= 530 - 550 nm), **a)** Control (without SAM) **b)** NH_2-SAM, **c)** BA-SAM, their 3-D surface plots and plot profiles respectively. Scale bar – 20 µm.

Control surface was analyzed after the activation treatment, no fluorescence was observed as shown in Figure (**Figure 5-3 a**). In the case of NH_2- SAM, as no fluorescence was expected, it was observed that ARS in spite of several washes showed affinity towards the NH_2-SAM (**Figure 5-3 b**). The immobilization of ARS on to the NH_2-SAM at pH 7.4 could have protonated the NH_2-SAM, resulting in an electrostatic interaction with the ARS, making the surface fluorescent [262]. In any case, the fluorescence intensity in BA-SAM treated with ARS was 10 times higher than NH_2-SAM, which could be confirmed from the plot profiles (**Figure 5-3 c**). Thus, confirming the immobilization of BA on surfaces and the higher binding affinity of ARS with the BA.

The BA functionalized surfaces were further characterized using XPS at each step of functionalization. **Figure 5-4 (a-c)** shows the most characteristic peaks of the activated surfaces, from which the following composition is obtained: C-13.92 %; O-18.07 %; Si-68.01 %. The presence of carbon is due to contamination of the surface, on the other hand, given the nature of the sample, the main element is silicon, for which two peaks are observed, one corresponding to oxide form of silicon at 99 eV and another at 104 eV corresponding to the element silicon. Finally, in the case of oxygen, a smaller amount than expected is obtained, but this could be due to the activation of the surfaces 24 hrs before the characterization.

On the other hand, **Figure 5-4** (**d-g**) shows the most characteristic peaks of the NH_2-SAM, from which the following composition is obtained: C-43.69 %; O-27.59 %; Si-18.71 %; N-10.02 %. There is a considerable increase in the amount of carbon, this is due to the alkyl chain of APTES; the amount of oxygen is lower as it is the point of interaction between the triethoxy group of the APTES and the surface; one of the peaks corresponding to the silicon element at 99 eV disappears, which also shows the coverage of the activated surface with the NH_2-SAM. Furthermore, the characteristic peak of nitrogen from the amino group of APTES is also observed at 403 eV.

Finally, **Figure 5-4** (**h-l**) shows the most characteristic peaks of the BA-SAM on surfaces, from which the following composition is obtained: C-51.81 %; O-3.53 %; Si-15.13 %; N-8.49 %; B-3.53 %. A significant increase in the amount of carbon is observed due to the phenyl group of the BA and an appearance of a new peak for nitrogen at 400 eV is observed, which indicates the change from being primary amine to secondary amine by the reaction with the BA [263]. Finally, a peak of Boron at 187 eV is also seen confirming the immobilization of BA on to the surfaces.

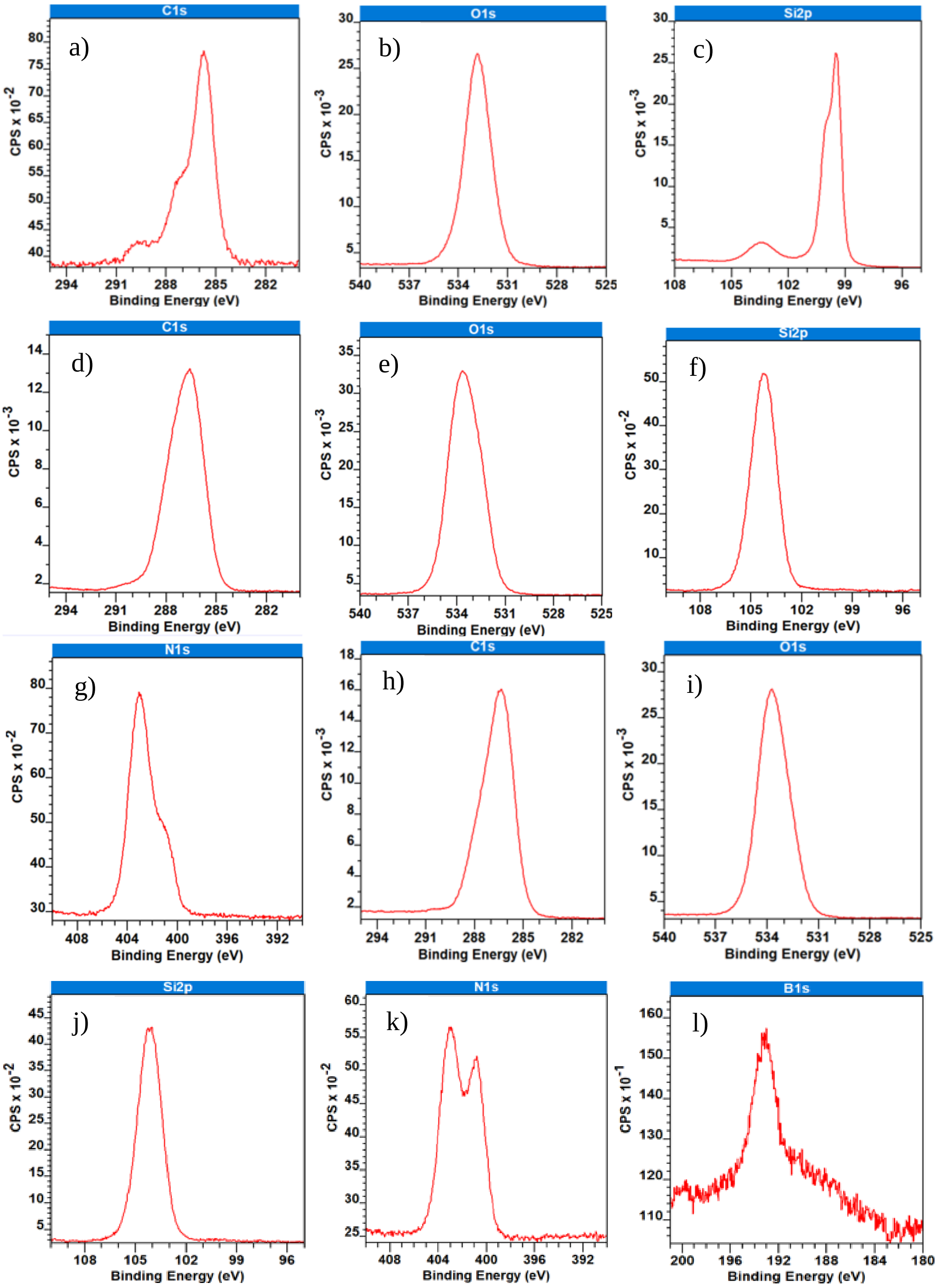

Figure 5-4. XPS spectra obtained after analysing the activated surface (**a-c**), NH_2-SAM (**d-g**) and the BA-SAM (**h-l**) on surfaces.

5.3. Functionalization and characterization on polysilicon microparticles in suspension using BA

After optimization and characterization on surfaces of **Batch 5** functionalized with the BA, functionalization of the released polysilicon microparticles of different shapes and sizes. In the case of star-shaped microparticles, **Batch 1** (20 µm in diameter, 500 nm thickness) and **Batch 2** (10 µm in diameter, 500 nm thickness) were selected. Whereas in the case of disc-shaped microparticles, **Batch 5** (20 µm in diameter, 500 nm thickness) and **Batch 6** (10 µm in diameter, 500 nm thickness) were selected. All the four batches were functionalized with BA following the previously optimized protocol on surfaces.

Fluorescence microscopy was chosen as a main technique to characterize the BA functionalized microparticles, after incubation in ARS solution. **Figure 5-5** shows the fluorescence microscopy images of BA functionalized microparticles characterized using ARS. From the images, it is certain that the microparticles are functionalized with BA, although the functionalization appears to be non-homogenous. Aggregates of ARS were observed on the microparticles, more on **Batch 1** microparticles. The aggregates of ARS were seen more on the arms of the star microparticle. Even after extensive and thorough washing of the microparticles from all the batches, some aggregates remained.

On comparing the fluorescence images obtained using ARS to lectin functionalized microparticles, the functionalization of microparticles using lectin was more uniform and homogenous. The aggregates in the case of ARS functionalized microparticles are seem bigger to lectin functionalized microparticles. The BA functionalized microparticles were further tested for carbohydrate interaction in solution.

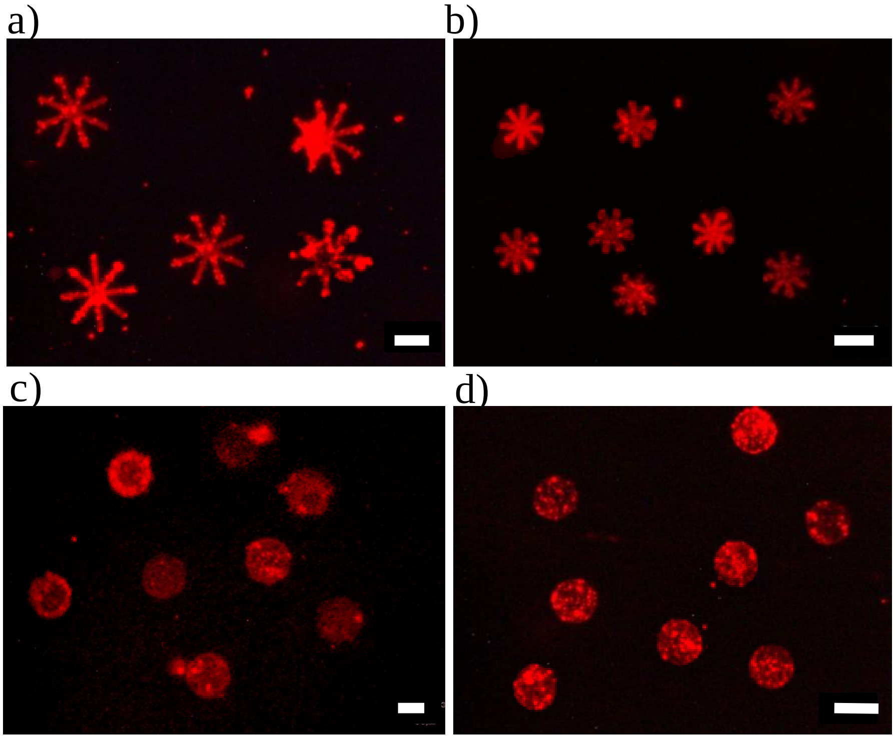

Figure 5-5. Fluorescence images of BA-ARS functionalized surfaces of **Batch 1**, **Batch 2**, **Batch 5** and **Batch 6**. Scale bar – 10 µm.

5.2.3. Study of BA-Carbohydrate interaction on polysilicon microparticles on surfaces

ARS is widely used for the evaluation of the interactions between BAs and cisdiol-containing compounds. In this method, two competing equilibrium between three species are involved. One is the equilibrium between a BA and ARS, which reports the binding through apparent changes in fluorescence intensity and colour. The other is between the BA and a cis-diol compound (such as carbohydrates), which competes with the former equilibrium. Thus this approach provides a strong fluorescence signal from the ARS when binding to a BA and weak fluorescence signal when dissociated, as represented in **Figure 5-6** [259-261].

Therefore, keeping this approach in mind, interaction of BA functionalized surfaces with carbohydrates was studied. The carbohydrate, N-acetylglucosamine (GlcNAc) was selected to study the interaction with BA, as shown in **Figure 5-6 c)** [264-265]. It is a key component present in most of the cell membranes, such as bacteria, fungi and the extracellular matrix of animal cells [177,183]. The carbohydrate binding study was performed on surfaces due to their easy handling and manipulation than BA functionalized microparticles. In this case, surfaces from **Batch 1** and **Batch 5** were selected as a representative surface of each shape of the microparticles, both having 20 µm in diameter and 500 nm thickness.

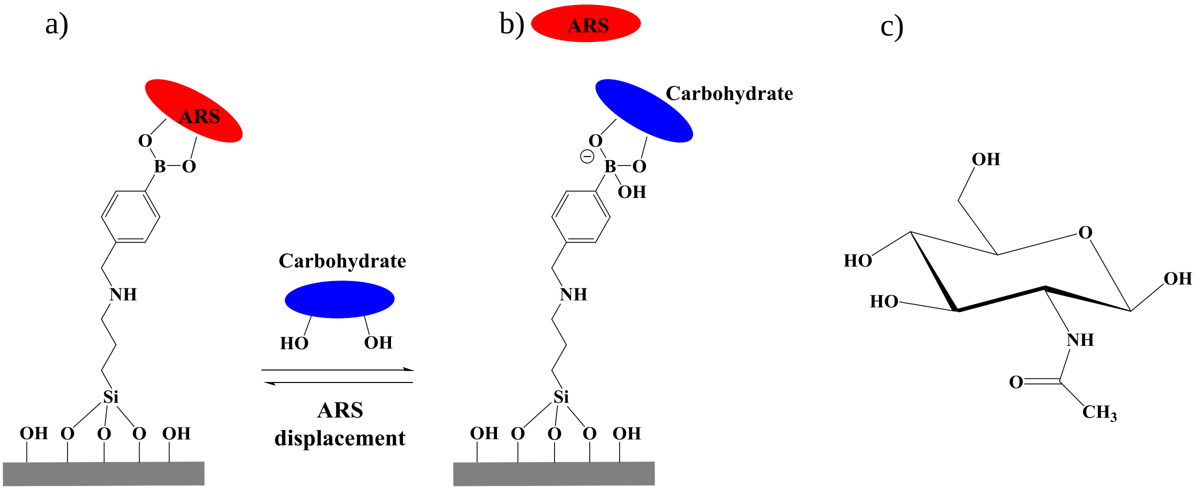

Figure 5-6. Displacement of ARS due to BA-Carbohydrate binding **a)** turn-on state, **b)** turn-off state and **c)** chemical structure of GlcNAc.

The BA-ARS functionalized surfaces were incubated in GlcNAc (5 mg/mL) in PBS at pH 7.4 for different time intervals and were later characterized using fluorescence microscopy. **Figure 5-7** shows the fluorescence images of **Batch 1** BA-ARS functionalized surfaces without GlcNAc incubation, after 5 mins, after 10 mins and overnight incubation in GlcNAc. As observed from the **Figure 5-7**, the average fluorescence intensity of the BA-ARS functionalized surfaces, without the GlcNAc treatment was higher, whereas after 5 mins of GlcNAc incubation, the average fluorescence intensity decreased. But this decrease was found at the top of the microparticles, mainly on the centre of the star shaped microparticle. As, the fluorescence was not completely turned-off, the surfaces were left in incubation for 10 mins in GlcNAc, and the fluorescence intensity observed for this surface was similar to the previous case. Thus, the BA-ARS functionalized surfaces were left for overnight incubation in GlcNAc. The following day, the surface was characterized, which showed resembling results as before.

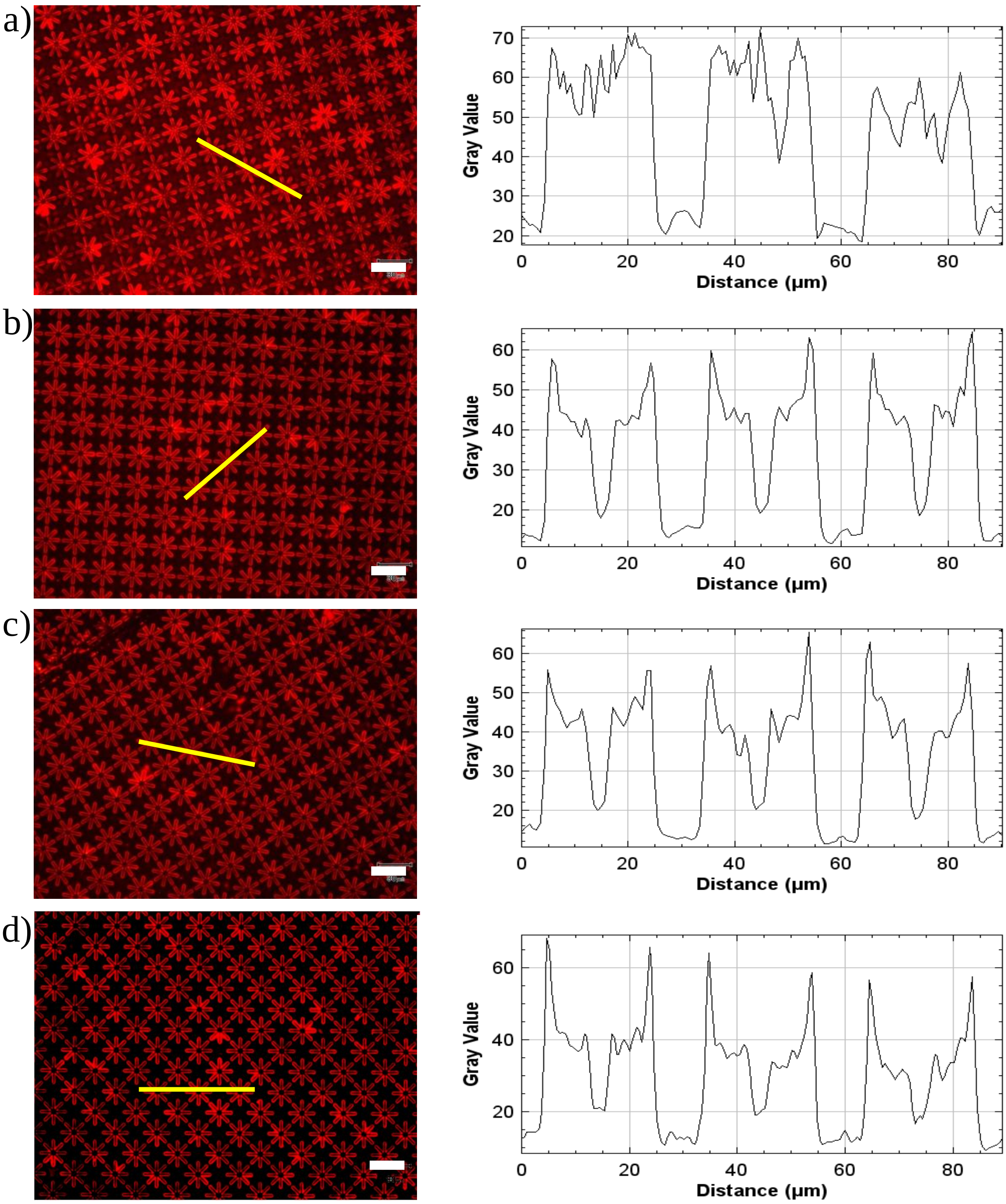

Figure 5-7. Fluorescence image of **Batch 1** BA functionalized surface **a)** without GlcNAc incubation **b)** after 5 mins in GlcNAc, **c)** after 10 mins in GlcNAc and **d)** overnight incubation in GlcNAc; and their plot profiles. Scale bar – 30 µm.

The fluorescence microscopy images before and after incubation with GlcNAc were studied carefully as shown in **Figure 5-8** (Zoom out of **Figure 5-7 a)** and **d)**). In the case of surfaces before GlcNAc incubation showed fluorescence on all the surface of the microparticle

(**Figure 5-8 a**). Whereas, in the case of after GlcNAc incubation, it can be observed that the fluorescence was on the perimeter of the microparticles, implying that the ARS was still bonded to the sides of the microparticles, as shown in **Figure 5-8 b)**. This could suggest that the BA was not functionalized homogenously on the sides of the star microparticles, and thus, ARS was electrostatically bonded to the surface (NH_2-SAM). Thus, when this surface is in contact with the carbohydrate, there is no displacement of the ARS, hence, remaining in turn-on state only on the sides of the microparticles. The 3-D surface plot shows a slight decrease in the fluorescence on the sides of the microparticles can be seen from the 3-D surface plots.

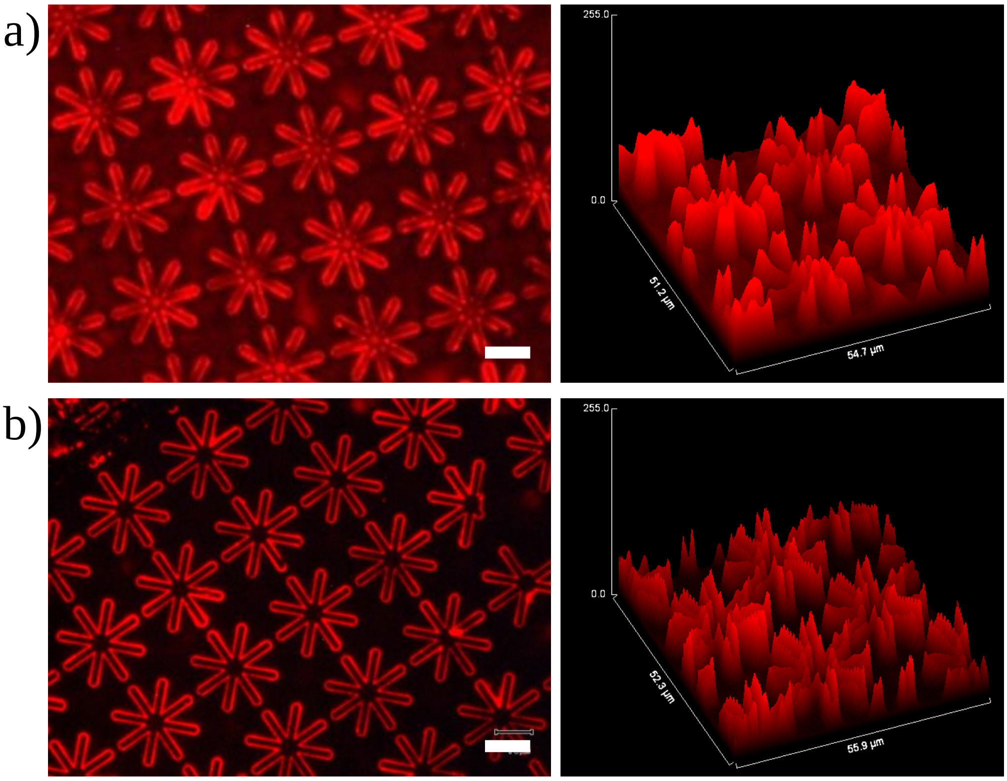

Figure 5-8. Fluorescence image of **Batch 1** BA functionalized surface **a)** without GlcNAc and **b)** overnight incubation in GlcNAc; with their 3-D surface plot profiles. Scale bar – 10 µm.

Another interpretation could also be due to the unavailability of the BAs on the sides of the microparticles for the ARS displacement when in contact with the carbohydrates, thus showing fluorescence by existing in the turn-on state.

On the other hand, in the case of **Batch 5** BA-ARS functionalized surfaces were treated with the carbohydrate, GlcNAc. **Figure 5-9** shows the fluorescence images of the surfaces before and after treatment with GlcNAc. Here, the displacement of ARS from the BA was noticed distinctly. The average fluorescence intensity before the GlcNAc treatment was higher which was reduced 10 times, after 5 mins of incubation in GlcNAc. The system fluorescence was turned-off successfully, implying the bonding of the carbohydrate with the BA functionalized surface.

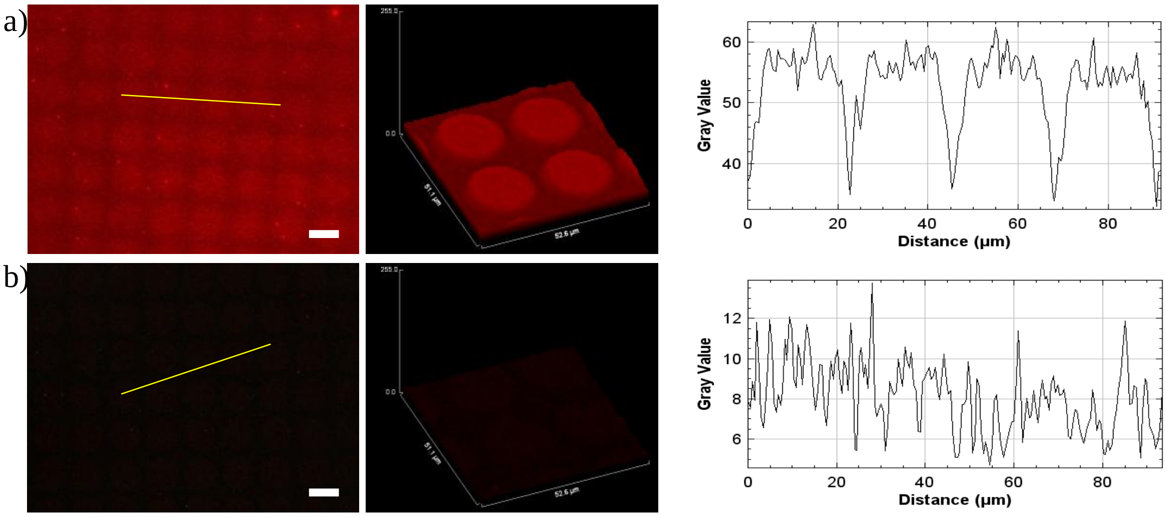

Figure 5-9. Fluorescence images of **Batch 5** BA functionalized surfaces **a)** before and **b)** after 5 mins of incubation in GlcNAc; with their 3-D surface plots and plot profiles. Scale bar – 20 µm.

This difference in interaction observed between the case of **Batch 1** and **Batch 5** shows the influence of morphology of the microparticles in functionalization.

Consequently, after demonstrating the interaction of BA functionalized surfaces with carbohydrates, GlcNAc in solution, the final step was to assess the cell adhesion of BA functionalized microparticles with the cell membranes of specific cell lines.

5.4. Biological Results

The optimized BA functionalized microparticles of different batches; **Batch 1** (20 µm in diameter, 500 nm thickness), **Batch 2** (10 µm in diameter, 500 nm thickness), **Batch 5** (20 µm in diameter, 500 nm thickness) and **Batch 6** (10 µm in diameter, 500 nm thickness) were tested on HeLa cells, together with the non-functionalized microparticles, in order to evaluate their attachment to the cell membrane.

In the case of star-shaped **Batch 1**, BA functionalized microparticles were seen attached to the cell membrane of the HeLa cells. **Figure 5-10** shows an optical image of a microparticle attached to the cell membrane of a cell at various positions. On comparing the non-functionalized and BA functionalized microparticles, the functionalized microparticles were adhered to the cell membrane for longer duration. From the images below, it is certain, that the microparticle, in spite of a moving cell, was attached to the cell membrane. Similar results were noted in the case of **Batch 2** BA functionalized microparticles. **Figure 5-10 (e-h)** shows a microparticle attached to a cell membrane at different positions. Regardless of the smaller size of Batch 2 to the HeLa cells, the microparticles were seen well adhered to the cell membrane.

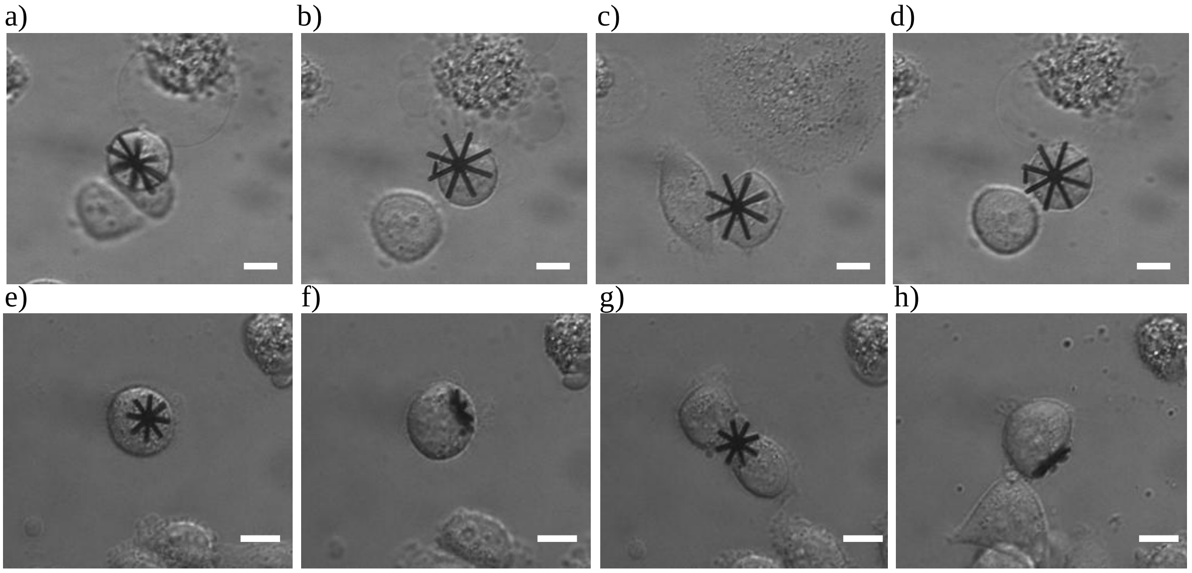

Figure 5-10. Various positions of BA functionalized microparticles attached to the cell membrane of HeLa cells, **Batch 1** (**a-d**) and **Batch 2** (**e-h**). Scale bar – 10 µm.

Furthermore, identical behaviour was observed in the case of disc shaped microparticles. **Batch 5** and **Batch 6** BA functionalized microparticles as shown in **Figure 5-11**, were found well attached to the cell.

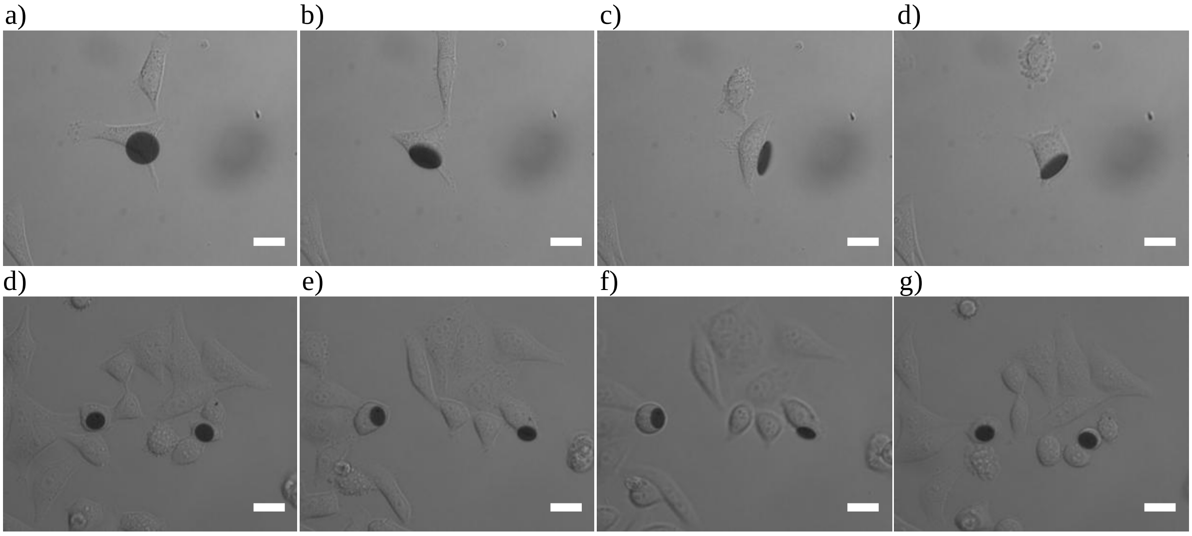

Figure 5-11. Various positions of BA functionalized microparticles attached to the cell membrane of HeLa cells, **Batch 5** (**a-d**) and **Batch 6** (**e-h**). Scale bar – 20 μm.

Thus, these positive results demonstrate a successful functionalization of the microparticles with different shapes and sizes using BA to achieve cell adhesion.

CHAPTER 6

CHAPTER 6

Functionalization of hexahedral bi-functional microparticles using fluorescent probes for pH sensing in cells

6.1. Introduction

pH sensing is of importance for the diagnosis of insidious pathologies such as cancers [266-268]. Cancer cells have a reversed pH gradient compared with normal differentiated cells, as shown in **Figure 6-1**. The extracellular pH (pH_e) of a cancer cell is more acidic than of normal cells, whereas the intracellular pH (pH_i) is neutral or slightly alkaline [268-269]. A combination of poor vascular perfusion, regional hypoxia, and increased flux of carbons through glycolysis leads to extracellular acidosis in cancer cells; with pH_e values as low as 6.5 [270-271]. Low pH_e and high pH_i are crucial for cancer cell proliferation, invasion, metastasis, drug resistance, and apoptosis [272-274].

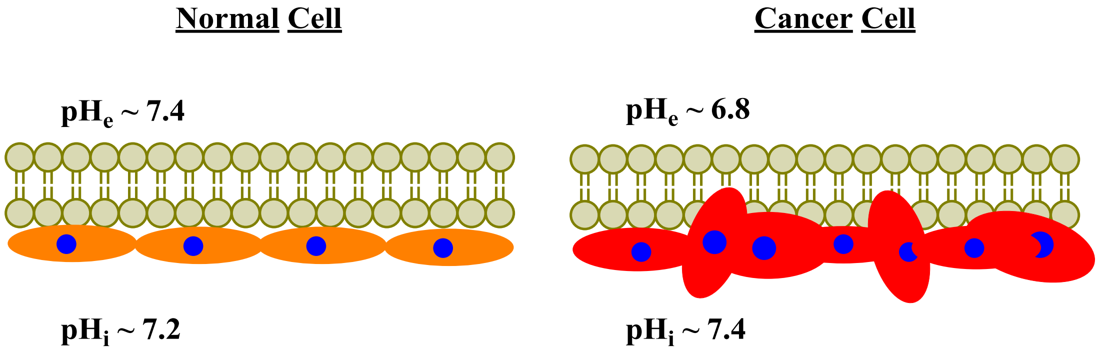

Figure 6-1. Reversed extracellular and intracellular pH in cancer cells compared to normal cells.

The importance of sensing many biological processes has led to the development of fluorescence based receptors which can be used as chemosensors exhibiting a variation on their intrinsic fluorescence. Supramolecular chemosensors are composed of a binding moiety -to guest the anabolite-, and a sensing moiety -to read information about the complexation, linked through a connector to the surface (**Figure 6-2**) [275]. Immobilized chemosensors have been studied in the last years for sensing important biological parameters at cellular level such as biological ions or radicals as well as enzyme activity, using fluorescence changes because it is one of the preferred methods for detection in living organisms [276-281].

In particular, fluorescent chemosensors for biologically and/or environmentally, cations, anions, small neutral molecules as well as biomacromolecules (such as proteins and DNA) have been developed along with a rapid advancement in microscopic imaging technologies [278,282-285]. Analyte detection by a fluorescent chemosensor is usually achieved through one or more common photophysical mechanisms, including chelation induced enhanced fluorescence, intramolecular charge transfer, photoinduced electron transfer, aggregation induced emission and the number of approaches is still expanding [286-289].

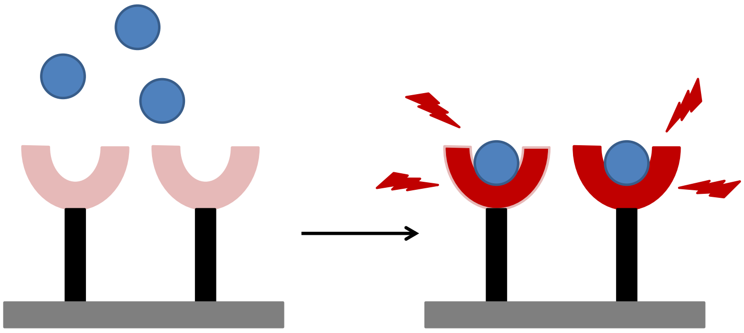

Figure 6-2. Model of fluorescence chemosensor.

Additionally, due to the high levels of sensitivity and in particular their ability to be used for temporal and spatial sampling for *in vivo* imaging applications, fluorescent chemosensors have been widely applied in a variety of fields [290]. With the advent of two or multi-photon excitation and high and super-resolution fluorescence microscopy, there will be an ever increasing need for highly sensitive and selective chemosensors for *in vivo* biological applications [291].

In this context, tools with the capability to measure these pH differences should be an important aim to differentiate between the normal and cancer cells (diagnosis) and also to exploit these differences therapeutically. However, despite the existence of many pH sensors to be used in solution, their toxicity for the cells hamper their use in long term studies in cell cultures [292]. Immobilization of any of these systems in either micro- or nanoparticles would offer the advantage of increasing their specificity and reduce their toxicity.

Keeping this as our main challenge we aim in developing a novel microtool for sensing pH. For accomplishing this goal, we envisaged the use of bi-functional hexahedral microparticles. Bi-functional microparticles allow avoiding the inconvenience of applying multi-functionalization procedures to a single material, which could ruin the efficient control on the immobilization of different molecules. Therefore, polysilicon and gold material was selected because of their well known chemistry and biocompatibility [113,156,219,293-296]. The selected 3x3 μm^2 bi-functional hexahedral microparticles had dimensions in micrometric scale, **Figure 6-3**. These microparticles were made up of 400 nm thick polysilicon and 100 nm thick gold, fabricated by our collaborators, explained in Appendix, Section 2.

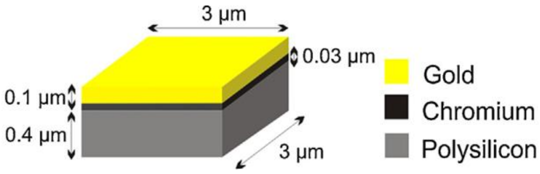

Figure 6-3. Conceptual representation of a hexahedral bi-functional microparticle.

The next step was to bi-functionalize these microparticles using pH dependent fluorophores. Different types of pH dependent fluorophores were selected and were studied in solution. As the final step was to immobilize these pH dependent fluorophores on to bi-functional microparticles, fluorophores bearing linking functional groups were chosen. Most commonly used functional groups are activated esters, carboxylic acids (COOH) or primary amines (NH_2). These functional groups make it feasible to immobilize the fluorophores on the microparticles, without influencing the pH sensitivity.

The majority of the selected fluorophores we selected was with NHS ester group. NHS esters are reactive groups formed by carbodiimide-activation of carboxylate molecules [297298]. They provide an efficient and convenient way to selectively link to primary amines (R-NH_2) forming a stable amide bond. Hence, four different commercially available pH dependent fluorophores were selected, Oregon green™ 488 carboxylic acid, succinimidyl ester, 6-isomer (**Oregon green**); pHrodo™ red, succinimidyl ester (**pHrodo**); Alexa fluor™ 647, succinimidyl ester (**Alexa fluor**) and SNARF™-1 carboxylic acid, acetate, succinimidyl ester (**SNARF**), (**Figure 6-4**).

The amine reactive **Oregon green** can be used to create green fluorescence with excitation/emission wavelength at 488/520 nm. This fluorinated analogue of fluorescein overcomes some of the key limitations of fluorescein, including greater photostability and a lower pK_a (~ 4.7), making its fluorescence essentially less pH sensitive in the physiological pH range. On the other hand, **pHrodo** is an amino rhodamine that increases in fluorescence intensity as the pH of its surroundings becomes more acidic [299-300]. **pHrodo** has an excitation and emission maxima of 560 and 595 nm, respectively. Whereas, **Alexa fluor** is a bright and photostable far-red fluorophore with excitation and emission maxima at 651 and 672 nm, respectively. The NHS ester of **Alexa fluor** is the most popular tool for bioconjugation. It is pH-insensitive from pH 4 to pH 10, and therefore we selected it in order to use as a reference fluorophore. **SNARF**, on the other hand has two fluorescence emission wavelength (590 and 650 nm), in which one of the emission peak decreases (590 nm) whereas the other increases (650 nm) with the increase in pH, hence ratiometric fluorescence pH indicator. It is typically used by exciting at 488 nm. The selected NHS ester of **SNARF** as shown in **Figure 6-4** bears an additional functional acetate group (CH_3COO-R) which is designed to exhibit fluorescence upon hydrolysis only when inside a cell.

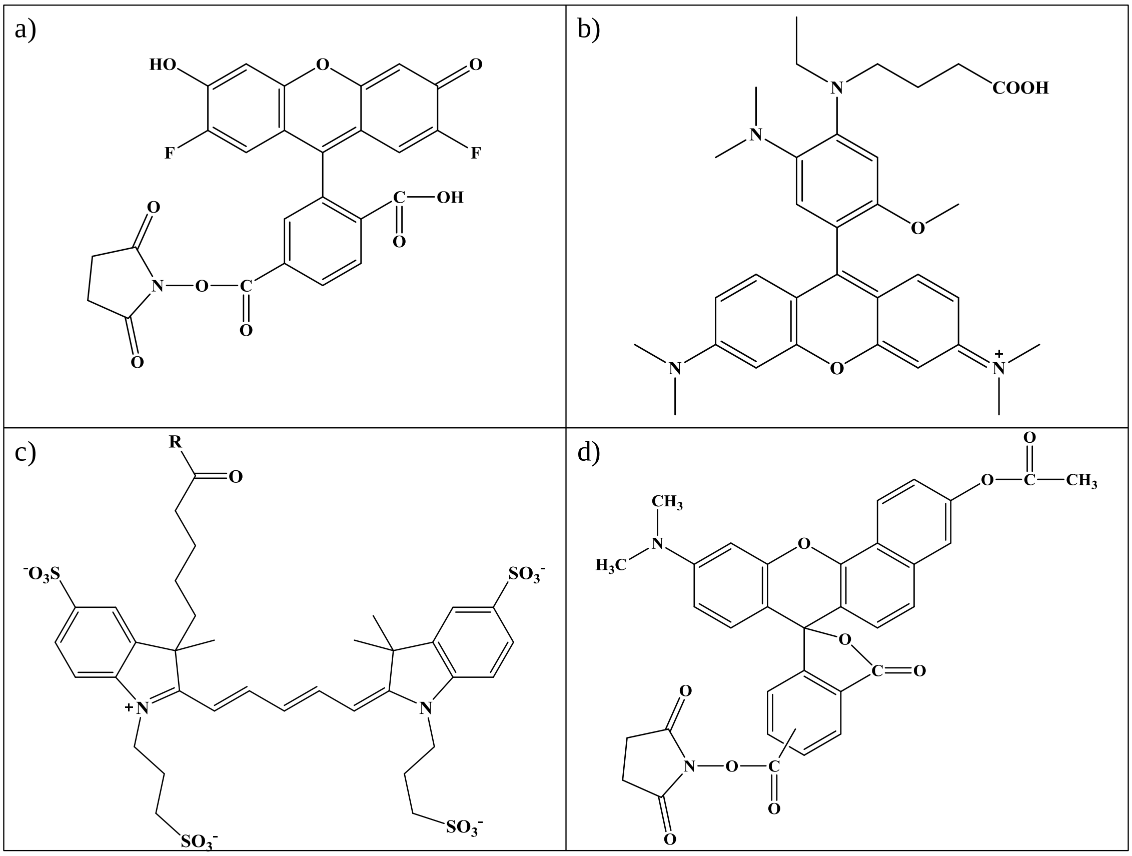

Figure 6-4. Chemical structures of **a) Oregon green** (with NHS derivative), **b)** proposed structure of pHrodo, **c)** proposed structure of Alexa fluor and **d) SNARF** (with NHS derivative).

Subsequently, the second step was to study the behaviour of these pH dependent fluorophores in solution. The fluorescence intensity of the selected fluorophores, 17 µM each in 1 mL of PBS solution was characterized using fluorescence spectroscopy at different values of pH ranging from pH 5-8, as illustrated in **Figure 6-5**. As observed in the case of **Oregon green** (excited at 488 nm), the fluorescence emission intensity at 524 nm increases as the pH increases (**Figure 6-5 a**), whereas for **pHrodo** (excited at 560 nm) there is a decrease in the fluorescence emission intensity at 585 nm with the increase in pH (**Figure 6-5 b**). In the case of **Alexa fluor** (excited at 651 nm), there is no variation in the fluorescence emission (672 nm) at this pH range (**Figure 6-5 c**). On the other hand, **SNARF** (excited at 488 nm) with two fluorescence emission wavelength (590 and 650 nm), one of the emission peak decreases (590 nm) whereas the other increases (650 nm) with the increase in pH, resulting in ratiometric fluorescence (**Figure 6-5 d**).

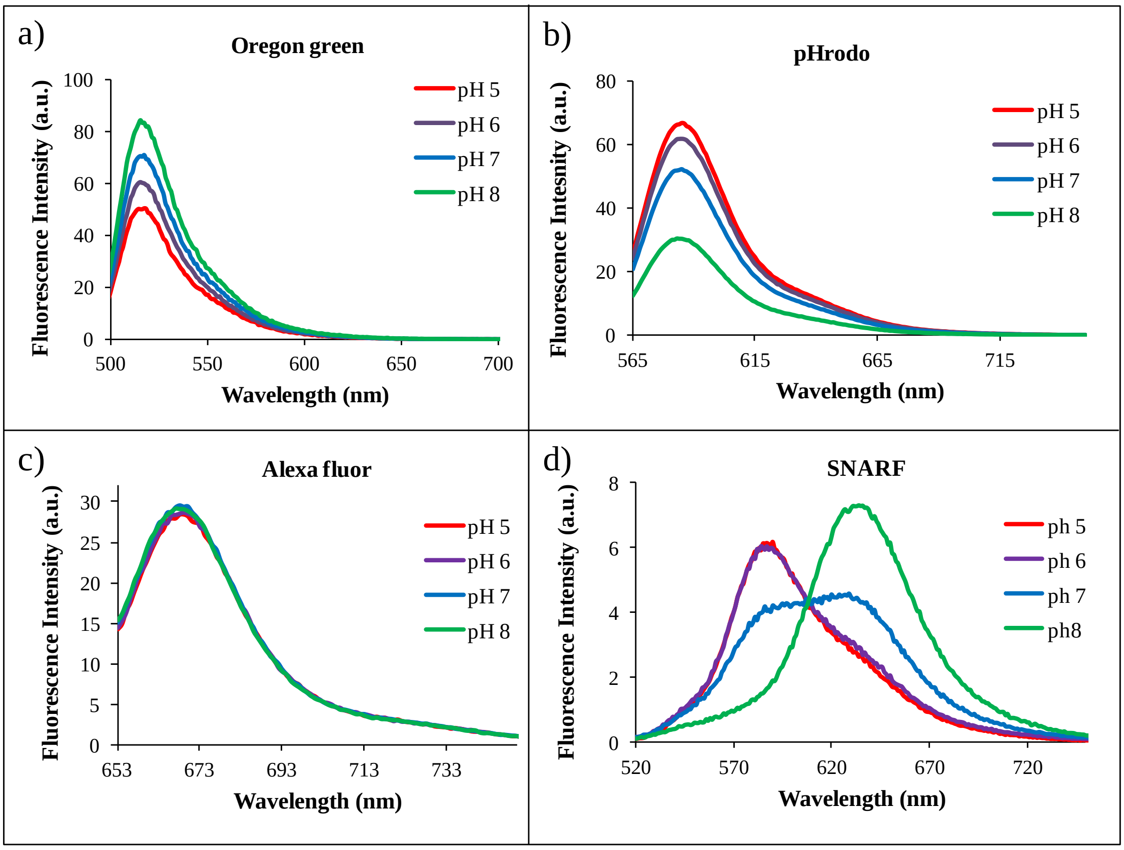

Figure 6-5. Fluorescence emission spectra of **a) Oregon green**, **b) pHrodo**, **c) Alexa fluor** and **d) SNARF** at pH range (5-8).

After examining the behaviour of these fluorophores in solution, the next step was to immobilize them on to the microparticles.

Results and Discussion

6.2. Functionalization of polysilicon surfaces using pH dependent fluorophores

Before using the bi-functional (polysilicon and gold) microparticles, the functionalization was optimized on only polysilicon materials, first surfaces (**Figure 6-6 a**) and then microparticles in suspension (**Figure 6-6 b**). For this reason, silicon surfaces bearing polysilicon microparticles, 3 x 3 µm^2 in size with 500 nm thickness was used, as shown in **Figure 6-6**. These polysilicon microparticles were attached to the silicon surface using a 100 nm thick silicon oxide layer (**Figure 6-6 a**)

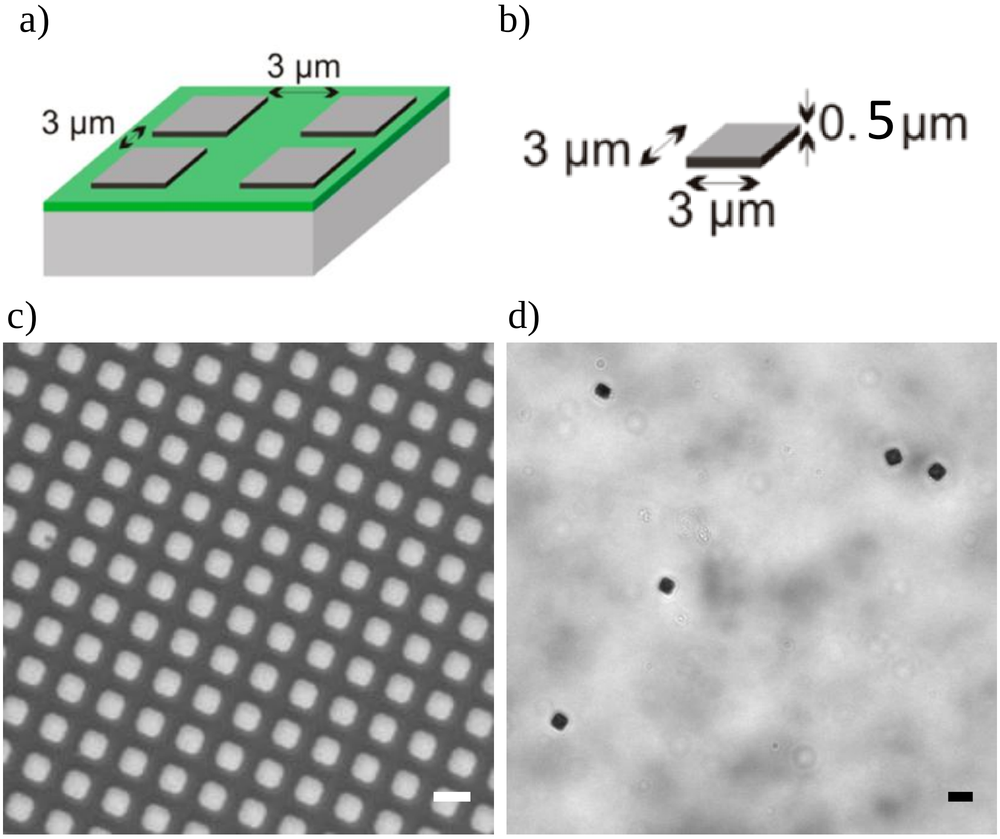

Figure 6-6. Ideal representation of **a)** surfaces incorporating polysilicon microparticles, **b)** microparticles, and bright field images of the polysilicon microparticles c) before and d) after release from the surface. Scale bar – 5 µm.

Thus, the following step was to immobilize and optimize the pH dependent fluorophores on surfaces. Due to the selection of amino reactive fluorophores, incorporating NHS moieties, the surfaces with primary amines were synthesized. Therefore, in order to achieve a monolayer of primary amines, the freshly hydroxylated surfaces using a similar protocol as described (Chapter 5), were treated with an amino silane, 2 % of 3-Aminopropyltriethoxysilane (APTES) for 3 hrs in absolute ethanol. The amino functionalized surfaces were then treated with the NHS ester derivative fluorophores (17 µM in 1 mL of anhydrous DMSO) in order to form stable conjugate amide bond. The hydrolysis of the NHS ester competes with the primary amine reaction. Therefore, all the reactions were performed in anhydrous conditions. **Scheme 6-1** shows the sequence of surface chemistry followed for the immobilization of the pH dependent fluorophores. The functionalized surfaces were finally washed with anhydrous DMSO and dried under nitrogen.

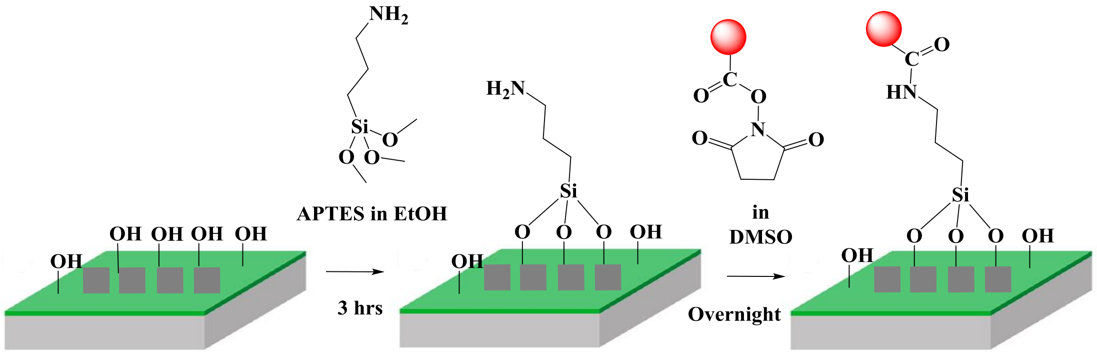

Scheme 6-1. Stepwise immobilization of pH dependent fluorophores.

The functionalized surfaces were initially characterized using contact angle measurements in order to differentiate the monolayers formed at each step of the functionalization. **Table 6-1** shows the contact angle values obtained after every treatment. The surfaces initially provided had a higher contact angle value of 39 ° due to the adsorption of dust particles on to the surfaces. This value after hydroxylation decreased to 8 ° confirming the existence of hydroxyl groups on the surface and resulting in a hydrophilic surface. These surfaces when treated with APTES solution became more hydrophobic, 45 ° due to the formation of monolayers of primary amines, which corresponds to the value reported in the literature [257]. The contact angle value increased to 75 ° due to the increase in the hydrophobicity of the surface on immobilization of the pH dependent fluorophores. A similar contact angle value of 75 ° was obtained for all the fluorophores [301-303].

Table 6-1. Contact angle values obtained after each step of functionalization.

Sample Name	Contact angle ϴ (⁰)
Initial surface	39 ± 2
After Activation	8 ± 1
After APTES	45 ± 3
After Fluorophore NHS	75 ± 1

The functionalized surfaces were further characterized using fluorescence microscopy. **Figure 6-7** shows the fluorescence images of the surfaces functionalized with **a) Oregon green**, **b) pHrodo**, **c) Alexa fluor** and **d) SNARF**. As observed from the figure, the fluorescence was brighter on the silicon oxide base rather than the polysilicon microparticles. This is due to the difference in the surface reactivity between the two different materials, polysilicon and silicon oxide, as explained in Chapter 4. As the reactivity of silicon oxide is higher than polysilicon, the fluorescence from the microparticles is lower when compared to the background.

In the first case (**Figure 6-7 a**), surfaces functionalized with **Oregon green**, showed homogenous fluorescence. The average fluorescence intensity was about 40 a.u.(gray value) on silicon oxide and 15 a.u. on polysilicon. Whereas, in the case of **pHrodo** (**Figure 6-7 b**), the fluorescence intensity observed was very low, 20 a.u. on silicon oxide and 4 a.u. on polysilicon. This decrease in the fluorescence intensity could be due to the lower fluorescence emission of pHrodo at higher pH. This correlates as the surfaces were last washed with DMSO (> pH 6). Inspite of having lower fluorescence, the functionalization was uniform and homogenous.

In the case of **Alexa fluor** (**Figure 6-7 c**), due to its far red emission wavelength, the functionalized surfaces were characterized using confocal microscopy. From the fluorescence image, we could see that the average fluorescence intensity on silicon oxide is much higher (60 a.u.) when compared to the first two cases. From the surface plot, as shown in **Figure 6-7 d)**, the functionalization on the surfaces was not homogenous. Also, no fluorescence was observed from the polysilicon microparticles.

On the other hand, surfaces functionalized with **SNARF** showed homogenous fluorescence (**Figure 6-7 d**). The average fluorescence intensity observed on silicon oxide was about 60 a.u. and 20 a.u. in the case of polysilicon microparticles. Although it is important to note that this ratiometric fluorophore consists of an additional acetate functional group, which shows fluorescence only on hydrolysis of the acetate group. Nevertheless we observe high fluorescence emission from the functionalized surface, illustrating the unstability of these acetate groups upon immobilization on surfaces. This implies that these groups can be easily hydrolyzed.

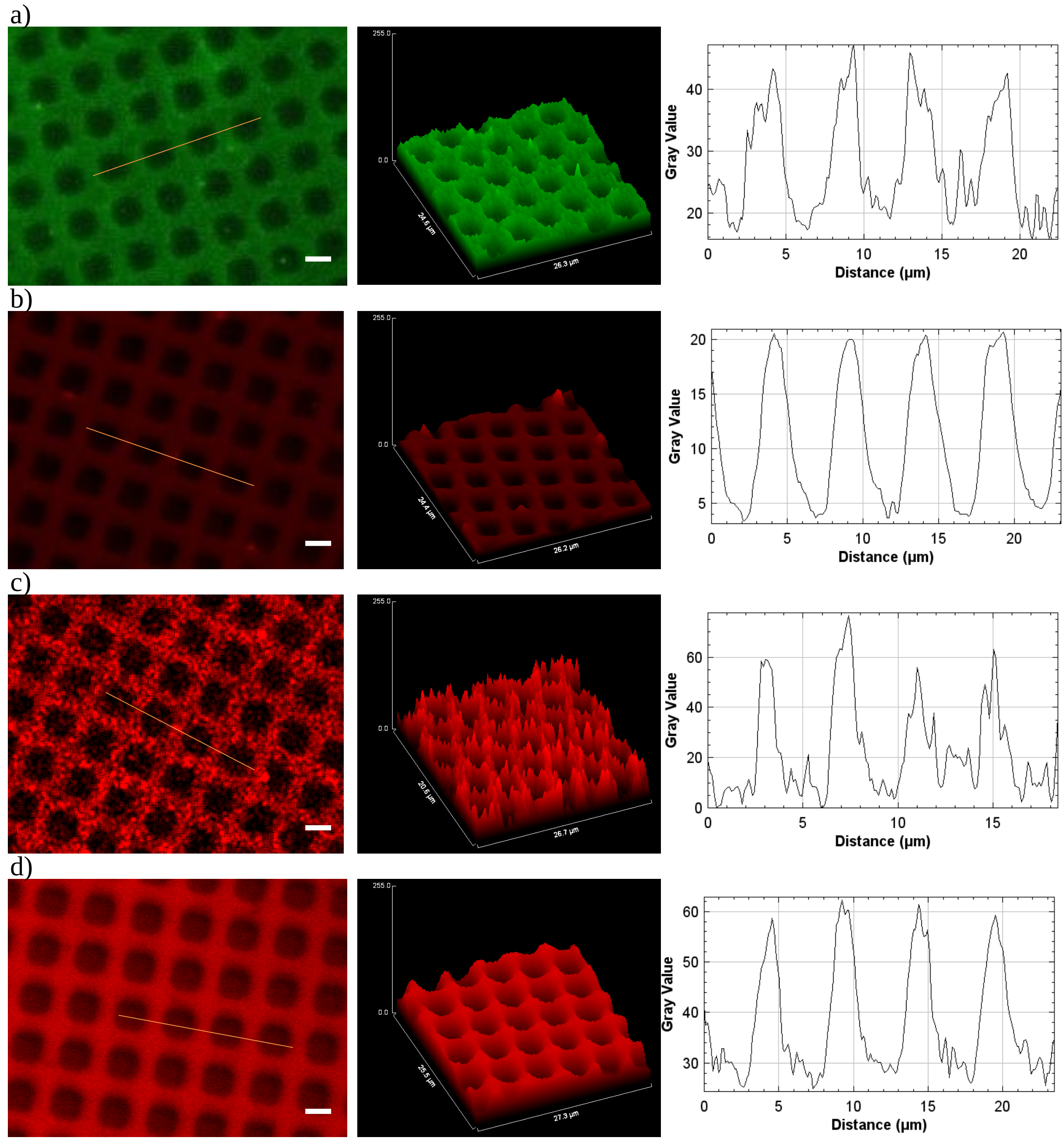
a)
255.0
0.0
24.6 µm
26.3 µm
Gray Value
40
30
20
0
5
10
15
20
Distance (µm)
b)
255.0
0.0
24.4 µm
26.2 µm
Gray Value
20
15
10
5
0
5
10
15
20
Distance (µm)
c)
255.0
0.0
20.6 µm
26.7 µm
Gray Value
60
40
20
0
0
5
10
15
Distance (µm)
d)
255.0
0.0
25.5 µm
27.3 µm
Gray Value
60
50
40
30
0
5
10
15
20
Distance (µm)

Figure 6-7. Fluorescence images of surfaces functionalized with **a) Oregon green**, **b) pHrodo**, **c) Alexa fluor** and **d) SNARF** with their 3D surface plot and plot profiles. Scale bar – 3 µm.

On analysing these results, it shows that **Oregon green** and **pHrodo** were the most suitable pH dependent fluorophores for immobilization. And thus, were further selected for functionalization on the microparticles.

Functionalization on polysilicon microparticles

The polysilicon microparticles in suspension were functionalized using the protocol established on surfaces, for immobilizing **Oregon green** and **pHrodo**. As the microparticles are in suspension, it is important to mention that all the functionalization steps were carried out in an eppendorf. During the functionalization, at each step the microparticles were centrifuged in order to change the previous solution to a new one. Thus, additional parameters such as volume of each solution, microparticle aggregation, speed and time of centrifugation were taken into account. **Figure 6-8** shows bright field and fluorescence images of microparticles treated with 2 % APTES for 3 hours in 100 µL of absolute ethanol, followed by overnight incubation in 17 µM of **Oregon green**/**pHrodo** in 100 µL of anhydrous DMSO, which were characterized using fluorescence microscopy.

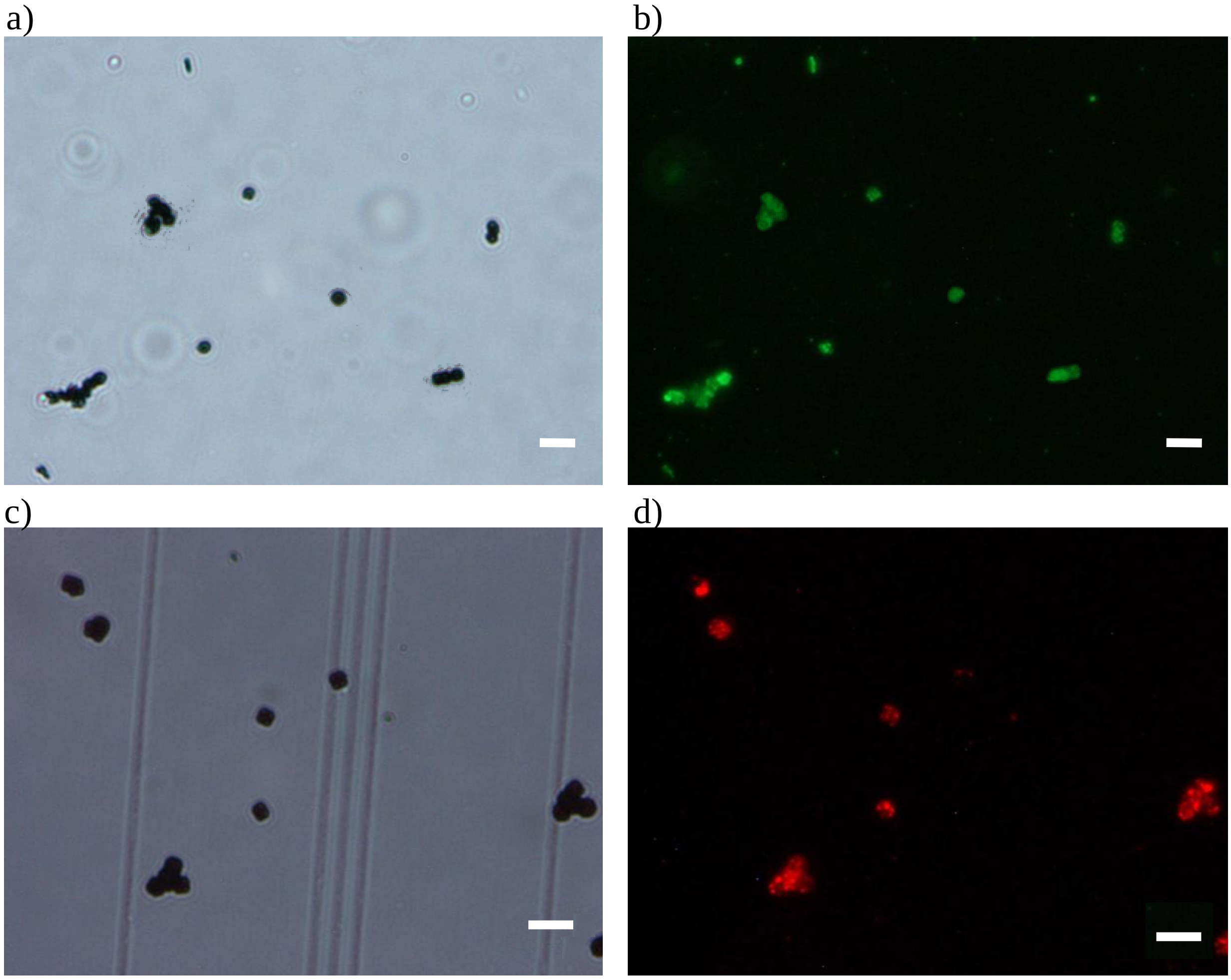

Figure 6-8. Microparticles functionalized with **Oregon green** at pH 7 **a)** bright field and **b)** fluorescence image; and **pHrodo** at pH 5 **c)** bright field image and **d)** fluorescence image. Scale bar – 10 µm.

In order to analyze the homogeneity in functionalization, the microparticles were suspended in corresponding pH solutions in order to see the enhancement of the fluorescence. Therefore, **Oregon green** functionalized microparticles were suspended in PBS (pH 7) and **pHrodo** functionalized microparticles in PBS (pH 5) solution, both exhibiting maximum fluorescence. **Figures 6-9** illustrates the 3D surface plot and mean plot profile of the microparticles functionalized with **Oregon green** and **pHrodo**. The mean plot profile was measured by always taking into account 10 representative functionalized microparticles. From the graphs below, the functionalization on the microparticles appears to be non-homogenous. The average fluorescence intensity in the case of **Oregon green** is about 40 a.u. (grey value), which is similar to **pHrodo** 45 a.u. (grey value). Thus, both displaying maximum fluorescence intensity at their respective pHs.

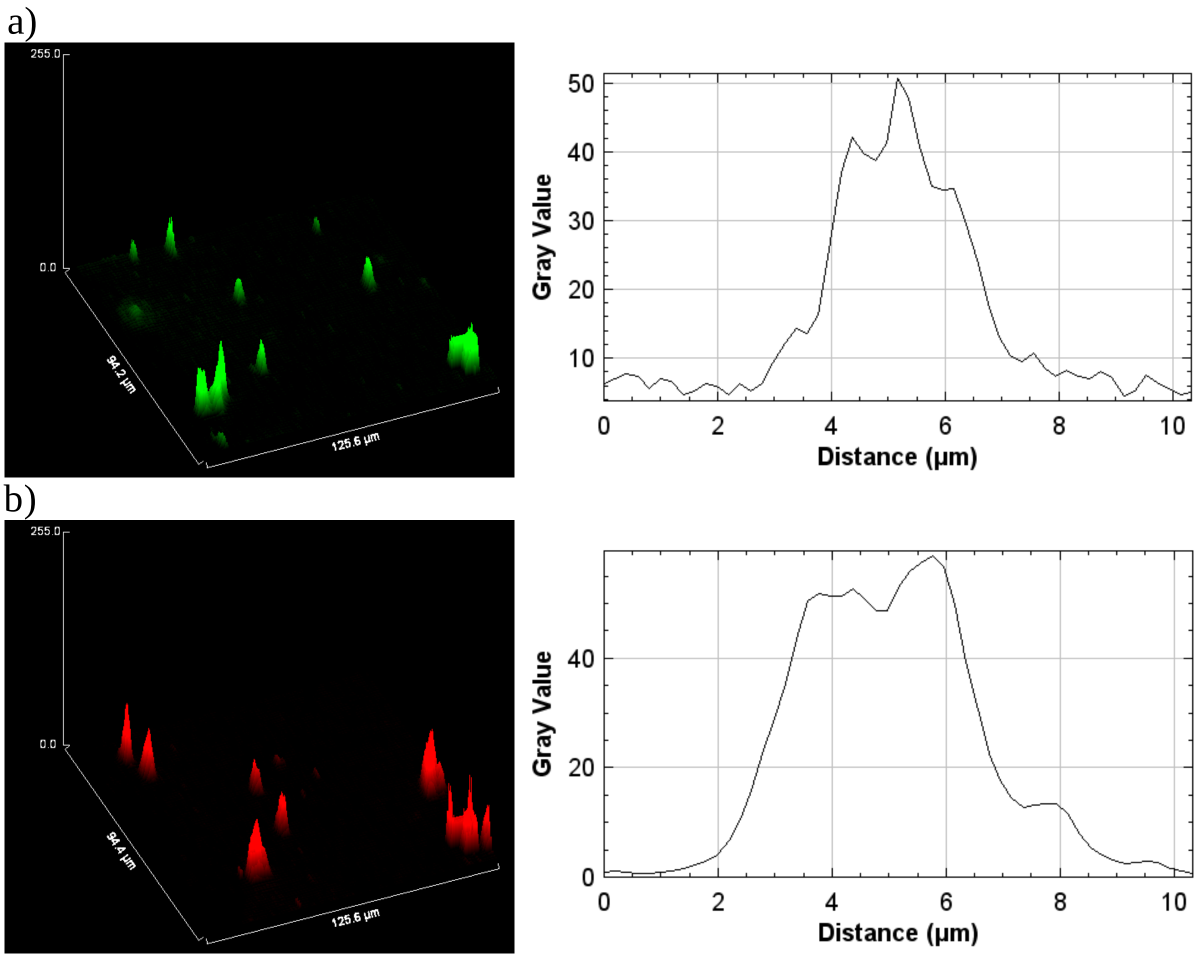

Figure 6-9. 3D surface plot and mean plot profiles of microparticles functionalized with **a) Oregon green** at pH 7 and **b) pHrodo** at pH 5.

Consequently, after establishing a successful protocol to functionalize the polysilicon microparticles with both the pH dependent fluorophores, the next step was to study the behaviour of the fluorophores on the gold surface.

6.3. Functionalization of gold surfaces using phrodo

We attempted the immobilization of **pHrodo** on gold surfaces (1x1 cm^2 in size) [304]. In this case, thiols were used as a linker molecule to immobilize the amine reactive **pHrodo** on to the gold surface. Two different thiols with primary amine in its terminal groups were selected: cysteamine, having short chain length (2 C) and 11-amino undecanethiol (AUT) with longer alkyl chain length (11 C). These two thiols were selected in order to study the influence of the chain length on the gold surfaces upon functionalization. Thus, the surfaces were first treated with either of the two thiols cysteamine and AUT (25 mM, 1 mL) in absolute ethanol for 3 hrs, resulting in the formation of a monolayer of primary amines, **Scheme 6-2**. Amino functionalized gold surfaces were then treated with the NHS ester derivative of **pHrodo** in order to form a stable amide bond.

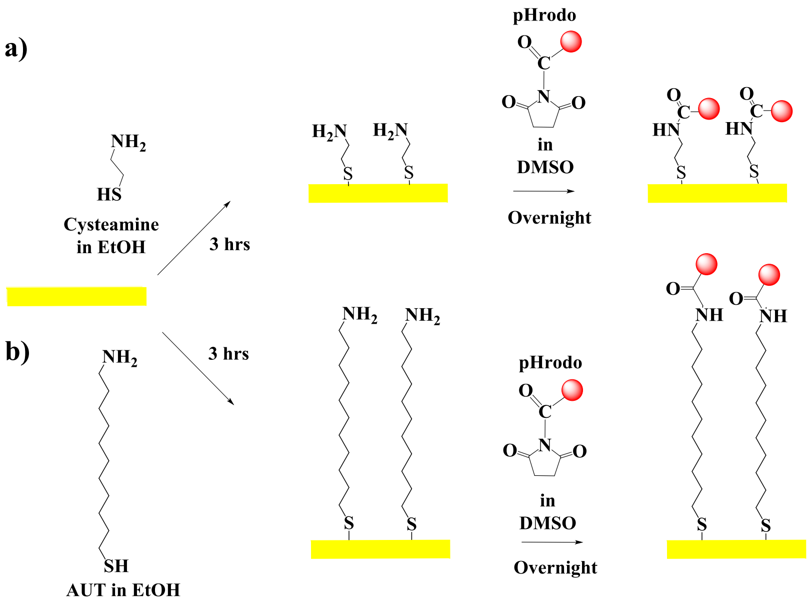
a)
pHrodo
O
C
N
O
O
in
DMSO
Overnight
NH2
HS
Cysteamine
in EtOH
3 hrs
H2N
S
HN
b)
NH2
SH
AUT in EtOH
3 hrs
NH2
S
pHrodo
in
DMSO
Overnight
NH

Scheme 6-2. Stepwise immobilization of **pHrodo** on a gold surface using **a)** cysteamine and **b)** AUT.

The functionalized surfaces were then characterized using fluorescence microscopy on the pH range (5-7). **Figure 6-10** shows the fluorescence images of **pHrodo** functionalized surfaces using cysteamine as a linker molecule.

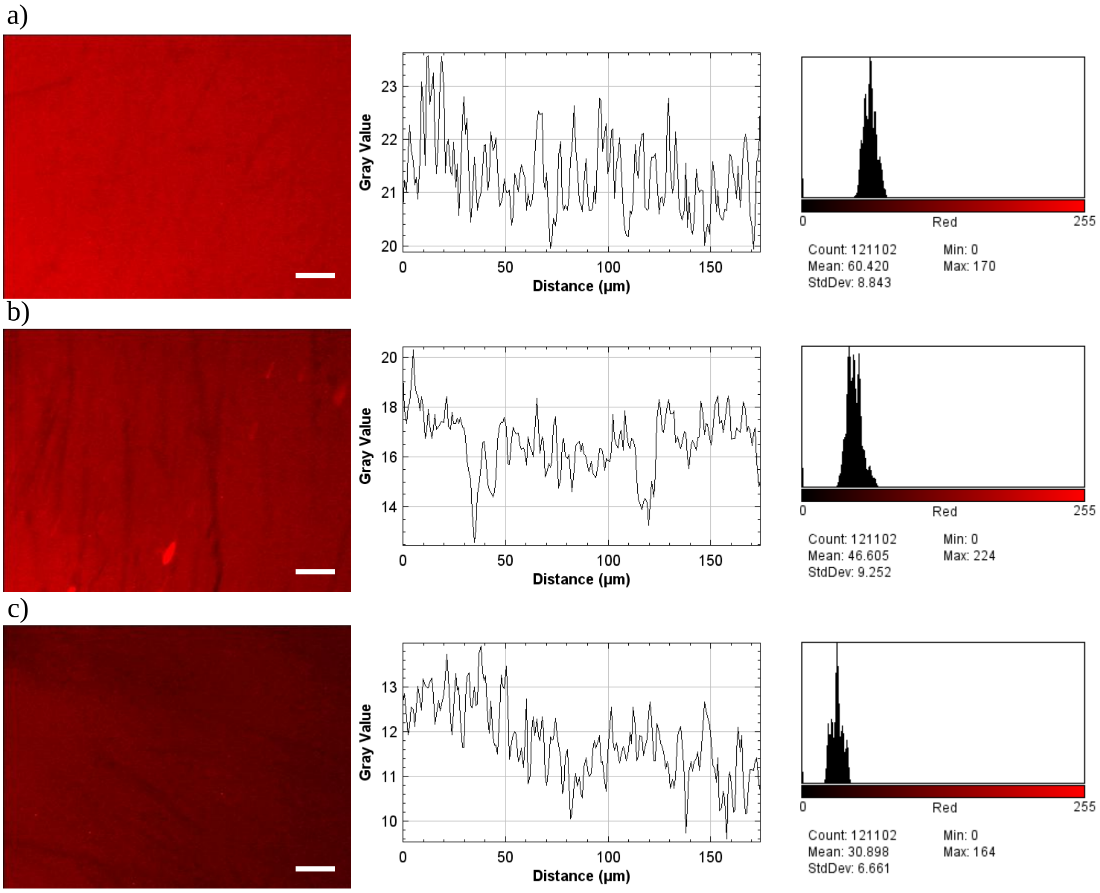

Figure 6-10. Fluorescence images of **pHrodo** functionalized gold surfaces using cysteamine at **a)** pH 5, **b)** pH 6 and **c)** pH 7; with their plot profiles and histogram. Scale bar – 30 µm.

From the images acquired, there is a noticeable difference in the fluorescence intensity with respect to pH. The surface at pH 5 shows higher fluorescence correlating to the behaviour of **pHrodo** exhibiting higher fluorescence emission at lower pH value. From the plot profiles, the functionalization on the surfaces appears to be uniform and homogenous. Additionally, the measured mean fluorescence intensity of the surfaces is also demonstrated in the histogram, a decrease in the mean fluorescence intensity is observed from pH 5 to pH 7.

On the other hand, **Figure 6-11** shows the fluorescence images of gold surfaces functionalized with **pHrodo** using AUT at pH 5, 6 or 7. Similar to what it was observed in the previous case, the fluorescence intensity was higher at pH 5, which decresed with the increase in the pH, although no much significant difference was observed at pH 6 and pH 7. The functionalization using AUT was as well homogenous and uniform, as shown in the plot profiles.

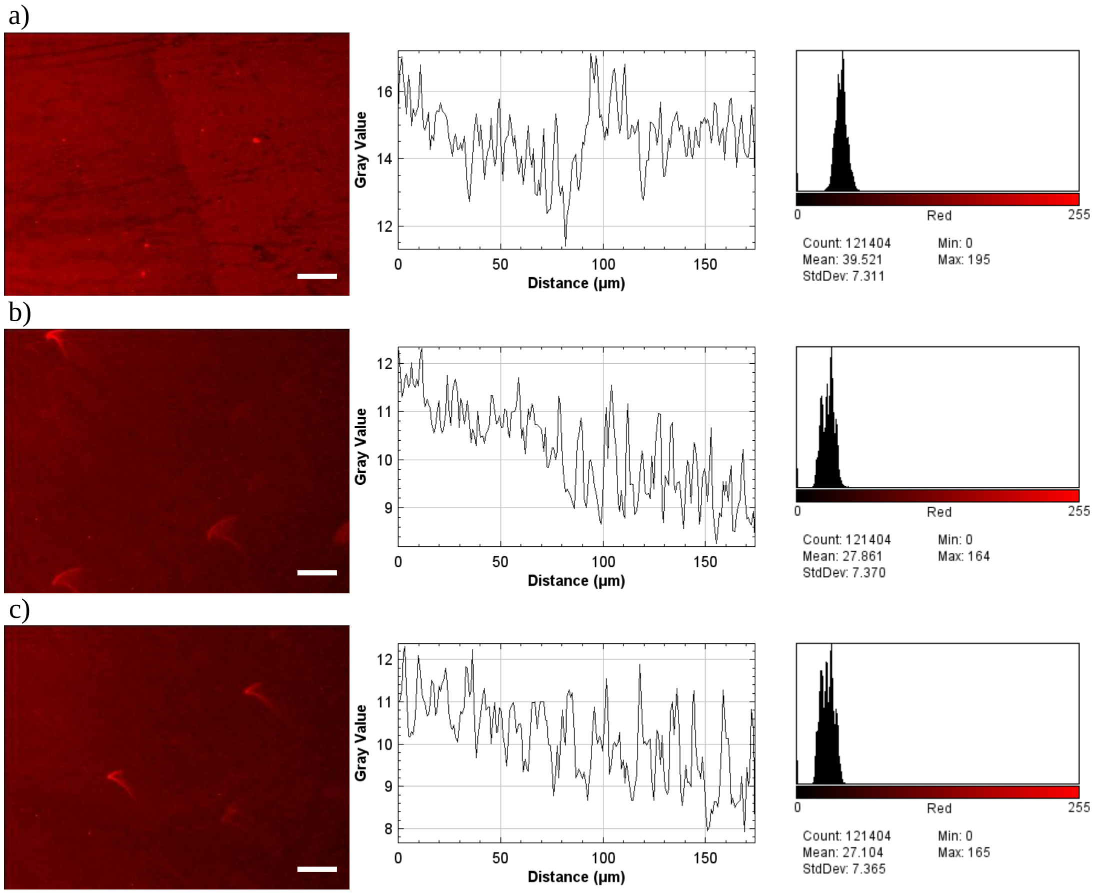

Figure 6-11. Fluorescence images of **pHrodo** functionalized gold surfaces using AUT at **a)** pH 5, **b)** pH 6 and **c)** pH 7; with their plot profiles and histogram. Scale bar – 30 µm.

Considering the results obtained, there is an influence in the chain length of the linker used to immobilize the **pHrodo** on to the gold surface. This could be due to the entanglement of the **pHrodo** molecule between the chains of the AUT and therefore, not being available for protonation or deprotonation with respect to different pH. Hence, exhibiting similar fluorescence.

Consequently, the linker cysteamine was selected for functionalization of gold of bi-functional microparticle.

6.4. Functionalization of bi-functional surfaces and microparticles using Oregon green and pHrodo

After studying the different strategies to immobilize the pH dependent fluorophores on both polysilicon and gold surfaces, the next step was to examine the bi-functionalization of the pH dependent fluorophores. Bi-functionalization was first tested on surfaces and then carried out on microparticles. **Figure 6-12** shows the SEM micrographs of bi-functional surface and microparticles made up of polysilicon and gold.

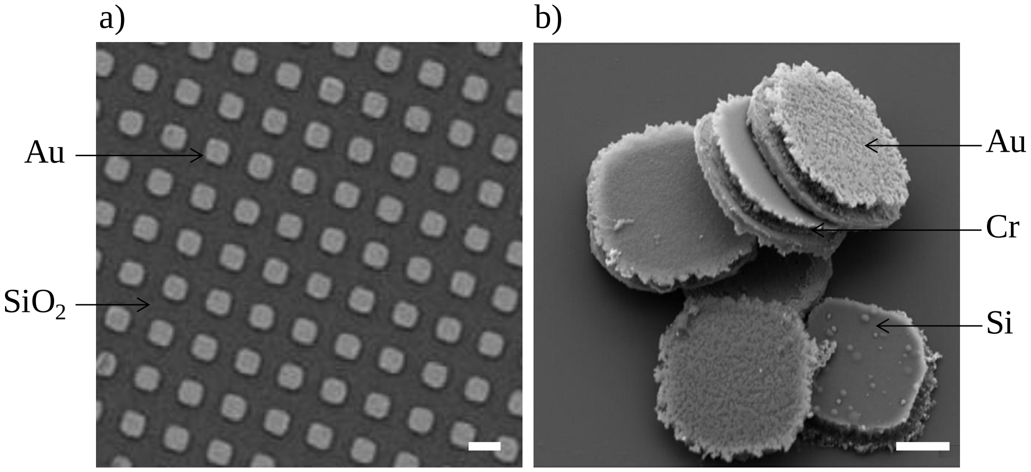

Figure 6-12. SEM micrographs of bi-functional **a)** surface and **b)** microparticle. Scale bar – 5 and 1 µm, respectively.

Figure 6-12 a) shows the silicon oxide surface bearing bi-functional microparticles, gold (top) and polysilicon (bottom) microparticles, linked by a thin layer of chromium. Here only the side of gold microparticle is visible, whereas the polysilicon side is hidden below the gold surface, explained in Appendix, Section 2. Thus, while characterizing the functionalization on bi-functional surfaces, the fluorescence on silicon oxide layer was studied, below the microparticles rather than the polysilicon surface. On the other hand, **Figure 6-12 b)** shows the image of released bi-functional microparticles from the surface. The different regions (polysilicon and gold) of the bi-functional microparticle are indicated in the **Figure 6-12 b)**.

Scheme 6-3 shows the stepwise immobilization of two selected fluorophores on a bi-functional surface. After cleaning and activation of the silicon surface, the gold surface is functionalized prior to the silicon surface. This step is preferred due to the high reactivity of the gold surface than silicon surface. Thus, by functionalizing the gold surface already with a desired molecule will avoid the contamination of the gold surface during the functionalization procedure. **pHrodo** was chosen to be immobilized first, due to the rhodamine derivative which is highly stable and thus can withstand the mechanical stress that the microparticle undergoes during functionalization [295-296]. On the other hand, **Oregon green**, a fluorescein derivative was chosen to be immobilized on to the silicon surface. Therefore, the freshly cleaned surfaces are treated with cysteamine solution to form a monolayer of primary amines to react with the NHS esters of the **pHrodo**. The next step was to functionalize the silicon oxide surface, by treating with APTES. This step resulted in the formation of free terminal amino groups ready to bond with the reactive group, NHS ester derivative of the **Oregon green**.

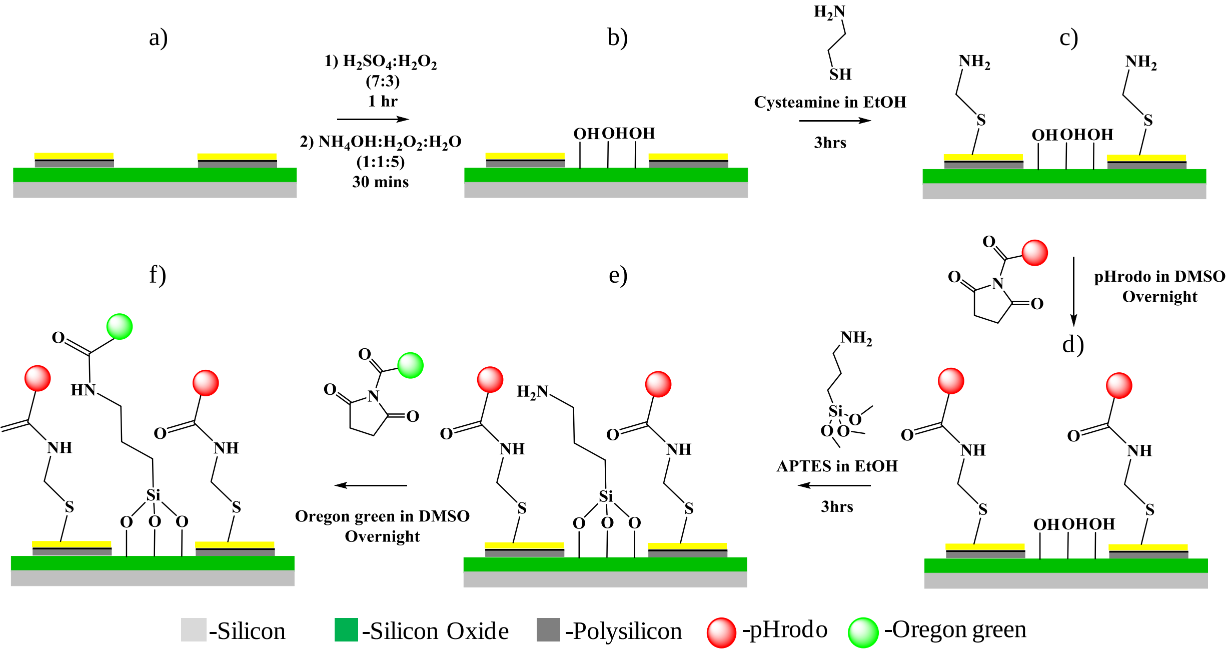
a)
1) H2SO4:H2O2
(7:3)
1 hr
2) NH4OH:H2O2:H2O
(1:1:5)
30 mins
b)
OH OH OH
H2N
SH
Cysteamine in EtOH
3hrs
c)
NH2
S
pHrodo in DMSO
Overnight
d)
NH
O
N
APTES in EtOH
3hrs
e)
H2N
Si
Oregon green in DMSO
Overnight
f)
HN
-Silicon
-Silicon Oxide
-Polysilicon
-pHrodo
-Oregon green

Scheme 6-3. Stepwise representation of bi-functionalization of **pHrodo** and **Oregon green** on a bi-functional surface.

Characterization of the functionalized surfaces was achieved using fluorescence microscopy. **Figure 6-13** shows the fluorescence image of a surface, green emission from **Oregon green**, red emission from **pHrodo** and their superimposed images showing fluorescence from both **Oregon green** and **pHrodo**. From the plot profiles of the bi-functionalized surfaces, functionalization of gold surface using **pHrodo** appeared uniform and homogenous. Whereas, in the case of **Oregon green** immobilization, some aggregates of the fluorophore were seen.

Despite of homogenous fluorescence observed from **Figure 6-13 (a) and (b)** the superimposed image **(c)** shows the overlapping of the two fluorescence, green and red. This could be due to the immobilization of the fluorophores on the non-desired surface. As both the surfaces, polysilicon and gold is functionalized with identical functional group (NH_2), the fluorophores might get immobilized on the non-desired surface. This also correlates with the higher fluorescence intensity observed on the gold surface. The higher value of the intensity could be contributed from the **Oregon green** functionalized on the gold surface instead of the silicon oxide. Therefore, resulting in lower fluorescence intensity on the silicon oxide surface.

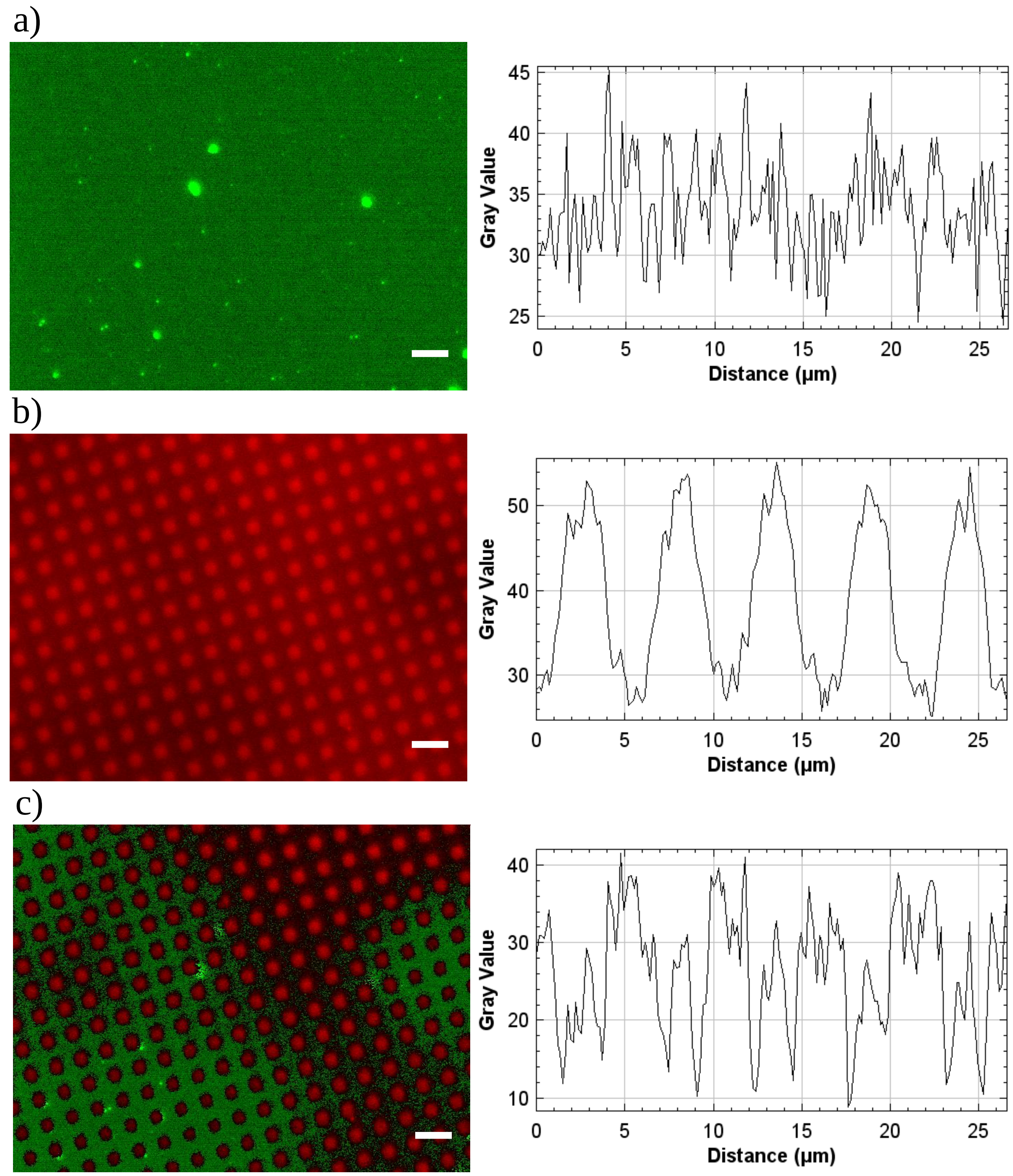

Figure 6-13. Fluorescence images of bi-functionalized surface washed in DMSO, and dried with nitrogen **a)** excited using blue filter (**Oregon green**), **b)** excited using green filter (**pHrodo**) and **c)** superimposed image of (a) and (b); with their plot profiles. Scale bar – 10 µm.

This interchange of the fluorophores could result only if there were still unreacted amino groups after the **pHrodo** immobilization. Thus, in order to avoid this problem, the surfaces were treated with a blocking agent to block the unreacted amino groups after the **pHrodo** immobilization. In this case we used an oligo ethylene glycol, 2-(1-hydroxy)ethoxyeth-1-yl methanesulfonate (EG2OMs) [88]. The chemical structure of the EG2OM is shown in **Figure 6-14**.

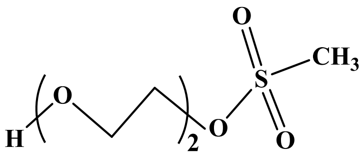

Figure 6-14. Chemical structure of 2-(1-hydroxy)ethoxyeth-1-yl methanesulfonate (EG2OMs).

Subsequently, **Figure 6-15** shows the fluorescence image of a bi-functional surface with **pHrodo** on gold and **Oregon green** on silicon oxide surface, using EG2OMs after the functionalization step of both, pHrodo and Oregon green. The functionalization appears homogenous; the mean average fluorescence intensity for both the cases is around 70 a.u. (grey value). Here, we could still observe some regions with both the fluorescence, but this could be also due to the overpacking of the fluorophores on the surface arising due to the similar chain lengths of the linker on gold and silicon oxide surface.

After these preliminary experiments, the functionalization was tested on the bi-functional microparticles.

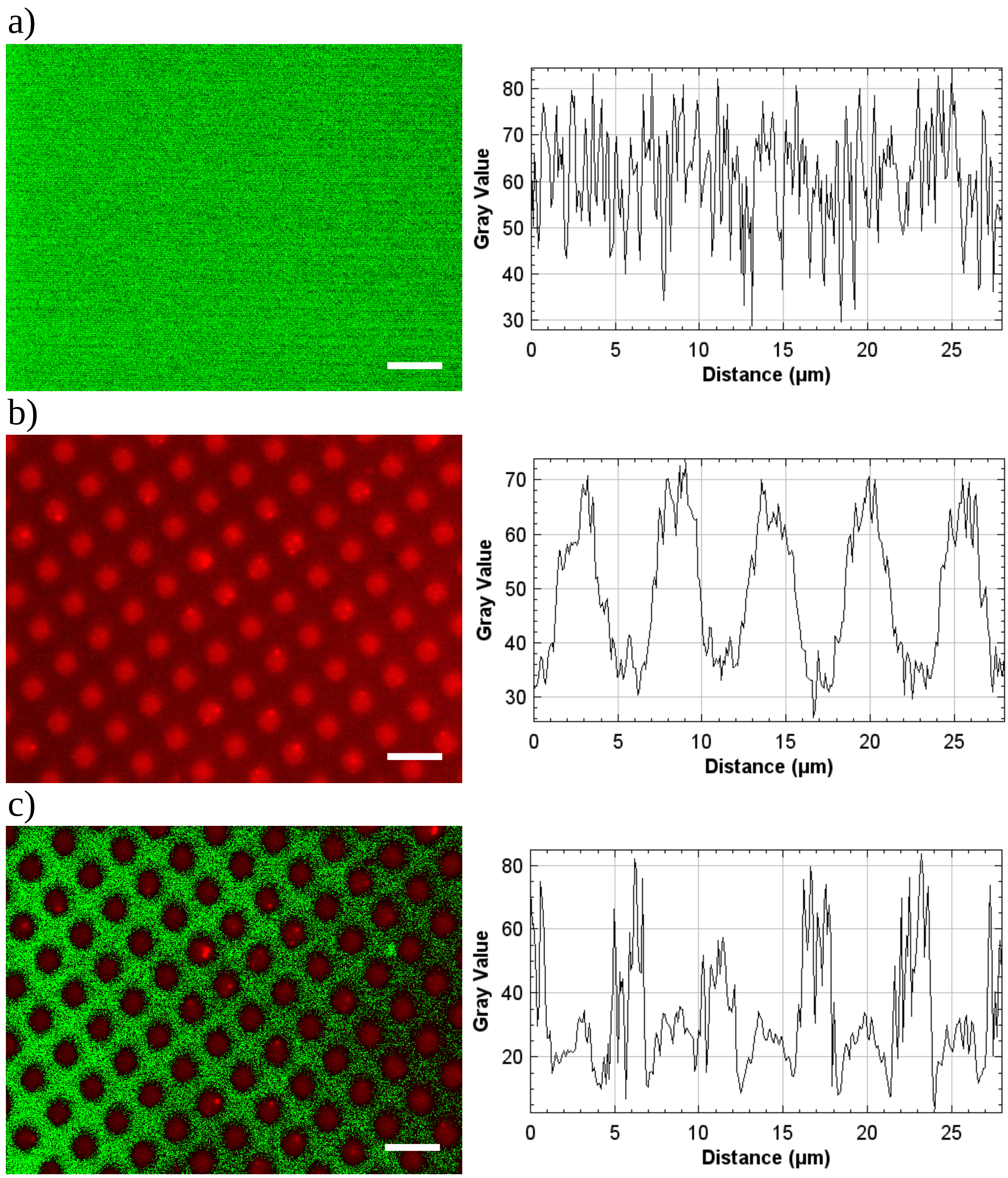
a)
Gray Value
80
70
60
50
40
30
0
5
10
15
20
25
Distance (μm)
b)
Gray Value
70
60
50
40
30
0
5
10
15
20
25
Distance (μm)
c)
Gray Value
80
60
40
20
0
5
10
15
20
25
Distance (μm)

Figure 6-15. Fluorescence images of bi-functionalized surface **a)** excited using blue filter (**Oregon green**), **b)** excited using green filter (**pHrodo**) and **c)** superimposed image of (a) and (b); with their plot profiles. Scale bar – 10 μm.

Bi-functionalization on microparticles

The functionalization was performed on bi-functional microparticles, made up of polysilicon and gold, following a similar protocol used for bi-functional surfaces. Primarily, the bi-functional microparticles were functionalized only on one side of the microparticle, in this case gold, using **pHrodo**. Here, the microparticles were treated with the blocking agent, EG2OMs after the **pHrodo** immobilization. The polysilicon surface of the microparticles was also functionalized with APTES, in order to eliminate any auto fluorescence from the polysilicon surface of the microparticle. The mono-functionalized microparticles were suspended in pH 5 solution and were characterized using fluorescence microscopy, as shown in **Figure 6-16**. It is worth mentioning that as these microparticles consists of two surfaces, either polysilicon or gold on each side, it becomes a challenge to characterize the functionalization on both the sides at the same time using optical fluorescence microscopy.

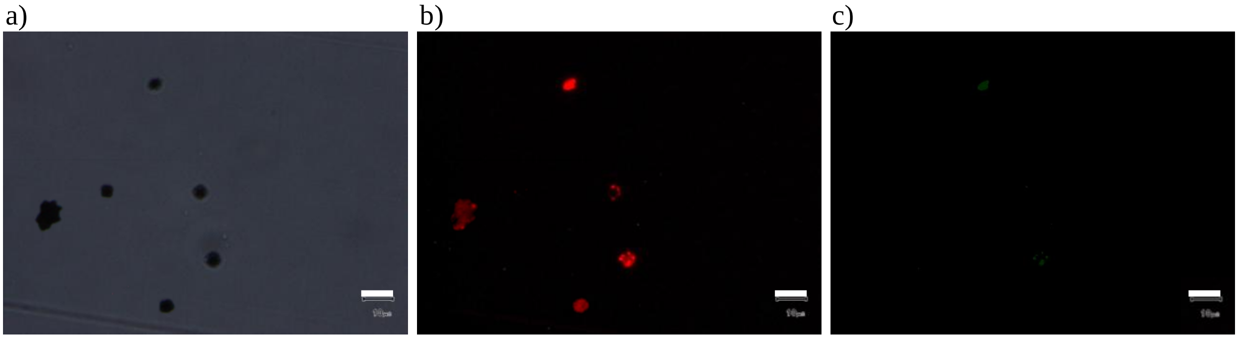

Figure 6-16. Fluorescence images of bi-functional microparticles functionalized only with **pHrodo**, **a)** in bright field, **b)** fluorescence from **pHrodo** using green filter and **c)** excited using blue filter, at pH 5. Scale bar – 10 µm.

Here we could see the red fluorescence from the **pHrodo** immobilized on the gold surface of the microparticles. The functionalization appeared uniform. Whereas, in **Figure 6-16 c)** when excited using a blue filter, no green fluorescence was observed, confirming zero auto fluorescence. On the other hand, we could also observe some microparticles in **Figure 6-16 b)** without any fluorescence. This could be either due to the silicon side of the microparticle facing upwards, thus not being able to see the fluorescence from the gold surface. The 3D surface plot in **Figure 6-17** clearly shows the non-homogenous functionalization on the microparticles. The functionalization appears to be higher on the centre of the microparticle.

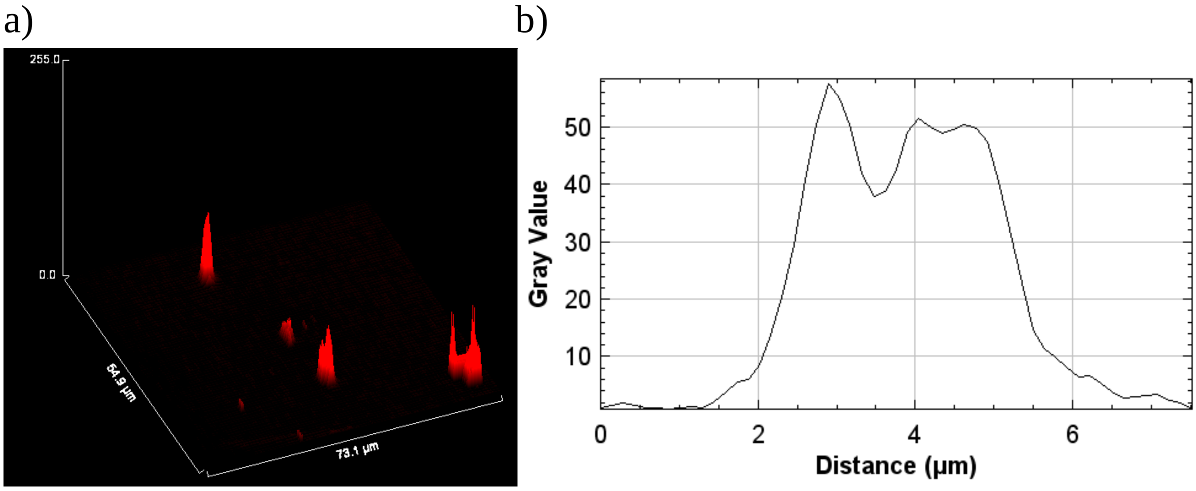

Figure 6-17. 3D surface plot and mean plot profile of bi-functional microparticles functionalized using only **pHrodo**.

The next step was to study the functionalization on the polysilicon surface of the microparticle. In this case, first, the gold surfaces after the cysteamine treatment were blocked using EG2OMs, and then were incubated in the APTES solution to create primary amines on the polysilicon surface. Finally, the microparticles were functionalized with **Oregon green**, as following a sequence schematized in **Scheme 6-4**.

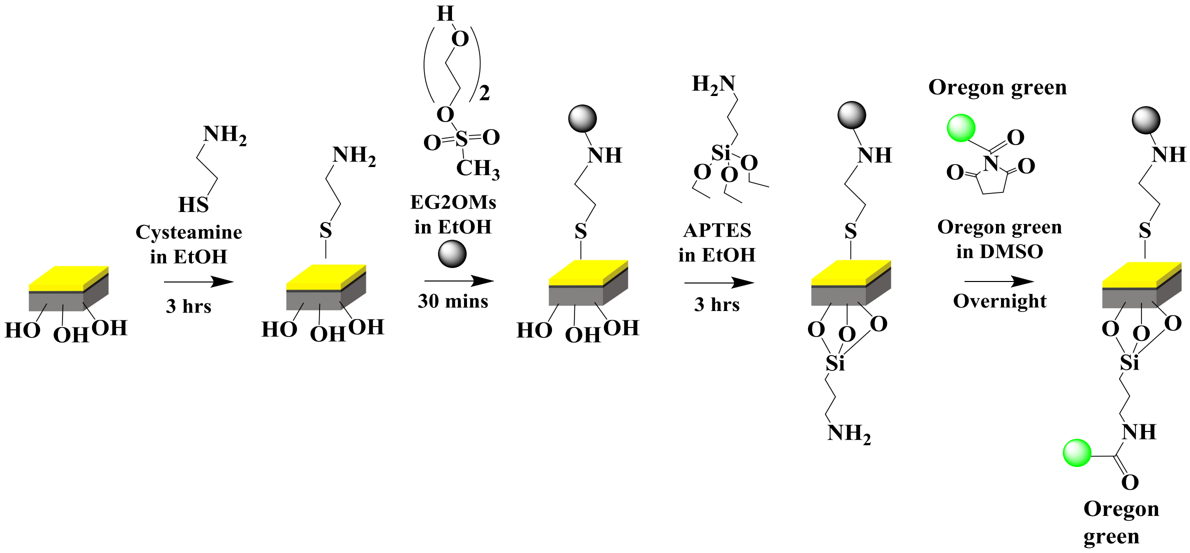
HO OH OH
NH2
HS
Cysteamine
in EtOH
3 hrs
NH2
S
HO OH OH
H
O
2
O
O=S=O
CH3
EG2OMs
in EtOH
30 mins
NH
S
HO OH OH
H2N
Si
O O O
APTES
in EtOH
3 hrs
NH
S
O O O
Si
NH2
Oregon green
O
O N O
Oregon green
in DMSO
Overnight
NH
S
O O O
Si
NH
O
Oregon
green

Scheme 6-4. Schematic representation of bi-functionalization of microparticles with only **Oregon green**.

The **Oregon green** mono-functionalized microparticles were suspended in pH 7 in order to acquire maximum fluorescence intensity from the functionalized microparticles. The fluorescence image below, **Figure 6-18**, confirms the functionalization of the polysilicon side of the microparticle with **Oregon green**. The fluorescence on the microparticles appeared homogenous, although in some microparticles, some aggregates of **Oregon green** were also seen. There was no red fluorescence observed from the microparticles when excited using the green filter.

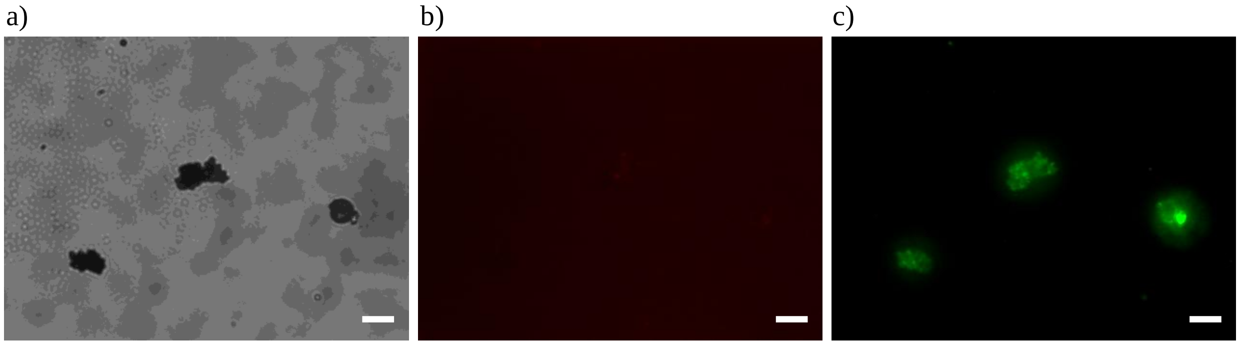

Figure 6-18. Fluorescence images of bi-functional microparticles functionalized only with **Oregon green**, **a)** in bright field, **b)** excited using green filter and **c)** fluorescence from **Oregon green**, at pH 7. Scale bar – 5 µm.

On comparing the 3D surface plot of **Oregon green** functionalized microparticle, **Figure 6-19** to **pHrodo**, the functionalization was more homogenous and uniform throughout the microparticle.

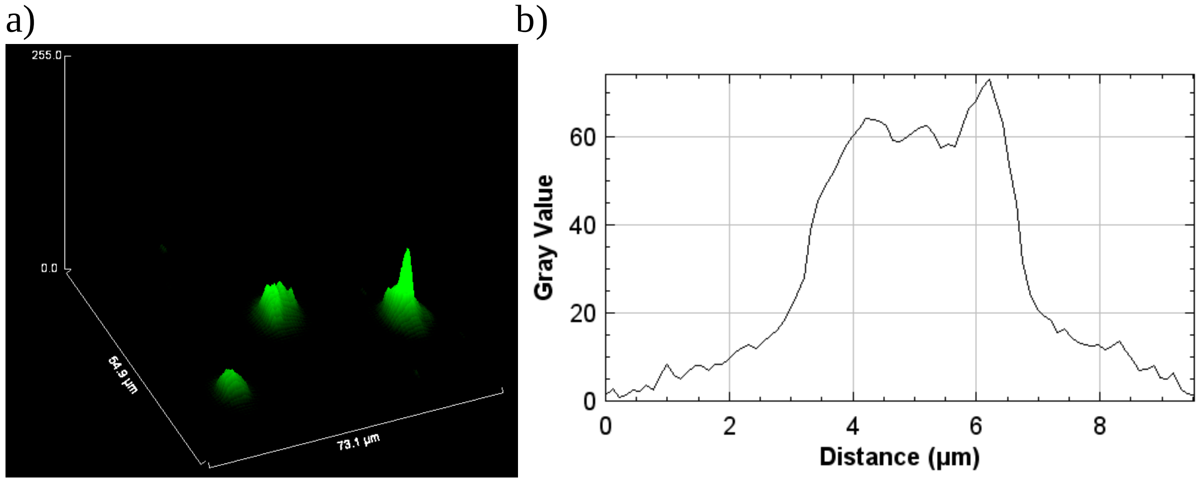

Figure 6-19. 3D surface plot and mean plot profile of bi-functional microparticles functionalized using only **Oregon green**.

Consequently, the final step was to bi-functionalize these microparticles with two pH dependent fluorophores, **pHrodo** and **Oregon green**. **Scheme 6-5** below shows the sequential steps of modifying the surface chemistry at each step of the bi-functionalization.

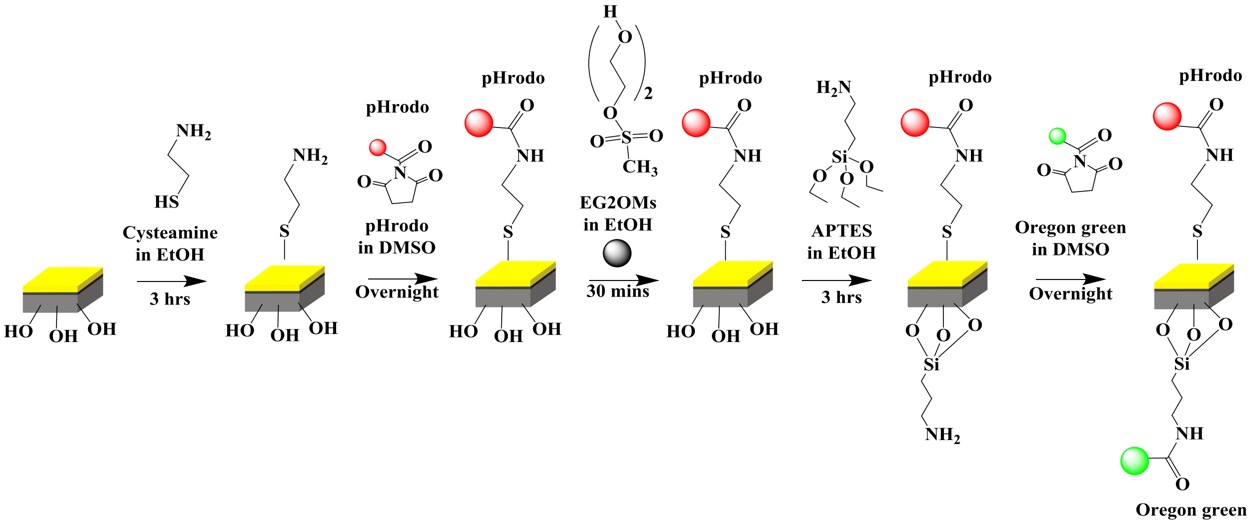

Scheme 6-5. Schematic representation of bi-functionalization of microparticles with **Oregon green-pHrodo**.

The bi-functional microparticles were initially treated with the piranha solution. Thus, the microparticles were treated with cysteamine solution in order to form monolayers of primary amines. The amine functionalized gold microparticles were then immobilized **pHrodo**, due to its higher stability than the **Oregon green** molecule. Therefore, the microparticles were further immobilized with **pHrodo** followed by blocking of the unreacted free amino groups on the gold surface with EG2OMs. After this step, the polysilicon surface was functionalized using APTES creating monolayers of amino groups, which was finally incubated in **Oregon green**.

Finally, the bi-functionalized microparticles were suspended in PBS solution (pH 7) and were characterized using fluorescence microscopy. Neutral pH 7 was chosen, to acquire sufficient fluorescence from both **pHrodo** and **Oregon green** immobilized on the microparticle. From **Figure 6-20**, we observe fluorescence in both red and green, there are some red and some green. There were some microparticles which had higher fluorescence in red, implying the gold surface of the microparticle on the top. Whereas, some microparticles showed higher fluorescence in green, suggesting the polysilicon surface of the microparticle on the top. As these microparticles (3 µm in size) were in suspension, they float around, and were not in contact with objective lens while characterizing in optical fluorescence microscopy. Therefore, sometimes microparticles were not visible in the bright field, but showed fluorescence. Similar case was noted in **Figure 6-20 a)**. No microparticle was observed in the bright field but showed fluorescence in red. Additionally, we could also see some aggregation of the microparticles, which increased the complexity in characterizing these bi-functionalized microparticles.

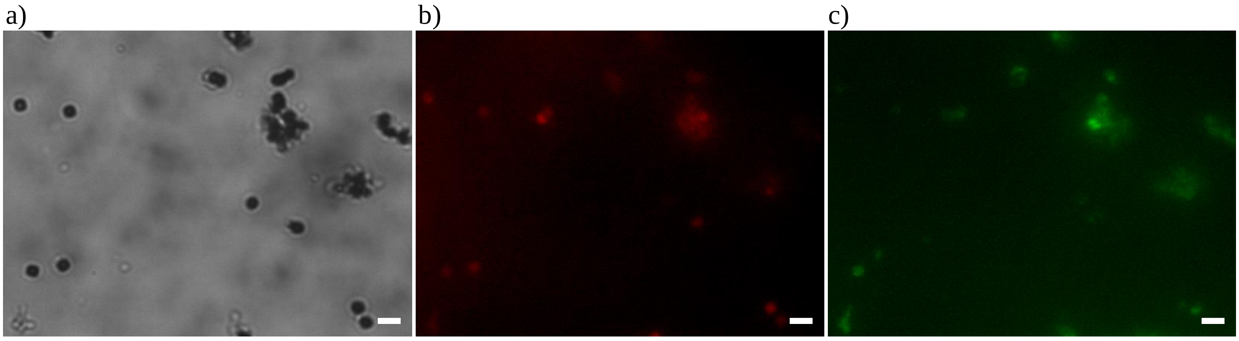

Figure 6-20. Fluorescence images of bi-functional microparticles functionalized with **pHrodo** and **Oregon green**, **a)** in bright field, **b)** fluorescence from **pHrodo** using green filter and **c)** fluorescence from **Oregon green** using blue filter. Scale bar – 5 µm.

The bi-functional microparticles were further characterized using confocal microscopy, **Figure 6-21**. From the image, the intensity between both the fluorophores can be clearly diffrentiated, suggesting which side of the microparticle was on the top.

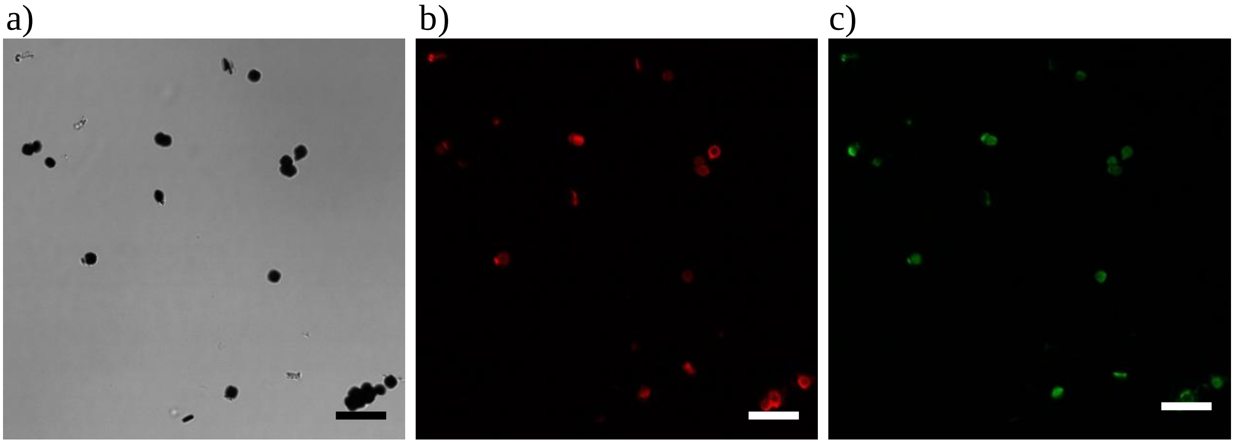

Figure 6-21. Confocal fluorescence images of bi-functionalized microparticles functionalized with **pHrodo** and **Oregon green**, **a)** in bright field, **b)** fluorescence from **pHrodo** and **c)** fluorescence from **Oregon green**. Scale bar – 10 µm.

3D surface plot of the bi-functionalized microparticles, as shown in **Figure 6-22** depicts the non-homogenous functionalization for both the cases **pHrodo** and **Oregon green**. The functionalization appears to be more on the centre of the microparticle. From the plot profile, it is noted that the average fluorescence intensity is higher for **Oregon green** than **pHrodo**. This behaviour corresponds to higher fluorescence emission of **Oregon green** at pH 7.

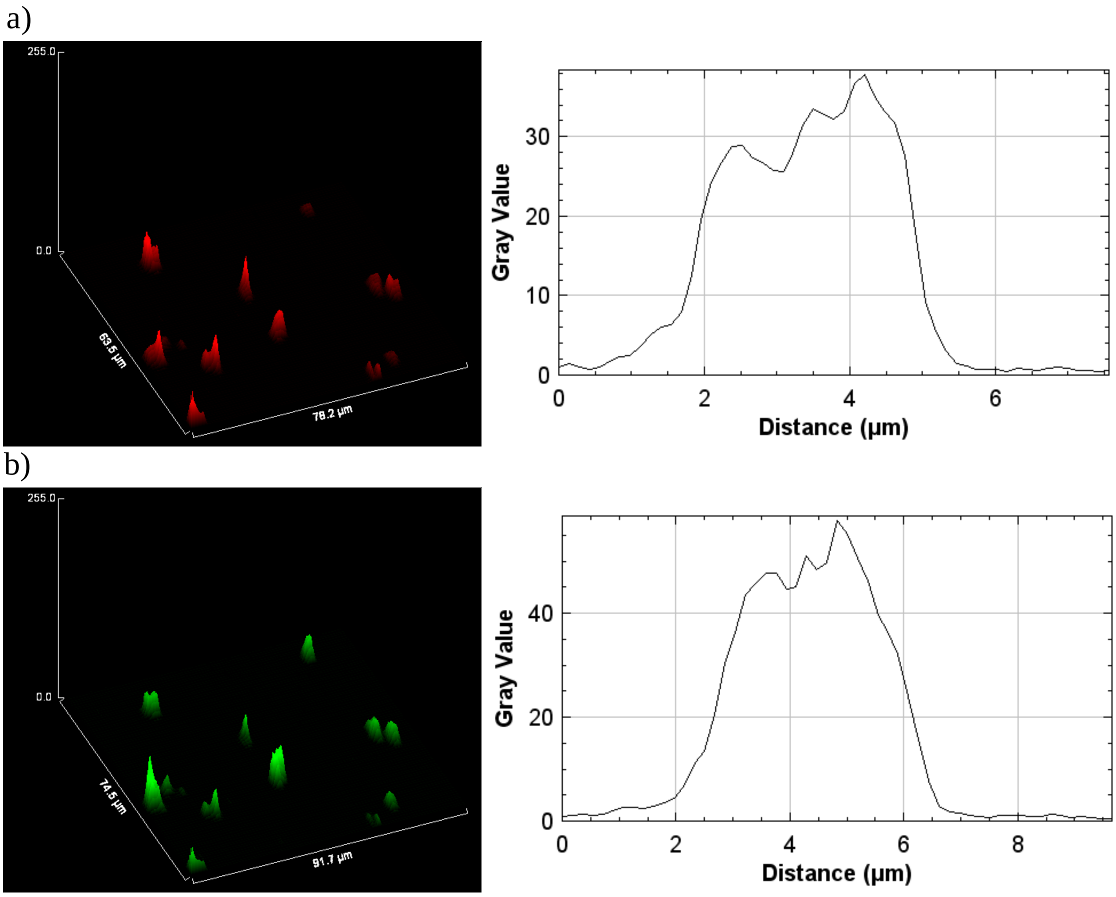

Figure 6-22. 3D surface plot and mean plot profiles of microparticles bi-functionalized with **a) Oregon green** and **b) pHrodo**.

Additionally, the in 3D plot profiles of the bi-functional microparticles were also analyzed in order to study simultaneously both the sides of the functionalized microparticle. **Figure 6-23** shows the fluorescence images obtained using confocal microscopy. **Figure 6-23 a)** shows fluorescence from the **pHrodo**, whereas **b)** shows fluorescence from **Oregon green**. **Figure 6-23 c)** and **d)** shows the fluorescence from the selected microparticles from top and the bottom, respectively. From the 2D image of the selected microparticles (**e-f**), it shows that the microparticles show higher green fluorescence intensity. This result also correlates to the fact that **Oregon green** shows higher fluorescence intensity at pH 7 rather than **pHrodo**. Another hypothesis for showing higher green fluorescence intensity could be due to the density of the microparticles. Polysilicon layer which is 400 nm thick, whereas gold is 100 nm thick. This difference of the density in the microparticles, could result in the polysilicon side of the microparticle to be on the bottom. Thus, when characterized in confocal microscopy, the sample is excited from below, hence showing higher fluorescence from the **Oregon green** immobilized on the polysilicon side of the microparticle.

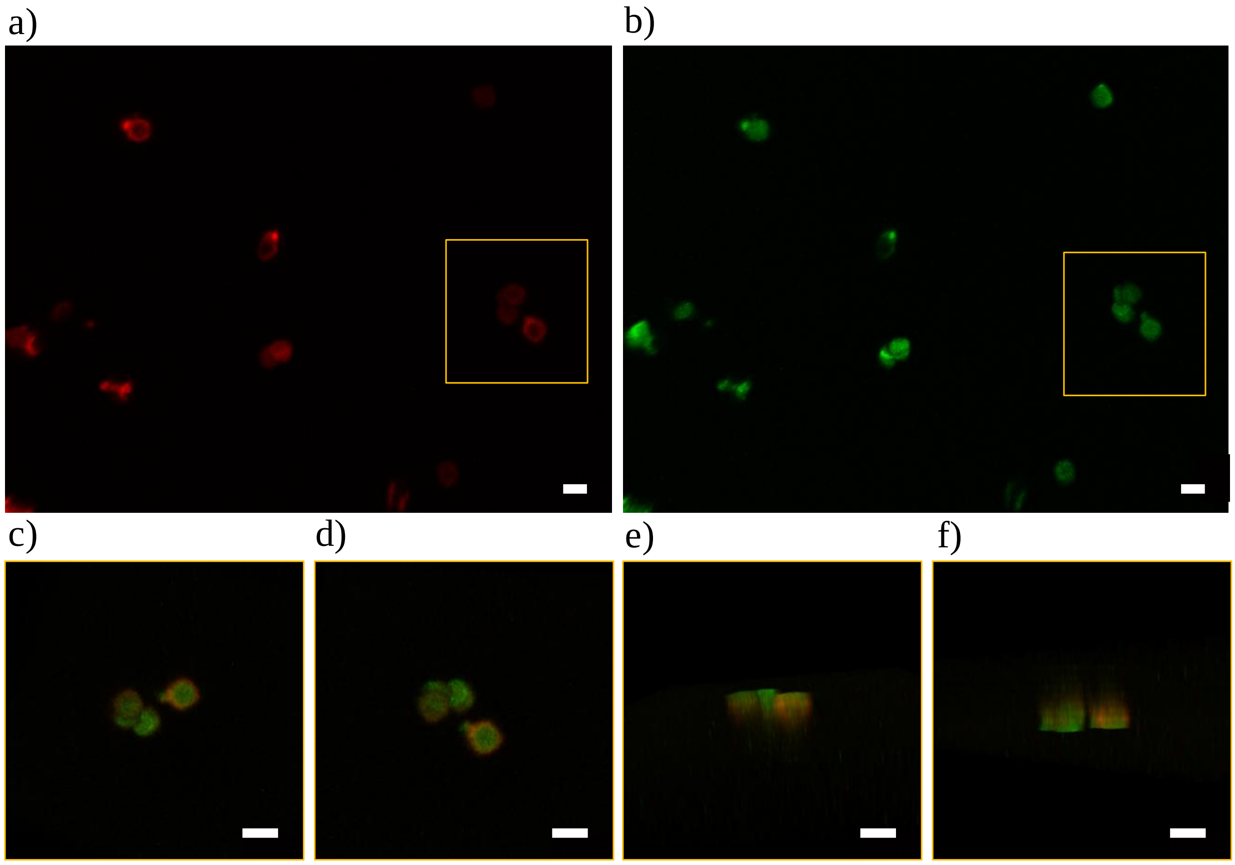

Figure 6-23. Confocal fluorescence images of bi-functional microparticles functionalized with **pHrodo** and **Oregon green**, **a)** fluorescence from **pHrodo**, **b)** fluorescence from **Oregon green** and magnified region from figure a-b; fluorescence of the microparticle **c)** from the top, **d)** from the bottom, **e-f)** 2D fluorescence from the either sides of the microparticles. Scale bar – 5 μm.

6.5. Quantification of Oregon green and pHrodo on bi-functional microparticles

Quantification of the functionalized fluorophores (**Oregon green** and **pHrodo**) on the bi-functional microparticles were estimated using fluorescence spectroscopy. The supernatants of the both the solutions were measured before and after the step of immobilization of the fluorophore on the microparticles.

A calibration curve was obtained for **Oregon green** by measuring the fluorescence intensity at different concentrations as shown in **Figure 6-24**. It was found that 9.5 µM of **Oregon green** was immobilized on the polysilicon microparticles, whereas, 7.6 µM of **Oregon green** was functionalized on the bi-functional microparticles. This difference corelates due to the difference in the surface area of both the microparticles. In the case of only polysilicon microparticles, the surface area of the polysilicon is 24 µm^2.

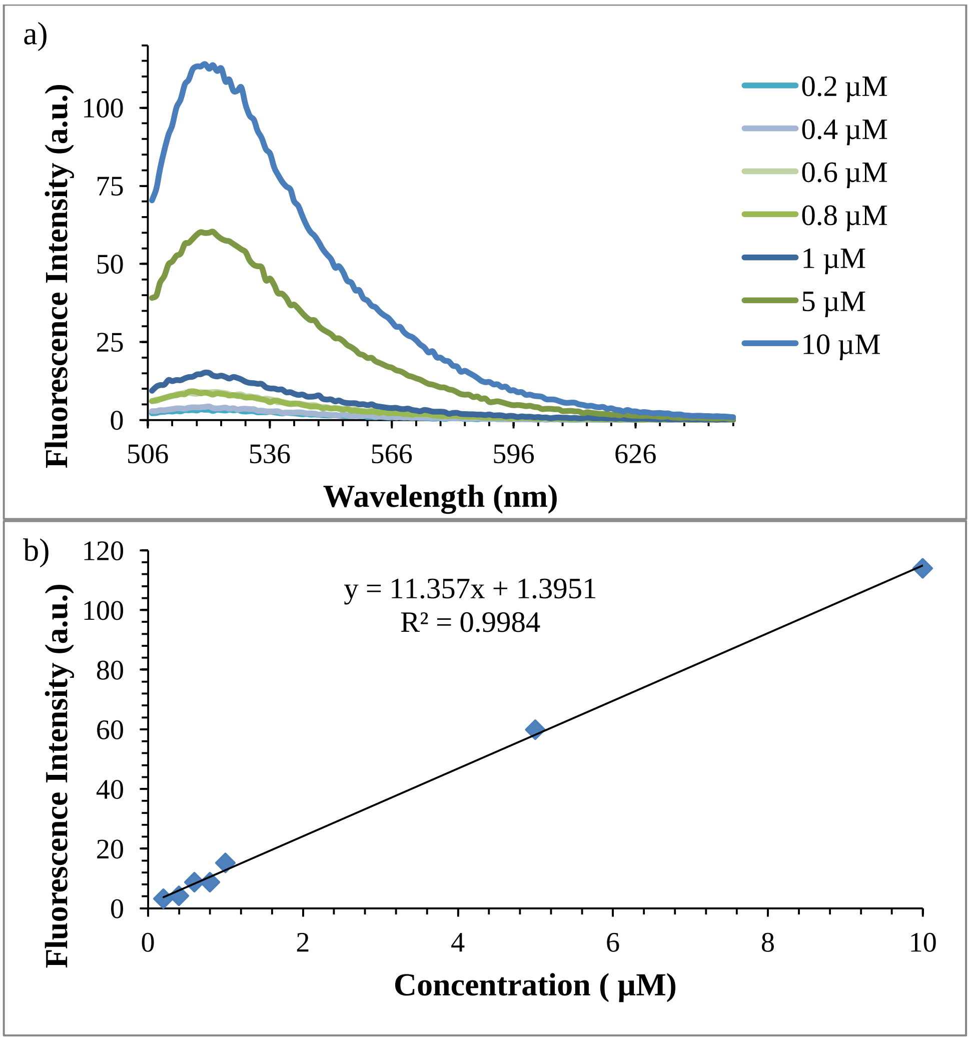

Figure 6-24. Different concentrations of **Oregon green** characterized using fluorescence spectroscopy **a)** Fluorescence spectra and **b)** calibration curve.

On the other hand, in the case of bi-functional microparticle, the surface area of polysilicon is 22.8 µm^2. Thus correponding to higher degree of functionalization in the case of only polysilicon microparticles.

Similar procedure was performed in order to quantify the functionalized **pHrodo** on the bi-functional microparticle, as shown in **Figure 6-25**. In this case, it was found that only 1.0 µM of **pHrodo** was functionalized on the bi-functional microparticles. This lower degree of functionalization could also contribute to the lower fluorescence observed earlier, from the fluorescence images. Also, the surface area of the gold surface in the bi-functional microparticle was taken into account, which is 19.2 µm^2.

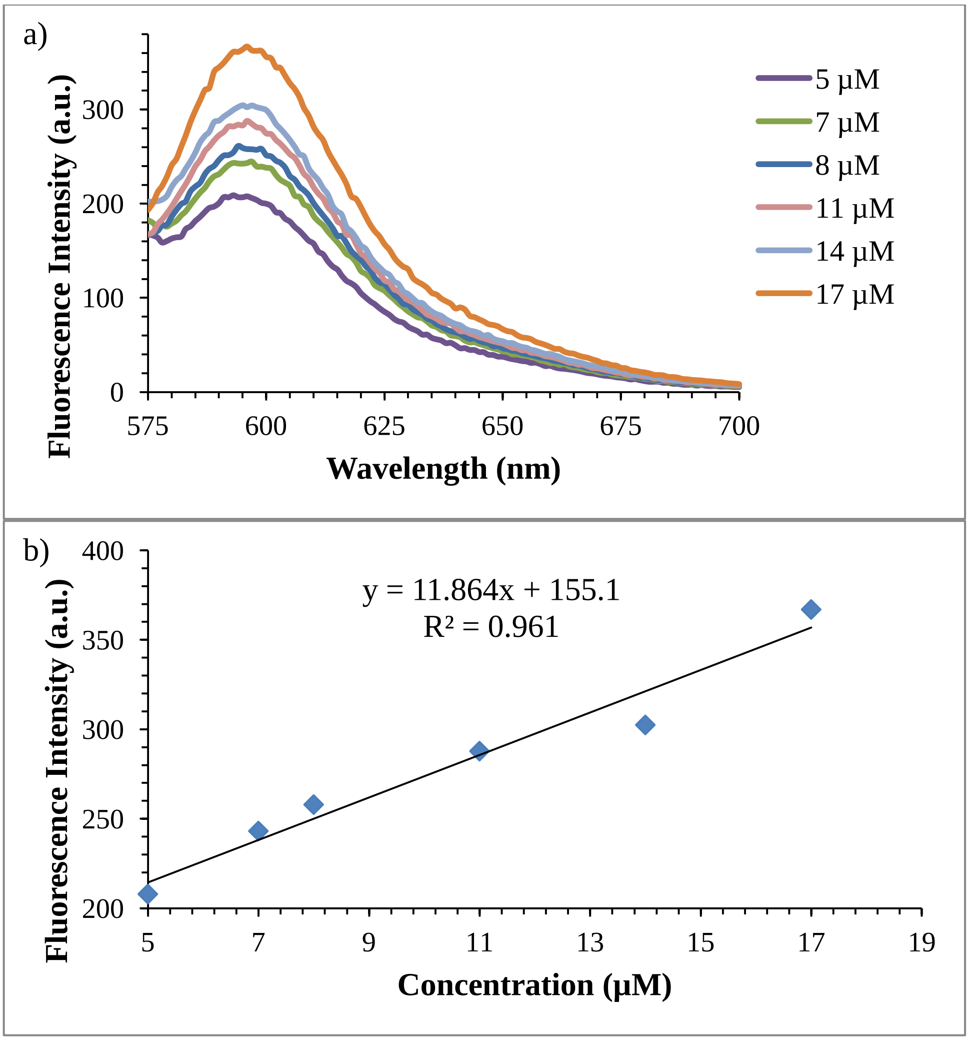

Figure 6-25. Different concentrations of **pHrodo** characterized using fluorescence spectroscopy **a)** Fluorescence spectra and **b)** calibration curve.

Finally, the percentage of microparticles bi-functionalized with two pH dependent fluorophores was calculated to be 30 %. This low yield is due to the loss of microparticles at each step of the functionalization. As, here the functionalization is performed twice, the loss of microparticles was also higher. Although, the initial number of microparticles when compared with Chapter 4, were much higher. In the case of bi-functional microparticles, the functionalization was started using 1,500,000 number of microparticles. Additionally, number of molecules of each fluorophore functionalized on the either side of the bi-functional microparticles was also calculated. **Table 6-2** summarizes the values obtained in the case of each fluorophore.

Table 6-2. Calculation of no. of molecules of **Oregon green** and **pHrodo** immobilized / µm^2

Fluoro-phore	Function-alized surface	No. of microparticles		**Conc. of immobil-ized fluoroph-ore (µM)**	Molecul-ar weight (g/mol)	Surface area (µm^2)	**No. of molecules/ µm^2 (x 10^8)**
		Initial	Final				
Oregon green	Poly-silicon	1,500,000	450,000	**7.6**	509.4	22.8	**8.8**
pHrodo	Gold	1,500,000	450,000	**1.0**	659.8	19.2	**1.0**

As observed from **Table 6.2**, no. of molecules of **Oregon green**/ µm^2 of polysilicon microparticle is about 8.8 x 10^8 molecules/ µm^2. On the other hand, in the case of **pHrodo**, 1.0 x 10^8 molecules/ µm^2 of **pHrodo** is functionalized on the gold microparticles. Which is found to be 9 times lower than the functionalized **Oregon green** on the polysilicon surface.

In the end, after analysing the obtained results it confirms the bi-functionalization of the microparticles with two pH dependent fluorophores, Oregon green on polysilicon and pHrodo on gold surface.

CHAPTER 7

CHAPTER 7

Functionalization of hexahedral bi-functional microparticles using Reactive Oxygen Species (ROS) generator and ROS sensor for Photodynamic therapy (PDT)

7.1. Introduction

PDT is an approach of cancer treatment based on the use of specific drugs, called photosensitizers, which can induce cell death after irradiation, due to the formation of ROS, **Figure 7-1** [107,305-306]. PDT has several advantages in the treatment of cancer, since it is less invasive, minimizes the secondary effects and allows more localized areas of the body to be treated. The major drawbacks of PDT are the non-specific distribution of the photosensitizer into the body, and the water-solubility of the photosensitizer, which can be low and thus requires a formulation to improve the administration.

In particular, porphyrins are one of the most studied photosensitizers in the last years, to be applied in PDT [107,110,307-309]. One of the main characteristics of the porphyrin's structure is the possibility to incorporate a metal into its core, in particular bivalent cations such as Fe^{2+}, Zn^{2+}, Mg^{2+} or Co^{2+}. These metalloporphyrins are intensely investigated for their ability to form ROS and thereby their interest as potent photosensitizers for use in PDT [308,310-312][11]. Furthermore, metalloporphyrins have shown to be more efficient as photosensitizer in PDT than the metal-free porphyrin [313]. However, they frequently present low water solubility, which results in low distribution and consequently low efficiency. For this reason, there have been a need of developing a target specific drug delivering system which could be achieved using nanomaterials micro- and nanoparticles [108,111,113,052]. On the other hand, the detection of ROS in biological systems is one of the major problems due to its high reactivity, which results in extremely short single oxygen lifetimes of about 200 nsec [89].

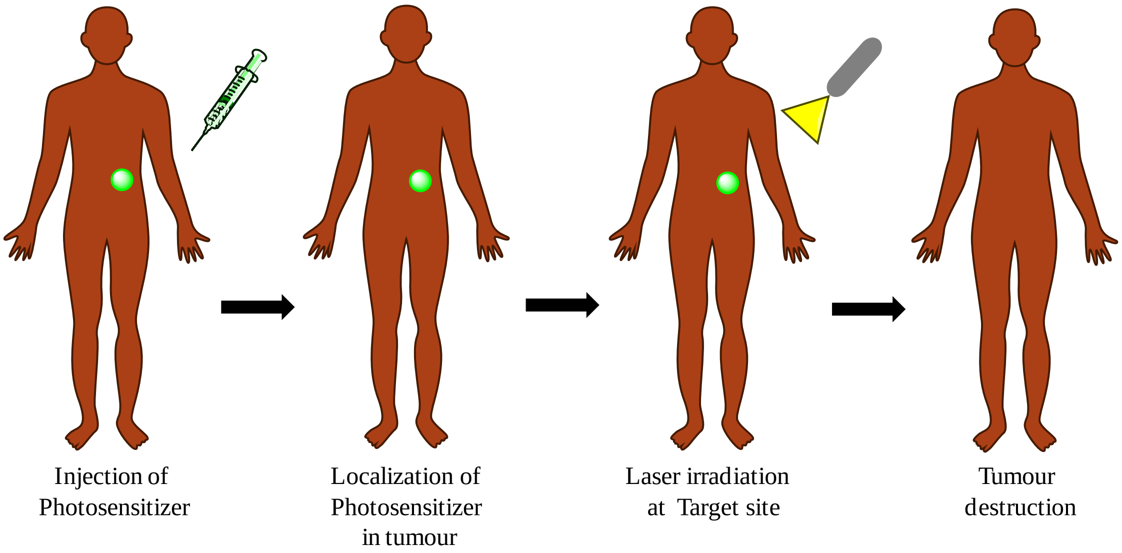
Injection of Photosensitizer
Localization of Photosensitizer in tumour
Laser irradiation at Target site
Tumour destruction

Figure 7-1. Schematic concept of the procedure involved in PDT.

As a step forward to the therapy of cancer treatment, our aim was to develop a microtool that is capable of simultaneously generate (therapy) and sense (diagnosis) the production of ROS, for cancer theranostics. Therefore, our approach was to prepare and optimize a protocol for bi-functionalizing hexahedral microparticles made of polysilicon and gold, with both ROS producer and a ROS sensor, as suggested in **Figure 7-2**.

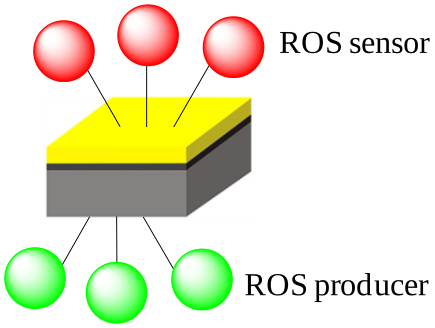

Figure7-2. Representation of a bi-functional microtool for PDT.

7.1.1. Selection of the ROS generator

The first objective was to select a suitable species acting as a photosensitizer for PDT. The use of different molecules containing heme rings or similar derivatives, such as porphyrins or phtalocyanines, have been described in PDT [314,315]. On this context, we selected a bio-photosensitizer, Cytochrome c (Cyt c), a heme containing protein, **Figure 7-3** [316]. It is localized in the compartment between the inner and outer mitochondrial membranes where it functions to transfer electrons between complexes in the respiratory chain. Cyt c is a redox-active molecule consisting of 104 amino acids, and with a molecular weight of about 12 kDa [316-320]. It is also known to have peroxidase activity [321-324]. The iron in Cyt c is bound above and below the plane of the porphyrin ring by proteins on one side while the other side is free for oxygen to bind. Thereby, switching the state of iron between Fe^{2+} (reduced) and Fe^{3+} (oxidized) [325-326].

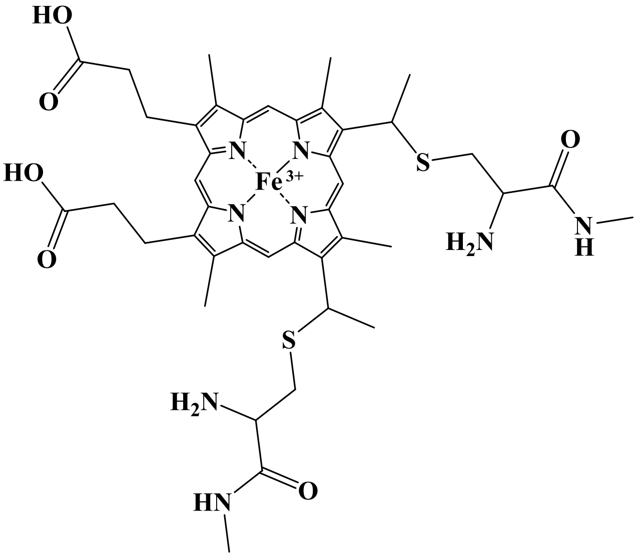

Figure 7-3. Chemical structure of heme fragment of Cyt c.

Furthermore, Cyt c is proposed as a promising target to induce apoptosis in cells [325,327-328]. Recent works have explored the possibility of apoptotic induction by direct microinjection of different concentrations of Cyt c in cancer cells [329-330]. On the other hand, the production of ROS by Cyt c, remains controversial [331-333]. Some studies have reported a late increase of ROS levels during apoptosis after Cyt c release [318]. Therefore, our idea was to study Cyt c's capability as a bio-photosensitizer for ROS production.

Primarily, the selected photosensitizer, Cyt c (Fe^{3+}) was characterized in solution using UV-Visible absorption and fluorescence spectroscopy respectively. **Figure 7-4 a)** shows the absorption spectrum of Cyt c in phosphate buffered saline (PBS) solution. There are two absorption bands, one at wavelength 408 nm called soret band and the other at 520 nm called the Q band [334]. **Figure 7-4 b)** shows the fluorescence emission of Cyt c in PBS. As noticed from the graph below, Cyt c is very low in fluorescence [335]. This is due to the presence of the paramagnetic Fe $^{(2+/3+)}$ ion. This iron enhances the intersystem crossing which results in the decrease of the fluorescence.

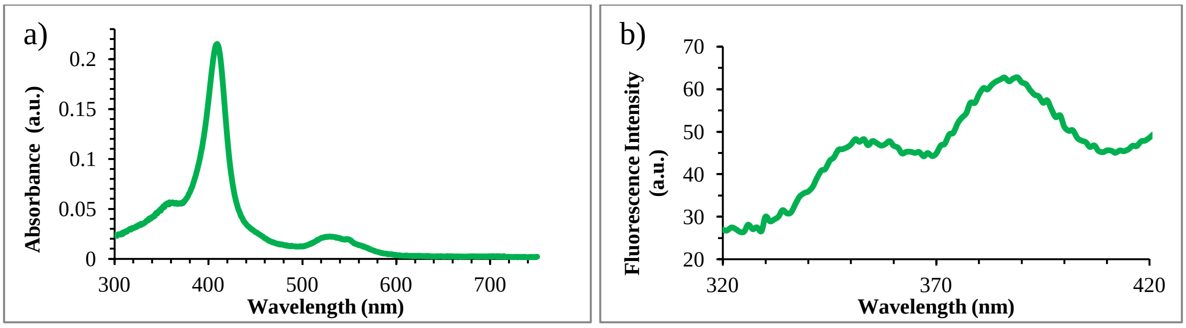

Figure 7-4. Spectra of Cyt c in PBS characterized using **a)** absorption and **b)** fluorescence emission.

7.1.2. Selection of the ROS sensor

To monitor the generation of ROS, BODIPY was selected as a ROS sensor [336]. In the presence of ROS, this fluorescent dye shows a shift in its fluorescence emission peak from red (590 nm) to green (520 nm) fluorescence, as shown in **Scheme 7-1**. The oxidation of the phenylbutadiene of the BODIPY in the presence of ROS results in the change of fluorescence emission from red to green [337-340]. This ratiometric shift in the fluorescence emission is of use to detect and quantify the production of ROS.

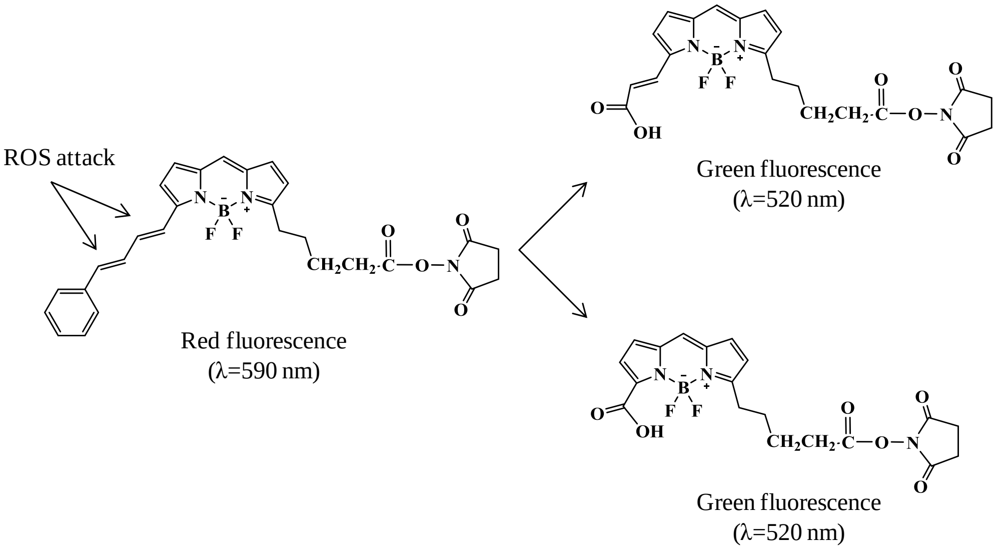

Scheme 7-1. Mechanism for the change of fluorescence emission in a BODIPY derivative (NHS-BODIPY).

Figure 7-5 shows the spectra of BODIPY in DMSO solution characterized using both absorption and fluorescence spectroscopy. In the case of absorbance spectrum, a sharp band was observed at 581 nm with an additional band at 550 nm. Whereas in the case of fluorescence emission spectrum, a sharp emission peak at 590 nm with two additional peaks at 542 and 626 nm was observed [341]. Due to the absence of ROS, the fluorescence emission peak at 520 nm is not visible.

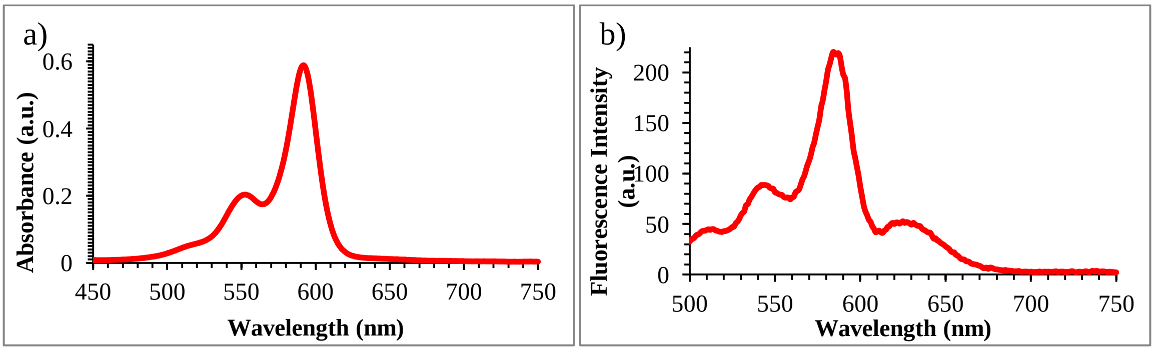

Figure 7-5. Spectra of BODIPY in DMSO characterized using **a)** absorption and **b)** fluorescence spectroscopy (λ_{exc} = 581 nm).

The consequent step was the ability of BODIPY using fluorescence spectroscopy to analyze the ROS sensing system in solution.

Results and Discussion

7.2. Testing the pair of ROS producer and BODIPY sensor: Controls in solution

The stability of BODIPY was analyzed by irradiating a solution of BODIPY in PBS at 408 nm to excite Cyt c (soret band) and the fluorescence emission spectra was measured at 590 nm (fluorescence emission of BODIPY), after 30 mins of irradiation. **Figure 7-6** below shows the kinetic behaviour of the fluorescence emission at 590 nm for duration of 30 mins. As noticed, there is no influence of the irradiation at 408 nm on the fluorescence emission peak of the BODIPY.

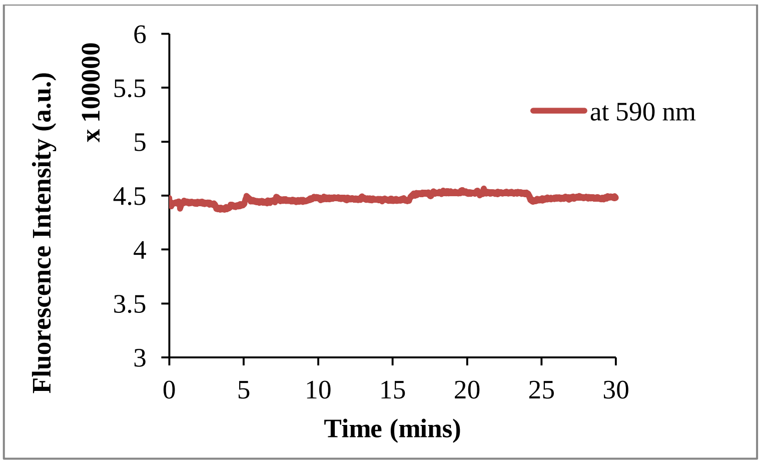

Figure 7-6. Kinetic study of fluorescence emission from BODIPY at 590 nm.

Cyt c, in the presence of BODIPY, were irradiated at 408 nm (soret band of Cyt C) for 30 mins in order to generate ROS, as shown in **Figure 7-7**.

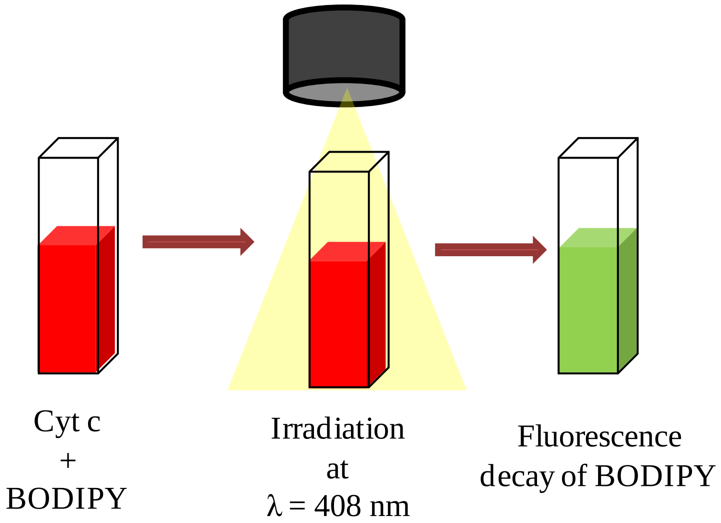

Figure 7-7. Representation of irradiating the ROS sensing system in solution.

The more intense peak at λ_{em} 590 nm was selected for monitoring the production of ROS, upon irradiation of Cyt c at λ_{exc} 408 nm following its intensity decay for a period of 30 mins (**Figure 7-8 a**) and **Figure 7-8 c)** shows the fluorescence decay of BODIPY at 590 nm. As noticed a sharp decay of the fluorescence is observed during the first 10 mins. Whereas, after 20 mins of irradiation the fluorescence decay is slowed. This corresponds to the shorter lifetimes of the ROS [89].

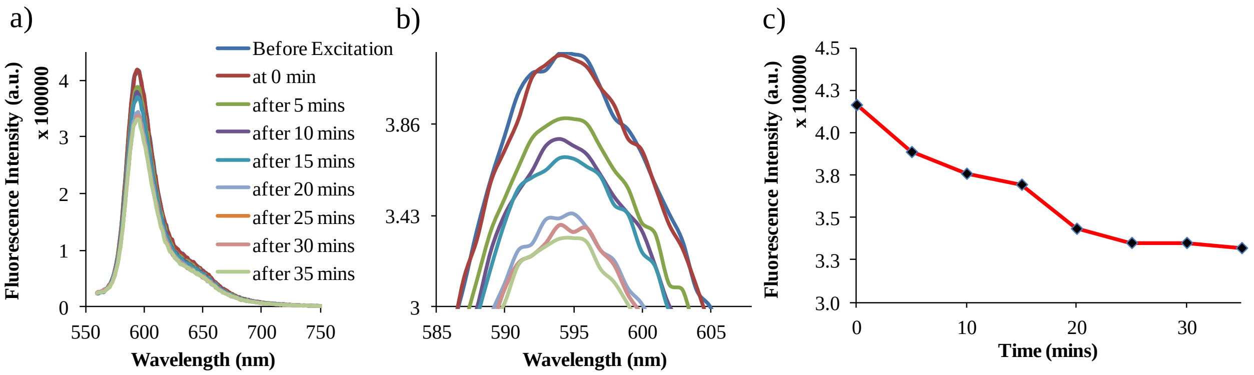

Figure 7-8. a) Emission fluorescence spectra of BODIPY at λ 590 nm after addition of Cyt c (10 μM) in PBS at λ 408 nm at 0 – 35 mins and **b)** enlargement of a) and **c)** fluorescence emission of BODIPY at 590 nm after irradiation of Cyt c.

After analyzing the successful ROS production and sensing system, the subsequent step was to immobilize these selected molecules.

7.3. Functionalization and characterization of Cyt c and BODIPY: Controls on surfaces

As the final goal is to bi-functionalize the ROS producer and sensor on a bi-functional microparticle, made up of gold and polysilicon. Cyt c was chosen to be immobilized on polysilicon surface whereas, BODIPY on gold surfaces. This selection was done, in order to avoid the denaturation of the Cyt c protein during the process of bi-functionalization and thus, was chosen to functionalize as the last step of the functionalization.

The surfaces used here for studying Cyt c and ROS functionalization were flat polysilicon and gold surfaces.

7.3.1. Immobilization of Cyt c on polysilicon surfaces

The functionalization strategy used in order to immobilize Cyt on polysilicon surfaces was based in our previous experience with immobilization of lectins. **Scheme 7-2** shows the stepwise immobilization of Cyt c on polysilicon surface, consisting of 3 steps: activation of the surfaces, surface functionalization with TESUD (135 mM in absolute ethanol) and Cyt c (35 µg/mL in PBS) immobilization through a reductive amination protocol.

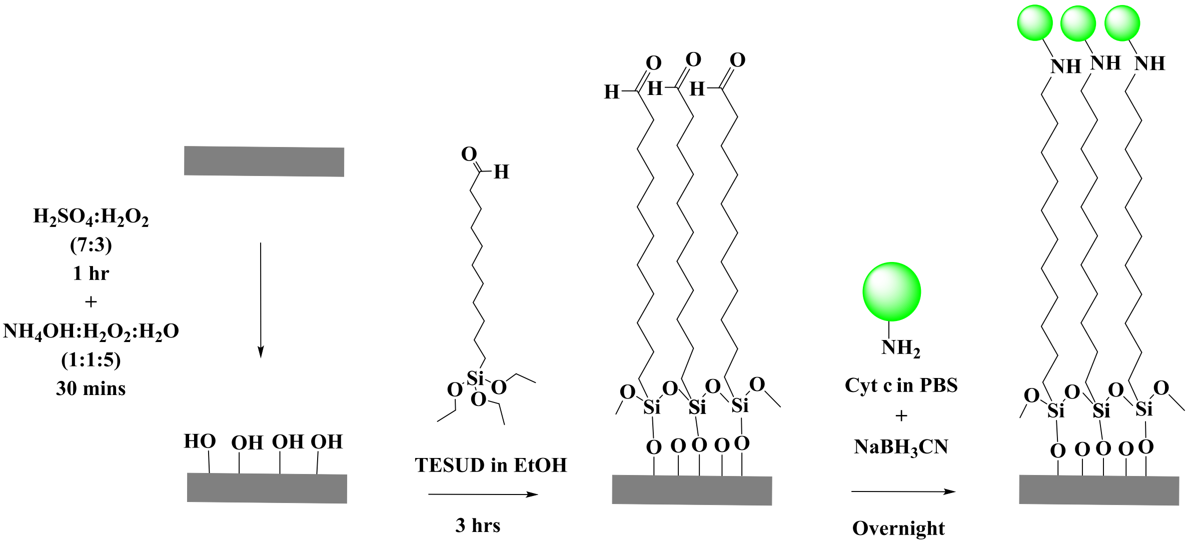

Scheme 7-2. Immobilization of Cyt c on polysilicon surfaces.

The Cyt c functionalized surfaces were then characterized using contact angle measurements. **Table 7-1** shows the contact angle values measured at each step of the functionalization. The initial surfaces had a higher contact angle of about 52 °. This higher degree of value was due to the adsorption of dust particles making the surface hydrophobic. The surfaces after the hydroxylation step resulted in hydrophilic surfaces, thus decreasing the contact angle value upto 8 °. After TESUD immobilization, the surfaces again became hydrophobic (80 °) due to the formation of aldehyde monolayers. This value corresponded to the values obtained in literature [206-207]. On immobilization of Cyt c, the contact angle value again decreased to 54 °, due to the presence of abundant amino acid residues present in the Cyt c, making the surface hydrophilic. This contact angle value measure for Cyt c also corresponds to the value obtained in literature, suggesting the presence of homogenous formation of Cyt c on polysilicon surfaces.

Table 7-1. Contact angle measurements on polysilicon surface functionalized with Cyt c

Sample Name	**Contact angle ϴ (^{0})**
Initial polysilicon surface	52 ± 4
After Piranha	12 ± 3
After Basic	8 ± 2
After TESUD	80 ± 1
After Cyt c	54 ± 2

On the other hand, it is clear that the Cyt c exists in both oxidized and reduced form, depending upon the oxidation state of the Fe ion present in its core. Generally, the Cyt c is in the oxidized form (due to the oxidizing environment) and is known to show no or very low fluorescence due to the presence of paramagnetic Fe ion. But it was found in literature that the reduced form of Cyt c exhibits higher fluorescence than oxidized form [342]. Therefore, the Cyt c functionalized surfaces were treated with sodium ascorbate solution in order to change the state from oxidized to its reduced form and its fluorescence was characterized using fluorescence microscopy [343]. **Figure 7-9** shows the fluorescence images obtained for Cyt c functionalized surfaces **b)** without sodium ascorbate (oxidized form) and **c)** with sodium ascorbate (reduced form). As observed in the first case, surfaces treated with sodium ascorbate shows very low fluorescence. This implies that there is no influence in the fluorescence from the sodium ascorbate. On the other hand, a very low fluorescence observed in for Cyt c immobilized on the surfaces. The mean intensity plot profile was around 22 a.u. (grey value) and the mean intensity from the histogram observed was 58 a.u. Upon treatment with sodium ascorbate, there was no observed change in the fluorescence emission from the Cyt c. The fluorescence intensity observed in this case was similar to the previous results, without the treatment of sodium ascorbate. Inspite of keeping the surfaces with reduced form of Cyt c in anhydrous conditions, the Cyt c must have been oxidized while characterizing the surfaces. And therefore, showing similar values in the fluorescence intensity.

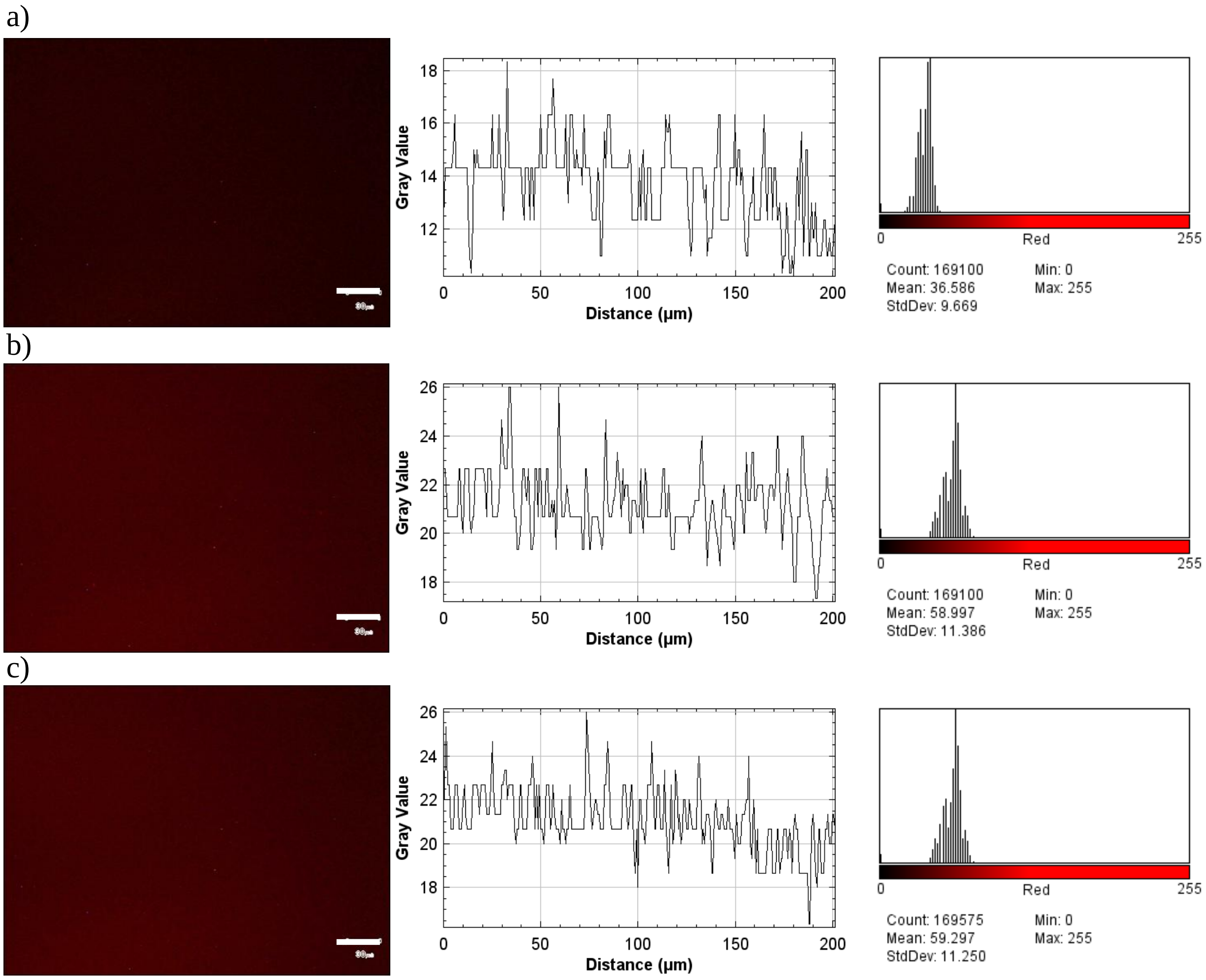

Figure 7-9. Fluorescence image of polysilicon surfaces functionalized with **a)** with only sodium ascorbate, **b)** with Cyt c oxidized form and **c)** Cyt c oxidized treated with sodium ascorbate, with their corresponding mean plot profile and histograms. Scale bar – 30 µm.

Thus, the results obtained from the fluorescence microscopy demonstrate the limitation in characterizing the functionalized surfaces using fluorescence.

7.3.2. Immobilization of Cyt c on polysilicon microparticles in suspension

As the final goal was to functionalize the microparticles with Cyt c, another strategy was adopted to characterize the functionalized Cyt c. The strategy was to measure and quantify the Cyt c immobilized on microparticles using absorbance spectroscopy.

Polysilicon microparticles of 3 x 3 μm^2 and 500 nm thickness were used.

In order to quantify the Cyt c functionalized on microparticles, a calibration curve was plotted by measuring the absorbance of Cyt c at various concentrations as shown in **Figure 7-10**.

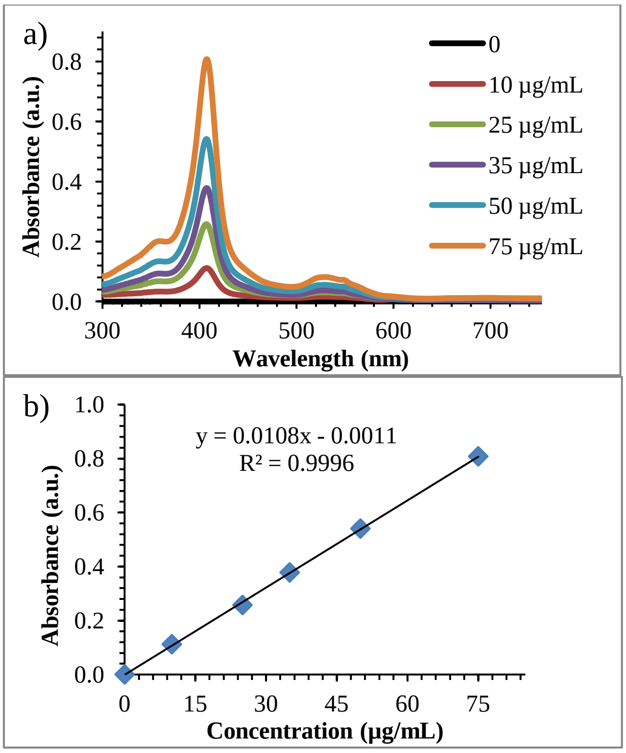

Figure 7-10. a) Absorbance spectra of Cyt c in PBS solution at different concentrations and **b)** calibration curve obtained for Cyt c in the same condition.

The Cyt c was immobilized on the polysilicon microparticles in suspension using the similar approach (**Scheme 7-2**) as for surfaces. For quantifying the Cyt c on the microparticles, the absorbance of the Cyt c of solutions, before and after functionalizing on the microparticles were measured and recorded as shown in **Figure 7-11**.

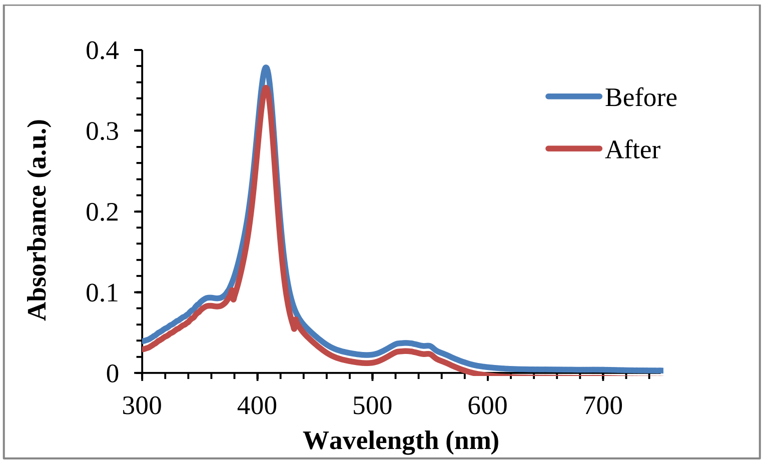

Figure 7-11. UV spectra of Cyt c solutions before and after functionalization.

There is a decrease in the absorbance of the supernatant after the Cyt c functionalization on microparticles. This decrease in absorbance corresponds to the Cyt c functionalized onto the microparticles.

Using the equation obtained from the calibration curve, it was found that concentration of Cyt c immobilized onto the microparticles was about 4 µg/mL containing 75,000 microparticles.

It is important to comment about the limitation in quantifying the amount of Cyt c using absorbance spectroscopy. This technique is not as sensitive as fluorescence spectroscopy. Therefore, various absorbance spectra were obtained multiple times for the same solution.

7.3.3. Immobilization of BODIPY on gold surfaces

The next step was to immobilize BODIPY onto the gold surfaces. The selected BODIPY is derivatized as N-hydroxysuccinimide (NHS) ester group in order to allow reaction with an amino functionalized gold surface, creating amide bonds with the linker on gold surface. **Scheme 7-3** shows the stepwise protocol for the immobilization of BODIPY on gold surfaces using cysteamine as a linker molecule.

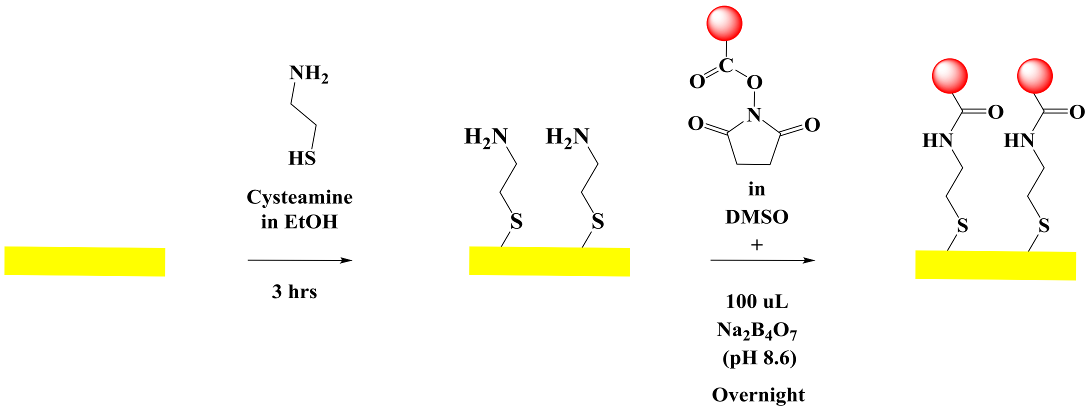

Scheme 7-3. Stepwise immobilization of cysteamine (25 mM in absolute ethanol) followed by BODIPY (20 µM in anhydrous DMSO) on gold surfaces.

The surfaces were initially treated with piranha solution in order to clean them, which were then incubated in cysteamine in absolute ethanol solution to form a self-assembled monolayer. The amino functionalized surfaces were then treated with the reactive NHS-BODIPY forming strong amide bonds. In this case, an additional buffer was required during the immobilization of the BODIPY. This step was performed to make sure that the amino groups remains in the non-protonated form for interacting with the NHS ester group.

The BODIPY functionalized surfaces were further characterized using fluorescence microscopy and **Figure 7-12** shows the fluorescence images of surfaces functionalized without BODIPY, as a control surface and with NHS-BODIPY.

The images acquired suggest successful immobilization of BODIPY onto the gold surfaces. The control surface, without BODIPY, shows some fluorescence, whereas, the surfaces functionalized with NHS-BODIPY shows a mean fluorescence intensity of about 35 units (grey value) from the plot profile and 99 a.u. (grey value) from the histogram, confirming the immobilization of BODIPY. The fluorescence from the plot profile appears to be uniform and homogenous.

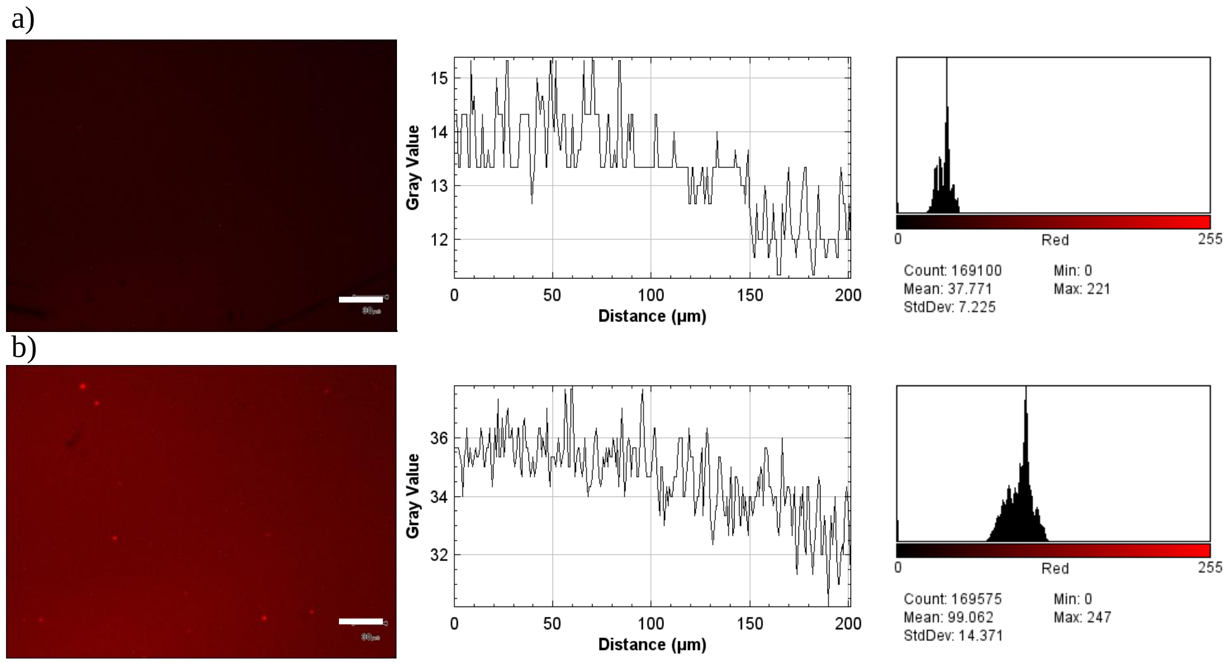

Figure 7-12. Fluorescence image of gold surfaces functionalized **a)** control and **b)** with NHS-BODIPY; with their corresponding mean plot profile and histograms. Scale bar – 30 μm.

7.4. Bi-functionalization and characterization of hexahedral bi-functional microparticles (polysilicon-gold) with Cyt c and BODIPY

Ater establishing the protocols for functionalizing the ROS producer Cyt c on polysilicon and ROS sensor BODIPY on gold, the subsequent step was to functionalize them on bi-functional microparticles.

The surface chemistry involved in the bi-functionalization of the microparticles was carried out following the sequential steps described in **Scheme 7-4**.

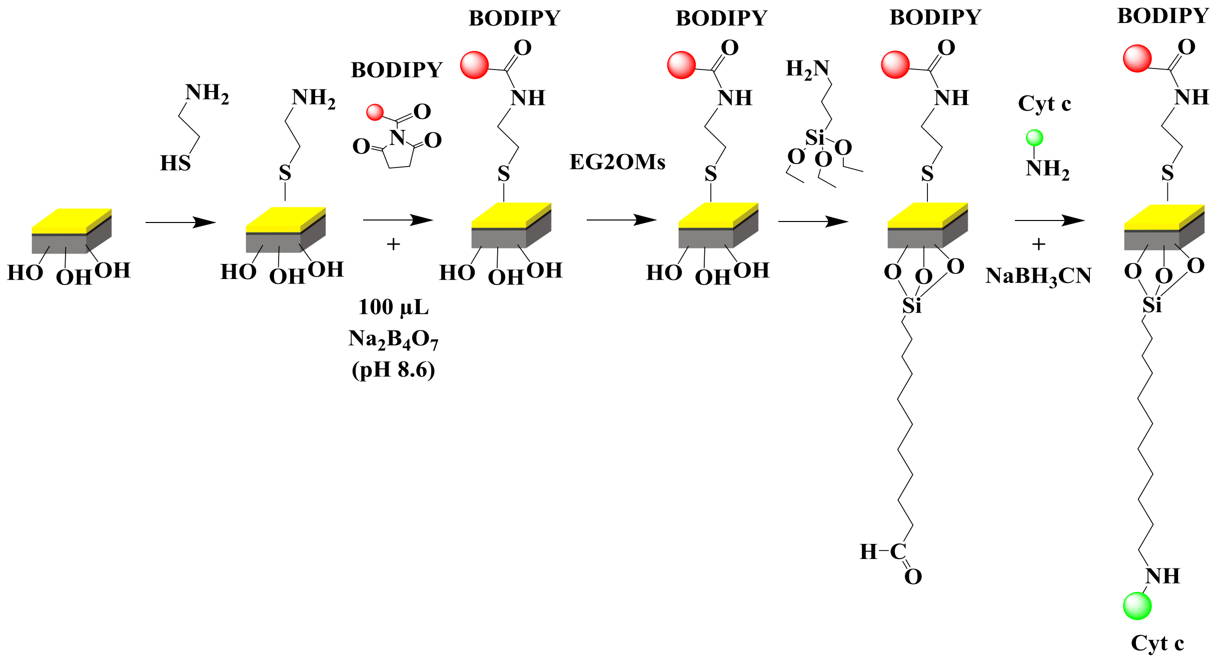

Scheme 7-4. Stepwise representation of orthogonal functionalization of bi-functional microparticles with BODIPY on the gold face and Cyt c on polysilicon face.

The microparticles were initially treated with piranha solution in order to clean the gold surface and activate the polysilicon surface. After which, they were treated with cysteamine solution in order to form amino terminated self-assembled monolayers. The amine functionalized surfaces were then treated with NHS-BODIPY in the presence of sodium tetraborate to form stable amide bond conjugates. The next step was to block the unreacted amino group after the BODIPY immobilization. Thus, treated with 2-(1-hydroxy)ethoxyeth-1-yl methanesulfonate (EG2OMs). The BODIPY functionalized microparticles were then treated with TESUD solution in order to form a monolayer of aldehyde functional groups. Aldehyde functionalized microparticles were then incubated in Cyt c solution to form stable secondary amine groups.

These bi-functionalized microparticles were characterized using confocal scanning microscopy. **Figure 7-13** shows the fluorescence images obtained for bi-functionalized microparticles with BODIPY on gold and Cyt c on polysilicon face.

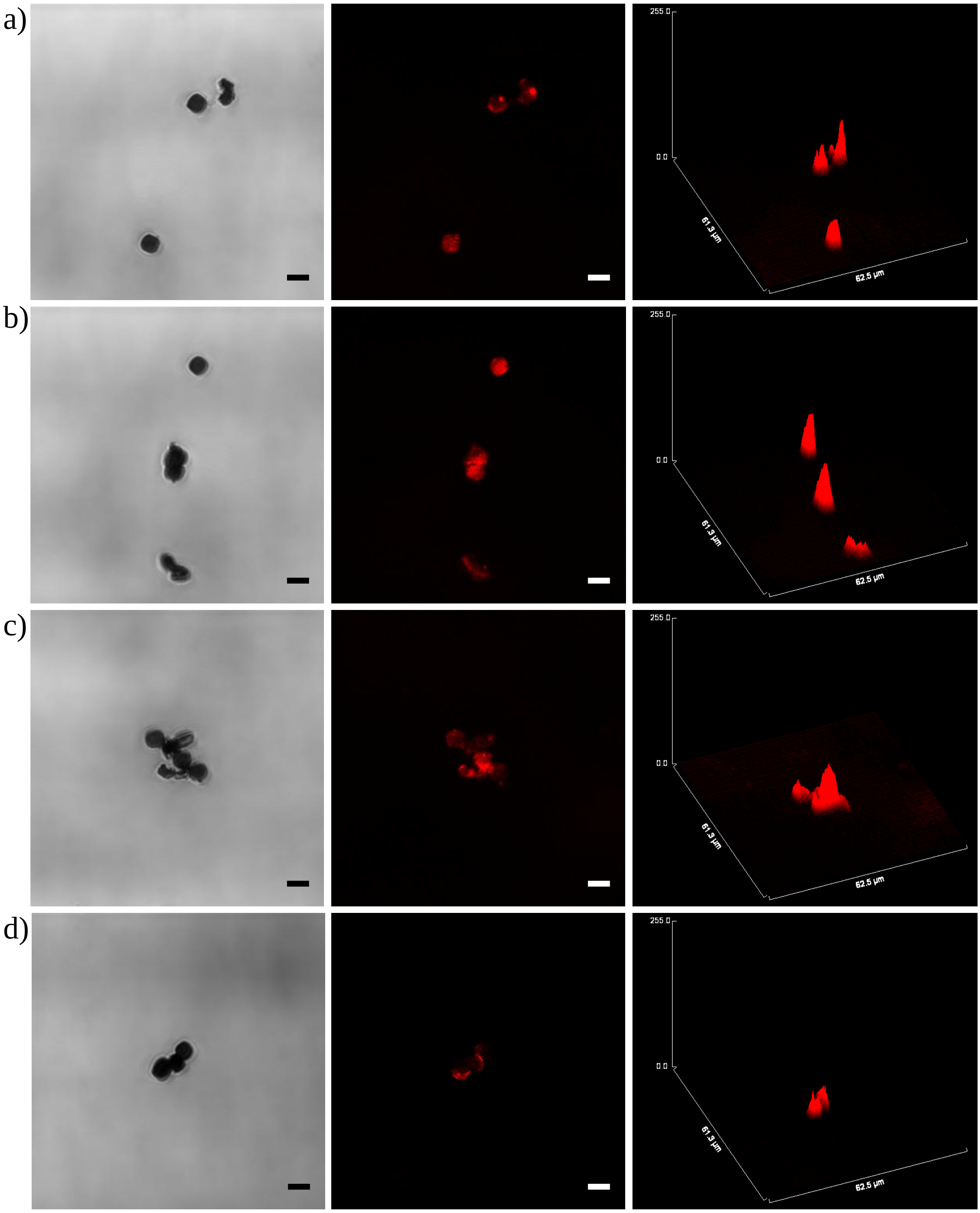
a)
255.0
0.0
61.3 µm
62.5 µm
b)
255.0
0.0
61.3 µm
62.5 µm
c)
255.0
0.0
61.3 µm
62.5 µm
d)
255.0
0.0
61.3 µm
62.5 µm

Figure 7-13. Bright field and fluorescence microscopy images of microparticles bi-functionalized with BODIPY on gold and Cyt c on polysilicon face and their 3D plot profiles. Scale bar – 3 µm.

As noticed, we could observe fluorescence only from the functionalized BODIPY face. Although, there were areas without fluorescence from Cyt c functionalized on the polysilicon face. From the 3D surface plot, it is observed that the functionalization is higher in the centre of the microparticles.

CHAPTER 8

CHAPTER 8

Delivery of anionic drugs using macrocyclic-imidazolium based gold nanoparticles

8.1. Introduction

Drug delivery systems (DDS) provide positive attributes to a 'free' drug by improving its pharmacokinetic properties, controlling its sustained release and, very importantly, lowering its systemic toxicity. The ideal nanoscale DDS ensures that the conjugated or bound drug–carrier complex arrives and acts specifically at the selected target [344-345]. The field of particle-based drug delivery is currently focused on two chemically distinct colloidal particles: liposomes and drug conjugated nanoparticles. Although liposomes have been studied for longer, AuNPs have been widely explored in recent years, especially in the context of emerging biomedical nanotechnology [346]. AuNPs, due to their unique physical and chemical properties, could be used in almost all medical applications [115,347] such as biosensors [348], target-specific drug delivery [114,349], immunoanalysis [350], clinical chemistry [351-352], photothermolysis of micro-organisms and cancer cells [118,353] and optical bioimaging [354]. AuNPs are also highly stable metal nanoparticles [355]. Together with their unique subcellular size, that allows them to enter human cells by endocytosis, and good biocompatibility, their low toxicity [356] and reduction of the level of reactive oxygen species [357], makes them promising drug delivery vehicles [116-117,358-359].

Numerous methods can be found in the literature for the synthesis of AuNPs, among which the Brust-Schiffrin biphasic methodology [360] is commonly used. The gold precursor is transferred from an aqueous phase to an organic phase – using a surfactant such as tetraoctylammonium bromide – where the gold is reduced and the newly formed AuNPs are frequently stabilized by a thiolate. Examples are also found in literature of imidazolium-based ionic liquids being able to stabilize AuNPs through coordination with the imidazolium cation [122].

Among all the potential surfactants one could consider for AuNPs synthesis, the gemini-type amphiphiles possess at least two hydrophobic chains and two ionic or polar groups, linked through spacers of varied flexibility [361]. The gemini structure presents some advantages when comparing to a simpler amphiphile structure, such as lower Critical Micelle Concentration (CMC) [362-363], higher capacity for reducing oil/water surface tension, and better wetting, solubilizing and foaming properties, which makes them attractive for drug entrapment and release applications.

Our group has developed a family of gemini-type imidazolium-based amphiphiles formed by two imidazolium rings linked by a 1,3-dimethylenebenzene spacer, and having an open chain structure [129] or cyclic structure [133]. This family of imidazolium-derived ligands are known to have the ability to recognize anions and also to behave as ionic liquid crystals [133]. The propensity of the imidazolium moiety to anion coordination has been studied by the ability of forming weak hydrogen bonds with their corresponding counterions [133,364-365]. This is important since anions are ubiquitous throughout biological systems, for example nucleic acids and also, the majority of enzyme substrates and co-factors are anionic [366]. Furthermore, from the synthesized compounds, the open chain structures **1·2Br** was found to interact with valproate and ibuprofenate, two model drugs used to assess their possible use in DDS [129].

We have previously developed AuNPs synthesis based on a modified Brust-Schiffrin method using the open chain bis-imidazolium amphiphile **1·2Br**, as shown in **Figure 8-1** where the imidazolium rings bear alkyl chains of 18 carbon atoms. In the reported synthesis of the AuNPs, the bis-imidazolium **1·2Br** amphiphile played two roles: transfer agent and stabilizer of the AuNPs, which resulted in the advantageous simplification of the synthetic process and subsequent purification [129]. Furthermore, our group successfully developed water soluble gold nanoparticles using the same ligand, that formed a double layer around the gold core [367]. Finally, in order to study their potential application as DDS, different anionic drugs such as sodium ibuprofenate and piroxicam were incorporated in the bis-imidazolium amphiphile particles [129-130]. Successful incorporation and release of the anionic drugs from different nanostructured particles with this imidazolium ligand confirms their possible use as DDS for anionic compounds.

Now we are going to explore how structural variations could affect their behavior as ionophores and in the synthesis of AuNPs. For this purpose, macrocyclic analogues **2·2Br** - **4·2Br** (**Figure 8-1**), with benzene rings bearing alkyl chains of either 1, 10 or 18 carbon atoms respectively, were used to study the influence of the polar head and the length of the alkyl substituent. **3·2Br** and **4·2Br** are known to behave as macrocyclic ionic liquid crystals [133].

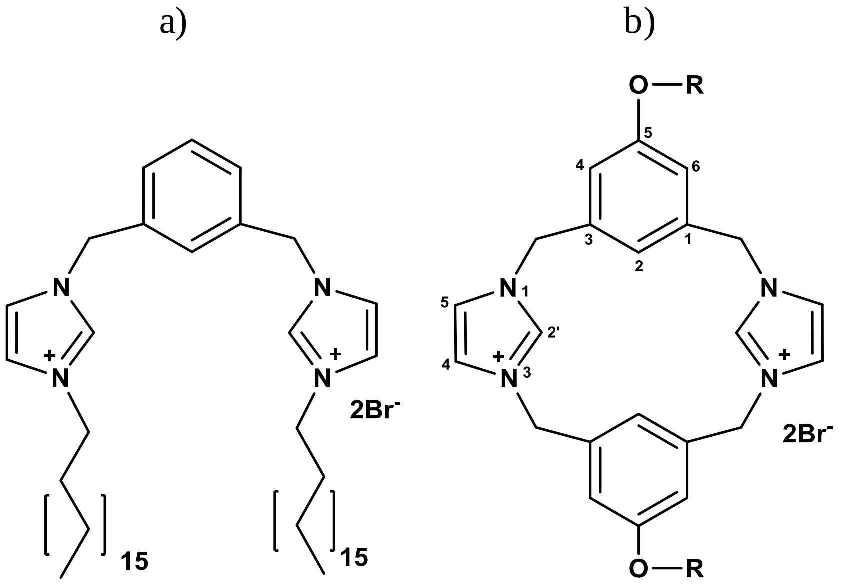

1·2Br

2·2Br ; R = CH_3
3·2Br ; R = $C_{10}H_{21}$
4·2Br ; R = $C_{18}H_{37}$

Figure 8-1. Structure of bis-imidazolium derivatives a) **1·2Br** and b) **2·2Br - 4·2Br**.

Macrocycles have more rigid conformations than open chain compounds and in principle could be useful for DDS because it is more likely to show slow and sustained drug release due to its stronger affinity with the drug. The aim of this work was to prepare AuNPs coated with bis-imidazolium amphiphilic macrocycles, in order to explore the ability of the colloids towards anion recognition, and their potential use in nanomedicine.

Thus, we describe the anion binding studies of the bis-imidazolium compounds **2·2Br - 4·2Br**, and the synthesis and characterization of AuNPs using imidazolium macrocyclic compounds **2·2Br - 4·2Br**. The successfully synthesized AuNPs were characterized using UV-Visible Absorption Spectroscopy, X-ray Photoelectron Spectroscopy (XPS), Matrix Assisted Laser Desorption Ionization – Time-of-Flight Mass Spectrometry (MALDI-TOF-MS), Thermogravimetric Analysis (TGA), Dynamic Light Scattering (DLS), Transmission Electron Microscopy (TEM) and Scanning Electron Microscopy (SEM). We also report on the molecular recognition ability towards sodium ibuprofenate, a model anionic drug, which could be successfully incorporated in the synthesized AuNPs, and the *in vitro* release studies of the incorporated drug.

8.2. Anion binding properties of bis-imidazolium salts

We have previously reported the anion binding properties of bis-imidazolium based open chain compounds, revealing the importance of weak hydrogen bonds ($C\text{-}H\cdots X^-$) controlling the anion binding specially for organic carboxylates [129]. Here, we study the binding affinity in solution of the bis-imidazolium salts for three different anions (chloride, dihydrogen phosphate and acetate) to have general data on the affinity for different anions found in biological systems. To do so, titration experiments were performed and the solutions were analyzed using ^1H NMR spectroscopy. It is possible to determine the anion complexation with the bis-imidazolium salts through this technique by observing changes in the chemical shifts ($\Delta\delta$) of the acidic protons that are more involved in the anion binding. Different bis-imidazolium salts were chosen for the study, **2·2Br**, **3·2Br** and **4·2Br** in order to determine how the structural differences in the alkyl chain length can affect the compound's affinity.

To study the anionic interaction, in some cases (**2·2Br** and **4·2Br**), the first step was to replace the bromide counter ions in the molecules with hexafluorophosphate, as this anion associates weakly with the imidazolium units and therefore does not have a competitive binding scenario. TBA salts TBA·X (X= Cl^-, $H_2PO_4^-$, AcO^-) were used as the source of the target anion. ^1H NMR analysis of the bis-imidazolium salt solutions (0.5 mM) were performed in $CDCl_3$ or $(CD_3)_2SO$, containing increasing concentrations of TBA salts and observing the chemical shifts of the acidic protons (C(2)-H and C(2)'-H) in the ^1H NMR spectrum of the solution, selected examples shown in **Figure 8-2**.

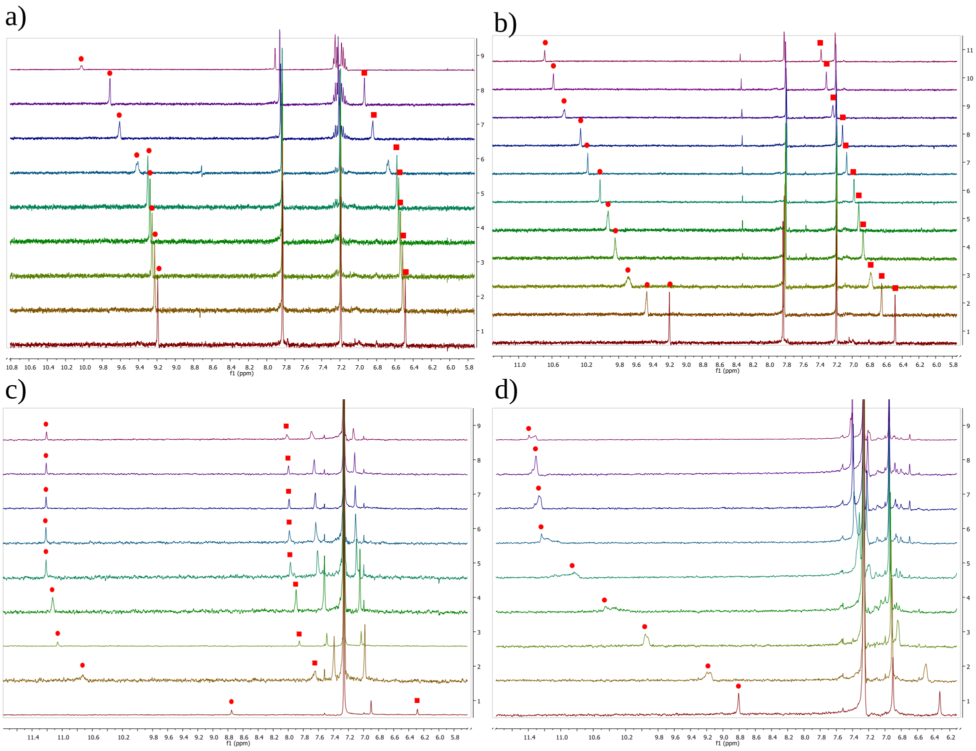

Figure 8-2. NMR spectra of **a)** 0.5 mM of **2·2PF$_6$** solution in $(CD_3)_2SO$ show the chemical shifts, depicting the downfield effect of the proton signals C(2)-H (●) and C(2)'-H (■), with increasing **2·2PF$_6$**: chloride ratio **(**from bottom to top: 1:0, 1:1, 1:2, 1:3, 1:7, 1:10, 1:13, 1:15 and 1:20). Similarly, **b**) **2·2PF$_6$**: acetate ratio, **c) 4·2PF$_6$**: chloride ratio and **d) 4·2PF$_6$**: acetate ratio.

The chemical shifts were then plotted as a function of the anion concentration (**Figure 8-3**) and the stability constant (K_a) and complexation free energy (-ΔGº) were calculated. The results are included in **Table 8-1**.

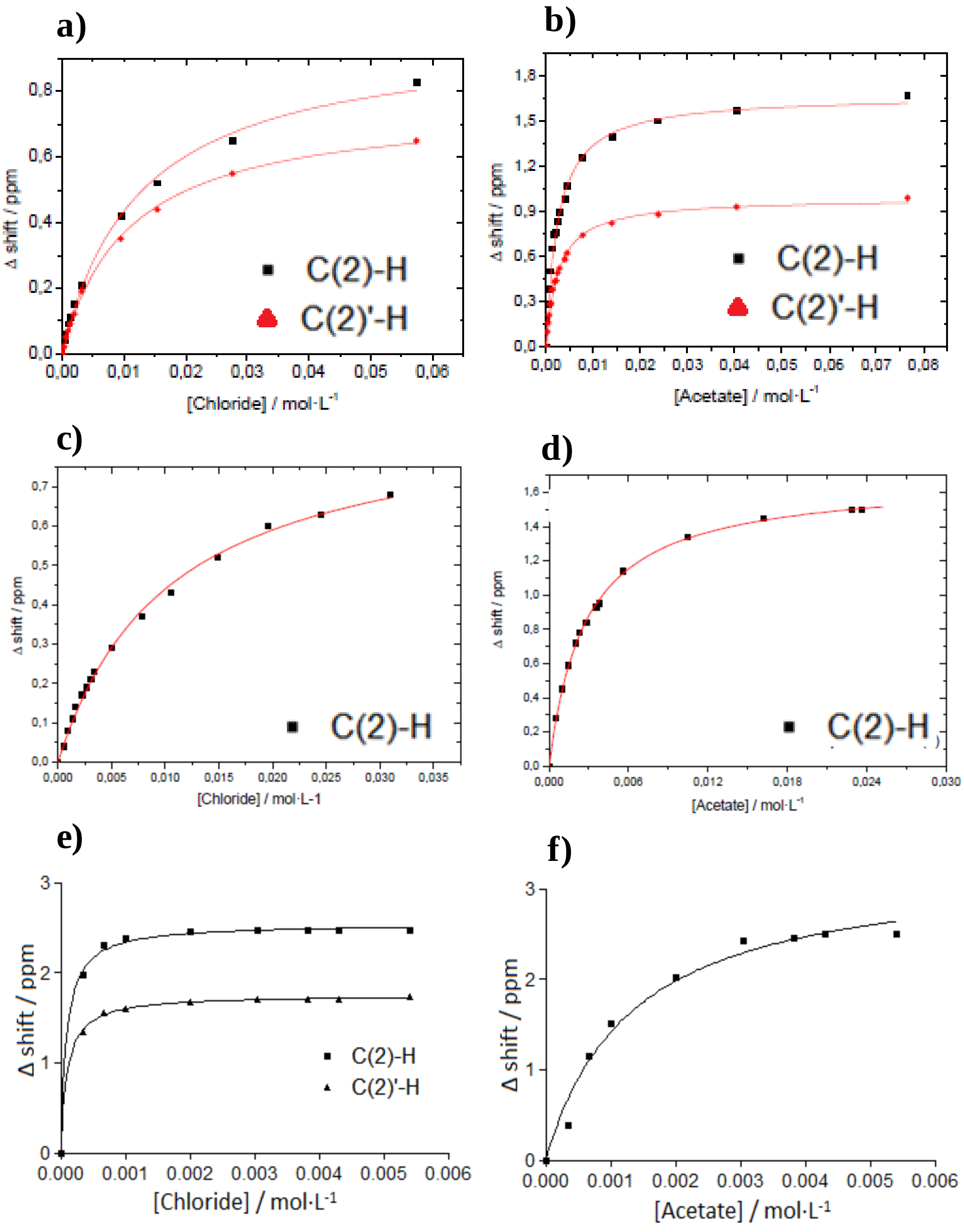

Figure 8-3. Experimental points and fitting (line) data from titrations with bis-imidazolium and TBA salts: **a) 2·2PF$_6$**: chloride, **b) 2·2PF$_6$**: acetate, **c) 3·2Br**: chloride, **d) 3·2Br**: acetate e) **4·2PF$_6$**: chloride and **f) 4·2PF$_6$**: acetate.

The first remark is that for the anions Cl$^-$ and AcO$^-$, upon addition of the inorganic salts a moderate to strong NMR shift of the protons corresponding to the imidazolium moieties C(2)-H and xylyl units C(2)'-H was observed. As shown in **Table 8-1**, it was found that **4·2PF$_6$** has more affinity for chloride. Regarding **3·2Br**, the ligand shows more affinity for acetate than for chloride. When comparing the macrocycle compounds, we can see that there is a trend for the affinity to increase with increase in the alkyl chain. Although the constant for **3·2Br** is lower than the one for **2·2PF$_6$**, one must take into account that the counterion is different. Also importantly, the solvent used for **4·2PF$_6$** was $CDCl_3$ and because **3·2Br** and **2·2PF$_6$** were not soluble, $(CD_3)_2SO$ was used. Finally, except **4·2PF$_6$**, which showed more affinity for chloride than for acetate, the remaining ligands showed more affinity for acetate than for chloride.

On the other hand, in the case for dihydrogen phosphate, the ^{1}H NMR spectra had no signal from the bis-imidazolium compound upon increasing additions of TBA·H_2PO_4 salt. The solution had a cloudy appearance as the concentration of the salt increased. One of the solutions, **4·2PF$_6$,** was further studied using DLS and particles with 2000 nm were detected in the sample, which might indicate the formation of solid particles thus explaining the absence of signal in the spectra.

Table 8-1. Values of K_a and $\Delta G°$ from anion binding studies with chloride and acetate for bis-imidazolium salts **2·2PF$_6$**, **3·2Br** and **4·2PF$_6$**

		TBA Salts			
		Cl$^-$		**AcO$^-$**	
		K_a / M^{-1}	$-\Delta G°$ /kJmol^{-1}	K_a / M^{-1}	$-\Delta G°$ /kJmol^{-1}
2·2PF$_6$[a]	C(2)-H	80.65	10.88	401.61	14.85
	C(2)'-H	92.42	11.21	389.11	14.78
3·2Br[a]	C(2)-H	96.15	11.31	364.96	14.62
	C(2)'-H	[a]	[a]	[a]	[a]
4·2PF$_6$[b]	C(2)-H	11,308	23.1	752.4	16.4
	C(2)'-H	10,133	22.9	[c]	[c]

[a] solution in $(CD_3)_2SO$; [b] solution in $CDCl_3$; [c] no significant shift is observed

8.3. Synthesis and characterization of AuNPs using imidazolium macrocycles

The general protocol for the synthesis of AuNPs involved taking $HAuCl_4.H_2O$ solution in water and mixing it with the solution of imidazolium salt in an extraction funnel. The organic phase is then separated and collected, and a solution of reducing agent, $NaBH_4$, was added dropwise under constant stirring, and the solution was kept under stirring for 4 hours in the dark. The organic phase was then separated and the solvent was removed. The residue was then washed and characterized.

We tested the macrocyclic gemini surfactants with different chain length: **2·2Br** (1 carbon atom), **3·2Br** (10 carbon atoms) and **4·2Br** (18 carbon atoms).

The solution obtained using **2·2Br** did not present the typical red-colored solution of colloidal AuNPs; instead, a precipitate was formed. Presumably the lack of alkyl chains means that the colloids agglomerate to form higher aggregates. A possible explanation is that **2·2Br** has high CMC value [133], because of the shorter alkyl chain, and therefore lacks the needed amphiphilic character that allows it to stabilize the gold nanoparticles. On the other hand, synthesis of AuNPs using longer chain macrocycles **3·2Br** and **4·2Br** resulted in red-colored solutions, and those nanoparticles were named as **3·AuNP** and **4·AuNP** respectively.

UV-Visible absorption spectra were recorded for all the above solutions. The solution obtained for the synthesis using **2·2Br** did not show any characteristic band of AuNPs, originated from Surface Plasmon Resonance (SPR) on the UV-Visible spectrum, confirming that no AuNPs were obtained. Consequently, the use of **2·2Br** for the synthesis of AuNPs was not further studied. Instead, **3·AuNP** solution in dichloromethane showed the characteristic SPR peak for AuNPs at 527 nm, the **4·AuNP** solution in chloroform showed the peak at 524 nm (**Figure 8-4**).

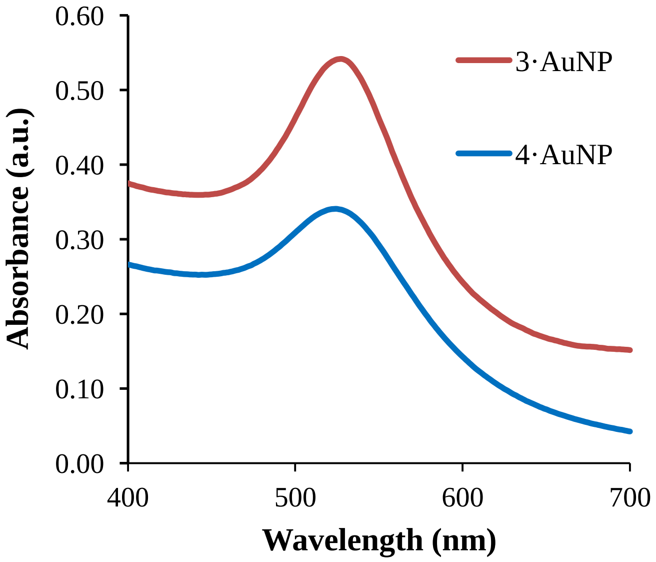

Figure 8-4. UV-Vis absorption spectra of **3·AuNP** in dichloromethane and **4·AuNP** in chloroform solution.

MALDI-TOF-MS was used to study **4·AuNP**. The data was obtained using 2,5-dihydroxybenzoic acid (DHB) as matrix. The sharpest peaks were at m/z = 1073.7, corresponding to loss of two bromide $[M+Au-2Br]^+$. A peak with very low intensity was found corresponding to loss of one bromide ($[M+Au-Br]^+$) at m/z = 1153.6, whereas in the case of **1·AuNP** the peaks for loss of each bromide [129] were not present. Additionally, peaks corresponding to the macrocycle with gain of one hydrogen and loss of two bromides ($[M+H-2Br]^+$) at m/z = 877.7 was also observed with very low intensity (**Table 8-2**). The same peak did not appear in the **1·AuNP** mass spectrum [129]. We found therefore that the particles **4·AuNP** show peaks corresponding to carbene species.

Table 8-2. Values of peaks from MALDI-TOF mass spectrometry for **4·AuNP**

$[M+Au-2Br]^+$ (*m/z*)	$[M+Au-Br]^+$ (*m/z*)	$[M-2Br+H]^+$ (*m/z*)
1072.7	1153.6	877.7
100%	2%	2%

Matrix – DHB

The oxidation state of gold in the synthesized nanoparticles was determined by XPS. Sputtering of the sample was necessary to identify clearly the peaks corresponding to gold (Au^0) in the **4·AuNP**. The obtained XPS spectrum (**Figure 8-5**) shows the binding energy of the typical peaks of $4f_{5/2}$ and $4f_{7/2}$ at 88.2 eV and 84.5 eV respectively for gold in the reduced state thereby confirming there are no residues of Au (III) precursor.

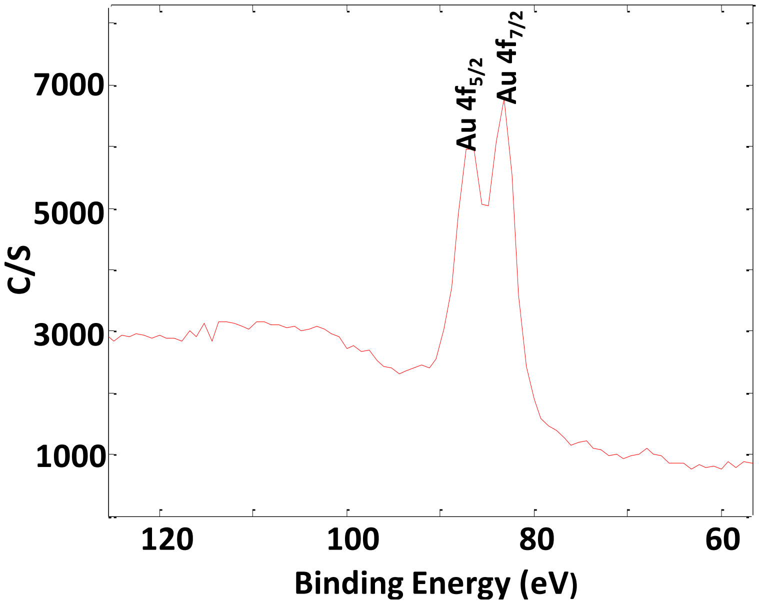

Figure 8-5. XPS spectrum of **4·AuNP** showing the Au $4f_{7/2}$ and $4f_{5/2}$ peaks with binding energies of 84.5 eV and 88.2 eV, respectively.

The AuNPs solutions were further characterized using TEM, DLS, and SEM. **Figure 8-6** shows TEM micrographs obtained for **3·AuNP** and **4·AuNP** colloidal solutions. All the AuNPs are spherical, and present low dispersity. **3·AuNP** shows an average size of 8.2 ± 3.7 nm and **4·AuNP** present an average size of 5.3 ± 3.0 nm.

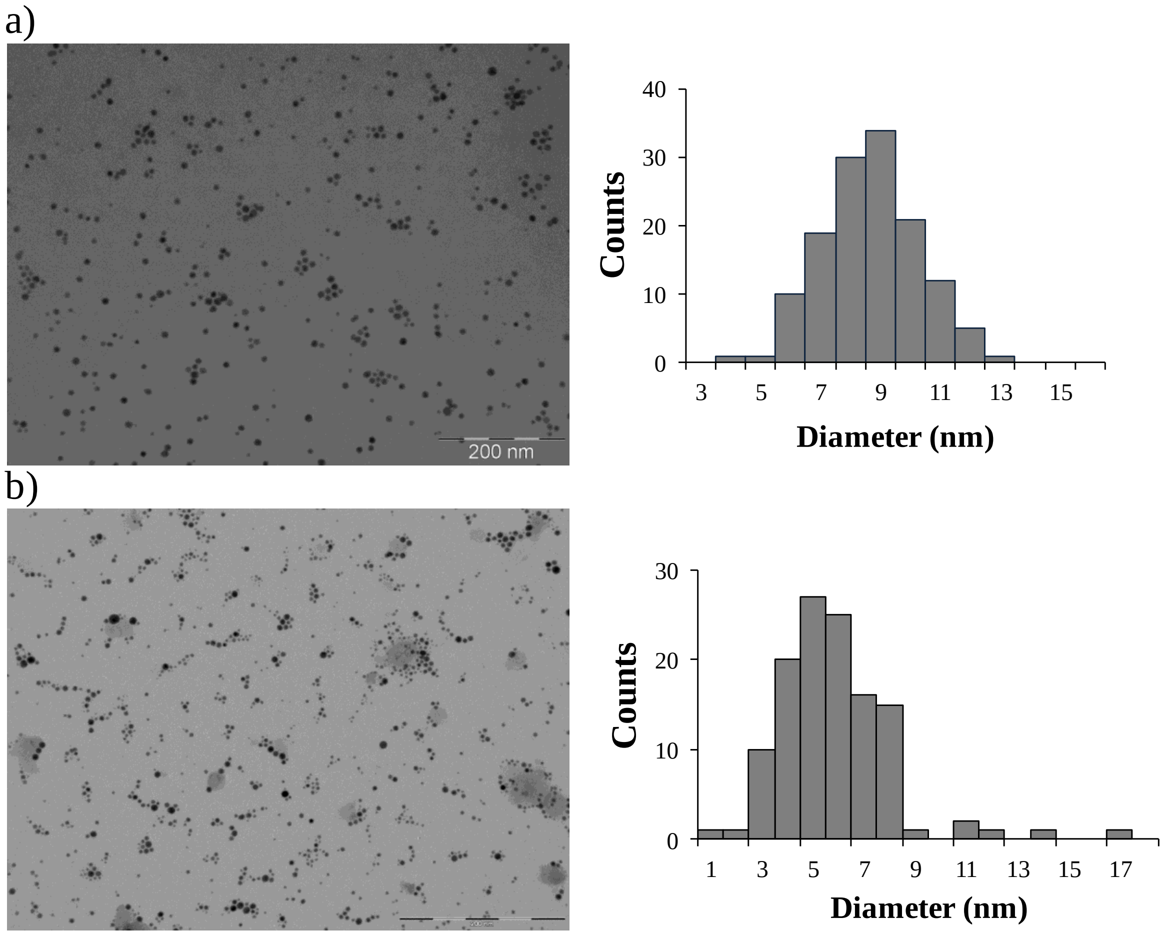

Figure 8-6. TEM micrographs for **a) 3·AuNP** and **b) 4·AuNP** and their corresponding size distribution histograms.

The size of **3·AuNP** and **4·AuNP** was also assessed by DLS at 25°C. **Table 8-3** summarizes the hydrodynamic diameter and Polydispersity Index (PDI) of the AuNPs, and also the SPR absorption band determined by UV spectroscopy and gold core sizes determined by TEM. Regarding the sizes obtained by DLS, the average size in the case of **3·AuNP** was 35 nm and for **4·AuNP** was 74 nm.

Table 8-3. Size of the gold core using TEM, and hydrodynamic size using DLS

Sample	λ (nm)	Size/nm (TEM)	Size/nm (DLS)	PDI[a]
3·AuNP	527	8.2 ± 3.6	34.8	0.1
4·AuNP	524	5.3 ± 3.0	73.5	0.2

[a] Polydispersity Index

The sizes measured by DLS are higher than those observed by TEM because this technique gives the hydrodynamic size of the particles that includes not only the core but also the alkyl chains of the coating ligands; instead TEM only indicates the gold core size, because no contrast agent was used. Knowing that the ligand **4·2Br** has a longer chain, it is normal that the hydrodynamic diameter is higher in the case of **4·AuNP**. On the other hand, in the case of **1·AuNP** the hydrodynamic diameter was around 20 nm, which is lower than that of the macrocycles. A possible explanation could be the structural orientation of the macrocycles that are more bulky than the open chain.

SEM was used to study the topography and morphology of the AuNPs, through secondary electron image, as well as their composition, using the backscattered image, which allows detecting the presence of metals (in our case, the reduced gold from the core). **Figure 8-7** shows the SEM micrographs of **3·AuNP** and **4·AuNP**. The samples were drop casted on carbon tabs, and selective areas with good contrast were sampled to record both the secondary and the backscattered images. In **Figure 8-7 a)** spherical particles are visible, whereas in the backscattered image shown in **Figure 8-7 b)** the gold core is visible, confirming that gold is present in its reduced form, as seen by XPS, and that the gold core has a spherical shape, which is in agreement with the observed by TEM.

Since in the secondary electron image the gold is not visible, the spherical particles seen correspond to the macrocycle layer around the gold core, thus confirming the presence of the coating. In the case **3·AuNP**, it is visible that the nanoparticles show a spherical morphology but formed aggregates in these experimental conditions. However, it was also possible to see the presence of the macrocycle layer around the core in **Figure 8-7 c)**, and the core of gold in reduced form with spherical shape in the backscattered image in Figure **8-7 d)**.

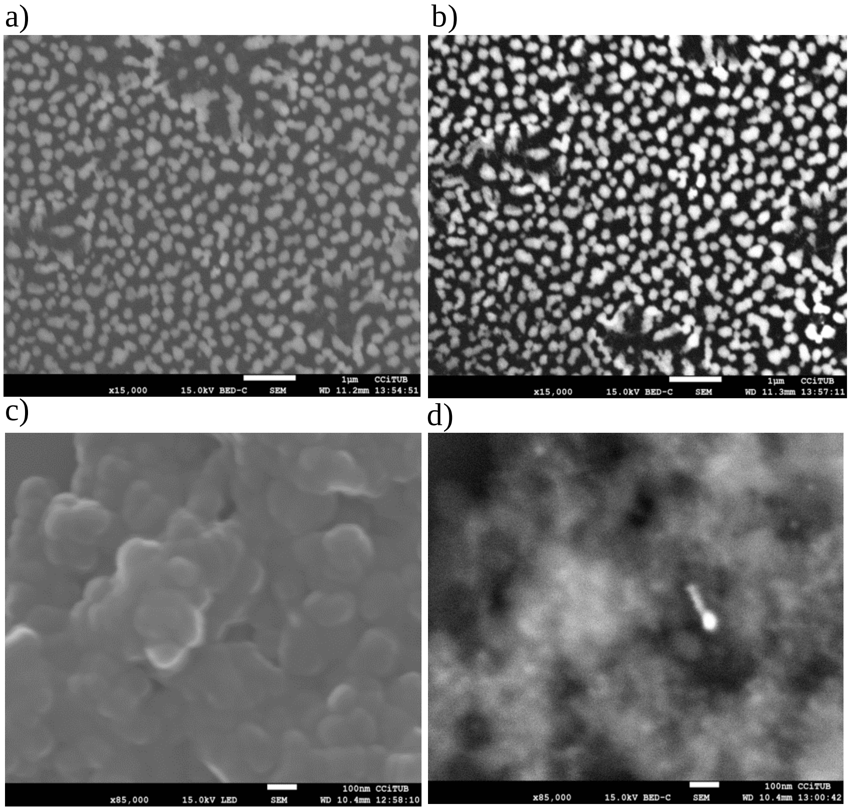
a)
b)
1µm CCiTUB
x15,000 15.0kV BED-C SEM WD 11.2mm 13:54:51
1µm CCiTUB
x15,000 15.0kV BED-C SEM WD 11.3mm 13:57:11
c)
d)
100nm CCiTUB
x85,000 15.0kV LED SEM WD 10.4mm 12:58:10
100nm CCiTUB
x85,000 15.0kV BED-C SEM WD 10.4mm 13:00:42

Figure 8-7. SEM micrographs obtained for **3·AuNP** of **a)** secondary electron image and **b)** backscattered electron image; and for **4·AuNP** of **c)** secondary electron image and **d)** backscattered electron image.

4·AuNP was further analyzed using thermogravimetric analysis (**Figure 8-8**), in order to assess the amount of organic material present in the AuNPs sample. Together with the size of the gold core measured by TEM, is possible to calculate the amount of ligands per nanoparticles, N using the following formula:

$$N = \frac{\pi \rho D^3}{6\ M}$$

Where,
ρ = face centered cubic (fcc) density of gold (19.3 g cm^{-3}),
D = average diameter of the nanoparticles gold core and
M = atomic mass of atomic gold (196.97 g mol^{-1}).

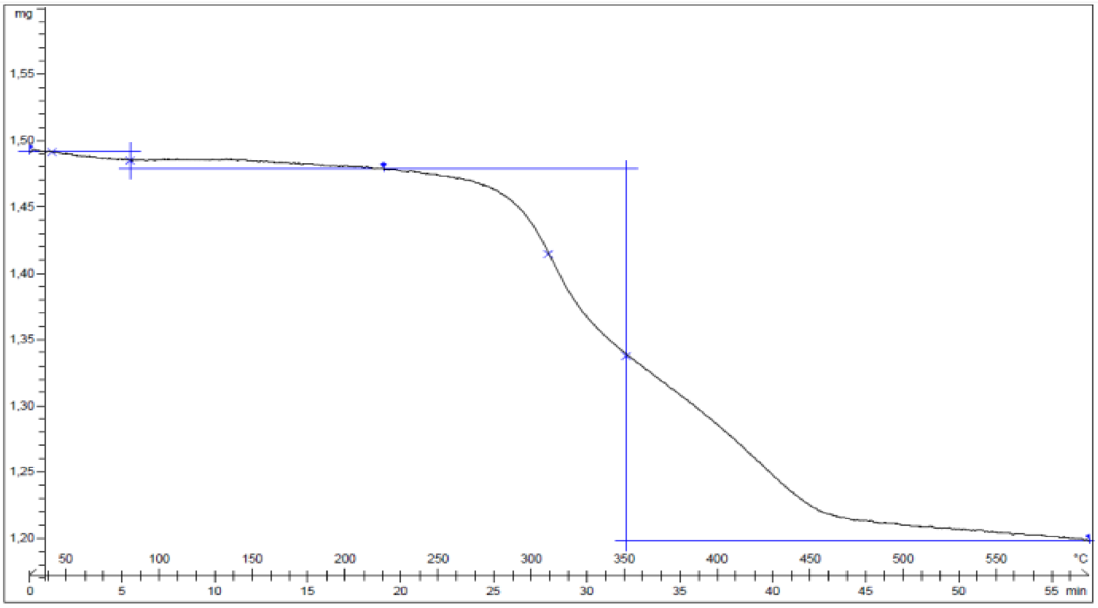

Figure 8-8. Thermogravimetry curve obtained for **4·AuNP**.

The calculated values are tabulated in **Table 8-4**. In the case of **4·AuNP** the amount of ligands resulted in ca 3 ligand molecules per nm^2. In the case of open chain **1·AuNP** synthesized by the same biphasic method, ca 28 ligand molecules per nm^2 were observed [129]. The higher number of ligands can be due to the non-bulky and open chain structure of the ligand, since the open chain structure confers molecular flexibility and both must adopt similar conformations on the surface of the AuNPs. Instead, the number of ligand molecules in **4·AuNP** is dramatically reduced to ca 3 ligand molecules per nm^2 as a consequence of the conformational rigidity of the macrocyclic structures, as well as of the larger dimensions of the polar head on the amphiphilic macrocycle.

Table 8-4. Thermogravimetry results and calculations of amount of ligand per nanoparticle and per area of nanoparticle surface based on the ratio of ligand to gold present in the AuNPs and their gold core size obtained by TEM.

Sample	Total mass (mg)	Ligand mass (mg)	Ligand:Au (mmol)	Average diameter[a] (nm)	Au/NP[b] ratio (mol mol^{-1})	Ligand/NP[b]	Ligand/ nm^2
4·AuNP	1.5	0.3	0.05	5.3	7.6 x 10^{-21}	242	2.7

[a] measured by TEM; [b] Nanoparticle

8.4. Interaction of carboxylate incorporating drugs and AuNPs: loading and release of sodium ibuprofenate

In vitro experiments were performed in order to study the interaction of an anionic drug with the AuNPs and to obtain the release profile of the drug incorporated in the AuNPs. The macrocycles used in the preparation of the AuNPs had already proven to have good recognition ability towards anions (see Section 8.2). Thus, to evaluate the anionic incorporation ability of the macrocycles, **4·2Br** was chosen in order to compare with **1·2Br,** that has the same alkyl chain present in the gold nanoparticles [129]. Sodium ibuprofenate was used as a model drug because it has a carboxylate group, and also because previous reports showed that this drug could be successfully incorporated in AuNPs with imidazolium ligands [129]. Sodium ibuprofenate dissolved in water could be successfully extracted from the aqueous phase into the organic phase containing the **4·AuNP**. This was confirmed by the UV-Visible absorption spectrum of the organic phase (**Figure 8-9**).

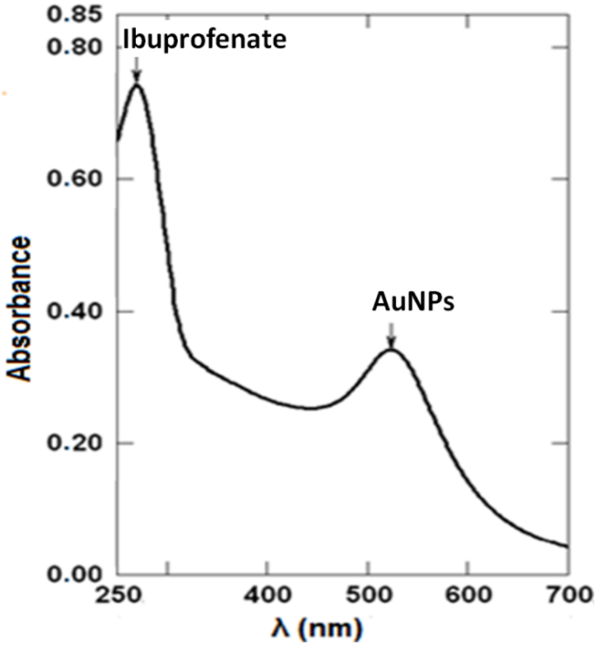

Figure 8-9. UV-Vis absorption spectrum of sodium **ibuprofenate-4·AuNP** from the organic phase

The organic phase was then further washed twice with milliQ water in order to remove the free ibuprofenate molecules that were not incorporated in the **4·AuNP**. Following each washing step, both the organic and aqueous phases were analyzed by UV-Visible absorption spectroscopy. In the organic phase there was a slight decrease in the absorption peak of ibuprofenate, whereas in the collected aqueous phases the peaks corresponding to ibuprofenate were visible, meaning recovery of unbound ibuprofenate from the organic phase. The total amount of ibuprofenate that was extracted into the aqueous phases during the washing steps allowed us to determine the amount of ibuprofenate that remained specifically bound in the **ibuprofenate-4·AuNP** complex. Since we know the initial mass of ibuprofenate, we can therefore say that we loaded 9.8 mg of ibuprofenate in the AuNPs, which was calculated to be ca 85 % of the total sodium ibuprofenate.

After it was confirmed that ibuprofenate could be incorporated in **4·AuNP**, the release rate of ibuprofenate from the **ibuprofenate-4·AuNP** complex was assessed using Franz-type diffusion cells with dialysis membranes, as described previously [33]. The samples were tested at pH 7.4 and 5.5, the first one corresponding to physiological pH and the second one to simulate the human skin pH. The samples were resuspended in Sorensen buffer with the appropriate pH and the release took place at 32°C for pH 5.5 and at 37°C for pH 7.4. The receptor solution used was NaOH 71 mM to ensure the ibuprofenate solubility, thus complying with the SINK conditions, so that the rate of release and diffusion across the dialysis membrane was only due to the release from the AuNPs and not because of low solubility of the drug in the receptor solution. **Figure 8-10** shows the plot of cumulative amount of ibuprofenate versus time, and **Table 8-5** the respective dissociation constant K_D and half life time $t_{1/2}$.

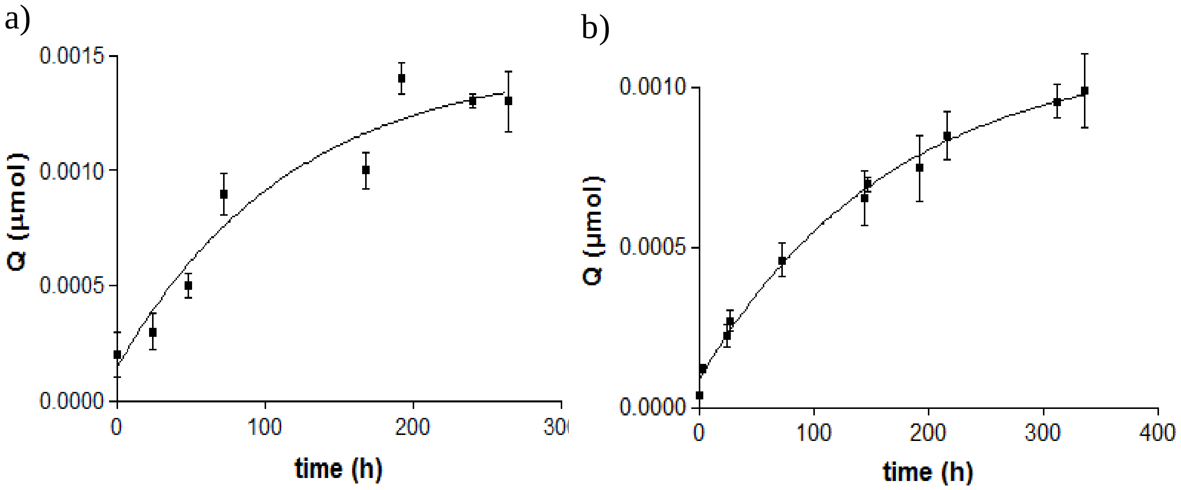

Figure 8-10. Release profile of ibuprofenate from sodium **ibuprofenate-4·AuNP** at (a) pH 5.5 and at (b) pH 7.4.

The kinetic profiles obtained in both cases are typical of a Fickian diffusion. Hence, they can be potentially used in local drug delivery system. When comparing with the previous work with **1·AuNP** [129], in the same conditions, ibuprofenate release kinetics changed in function of the pH, which means that the interaction of the drug with the macrocyclic ligand is different. Thus, it is clear that the limiting factor in this case is the strong interaction of the macrocycle with the drug whereas in the case of the open chain analogue was the pH of the surrounding media. The fact that the pH does not significantly influences the release can be seen as an advantage, because although the skin pH is 5.5, it can present some variations that in the case of the macrocycle will not affect the release rate of the drug from the formulation.

The analysis of the data showed that the release at pH 5.5 followed a first order kinetics, with a value of the dissociation constant K_D of 0.0085 h^{-1}. At physiological conditions, the same kinetics was observed, and the dissociation constant found was 0.0060 h^{-1}.

Table 8-5 Modelistic and amodelistic parameters for the release of ibuprofenate from the **ibuprofenate-4·AuNP**.

	Modelistic		**Amodelistic**	
pH	K_D[a] (h^{-1})	$t_{1/2}$[b] (h)	MRT[c] (h)	Efficiency (%)
5.5	0.0085	82.8	72.9	72.4
7.3	0.0060	116.3	108.5	67.7

[a] Dissociation constant; [b] Half life time; [c] Mean Release Time

Additionally, the amodelistic parameters were calculated and are also shown on **Table 8-6**. The calculated half life time and mean release time (MRT) were lower in the case of the release at pH 5.5 (82.8 h and 72.9 h respectively at pH 5.5 versus 116.3 h and 108.5 h at pH 7.4). The release efficiency shows similar results in both cases. Therefore, Student´s t-test analysis was performed and no significant differences were found between the release at pH 5.5 and 7.4 (**Table 8-6**).

Table 8-6. Results obtained from Student´s t-test

	K_D[a]	MRT[b]	Efficiency
N[c]	3	3	3
P[d]	0.37	0.06	0.2
Mean ± SEM[e] (pH 7.4)	0.01 ± 0.002	72.9 ± 12.12	72.40 ± 3.00
Mean ± SEM[e] (pH 5.5)	0.01 ± 0.0004	108.5 ± 5.77	67.70 ± 1.04
Significant difference	No	No	No

[a] Dissociation constant; [b] Mean Release Time; [c] Number of replicates; [d] probability; [e] Standard error of the mean (SEM)

CHAPTER 9

CHAPTER 9

Conclusions

- ***Functionalization of star-shaped and discoidal polysilicon microparticles with lectins for their adhesion to cell membranes* (Chapter 4)**

  - An optimized protocol for bio-functionalization of polysilicon microparticles with lectins (WGA and Con A), both on surfaces and in suspension, has been developed. The best chemical conditions to afford well-organized self-assembled monolayers (SAM) were found to be using the silane (TESUD) concentration of 135 mM in absolute ethanol for 3 hours and 35 µg/mL of lectin in PBS overnight.
  - Influence of different shapes in bio-functionalization of the microparticles was also observed. In the case of star shaped microparticles, mixed-monolayers of lectins and triglycolamine (TGA) in the ratio (3:1) showed improved functionalization, whereas, in the case of disc shaped microparticles, no improvement was observed.
  - The final yield of the number of bio-functionalized microparticles was between 12-21 % with a major loss of approximately 50 % of microparticles during the activation step. These bio-functionalized microparticles in suspension were stable for three consecutive weeks, stored in PBS at room temperature.
  - Con A bio-functionalized **Batch 2** microparticles adhered to the membrane of the Dictyostelium discoideum (Dicty) whereas, WGA bio-functionalized microparticles did not adhere to the cell membrane of Dicty or HeLa cells.

- ***Functionalization of star-shaped and discoidal polysilicon microparticles with Boronic Acids (BAs) for their adhesion to cell membranes* (Chapter 5)**

  - An optimized protocol for functionalization of polysilicon microparticles with 4-formylphenylboronic acid (PBA), through stable secondary amine bonds has been developed. The best chemical conditions to afford well-organized self-assembled monolayers (SAM) were found to be using the 2 % silane (APTES) solution in absolute ethanol for 3 hours followed by overnight incubation in 5 mg/mL of PBA in absolute ethanol.
  - Interaction of BA functionalized surfaces with carbohydrate, *N*-acetylglucosamine (GlcNAc) was studied on **Batch 1** and **Batch 5** surfaces using ARS, which indicates

stronger interaction between BA and GlcNAc (5 mins of interaction time between BA and GlcNAc was sufficient to displace the ARS molecule).

- Star and disc shaped polysilicon microparticles of different sizes (**Batch 1**, **Batch 2**, **Batch 5** and **Batch 6**) functionalized using BA showed adhesion to the cell membranes of Dicty and HeLa cells.

- ***Functionalization of hexahedral bi-functional microparticles using fluorescent probes for pH sensing in cells*** **(Chapter 6)**

  - Immobilization of pH dependent fluorophores, **Oregon green**, **pHrodo**, **SNARF** and **Alexa fluor** on to polysilicon surfaces was achieved successfully using 2 % silane (APTES) solution in absolute ethanol for 3 hours followed by overnight incubation in 17 µM of the fluorophores in anhydrous DMSO.
  - Immobilization of **pHrodo** on gold surfaces was achieved using 25 mM of thiols with two different chain lengths (2 C and 11 C) in absolute ethanol for 3 hrs, followed by 17 µM of **pHrodo** in anhydrous DMSO for overnight. From which 2 C thiol showed improved and homogenous functionalization.
  - An optimized protocol for the bi-functionalization of two pH dependent fluorophores, **Oregon green** (on polysilicon) and **pHrodo** (on gold) on to a hexahedral bi-functional microparticle (polysilicon-gold) was achieved.

- ***Functionalization of hexahedral bi-functional microparticles using Reactive Oxygen Species (ROS) generator and ROS sensor for Photodynamic therapy (PDT)*** **(Chapter 7)**

  - The selected bio-photosensitizer, Cytochrome c (Cyt c) showed generation of ROS in solution. BODIPY was able to sense the production of ROS from the Cyt c in solution.
  - An optimized protocol for immobilizing Cyt c on to the polysilicon surfaces and BODIPY on gold surfaces and microparticles was achieved. The best chemical conditions for Cyt c immobilization was 135 mM of silane (TESUD) in absolute ethanol followed by overnight incubation of 35 µg/mL of Cyt in PBS and to immobilize BODIPY, 2 % silane (APTES) solution in absolute ethanol for 3 hours followed by overnight incubation in 20 µM of BODIPY in anhydrous DMSO.
  - Protocol for bi-functionalization of ROS generator: Cyt c and ROS sensor: BODIPY on hexahedral bi-functional microparticles was developed.

- ***Delivery of anionic drugs using macrocyclic-imidazolium based gold nanoparticles* (Chapter 8)**

    - Macrocyclic-imidazolium based compound's ability to recognize anions was studied, **3·2Br** has more affinity towards acetate (AcO^-), whereas **4·2PF$_6$** has more affinity for chloride (Cl^-).
    - The influence of the chain length of the imidazolium based macrocycles in the stabilization process of the AuNPs was also studied: **2·2Br**, which has a shorter chain length, does not have the amphiphilic character required to form AuNPs, while **3·2Br** and **4·2Br**, that have longer chains, could be successfully used in the synthesis and stabilization of the **3·AuNP** and **4·AuNP** respectively.
    - The ability of **4·AuNP** to extract and incorporate ibuprofenate from an aqueous phase was calculated to be ca 85 %. The release of ibuprofenate from **ibuprofenate-4·AuNP** complex follows Fickian diffusion, which can be potentially used in local drug delivery applications. The release is slower, indicating that this new AuNPs could be used as vehicle for delivery that requires long-term release.

BIBLIOGRAPHY

BIBLIOGRAPHY

[1] J. Shi, P. W. Kantoff, R. Wooster and O. C. Farokhzad, *Nat. Rev. Cancer*, **2016**, 17, 20–37.

[2] S. Tran, P.-J. DeGiovanni, B. Piel and P. Rai, *Clin. Transl. Med.*, **2017**, 6, 1–21.

[3] R. Sebastian, *J. Cancer Prev. Curr. Res.*, **2017**, 8, 1–6.

[4] M. Haddad, R. Popovtzer, I. Yariv, M. Motiei and D. Fixler, *Harefuah*, **2018**, 157, 232—236.

[5] Y. S. Youn and Y. H. Bae, *Adv. Drug Deliv. Rev.*, **2018**, 130, 3–11.

[6] Y. F. Li and C. Chen, *Small*, **2011**, 7, 2965–2980.

[7] I. Brigger, C. Dubernet and P. Couvreur, *Adv. Drug Deliv. Rev.*, **2012**, 64, 24–36.

[8] J. a Rogers, M. G. Lagally and R. G. Nuzzo, *Nature*, **2011**, 477, 45–53.

[9] X. Zhao, P. Gao, Y. Yan, X. Li, Y. Xing, H. Li, Z. Peng, J. Yang and J. Zeng, *J. Mater. Chem. A*, **2017**, 5, 20202–20207.

[10] G. Huang and Y. Mei, *Small*, **2018**, 14, 1–23.

[11] X. Zhao, Q. Di, X. Wu, Y. Liu, Y. Yu, G. Wei, J. Zhang and Z. Quan, *Chem. Commun.*, **2017**, 53, 11001–11004.

[12] A. Kosloff, O. Heifler, E. Granot and F. Patolsky, *Nano Lett.*, **2016**, 16, 6960–6966.

[13] M. A. Boles, D. Ling, T. Hyeon and D. V. Talapin, *Nat. Mater.*, **2016**, 15, 141–153.

[14] E. Katz and I. Willner, *Angew. Chemie - Int. Ed.*, **2004**, 43, 6042–6108.

[15] S. A. Kumar and M. I. Khan, *J. Nanosci. Nanotechnol.*, **2010**, 10, 4124–4134.

[16] Y. Guo, K. Xu, C. Wu, J. Zhao and Y. Xie, *Chem. Soc. Rev.*, **2015**, 44, 637–646.

[17] P. C. Ray, *Chem. Rev.*, **2010**, 110, 5332–5365.

[18] Y. S. Zhao, H. Fu, A. Peng, Y. Ma, D. Xiao and J. Yao, *Adv. Mater.*, **2008**, 20, 2859–2876.

[19] J. Li and J. Z. Zhang, *Coord. Chem. Rev.*, **2009**, 253, 3015–3041.

[20] I. Khan, K. Saeed and I. Khan, *Arab. J. Chem.*, **2017**, 1–24.

[21] X. Liu, Z. Zhong, Y. Tang and B. Liang, *J. Nanomater.*, **2013**, 2013, 1–7.

[22] N. Sharma, H. Ojha, A. Bharadwaj, D. P. Pathak and R. K. Sharma, *RSC Adv.*, **2015**, 5, 53381–53403.

[23] L. Soler and S. Sánchez, *Nanoscale*, **2014**, 6, 7175–7182.

[24] E. Ellis, S. Moorthy, W.-I. K. Chio and T.-C. Lee, *Chem. Commun.*, **2018**, 54, 4075–4090.

[25] W. Gao and J. Wang, *ACS Nano*, **2014**, 8, 3170–3180.

[26] A. Alabi, A. AlHajaj, L. Cseri, G. Szekely, P. Budd and L. Zou, *npj Clean Water*, **2018**, 10, 1–22.

[27] F. W. Low and C. W. Lai, *Renew. Sustain. Energy Rev.*, **2018**, 82, 103–125.

[28] R. K. Thines, N. M. Mubarak, S. Nizamuddin, J. N. Sahu, E. C. Abdullah and P. Ganesan, *J. Taiwan Inst. Chem. Eng.*, **2017**, 72, 116–133.

[29] A. M. Abdalla, S. Hossain, A. T. Azad, P. M. I. Petra, F. Begum, S. G. Eriksson and A. K. Azad, *Renew. Sustain. Energy Rev.*, **2018**, 82, 353–368.

[30] D. R. Walt, *Nat. Mater.*, **2002**, 1, 17–18.

[31] G. Schmid, *The nature of nanotechnology*, **2008**.

[32] P. J. Cragg, *Supramolecular chemistry-From biological inspiration to biomedical applications*, **2010**.

[33] Y. X. Chen, K. J. Huang and K. X. Niu, *Biosens. Bioelectron.*, **2018**, 99, 612–624.

[34] M. Ahmadi, H. Elmongy, T. Madrakian and M. Abdel-Rehim, *Anal. Chim. Acta*, **2017**, 958, 1–21.

[35] M. Hasanzadeh and N. Shadjou, *Microchim. Acta*, **2017**, 184, 389–414.

[36] M. Holzinger, A. Le Goff and S. Cosnier, *Front. Chem.*, **2014**, 2, 1–10.

[37] P. Pandey, M. Datta and B. D. Malhotra, *Anal. Lett.*, **2008**, 41, 159–209.

[38] J. Wang, *Analyst*, **2005**, 130, 421–426.

[39] J. Lei and H. Ju, *Chem. Soc. Rev.*, **2012**, 41, 2122–2134.

[40] N. G. Sahoo, H. Bao, Y. Pan, M. Pal, M. Kakran, H. K. F. Cheng, L. Li and L. P. Tan, *Chem. Commun.*, **2011**, 47, 5235–5237.

[41] D. F. Williams, *Biomaterials*, **2008**, 29, 2941–2953.

[42] A. Kunzmann, B. Andersson, T. Thurnherr, H. Krug, A. Scheynius and B. Fadeel, *Biochim. Biophys. Acta - Gen. Subj.*, **2011**, 1810, 361–373.

[43] A. Bianco, K. Kostarelos and M. Prato, *Chem. Commun.*, **2011**, 47, 10182–10188.

[44] Q. Zhang, Z. Wu, N. Li, Y. Pu, B. Wang, T. Zhang and J. Tao, *Mater. Sci. Eng. C*, **2017**, 77, 1363–1375.

[45] J. J. Lee, L. S. Yazan and C. A. C. Abdullah, *Int. J. Nanomedicine*, **2017**, 12, 2373–2384.

[46] A. Khan, J. Wang, J. Li, X. Wang, Z. Chen, A. Alsaedi, T. Hayat, Y. Chen and X. Wang, *Environ. Sci. Pollut. Res.*, **2017**, 24, 7938–7958.

[47] J. L. Conyers, **2018**, 261–275.

[48] G. Lamanna, A. Battigelli, C. Ménard-Moyon and A. Bianco, *Nanotechnol. Rev.*, **2012**, 1, 17–29.

[49] Q. Tang, Z. Zhou and Z. Chen, *Nanoscale*, **2013**, 5, 4541–4583.

[50] H. Zhang, *J. Nanosci. Nanotechnol.*, **2012**, 12, 4012–4018.

[51] X. Zhou, L. Yuan, C. Wu, C. Chen, G. Luo, J. Deng and Z. Mao, *RSC Adv.*, **2018**, 8, 17656–17676.

[52] E.-K. Lim, T. Kim, S. Paik, S. Haam, Y.-M. Huh and K. Lee, *Chem. Rev.*, **2015**, 115, 327–394.

[53] H. Huang and J. F. Lovell, *Adv. Funct. Mater.*, **2017**, 27, 1–22.

[54] C. G. Qian, Y. L. Chen, P. J. Feng, X. Z. Xiao, M. Dong, J. C. Yu, Q. Y. Hu, Q. D.

Shen and Z. Gu, *Acta Pharmacol. Sin.*, **2017**, 38, 764–781.

[55] H. Peng, X. Liu, G. Wang, M. Li, K. M. Bratlie, E. Cochran and Q. Wang, *J. Mater. Chem. B*, **2015**, 3, 6856–6870.

[56] K. Kulangara, J. Yang, M. Chellappan, Y. Yang and K. W. Leong, *PLoS One*, **2014**, 9, 1–12.

[57] A. Jaiganesh, Y. Narui, R. Araya-Secchi and M. Sotomayor, *Cold Spring Harb. Perspect. Biol.*, **2017**, 24, 1–25.

[58] O. Penon, S. Novo, S. Durán, E. Ibañez, C. Nogués, J. Samitier, M. Duch, J. A. Plaza and L. Pérez-Garcia, *Bioconjug. Chem.*, **2012**, 23, 2392–2402.

[59] E. Fernandez-Rosas, R. Gómez, E. Ibañez, L. Barrios, M. Duch, J. Esteve, C. Nogués and J. A. Plaza, *Small*, **2009**, 5, 2433–2439.

[60] A. A. Khalili and M. R. Ahmad, *Int. J. Mol. Sci.*, **2015**, 16, 18149–18184.

[61] C. Cerutti and A. J. Ridley, *Exp. Cell Res.*, **2017**, 358, 31–38.

[62] N. G. Maremanda, K. Roy, R. K. Kanwar, V. Shyamsundar, V. Ramshankar, A. Krishnamurthy, S. Krishnakumar and J. R. Kanwar, *Biomicrofluidics*, **2017**, 11, 2015–2017.

[63] G. Bendas and L. Borsig, *Int. J. Cell Biol.*, **2012**, 2012, 1–10.

[64] J. C. M. Morel, C. C. Park, K. Zhu, P. Kumar, J. H. Ruth and A. E. Koch, *J. Biol. Chem.*, **2002**, 277, 34679–34691.

[65] H. Perinpanayagam, R. Zaharias, C. Stanford, R. Brand, J. Keller and G. Schneider, *J. Orthop. Res.*, **2001**, 19, 993–1000.

[66] U. Cavallaro and G. Christofori, *Biochim. Biophys. Acta - Rev. Cancer*, **2001**, 1552, 39–45.

[67] S. Blankenberg, S. Barbaux and L. Tiret, *Atherosclerosis*, **2003**, 170, 191–203.

[68] E. Farahani, H. K. Patra, J. R. Jangamreddy, I. Rashedi, M. Kawalec, R. K. Rao Pariti, P. Batakis and E. Wiechec, *Carcinogenesis*, **2014**, 35, 747–759.

[69] T. Okegawa, R.-C. Pong, Y. Li and J.-T. Hsieh, *Acta Biochim. Pol.*, **2004**, 51, 445–457.

[70] J. P. Thiery, *Comptes Rendus Phys.*, **2003**, 4, 289–304.

[71] M. Murphy, *Genet. Eng. Biotechnol. News*, **2017**, 37, 18–19.

[72] J. Y. Chen, L. S. Penn and J. Xi, *Biosens. Bioelectron.*, **2018**, 99, 593–602.

[73] K. Ohashi, S. Fujiwara and K. Mizuno, *J. Biochem.*, **2017**, 161, 245–254.

[74] B. L. Frey, C. E. Jordan, R. M. Corn and S. Komguth, *Anal. Chem.*, **1995**, 67, 4452–4457.

[75] I. H. Madshus, *Biochem. J.*, **1988**, 250, 1–8.

[76] J. A. Mindell, *Annu. Rev. Physiol.*, **2012**, 74, 69–86.

[77] D. Lagadic-Gossmann, L. Huc and V. Lecureur, *Cell Death Differ.*, **2004**, 11, 953–961.

[78] A. Hulikova, A. L. Harris, R. D. Vaughan-Jones and P. Swietach, *J. Cell. Physiol.*, **2013**, 228, 743–752.

[79] B. A. Webb, M. Chimenti, M. P. Jacobson and D. L. Barber, *Nat. Rev. Cancer*, **2011**, 11, 671–677.

[80] J. Barar and Y. Omidi, *BioImpacts*, **2013**, 3, 149–162.

[81] I. Parolini, C. Federici, C. Raggi, L. Lugini, S. Palleschi, A. De Milito, C. Coscia, E. Iessi, M. Logozzi, A. Molinari, M. Colone, M. Tatti, M. Sargiacomo and S. Fais, *J. Biol. Chem.*, **2009**, 284, 34211–34222.

[82] P. Montcourrier, P. H. Mangeat, C. Valembois, G. Salazar, a Sahuquet, C. Duperray and H. Rochefort, *J. Cell Sci.*, **1994**, 107 (Pt 9, 2381–91.

[83] L. C. Ho, C. M. Ou, C. L. Li, S. Y. Chen, H. W. Li and H. T. Chang, *J. Mater. Chem. B*, **2013**, 1, 2425–2432.

[84] L. Yin, C. He, C. Huang, W. Zhu, X. Wang, Y. Xu and X. Qian, *Chem. Commun.*, **2012**, 48, 4486–4488.

[85] S. Shekhar, A. Klaver, C. G. Figdor, V. Subramaniam and J. S. Kanger, *Sensors Actuators, B Chem.*, **2010**, 148, 531–538.

[86] J. Han and K. Burgess, *Chem. Rev.*, **2009**, 110, 2709–2728.

[87] M. J. Marín, F. Galindo, P. Thomas and D. A. Russell, *Angew. Chemie - Int. Ed.*, **2012**, 51, 9657–9661.

[88] N. Torras, J. P. Agusil, P. Vázquez, M. Duch, A. M. Hernández-Pinto, J. Samitier, E. J. De La Rosa, J. Esteve, T. Suárez, L. Pérez-García and J. A. Plaza, *Adv. Mater.*, **2016**, 28, 1449–1454.

[89] D. E. J. G. J. Dolmans, D. Fukumura and R. K. Jain, *Nat. Rev. Cancer*, **2003**, 3, 380–387.

[90] G. Calixto, J. Bernegossi, L. de Freitas, C. Fontana and M. Chorilli, *Molecules*, **2016**, 21, 1–18.

[91] J. Soriano, I. Mora-Espí, M. E. Alea-Reyes, L. Pérez-García, L. Barrios, E. Ibáñez and C. Nogués, *Sci. Rep.*, **2017**, 7, 1–13.

[92] W. T. Li, J. R. Peng, L. W. Tan, J. Wu, K. Shi, Y. Qu, X. W. Wei and Z. Y. Qian, *Biomaterials*, **2016**, 106, 119–133.

[93] K. Kim, P. A. Watson, S. Jebiwott, A. J. Somma, S. P. La Rosa, D. Mehta, K. S. Murray, H. Lilja, D. Ulmert, A. Scherz and J. Coleman, *Cancer Res.*, **2016**, 76, 3389–3389.

[94] S. Beack, W. H. Kong, H. S. Jung, I. H. Do, S. Han, H. Kim, K. S. Kim, S. H. Yun and S. K. Hahn, *Acta Biomater.*, **2015**, 26, 295–305.

[95] M. Bassetti, D. Schär, B. Wicki, S. Eick, C. A. Ramseier, N. B. Arweiler, A. Sculean and G. E. Salvi, *Clin. Oral Implants Res.*, **2014**, 25, 279–287.

[96] A. Kawczyk-Krupka, A. M. Bugaj, W. Latos, K. Zaremba, K. Wawrzyniec and A. Sieroń, *Photodiagnosis Photodyn. Ther.*, **2015**, 12, 545–553.

[97] T. J. Dougherty, C. J. Gomer, B. W. Henderson, G. Jori, D. Kessel, M. Korbelik, J. Moan and Q. Peng, *J. Clin. Oncol.*, **1988**, 6, 380–391.

[98] H. Abrahamse and M. R. Hamblin, *Biochem. J.*, **2016**, 473, 347–364.

[99] A. P. Castano, T. N. Demidova and M. R. Hamblin, *Photodiagnosis Photodyn. Ther.*,

2004, 1, 279–293.

[100] Y. N. Konan, R. Gurny and E. Allémann, *J. Photochem. Photobiol. B Biol.*, **2002**, 66, 89–106.

[101] J. Melorose, R. Perroy and S. Careas, *Statew. Agric. L. Use Baseline 2015*, **2015**, 1, 376–400.

[102] R. R. Allison, G. H. Downie, R. Cuenca, X. H. Hu, C. J. H. Childs and C. H. Sibata, *Photodiagnosis Photodyn. Ther.*, **2004**, 1, 27–42.

[103] J. F. Lovell, T. W. B. Liu, J. Chen and G. Zheng, *Chem. Rev.*, **2010**, 110, 2839–2857.

[104] J. Lin, S. Wang, P. Huang, Z. Wang, S. Chen, G. Niu, W. Li, J. He, D. Cui, G. Lu, X. Chen and Z. Nie, *ACS Nano*, **2013**, 7, 5320–5329.

[105] P. Huang, J. Lin, S. Wang, Z. Zhou, Z. Li, Z. Wang, C. Zhang, X. Yue, G. Niu, M. Yang, D. Cui and X. Chen, *Biomaterials*, **2013**, 34, 4643–4654.

[106] A.-C. Niehoff, A. Moosmann, J. Söbbing, A. Wiehe, D. Mulac, C. A. Wehe, O. Reifschneider, F. Blaske, S. Wagner, M. Sperling, H. von Briesen, K. Langer and U. Karst, *Metallomics*, **2014**, 6, 77–81.

[107] O. Penon, M. J. Marín, D. A. Russell and L. Pérez-García, *J. Colloid Interface Sci.*, **2017**, 496, 100–110.

[108] M. E. Alea-Reyes, O. Penon, P. García Calavia, M. J. Marín, D. A. Russell and L. Pérez-García, *J. Colloid Interface Sci.*, **2018**, 521, 81–90.

[109] M. E. Alea-Reyes, J. Soriano, I. Mora-Espí, M. Rodrigues, D. A. Russell, L. Barrios and L. Pérez-García, *Colloids Surfaces B Biointerfaces*, **2017**, 158, 602–609.

[110] O. Penon, T. Patiño, L. Barrios, C. Nogués, D. B. Amabilino, K. Wurst and L. Pérez-García, *ChemistryOpen*, **2015**, 4, 127–136.

[111] O. Penon, M. J. Marín, D. B. Amabilino, D. A. Russell and L. Pérez-García, *J. Colloid Interface Sci.*, **2016**, 462, 154–165.

[112] M. E. Alea-Reyes, M. Rodrigues, A. Serrà, M. Mora, M. L. Sagristá, A. González, S. Durán, M. Duch, J. A. Plaza, E. Vallés, D. A. Russell and L. Pérez-García, *RSC Adv.*, **2017**, 7, 16963–16976.

[113] J. Fan and P. K. Chu, *Small*, **2010**, 6, 2080–2098.

[114] S. Manju and K. Sreenivasan, *J. Colloid Interface Sci.*, **2012**, 368, 144–151.

[115] E. C. Dreaden, A. M. Alkilany, X. Huang, C. J. Murphy and M. A. El-Sayed, *Chem. Soc. Rev.*, **2012**, 41, 2740–2779.

[116] P. Ghosh, G. Han, M. De, C. K. Kim and V. M. Rotello, *Adv. Drug Deliv. Rev.*, **2008**, 60, 1307–1315.

[117] V. Voliani, F. Ricci, G. Signore, R. Nifosì, S. Luin, F. Beltram, R. Nifosi and R. Nifosí, *Recent Pat. nanomedicine*, **2012**, 2, 34–44.

[118] Y. Malam, M. Loizidou and A. M. Seifalian, *Trends Pharmacol. Sci.*, **2009**, 30, 592–599.

[119] J. L. Fenton, J. M. Hodges and R. E. Schaak, *Chem. Mater.*, **2017**, 29, 6168–6177.

[120] E. Amirthalingam, M. Rodrigues, L. Casal-Dujat, A. C. Calpena, D. B. Amabilino, D. Ramos-López and L. Pérez-García, *J. Colloid Interface Sci.*, **2015**, 437, 132–139.

[121] J. Turkevich, J., Stevenson, P. C., Hillier, *Discuss. Faraday Soc.*, **1951**, 11, 55–75.

[122] M. Brust, M. Walker, D. Bethell, D. J. Schiffrin and R. Whyman, *J. Chem. Soc., Chem Commun.*, **1994**, 801–802.

[123] K. Saha, S. S. Agasti, C. Kim, X. Li and V. M. Rotello, *Chem. Rev.*, **2012**, 112, 2739–2779.

[124] T. Curry, R. Kopelman, M. Shilo and R. Popovtzer, *Contrast Media Mol. Imaging*, **2014**, 9, 53–61.

[125] N. Li, P. Zhao, N. Liu, M. Echeverria, S. Moya, L. Salmon, J. Ruiz and D. Astruc, *Chem. - A Eur. J.*, **2014**, 20, 8363–8369.

[126] X. Huang and M. A. El-Sayed, *J. Adv. Res.*, **2010**, 1, 13–28.

[127] S. Rana, A. Bajaj, R. Mout and V. M. Rotello, *Adv. Drug Deliv. Rev.*, **2012**, 64, 200–216.

[128] B. Duncan, C. Kim and V. M. Rotello, *J. Control. Release*, **2010**, 148, 122–127.

[129] L. Casal-Dujat, M. Rodrigues, A. Yagüe, A. C. Calpena, D. B. Amabilino, J. González-Linares, M. Borràs and L. Pérez-García, *Langmuir*, **2012**, 28, 2368–2381.

[130] M. Rodrigues, A. C. Calpena, D. B. Amabilino, D. Ramos-López, J. de Lapuente and L. Pérez-García, *RSC Adv.*, **2014**, 4, 9279.

[131] M. E. Alea-Reyes, A. González, A. C. Calpena, D. Ramos-López, J. de Lapuente and L. Pérez-García, *J. Colloid Interface Sci.*, **2017**, 502, 172–183.

[132] J. Wiley, **2009**, 393–397.

[133] L. Casal-Dujat, O. Penon, C. Rodríguez-Abreu, C. Solans and L. Pérez-García, *New J. Chem.*, **2012**, 36, 558–561.

[134] J. R. Siqueira, L. Caseli, F. N. Crespilho, V. Zucolotto and O. N. Oliveira, *Biosens. Bioelectron.*, **2010**, 25, 1254–1263.

[135] D. Samanta and A. Sarkar, *Chem. Soc. Rev.*, **2011**, 40, 2567–2592.

[136] F. Cheng, J. Shang and D. M. Ratner, *Bioconjug. Chem.*, **2011**, 22, 50–57.

[137] H. Wang, Y. Zhang, X. Yuan, Y. Chen and M. Yan, *Bioconjug. Chem.*, **2011**, 22, 26–32.

[138] T. Ekblad and B. Liedberg, *Curr. Opin. Colloid Interface Sci.*, **2010**, 15, 499–509.

[139] M. Dettin, N. Muncan, A. Bugatti, F. Grezzo, R. Danesin and M. Rusnati, *Bioconjug. Chem.*, **2011**, 22, 1753–1757.

[140] J. Sołoducho, J. Cabaj and A. Świst, *Sensors*, **2009**, 9, 7733–7752.

[141] M. Frasconi, F. Mazzei and T. Ferri, **2010**, 1545–1564.

[142] C. Haensch, S. Hoeppener and U. S. Schubert, *Chem. Soc. Rev.*, **2010**, 39, 2323–2334.

[143] A. Ulman, *Chem. Rev.*, **1996**, 96, 1533–1554.

[144] J. C. Love, L. A. Estroff, J. K. Kriebel, R. G. Nuzzo and G. M. Whitesides, *Self-assembled monolayers of thiolates on metals as a form of nanotechnology*, **2005**, vol. 105.

[145] C. D. Hodneland, Y.-S. Lee, D.-H. Min and M. Mrksich, *Proc. Natl. Acad. Sci.*, **2002**, 99, 5048–5052.

[146] N. K. Chaki and K. Vijayamohanan, *Biosens. Bioelectron.*, **2002**, 17, 1–12.

[147] J. J. Gooding and S. Ciampi, *Chem. Soc. Rev.*, **2011**, 40, 2704–2718.

[148] T. Wink, S. J. van Zuilen, A. Bult and W. P. van Bennekom, *Analyst*, **1997**, 122, 43R–50R.

[149] K. C. Grabar, K. R. Brown, C. D. Keating, S. J. Stranick, S. L. Tang and M. J. Natan, *Anal. Chem.*, **1997**, 69, 471–477.

[150] S. A. Claridge, W. S. Liao, J. C. Thomas, Y. Zhao, H. H. Cao, S. Cheunkar, A. C. Serino, A. M. Andrews and P. S. Weiss, *Chem. Soc. Rev.*, **2013**, 42, 2725–2745.

[151] R. E. Morris and P. S. Wheatley, *Angew. Chemie - Int. Ed.*, **2008**, 47, 4966–4981.

[152] V. Stroganov, J. Pant, G. Stoychev, A. Janke, D. Jehnichen, A. Fery, H. Handa and L. Ionov, *Adv. Funct. Mater.*, **2018**, 28, 1–8.

[153] I. A. Ovid’ko, R. Z. Valiev and Y. T. Zhu, *Prog. Mater. Sci.*, **2018**, 94, 462–540.

[154] D. B. Weibel, W. R. DiLuzio and G. M. Whitesides, *Nat. Rev. Microbiol.*, **2007**, 5, 209–218.

[155] E. Fernández-Rosas, A. Baldi, E. Ibañez, L. Barrios, S. Novo, J. Esteve, J. A. Plaza, M. Duch, R. Gómez, O. Castell, C. Nogués and C. Fernández-Sánchez, *Langmuir*, **2011**, 27, 8302–8308.

[156] O. Penon, S. Novo, S. Durán, E. Ibañez, Carme Nogués, J. Samitier, M. Duch, J. A. Plaza and L. Pérez-García, *Bioconjug. Chem.*, **2012**, 23, 2392–2402.

[157] N. X. Arndt, J. Tiralongo, P. D. Madge, M. Von Itzstein and C. J. Day, *J. Cell. Biochem.*, **2011**, 112, 2230–2240.

[158] N. Sharon and H. Lis, *Science.*, **1989**, 246, 227–234.

[159] S. Elgavish and B. Shaanan, *Trends Biochem. Sci.*, **1997**, 22, 462–467.

[160] R. T. Lee and Y. C. Lee, *Glycoconj. J.*, **2000**, 17, 543–551.

[161] N. Sharon, *FEBS Lett.*, **1987**, 217, 145–157.

[162] M. A. Lemmon, *Nat. Rev. Mol. Cell Biol.*, **2008**, 9, 99–111.

[163] W. I. Weis and K. Drickamer, **1996**, 65, 441–471.

[164] I. J. Goldstein and C. E. Hayes, *Adv. Carbohydr. Chem. Biochem.*, **1978**, 35, 127–340.

[165] C. Ke, H. Destecroix, M. P. Crump and A. P. Davis, *Nat. Chem.*, **2012**, 4, 718–723.

[166] E. Evans and A. Leung, *J. Cell Biol.*, **1984**, 98, 1201–1208.

[167] Y. Nagata and M. M. Burger, *J. Biol. Chem.*, **1972**, 247, 2248–2250.

[168] Y. Nagata and M. M. Burger, *J. Biol. Chem.*, **1974**, 249, 3116–3122.

[169] D. Schwefel, C. Maierhofer, J. G. Beck, S. Seeberger, K. Diederichs, H. M. Möller, W. Welte and V. Wittmann, *J. Am. Chem. Soc.*, **2010**, 132, 8704–8719.

[170] M. D. C. Portillo-Téllez, M. Bello, G. Salcedo, G. Gutiérrez, V. Gómez-Vidales and E. García-Hernández, *Biophys. J.*, **2011**, 101, 1423–1431.

[171] K. Harata, H. Nagahora and Y. Jigami, *Acta Crystallogr. Sect. D Biol. Crystallogr.*, **1995**, 51, 1013–1019.

[172] K. J. Neurohr, N. Lacelle, H. H. Mantsch and I. C. Smith, *Biophys. J.*, **1980**, 32, 931–

938.

[173] J. -P Privat and M. Monsigny, *Eur. J. Biochem.*, **1975**, 60, 555–567.

[174] S. Lehrer and G. D. Fasman, *J. Biol. Chem.*, **1967**, 242, 4644–4651.

[175] R. Lotan and N. Sharon, *Biochem. Biophys. Res. Commun.*, **1973**, 55, 1340–1346.

[176] J. S. Anderson, M. Matsuhashi, M. A. Haskin and J. L. Strominger, **1967**, 242, 3660–3666.

[177] B. de Kruijff, V. van Dam and E. Breukink, *Prostaglandins Leukot. Essent. Fat. Acids*, **2008**, 79, 117–121.

[178] S. Mesnage, M. Dellarole, N. J. Baxter, J. B. Rouget, J. D. Dimitrov, N. Wang, Y. Fujimoto, A. M. Hounslow, S. Lacroix-Desmazes, K. Fukase, S. J. Foster and M. P. Williamson, *Nat. Commun.*, **2014**, 5, 1–11.

[179] E. Severi, D. W. Hood and G. H. Thomas, *Microbiology*, **2007**, 153, 2817–2822.

[180] N. M. Varki and A. Varki, *Lab. Investig.*, **2007**, 87, 851–857.

[181] R. Schauer, *Trends Biochem. Sci.*, **1985**, 10, 357–360.

[182] J. S. Rush, R. J. Edgar, P. Deng, J. Chen, H. Zhu, N. M. Van Sorge, A. J. Morris, K. V Korotkov and N. Korotkova, **2017**, 1–35.

[183] J. B. Konopka, *Scientifica (Cairo).*, **2012**, 2012, 631–632.

[184] R. E. Schwarz, D. C. Wojciechowicz, A. I. Picon, M. A. Schwarz and P. B. Paty, *Br. J. Cancer*, **1999**, 80, 1754–1762.

[185] J. Baeten, A. Suresh, A. Johnson, K. Patel, M. Kuriakose, A. Flynn and D. Kademani, *Transl. Oncol.*, **2014**, 7, 213–220.

[186] N. Lochner, F. Pittner, M. Wirth and F. Gabor, *Pharm. Res.*, **2003**, 20, 833–839.

[187] M. Inbar and L. Sachs, *Proc. Natl. Acad. Sci. U. S. A.*, **1969**, 63, 1418–25.

[188] S. J. Hamodrakas, P. N. Kanellopoulos, K. Pavlou and P. A. Tucker, *J. Struct. Biol.*, **1997**, 118, 23–30.

[189] K. D. Hardman and C. F. Ainsworth, *Biochemistry*, **1972**, 11, 4910–4919.

[190] J. W. Becker, G. M. Edelman, N. Reeke, J. L. Wang and B. a Cunningham, *Biol. Chem.*, **1975**, 260, 1513–1524.

[191] D. K. Mandal, L. Bhattacharyya, S. H. Koenig, R. D. Brown, S. Oscarson and C. F. Brewer, *Biochemistry*, **1994**, 33, 1157–1162.

[192] R. Loris, T. Hamelryck, J. Bouckaert and L. Wyns, *Biochim. Biophys. Acta - Protein Struct. Mol. Enzymol.*, **1998**, 1383, 9–36.

[193] S. J. Annesley and P. R. Fisher, *Mol. Cell. Biochem.*, **2009**, 329, 73–91.

[194] J. S. King and R. H. Insall, *Trends Cell Biol.*, **2009**, 19, 523–530.

[195] I. Eichinger, J. A. Pachebat, G. Glöckner, M. A. Rajandream, R. Sucgang, M. Berriman, J. Song, R. Olsen, K. Szafranski, Q. Xu, B. Tunggal, S. Kummerfeld, M. Madera, B. A. Konfortov, F. Rivero, A. T. Bankier, R. Lehmann, N. Hamlin, R. Davies, P. Gaudet, P. Fey, K. Pilcher, G. Chen, D. Saunders, E. Sodergren, P. Davis, A. Kerhornou, X. Nie, N. Hall, C. Anjard, L. Hemphill, N. Bason, P. Farbrother, B. Desany, E. Just, T. Morio, R. Rost, C. Churcher, J. Cooper, S. Haydock, N. Van

Driessche, A. Cronin, I. Goodhead, D. Muzny, T. Mourier, A. Pain, M. Lu, D. Harper, R. Lindsay, H. Hauser, K. James, M. Quiles, M. Madan Babu, T. Saito, C. Buchrieser, A. Wardroper, M. Felder, M. Thangavelu, D. Johnson, A. Knights, H. Loulseged, K. Mungall, K. Oliver, C. Price, M. A. Quail, H. Urushihara, J. Hernandez, E. Rabbinowitsch, D. Steffen, M. Sanders, J. Ma, Y. Kohara, S. Sharp, M. Simmonds, S. Spiegler, A. Tivey, S. Sugano, B. White, D. Walker, J. Woodward, T. Winckler, Y. Tanaka, G. Shaulsky, M. Schleicher, G. Weinstock, A. Rosenthal, E. C. Cox, R. L. Chisholm, R. Gibbs, W. F. Loomis, M. Platzer, R. R. Kay, J. Williams, P. H. Dear, A. A. Noegel, B. Barrell and A. Kuspa, *Nature*, **2005**, 435, 43–57.

[196] P. Devreotes, *Science.*, **1989**, 245, 1054–1058.

[197] T. T. Puck, P. I. Marcus and S. J. Cieciura, *J. Exp. Med.*, **1955**, 103, 273–284.

[198] T. Terasima and L. J. Tolmach, *Exp. Cell Res.*, **1963**, 30, 344–362.

[199] J. A. Titus, R. Haugland, S. O. Sharrow and D. M. Segal, **1982**, 50, 193–204.

[200] J. R. Unruh, G. Gokulrangan, G. S. Wilson and C. K. Johnson, *Photochem. Photobiol.*, **2005**, 81, 682–690.

[201] O. Penon, D. Siapkas, S. Novo, S. Durán, G. Oncins, A. Errachid, L. Barrios, C. Nogués, M. Duch, J. A. Plaza and L. Pérez-García, *Colloids Surfaces B Biointerfaces*, **2014**, 116, 104–113.

[202] G. L. Witucki, *J. Coatings Technol.*, **1993**, 65, 57–60.

[203] S. Sterman and J. G. Marsden, *Ind. Eng. Chem.*, **1966**, 58, 33–37.

[204] F. S. Eigler, J. Georger, Suresh K. Bhatia, J. Calvert, L. C. Shriver-Lake and R. Bredehorst, *United States Pat. 5,077,210*.

[205] A. Hozumi, H. Taoda, T. Saito and N. Shirahata, *Surf. Interface Anal.*, **2008**, 40, 408–411.

[206] A. Hozumi, M. Inagaki and N. Shirahata, *Surf. Sci.*, **2006**, 600, 4044–4047.

[207] A. Hozumi, M. Inagaki and N. Shirahata, *Appl. Surf. Sci.*, **2006**, 252, 6111–6114.

[208] P. Silberzan, L. Léger, D. Ausserré and J. J. Benattar, *Langmuir*, **1991**, 7, 1647–1651.

[209] J. Sagiv, *J. Am. Chem. Soc.*, **1980**, 102, 92–98.

[210] R. E. H. Miles, J. F. Davies and J. P. Reid, *Phys. Chem. Chem. Phys.*, **2016**, 18, 19847–19858.

[211] D. Risović, A. Penezić, V. Čadež, S. Šegota and B. Gašparović, *RSC Adv.*, **2016**, 6, 52475–52484.

[212] F. B. Sheinerman, R. Norel and B. Honig, *Curr. Opin. Struct. Biol.*, **2000**, 10, 153–159.

[213] H. Nakamura, *Q. Rev. Biophys.*, **1996**, 29, 1–90.

[214] H.-X. Zhou and X. Pang, *Chem. Rev.*, **2018**, 118, 1691–1741.

[215] K. Ziani, J. Oses, V. Coma and J. I. Maté, *LWT - Food Sci. Technol.*, **2008**, 41, 2159–2165.

[216] C. Lin, C. Yu, Y. Lin and W. Tseng, *Anal. Chem.*, **2010**, 82, 6830–6837.

[217] B. Batteiger, W. J. Newhall V and R. B. Jones, *J. Immunol. Methods*, **1982**, 55, 297–307.

[218] D. K. Chou, R. Krishnamurthy, T. W. Randolph, J. F. Carpenter and M. C. Manning, *J. Pharm. Sci.*, **2005**, 94, 1368–1381.

[219] E. Fernández-Rosas, R. Gómez, E. Ibañez, L. Barrios, M. Duch, J. Esteve, J. A. Plaza and C. Nogués, *Biomed. Microdevices*, **2010**, 12, 371–379.

[220] H. P. Erickson, *Biol. Proced. Online*, **2009**, 11, 32–51.

[221] A. G. Podoleanu, G. M. Dobre, D. J. Webb and D. A. Jackson, *Opt. Lett.*, **1996**, 21, 1789–1791.

[222] G. B. Airy, *Philos. Mag.*, **1832**, 1, 20–30.

[223] C. Logofatu, C. C. Negrila, R. V Ghita, F. Ungureanu, C. Cotirlan and C. G. A. S. M. and M. F. Lazarescu, *Cryst. Silicon*, **2011**, 1, 2–42.

[224] C. C. Negrila, C. Cotirlan, F. Ungureanu, C. Logofatu, R. V. Ghita and M. F. Lazarescu, *J. Optoelectron. Adv. Mater.*, **2008**, 10, 1379–1383.

[225] X. H. Sun, S. D. Wang, N. B. Wong, D. D. D Ma, S. T. Lee and B. K. Teo, **2003**, 42, 5213–5216.

[226] R. Molday, R. Jaffe and D. McMahon, *J. Cell Biol.*, **1976**, 71, 314–322.

[227] G. G. Weeks, *J. Biol. Chem.*, **1975**, 250, 6706–6710.

[228] C. M. West and D. Mcmahon, **1977**, 74, 264–273.

[229] G. Weeks, *Exp. Cell Res.*, **1973**, 76, 467–470.

[230] E. Eitle and G. Gerisch, *Cell Differ.*, **1977**, 6, 339–346.

[231] C. M. West and D. McMahon, *J. Cell Biol.*, **1977**, 74, 264–273.

[232] W. Zhai, X. Sun, T. D. James and J. S. Fossey, *Chem. - An Asian J.*, **2015**, 10, 1836–1848.

[233] B. Pappin, M. J. and T. A., *Carbohydrates - Compr. Stud. Glycobiol. Glycotechnol.*, **2012**, 1, 38–54.

[234] A. Manuscript and S. Molecules, *Med. Res. Rev.*, **2011**, 30, 171–257.

[235] Z. Bie, Y. Chen, J. Ye, S. Wang and Z. Liu, *Angew. Chemie - Int. Ed.*, **2015**, 54, 10211–10215.

[236] C. Lü, H. Li, H. Wang and Z. Liu, *Anal. Chem.*, **2013**, 85, 2361–2369.

[237] A. Stephenson-Brown, S. Yong, M. H. Mansor, Z. Hussein, N.-C. Yip, P. M. Mendes, J. S. Fossey and F. J. Rawson, *Chem. Commun.*, **2015**, 51, 17213–17216.

[238] M. Rosenberg, J. L. Wiebers and P. T. Gilham, *Biochemistry*, **1972**, 11, 3623–3628.

[239] A. Pal, M. Bérubé and D. G. Hall, *Angew. Chemie - Int. Ed.*, **2010**, 49, 1492–1495.

[240] W. Zhang, D. I. Bryson, J. B. Crumpton, J. Wynn and W. L. Santos, *Chem. Commun.*, **2013**, 49, 2436–2438.

[241] M. S. Melicher, A. S. Walker, J. Shen, S. J. Miller and A. Schepartz, *Org. Lett.*, **2015**, 17, 4718–4721.

[242] H. Peng, X. Ning, G. Wei, S. Wang, G. Dai and A. Ju, *Carbohydr. Polym.*, **2018**, 195, 349–355.

[243] R. Aharoni, M. Bronstheyn, A. Jabbour, B. Zaks, M. Srebnik and D. Steinberg,

Bioorg. Med. Chem., **2008**, 16, 1596–1604.

[244] J. Yoon and A. W. Czarnik, *J. Am. Chem. Soc.*, **1992**, 114, 5874–5875.

[245] A. Jabbour, D. Steinberg, V. M. Dembitsky, A. Moussaieff, B. Zaks and M. Srebnik, *J. Med. Chem.*, **2004**, 47, 2409–2410.

[246] B. D. Smith, S. J. Gardiner, T. A. Munro, M.-F. Paugam and J. A. Riggs, *J. Incl. Phenom. Mol. Recognit. Chem.*, **1998**, 32, 121–131.

[247] W. Yang, X. Gao and B. Wang, *Med. Res. Rev.*, **2003**, 23, 346–368.

[248] J. Adams and M. Kauffman, *Cancer Invest.*, **2004**, 22, 304–311.

[249] B. Fabre and F. Hauquier, *Langmuir*, **2017**, 33, 8693–8699.

[250] B. C. Dickinson and C. J. Chang, *J. Am. Chem. Soc.*, **2008**, 130, 9638–9639.

[251] M. C. Y. Chang, A. Pralle, E. Y. Isacoff and C. J. Chang, *J. Am. Chem. Soc.*, **2004**, 126, 15392–15393.

[252] W. Zhan, Y. Qu, T. Wei, C. Hu, Y. Pan, Q. Yu and H. Chen, *ACS Appl. Mater. Interfaces,* **2018**, 10, 10647–10655.

[253] D. Zhao, J. Q. Xu, X. Q. Yi, Q. Zhang, S. X. Cheng, R. X. Zhuo and F. Li, *ACS Appl. Mater. Interfaces,* **2016**, 8, 14845–14854.

[254] H. Li and Z. Liu, *TrAC - Trends Anal. Chem.*, **2012**, 37, 148–161.

[255] A. Matsumoto, H. Cabral, N. Sato, K. Kataoka and Y. Miyahara, *Angew. Chemie Int. Ed.*, **2010**, 49, 5494–5497.

[256] H. Liu, Y. Li, K. Sun, J. Fan, P. Zhang, J. Meng, S. Wang and L. Jiang, *J. Am. Chem. Soc.*, **2013**, 135, 7603–7609.

[257] X. Zeng, G. Xu, Y. Gao and Y. An, *J. Phys. Chem. B*, **2011**, 115, 450–454.

[258] X. Sun, W. Zhai, J. S. Fossey and T. D. James, *Chem. Commun.*, **2016**, 52, 3456–3469.

[259] G. Springsteen and B. Wang, *Chem. Commun.*, **2001**, 17, 1608–1609.

[260] X. Bi, D. Li and Z. Liu, *Anal. Chem.*, **2015**, 87, 4442–4447.

[261] X. Liang and M. Bonizzoni, *J. Mater. Chem. B*, **2016**, 4, 3094–3103.

[262] X.-H. Wu, J.-G. Miao, Y.-Q. Miao and J.-R. Chen, *Spectrosc. Spectr. Anal.*, **2007**, 27, 1168–1171.

[263] W. Qin, F. Vautard and P. Askeland, *RSC Adv.*, **2014**, 5, 2457–2465.

[264] H. Otsuka, E. Uchimura, H. Koshino, T. Okano and K. Kataoka, *J. Am. Chem. Soc.*, **2003**, 125, 3493–3502.

[265] M. Pikulski, A. Hargrove, S. H. Shabbir, E. V. Anslyn and J. S. Brodbelt, *J. Am. Soc. Mass Spectrom.*, **2007**, 18, 2094–2106.

[266] H. Hou, Y. Zhao, C. Li, M. Wang, X. Xu and Y. Jin, *Sci. Rep.*, **2017**, 7, 1–8.

[267] M. V. Shirmanova, I. N. Druzhkova, M. M. Lukina, M. E. Matlashov, V. V. Belousov, L. B. Snopova, N. N. Prodanetz, V. V. Dudenkova, S. A. Lukyanov and E. V. Zagaynova, *Biochim. Biophys. Acta - Gen. Subj.*, **2015**, 1850, 1905–1911.

[268] M. Damaghi, J. W. Wojtkowiak and R. J. Gillies, *Front. Physiol.*, **2013**, 4, 1–10.

[269] M. Stubbs, L. Rodrigues, F. A. Howe, M. Stubbs, L. Rodrigues, F. A. Howe, J. Wang, K. Jeong, R. L. Veech and J. I. Griffiths, *Cancer Res.*, **1994**, 54, 4011–4016.

[270] A. Manuscript, **2013**, 24, 582–591.

[271] Y. Kato, S. Ozawa, C. Miyamoto, Y. Maehata, A. Suzuki, T. Maeda and Y. Baba, *Cancer Cell Int.*, **2013**, 13, 1–8.

[272] A. J. Bradley, Y. Y. Lim and F. M. Singh, *Clin. Radiol.*, **2011**, 66, 1129–1139.

[273] M. C. Brahimi-Horn, J. Chiche and J. Pouysségur, *J. Mol. Med.*, **2007**, 85, 1301–1307.

[274] A. L. Harris, *Nat. Rev. Cancer*, **2002**, 2, 38–47.

[275] J. Wu, W. Liu, J. Ge, H. Zhang and P. Wang, *Chem. Soc. Rev.*, **2011**, 40, 3483–3495.

[276] D. Arosio, F. Ricci, L. Marchetti, R. Gualdani, L. Albertazzi and F. Beltram, *Nat. Methods*, **2010**, 7, 516–518.

[277] V. M. Chauhan, G. Orsi, A. Brown, D. I. Pritchard and J. W. Aylott, *ACS Nano*, **2013**, 7, 5577–5587.

[278] A. Battisti, M. A. Digman, E. Gratton, B. Storti, F. Beltram and R. Bizzarri, *Chem. Commun.*, **2012**, 48, 5127–5129.

[279] J. Nandre, S. Patil, P. Patil, S. Sahoo, C. Redshaw, P. Mahulikar and U. Patil, *J. Fluoresc.*, **2014**, 24, 1563–1570.

[280] C. A. Huerta-Aguilar, P. Raj, P. Thangarasu and N. Singh, *RSC Adv.*, **2016**, 6, 37944–37952.

[281] D. Staneva, M. S. I. Makki, T. R. Sobahi, P. Bosch, R. M. Abdel-Rahman, A. Asiri and I. Grabchev, *J. Lumin.*, **2015**, 162, 149–154.

[282] P. Peng, L. Shi, H. Wang and T. Li, *Nucleic Acids Res.*, **2017**, 45, 541–546.

[283] R. Guo, B. Chen, F. Li, S. Weng, Z. Zheng, M. Chen, W. Wu, X. Lin and C. Yang, *Sensors Actuators, B Chem.*, **2018**, 264, 193–201.

[284] L. J. Nielsen, S. Eyley, W. Thielemans and J. W. Aylott, *Chem. Commun.*, **2010**, 46, 8929–8931.

[285] R. Bizzarri, C. Arcangeli, D. Arosio, F. Ricci, P. Faraci, F. Cardarelli and F. Beltram, *Biophys. J.*, **2006**, 90, 3300–3314.

[286] A. de Silva, *Coord. Chem. Rev.*, **2000**, 205, 41–57.

[287] B. Daly, J. Ling and A. P. De Silva, *Chem. Soc. Rev.*, **2015**, 44, 4203–4211.

[288] R. T. K. Kwok, C. W. T. Leung, J. W. Y. Lam and B. Z. Tang, *Chem. Soc. Rev.*, **2015**, 44, 4228–4238.

[289] H. L. Corwin, R. A. Bray and M. H. Haber, *Arch. Pathol. Lab. Med.*, **1989**, 113, 1256–1258.

[290] C. Galés, R. V. Rebois, M. Hogue, P. Trieu, A. Breit, T. E. Hébert and M. Bouvier, *Nat. Methods*, **2005**, 2, 177–184.

[291] R. Xu, Y. Wang, X. Duan, K. Lu, D. Micheroni, A. Hu and W. Lin, *J. Am. Chem. Soc.*, **2016**, 138, 2158–2161.

[292] J. M. Gostner, J. Zeisler, M. T. Alam, P. Gruber, D. Fuchs, K. Becker, K. Neubert, M. Kleinhappl, S. Martini and F. Überall, *Sci. Rep.*, **2016**, 6, 1–14.

[293] P. Pyykkö, *Angew. Chemie - Int. Ed.*, **2004**, 43, 4412–4456.

[294] T. Shirman, R. Kaminker, D. Freeman and M. E. Van Der Boom, *ACS Nano*, **2011**, 5, 6553–6563.

[295] T. Patiño, J. Soriano, E. Amirthalingam, S. Durán, A. González-Campo, M. Duch, E. Ibáñez, L. Barrios, J. A. Plaza, L. Pérez-García and C. Nogués, *Nanoscale*, **2016**, 8, 8773–8783.

[296] S. Durán, M. Duch, T. Patiño, A. Torres, O. Penon, R. Gómez-Martínez, L. Barrios, J. Esteve, C. Nogués, L. Pérez-García and J. A. Plaza, *Sensors Actuators, B Chem.*, **2015**, 209, 212–224.

[297] G. W. Cline and S. B. Hanna, *J. Am. Chem. Soc.*, **1987**, 109, 3087–3091.

[298] F. Cheng, L. J. Gamble, D. W. Grainger and D. G. Castner, *Anal. Chem.*, **2007**, 79, 8781–8788.

[299] M. Miksa, H. Komura, R. Wu, K. G. Shah and P. Wang, *J. Immunol. Methods*, **2009**, 342, 71–77.

[300] M. Ogawa, N. Kosaka, C. A. S. Regino, M. Mitsunaga, P. L. Choyke and H. Kobayashi, *Mol. Biosyst.*, **2010**, 6, 888.

[301] N. Li, X. Zhang, Q. Song, R. Su, Q. Zhang, T. Kong, L. Liu, G. Jin, M. Tang and G. Cheng, *Biomaterials*, **2011**, 32, 9374–9382.

[302] P. Mela, S. Onclin, M. H. Goedbloed, S. Levi, M. F. García-Parajó, N. F. Van Hulst, B. J. Ravoo, D. N. Reinhoudt and A. Van Den Berg, *Lab Chip*, **2005**, 5, 163–170.

[303] T. C. McDevitt, K. A. Woodhouse, S. D. Hauschka, C. E. Murry and P. S. Stayton, *J. Biomed. Mater. Res. - Part A*, **2003**, 66, 586–595.

[304] I. Rosenthal, *Opt. Commun.*, **1978**, 24, 164–166.

[305] M. Triesscheijn, P. Baas, J. H. M. Schellens and F. A. Stewart, *Oncologist*, **2006**, 11, 1034–1044.

[306] H. I. Lee and Y. J. Kim, *Colloids Surfaces B Biointerfaces*, **2016**, 142, 182–191.

[307] E. D. Sternberg, D. Dolphin and C. Brückner, *Tetrahedron*, **1998**, 54, 4151–4202.

[308] P. M. Antoni, A. Naik, I. Albert, R. Rubbiani, S. Gupta, P. Ruiz-Sanchez, P. Munikorn, J. M. Mateos, V. Luginbuehl, P. Thamyongkit, U. Ziegler, G. Gasser, G. Jeschke and B. Spingler, *Chem. - A Eur. J.*, **2015**, 21, 1179–1183.

[309] Z. Hu, Y. Pan, J. Wang, J. Chen, J. Li and L. Ren, *Biomed. Pharmacother.*, **2009**, 63, 155–164.

[310] L. Jayashankar, B. S. Sundar, R. Vijayaraghavan, K. S. Betanabhatla, C. Ajm, J. Athimoolam and K. S. Saravanan, *Pharmacologyonline*, **2008**, 1, 66–77.

[311] A. S. Lavado, V. M. Chauhan, A. Alhaj Zen, F. Giuntini, D. R. E. Jones, R. W. Boyle, A. Beeby, W. C. Chan and J. W. Aylott, *Nanoscale*, **2015**, 7, 14525–14531.

[312] S. Horie, H. Hasumi and N. Takizawa, *J. Biochem.*, **1985**, 97, 281–93.

[313] Q. Yu, W.-X. Xu, Y.-H. Yao, Z.-Q. Zhang, S. Sun and J. Li, *J. Porphyr. Phthalocyanines*, **2015**, 19, 1107–1113.

[314] M. Guleria, C. Kumar, T. Das, J. Amirdhanayagam, R. Sharma, H. D. Sarma and A. Dash, *Medchemcomm*, **2018**, 9, 657–666.

[315] A. Tillo, D. T. Mlynarczyk, L. Popenda, B. Wicher, M. Kryjewski, W. Szczolko, S. Jurga, J. Mielcarek, M. Gdaniec, T. Goslinski and E. Tykarska, *New J. Chem.*, **2017**, 41, 3586–3594.

[316] G. Jiang, W. Lei, Y. Hou and X. Wang, *New J. Chem.*, **2012**, 36, 2180–2183.

[317] Z. Yu, Q. Sun, W. Pan, N. Li and B. Tang, *ACS Nano*, **2015**, 9, 11064–11074.

[318] Q. Chen, Y. C. Chai, S. Mazumder, C. Jiang, R. M. Macklis, G. M. Chisolm and A. Almasan, *Cell Death Differ.*, **2003**, 10, 323–334.

[319] L.-L. Qu, D.-W. Li, L.-X. Qin, J. Mu, J. S. Fossey and Y.-T. Long, *Anal. Chem.*, **2013**, 85, 9549–9555.

[320] Y. Zhao, Z. B. Wang and J. X. Xu, *J. Biol. Chem.*, **2003**, 278, 2356–2360.

[321] A. N. Volkov, P. Nicholls and J. A. R. Worrall, *Biochim. Biophys. Acta - Bioenerg.*, **2011**, 1807, 1482–1503.

[322] T. I. Karu, *IUBMB Life*, **2010**, 62, 607–610.

[323] S. E. J. Bowman and K. L. Bren, *Nat. Prod. Rep.*, **2008**, 25, 1118–1130.

[324] S. S. Korshunov, B. F. Krasnikov, M. O. Pereverzev and V. P. Skulachev, *FEBS Lett.*, **1999**, 462, 192–198.

[325] G. C. Brown and V. Borutaite, *Biochim. Biophys. Acta - Bioenerg.*, **2008**, 1777, 877–881.

[326] S. Casalini, G. Battistuzzi, M. Borsari, C. A. Bortolotti, G. Di Rocco, A. Ranieri and M. Sola, *J. Phys. Chem. B*, **2010**, 114, 1698–1706.

[327] A. V. Kulikov, E. S. Shilov, I. A. Mufazalov, V. Gogvadze, S. A. Nedospasov and B. Zhivotovsky, *Cell. Mol. Life Sci.*, **2012**, 69, 1787–1797.

[328] H. Bayir, B. Fadeel, M. J. Palladino, E. Witasp, I. V. Kurnikov, Y. Y. Tyurina, V. A. Tyurin, A. A. Amoscato, J. Jiang, P. M. Kochanek, S. T. DeKosky, J. S. Greenberger, A. A. Shvedova and V. E. Kagan, *Biochim. Biophys. Acta - Bioenerg.*, **2006**, 1757, 648–659.

[329] F. Li, A. Srinivasan, Y. Wang, R. C. Armstrong, K. J. Tomaselli and L. C. Fritz, *J. Biol. Chem.*, **1997**, 272, 30299–30305.

[330] B. Zhivotovsky, S. Orrenius, O. T. Brustugun and S. O. Døskeland, *Nature*, **1998**, 391, 449–450.

[331] G. Paradies, G. Petrosillo, M. Pistolese and F. M. Ruggiero, *FEBS Lett.*, **2000**, 466, 323–326.

[332] A. K. Yagati, T. Lee, J. Min and J. W. Choi, *Colloids Surfaces B Biointerfaces*, **2012**, 92, 161–167.

[333] O. V. Akopova, L. I. Kolchinskaya, V. I. Nosar, V. A. Bouryi, I. N. Mankovska and V. F. Sagach, *Fiziol. Zh.*, **2012**, 58, 3–12.

[334] W. Zheng, N. Shan, L. Yu and X. Wang, *Dye. Pigment.*, **2008**, 77, 153–157.

[335] J. M. Strottmann, A. Stellwagen, C. Bryant and E. Stellwagen, *J. Biol. Chem.*, **1984**, 259, 6931–6936.

[336] A. Vázquez-Romero, N. Kielland, M. J. Arévalo, S. Preciado, R. J. Mellanby, Y. Feng, R. Lavilla and M. Vendrell, *J. Am. Chem. Soc.*, **2013**, 135, 16018–16021.

[337] G. P. C. Drummen, L. C. M. Van Liebergen, J. A. F. Op den Kamp and J. A. Post, *Free Radic. Biol. Med.*, **2002**, 33, 473–490.

[338] G. P. C. Drummen, B. M. Gadella, J. A. Post and J. F. Brouwers, *Free Radic. Biol. Med.*, **2004**, 36, 1635–1644.

[339] E. H. W. Pap, G. P. C. Drummen, V. J. Winter, T. W. a. Kooij, P. Rijken, K. W. a. Wirtz, J. a. F. Op den Kamp, W. J. Hage and J. a. Post, *FEBS Lett.*, **1999**, 453, 278–282.

[340] J. F. Brouwers, P. F. N. Silva and B. M. Gadella, *Theriogenology*, **2005**, 63, 458–469.

[341] A. Loudet and K. Burgess, *Chem. Rev.*, **2007**, 107, 4891–4932.

[342] A. Esteve-Núñez, J. Sosnik, P. Visconti and D. R. Lovley, *Environ. Microbiol.*, **2008**, 10, 497–505.

[343] H. B. F. DIXON and R. McINTOSH, *Nature*, **1967**, 213, 399–400.

[344] K. Park, *J. Control. Release*, **2014**, 178, 126.

[345] R. K. Upadhyay, *Biomed Res. Int.*, , DOI:10.1155/2014/869269.

[346] E. Boisselier and D. Astruc, *Chem. Soc. Rev.*, **2009**, 38, 1759.

[347] L. A. Dykman and N. G. Khlebtsov, *Acta Naturae*, **2011**, 3, 34–55.

[348] M. Kajiura, T. Nakanishi, H. Iida, H. Takada and T. Osaka, *J. Colloid Interface Sci.*, **2009**, 335, 140–145.

[349] G. F. Paciotti, L. Myer, D. Weinreich, D. Goia, N. Pavel, R. E. McLaughlin and L. Tamarkin, *Drug Deliv. J. Deliv. Target. Ther. Agents*, **2004**, 11, 169–183.

[350] R. Cui, H. Huang, Z. Yin, D. Gao and J. J. Zhu, *Biosens. Bioelectron.*, **2008**, 23, 1666–1673.

[351] D. Tang, R. Yuan and Y. Chai, *Anal. Chem.*, **2008**, 80, 1582–1588.

[352] A. T. N. Lam, J. Yoon, E. O. Ganbold, D. K. Singh, D. Kim, K. H. Cho, S. J. Son, J. Choo, S. Y. Lee, S. Kim and S. W. Joo, *J. Colloid Interface Sci.*, **2014**, 425, 96–101.

[353] D. O. Lapotko, E. Lukianova and A. A. Oraevsky, *Lasers Surg. Med.*, **2006**, 38, 631–642.

[354] H. S. Mader, P. Kele, S. M. Saleh and O. S. Wolfbeis, *Curr. Opin. Chem. Biol.*, **2010**, 14, 582–596.

[355] S. K. Balasubramanian, L. Yang, L. Y. L. Yung, C. N. Ong, W. Y. Ong and L. E. Yu, *Biomaterials*, **2010**, 31, 9023–9030.

[356] E. E. Connor, J. Mwamuka, A. Gole, C. J. Murphy and M. D. Wyatt, *Small*, **2005**, 1, 325–327.

[357] A. M. Alkilany and C. J. Murphy, *J. Nanoparticle Res.*, **2010**, 12, 2313–2333.

[358] and V. M. R. Subinoy Rana, Avinash Bajaj, Rubul Mout, *Adv. Drug Deliv. Rev.*, **2013**, 64, 200–216.

[359] R. Raghavendra, K. Arunachalam, S. K. Annamalai and M. Aarrthy, *Inernational J. Pharm. Pharm. Sci.*, **2014**, 6, 74–87.

[360] C. N. R. Rao, H. S. S. Ramakrishna Matte, R. Voggu and A. Govindaraj, *Dalt. Trans.*, **2012**, 41, 5089–5120.

[361] S. K. Hait and S. P. Moulik, *Curr. Sci.*, **2002**, 82, 1101–1111.

[362] T. A. Camesano and R. Nagarajan, *Colloids Surfaces A Physicochem. Eng. Asp.*, **2000**, 167, 165–177.

[363] M. Q. Ao, G. Y. Xu, Y. Y. Zhu and Y. Bai, *J. Colloid Interface Sci.*, **2008**, 326, 490–495.

[364] J. Yoon, S. K. Kim, N. J. Singh and K. S. Kim, *Chem. Soc. Rev.*, **2006**, 35, 355–360.

[365] L. Casal-Dujat, P. C. Griffiths, C. Rodríguez-Abreu, C. Solans, S. Rogers and L. Pérez-García, *J. Mater. Chem. B*, **2013**, 1, 4963–4971.

[366] C. Tarmann and A. Jungbauer, *J. Sep. Sci.*, **2008**, 31, 2605–2618.

[367] H. S. Schrekker, M. A. Gelesky, M. P. Stracke, C. M. L. Schrekker, G. Machado, S. R. Teixeira, J. C. Rubim and J. Dupont, *J. Colloid Interface Sci.*, **2007**, 316, 189–195.

APPENDIX

I Abbreviations and acronyms

^{1}H NMR – Proton Nuclear Magnetic Resonance Spectroscopy
AFM – Atomic Force Microscopy
APTES – Aminopropyltriethoxysilane
AuNP – Gold Nanoparticles
DLS – Dynamic Light Scattering
EDC –*N*-(3-Dimethylaminopropyl)-*N′*-ethylcarbodiimide hydrochloride
HRTEM – High Resolution Transmission Electron Microscopy
Cyt c – Cytochrome c
EtOH – Ethanol
DMSO – Dimethylsulfoxide
NHS –*N*-Hydroxysuccinimide
PDT – Photodynamic Therapy
ROS – Reactive Oxygen Species
SAM – Self-Assembled Monolayer
SEM – Scanning Electron Microscopy
SPR – Surface Plasmon Resonance
TEM – Transmission Electronic Microscopy
TESUD – 11-(Triethoxysilyl)undecanal
XPS – X-ray Photoelectron Spectroscopy
EG2OMs – 2-(1-Hydroxy)ethoxyeth-1-yl methanesulfonate
WGA – Wheat Germ Agglutinin
Con A – Concanavalin A
TGA – Triglycolamine
Dicty – Dictyostelium discoideum
BA – Boronic Acids
PBA – 4-Formylphenylboronic acid
STORM – Stochastic Optical Reconstruction Microscopy
TIRF – Total Internal Reflection Fluorescence
GlcNAc – N-acetyl-D-glucosamine
TBA salts – Tetrabutylammonium salts

II Fabrication of the microparticles

Fabrication process of the polysilicon microparticles

The initial substrates were 100 mm in diameter and 300 µm thick p-type (100) silicon wafers (**Figure A1**). First, a 1 µm thick thermal silicon oxide (SiO_2), layer was grown by thermal oxidation (1100°C) on top of the wafer. Second, 0.5 µm thick layer of polysilicon was deposited using low pressure chemical vapour deposition (LPCVD). Third, a 1 µm positive photoresist was spun onto the polysilicon layer. Then, exposure to UV light was performed through the photomask to define the lateral dimensions of the chips and their shape. The resist was developed and baked (30 min, 200 °C). Fourth, the top 0.5 µm thick polysilicon layer was dry-etched with C_2F_6 and CHF_3 mixture. The polysilicon etching was stopped at the silicon oxide layer and the photoresist was removed by plasma etching. Finally, the chips were released by a sacrificial etching of the silicon oxide layer in vapors of 40% HF for 40 min. The polysilicon microparticles were suspended by ultrasound in absolute ethanol (1mL), centrifuged, and collected at 14,000 rpm for 5 min.

Fabrication process of the bi-functional (polysilicon-chromium-gold) microparticles

A p-type silicon wafer of 100 mm in diameter was chosen for the fabrication process. On top of this wafer, a 1 µm thick silicon oxide was deposited as a sacrificial layer (**Figure A2**). Then, a 400 nm thick polysilicon layer using SiH_4 was deposited with a flow rate of at 40 sccm (580 °C, 350 mTorr) as a first layer using LPCVD. Then, a photolithographic step was performed which created a photoresist inverse pattern. The next step was the deposition of a 30 nm thick chromium layer as an adherent interlayer and then, a 100 nm thick gold layer was deposited as the second layer, both layer were deposited by evaporation method. Next, a lift-off process was carried out for 2 min in an acetone solution. A polysilicon dry etching was performed for 25 s using the gold as a mask defining the microparticles. Finally, the microparticles were released by a sacrificial etching of the silicon oxide in vapors of HF (49 %) for 40 min. The microparticles were then suspended in 96 % of absolute ethanol, centrifuged at 14,000 rpm for 5 min and were collected in eppendorfs for further studies.

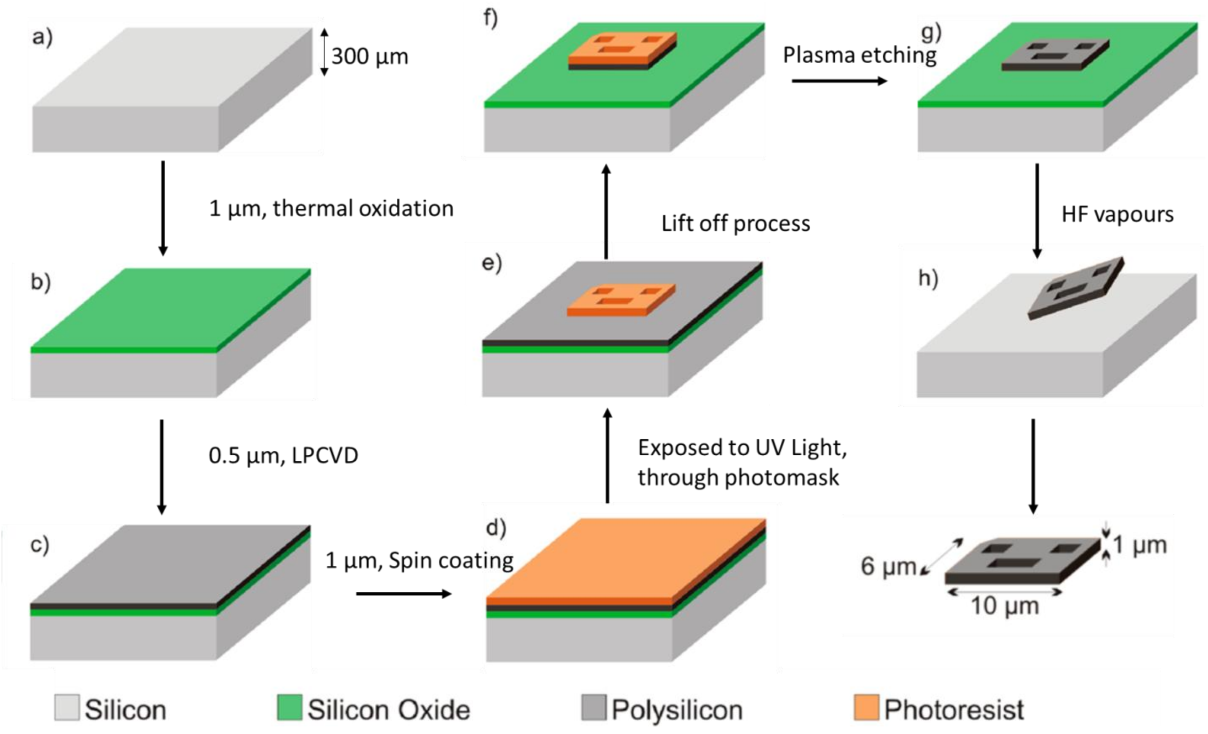
a)
300 µm
1 µm, thermal oxidation
b)
0.5 µm, LPCVD
c)
1 µm, Spin coating
d)
Exposed to UV Light, through photomask
e)
Lift off process
f)
Plasma etching
g)
HF vapours
h)
6 µm
1 µm
10 µm
Silicon
Silicon Oxide
Polysilicon
Photoresist

Figure A1. Detailed sequence of steps for the fabrication of the microparticles (barcodes) [156]. Similar protocol was adopted for the fabrication of star and disc shaped microparticles. **(a)** Silicon wafer as initial substrate, **(b)** thermal growth of a silicon oxide as a sacrificial layer, **(c)** deposition of a polysilicon layer, **(d)** covering of the wafer with photoresist by spin coating, **(e)** photolithographic step, **(f)** polysilicon patterning by dry etching, **(g)** removal of photoresist by plasma etching, **(h)** release of microparticles by HF etching of the silicon oxide sacrificial layer, and finally, **(i)** centrifugation and collection of the barcodes inside an eppendorf (not showed in the figure). Similar steps were performed to fabricate the following polysilicon microparticles, star shaped, disc shaped and 3 µm square shaped microparticles.

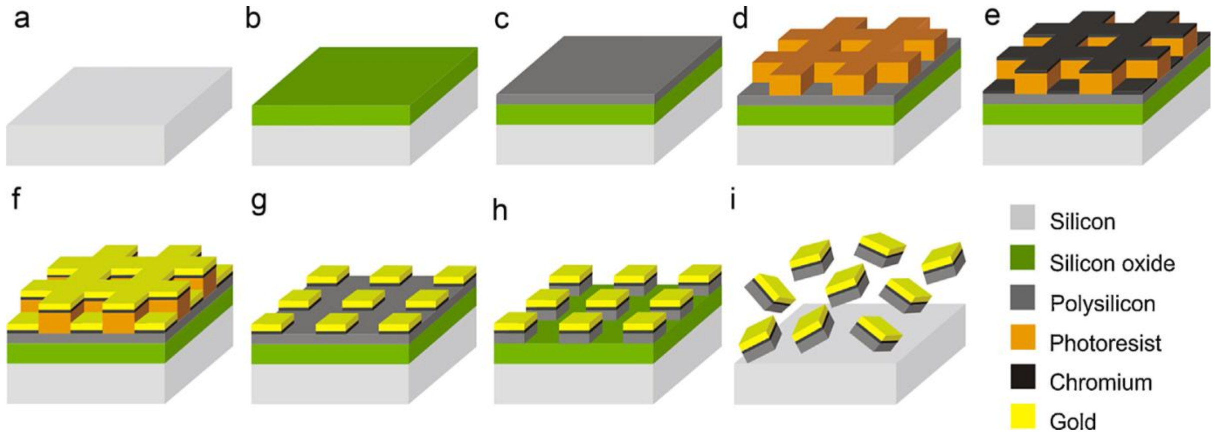

Figure A2. Detailed sequence of steps for the fabrication of the bi-functional (polysilicon–chromium–gold) microparticles [296]. **(a)** microparticles were fabricated using a silicon wafer as a starting material. **(b)** a 1 µm silicon oxide as a sacrificial layer and **(c)** a 400 nm polysilicon as a first layer was deposited. **(d)** A photoresist layer was spun and exposed to UV light to define the dimensions of the microparticles. **(e)** A 30 nm thick chromium and **(f)** a 100 nm thick gold layers were deposited by sputtering process as an adherent and second layer, respectively. **(g)** A lift-off process was performed and **(h)** the polysilicon layer was patterned using the chromium and gold layer as masks. Finally, **(i)** the bi-functional microparticles were released in HF vapours and suspended in ethanol.

III. Dissemination of Results

PUBLICATIONS

- **Macrocyclic imidazolium-based amphiphiles for the synthesis of gold nanoparticles and delivery of anionic drugs**
  Journal of Colloid and Interface Science **2015**, 437, 132-139 (**13 citations**)
  Impact factor – 5.091, **Q1**
  Authors: **Ezhil Amirthalingam**, Mafalda Rodrigues, Lucía Casal-Dujat, Ana C. Calpena, David B. Amabilino, David Ramos-López and Lluïsa Pérez-García.

- **Polysilicon-chromium-gold intracellular chips for multi-functional biomedical applications**
  Nanoscale **2016**, 8, 8773-8783 (**5 citations**)
  Impact factor – 7.233, **Q1**
  Authors: Tania Patiño, Jorge Soriano, **Ezhil Amirthalingam**, Sara Durán, Arántzazu González-Campo, Marta Duch, Elena Ibáñez, Leonardo Barrios, Jose Antonio Plaza, Lluïsa Pérez-García and Carme Nogués.

CONGRESS CONTRIBUTIONS

Oral Communications:

- **E. Amirthalingam**, A. González-Campo and L. Pérez-García. "Multi-functionalization of microparticles for cancer diagnostics". Self-Assembly 2016. *June 2016.* ICMAB-CSIC, Bellaterra, Spain.

- **E. Amirthalingam**, J. Soriano, S. Durán, J. A. Plaza, I. Mora-Espí, A. González-Campo and L. Pérez-García. "Reactive oxygen species (ROS) using bi-functional microparticles for cancer theranostics". Novena Trobada de Joves Investigadors dels Països Catalans. *February 2016.* Perpignan, France.

- **E. Amirthalingam**, J. Soriano, S. Durán, J. A. Plaza, I. Mora-Espí, A. González-Campo and L. Pérez-García. "Reactive oxygen species (ROS) using bi-functional microparticles for cancer theranostics". XII Simposio de Investigadores Jóvenes Químicos RSEQ-Sigma Aldrich. *November 2015.* Barcelona, Spain.

Poster Communications:

- **E. Amirthalingam**, J. Soriano, S. Durán, J. A. Plaza, I. Mora-Espí, A. González-Campo and L. Pérez-García. "Intracellular Reactive oxygen species (ROS) sensing using bi-functional microparticles for cancer theranostics". NanoBio&Med 2015, *November 2015.* Barcelona, Spain.

- O. Penon, **E. Amirthalingam**, M.E. Alea, S. Duran, A. Gonzalez, J.A. Plaza, M.L. Perez-Garcia. "Immobilization of porphyrin derivatives into micro and nanoparticles as potential delivery agents for photodynamic therapy". Fourth International Conference on Multifunctional, Hybrid and Nanomaterials. *March 2015.* Sitges,Spain.